# Single wall carbon nanotube growth from bimetallic nanoparticles : a parametric study of the synthesis up to potential application in nano-electronics.

Salomé Forel

NNT : 2017SACLX094

# Thèse de doctorat de l'Université Paris-Saclay préparée Ecole Polytechnique

Ecole doctorale n°573
Interfaces : Approches Interdisciplinaires, Fondements, Applications et Innovation
Spécialité de doctorat : Physique

par

**Mme. Salomé Forel**

## SWCNT growth from bimetallic nanoparticles : a parametric study of the synthesis up to potential applications in nano-electronics

Thèse présentée et soutenue à l'Ecole Polytechnique, le 06.12.17.

Composition du Jury :

| | | |
|---|---|---|
| Mrs. | Catherine JOURNET-GAUTIER<br>Professeur | (Rapportrice) |
| Mrs. | Céline TERNON<br>Maitre de Conférences | (Rapportrice) |
| Mrs. | Martine MAYNE-L'HERMITE<br>Chercheur CEA | (Examinatrice) |
| M. | Erik DUJARDIN<br>Directeur de Recherche CNRS | (Président du jury) |
| M. | Costel-Sorin Cojocaru<br>Directeur de Recherche CNRS | (Directeur de thèse) |
| Mrs. | Laure Catala<br>Professeur | (Invitée) |
| M. | Talal Mallah<br>Professeur | (Invité) |
| Mrs. | Annick Loiseau<br>Directrice de Recherche ONERA | (Invitée) |

# Remerciement

Ce travail de thèse a été réalisé au laboratoire de Physique et interface des couches minces, en étroite collaboration avec l'équipe de chimie inorganique (LCI) de l'institut de Chimie Moléculaire et de matériaux d'Orsay (ICMMO) et le laboratoire d'études des microstructures (LEM) de l'ONERA. Je remercie donc les directeurs de ces trois laboratoires, Pere Roca, Talal Mallah et Alphonse Finel qui m'ont permis de travailler dans de bonnes conditions. Je remercie aussi les équipes administratives et supports de chacun des laboratoires, sans qui le bon déroulement de cette thèse n'aurait pas été possible.

Je tiens à remercier Catherine Journet et Céline Ternon d'avoir accepté d'évaluer ce travail de thèse en tant que rapportrices. Je remercie aussi Martine Mayne, (déjà présente pour mon rapport de mi-thèse et dont les conseils m'ont été précieux pour finir ce travail) et Erik Dujardin d'avoir accepté de faire partie de mon jury. Merci aussi à Laure, Annick et Talal d'avoir aussi accepté de faire partie des invités de ce jury. Je vous remercie pour votre implication dans l'évaluation de ces travaux et pour la discussion scientifique qui a suivi la présentation. Je voudrais aussi remercier sincèrement Costel, mon directeur de thèse. Costel, je te remercie pour tout ce que tu as pu m'apprendre sur le plan scientifique, pour ta disponibilité énorme et pour la liberté de choix que tu m'as laissée. Merci aussi pour ton soutien dans les moments plus difficiles de ce travail. J'ai été ravie de pouvoir partager ces trois ans de thèse sous ton encadrement.

Ce travail de thèse a été un travail collaboratif, et j'ai eu la chance d'être encadrée et soutenue par de nombreuses personnes et je voudrais les en remercier.

Merci Laure pour ton soutien et ton aide incommensurable tout au long de ce travail de thèse, merci pour ton investissement dans ma thèse et pour tous les bons moments passés aux laboratoires mais aussi ailleurs... Je voudrais aussi remercier Talal, merci de m'avoir permis de travailler sur un de tes projets, pour les nombreuses discussions que nous avons pu avoir et les conseils que tu as pu me donner. Merci aussi à Vincent, qui m'a fait découvrir ce sujet lors de mon stage de M2 et qui m'a aidé et conseillé tout au long de cette thèse. Je remercie aussi Annick, pour son aide et son soutien durant cette thèse. Hakim et Christophe (et Yann), merci pour toutes les discussions, et vos travaux théoriques qui m'ont permis de mieux comprendre le sujet et de débloquer de nombreuses interprétations de ma thèse, merci aussi pour les relectures de chapitres de ma thèse.

J'ai aussi eu la chance de collaborer avec Jean-Sebastien Lauret durant cette thèse que je voudrais sincèrement remercier pour le nouvel aspect des nanotubes

que j'ai pu découvrir dans son équipe. Merci pour ton soutien, tes explications et pour la relecture de ma thèse cet été pendant tes vacances. Je remercie aussi Géraud et Lucile pour leurs aides pour toutes les manips optiques.

Merci aussi à tous les gens qui ont contribué à ce travail, Ileana, pour les super clichés TEM, pour sa capacité à remonter le moral derrière le microscope, pour sa disponibilité incroyable, son savoir-faire hors pair pour trouver les SWCNT sur une grille et pour les moments passés hors du laboratoire. Côté TEM, je remercie aussi Frédéric pour ces bons moments passés entre le Titan à Centrale et le Zeiss au LEM, pour les belles images qu'on a eu mais aussi pour les bigoûts, et pour la découverte des nombreuses impuretés qui peuplent parfois les grilles ( tu as du plomb dans ton process ? Euh. . . ). Merci à Amandine pour sa maitrise du transfert sur grille. Merci aussi à Leandro pour son aide durant cette thèse, pour notre collaboration sur la partie capteur et pour le Fernet. Merci aussi à Costel, Léo et Gary d'avoir veillé au bon fonctionnement des manips et d'avoir toujours fait le nécessaire en cas de problème. Merci à Sandra pour les images AFM, à François Brisset pour les analyses MEB-EDS et Christian pour la RPE (mais pas que. . . ).

Je voudrais aussi remercier Alice (#jumelledethese), avec qui j'ai pu travailler tout au long de ma thèse grâce à la proximité de nos sujets. Sur le plan scientifique, les échanges que nous avons pu avoir (sans oublier les mails en majuscule), les nombreuses relectures que tu as faites et l'aide mutuelle pendant les manips (film à l'appui) m'ont énormément apporté. Sur un plan, plus personnel, même si ce n'est pas mon genre de m'étaler dans mes remerciements de thèse, ça a vraiment été un réel bonheur de partager ces trois ans, les chambres de conférences et voyages en avion (ahaha), ces nombreuses bières, grosses marrades et restaurants BONS.

Un très grand merci à tous mes collègues au PICM, plus particulièrement ceux de mon équipe, l'équipe Nanomade (Costel, Mariam, Leo, Fatima, Lucie, Leandro, Ileana , Mihai, Marc et Didier) aux autres permanents et plus particulièrement, Eric P. , Fred, Jerôme, Holger, Yvan, Jean-Charles, Cyril, Gaël, Bérengère, Pere, Erik J. , Rasvigor, Jean-Luc, Laurence, Gaby, Fabienne. Merci aussi aux non permanents, et plus particulièrement Loïc (mon consultant préféré) Mariam et Fatima, mes co-bureaux (toujours là en cas de besoin), Anna, Stan, Jean, Chiara, Alba, Federico (mention concerto), Ronan, Paul, Aliénor, Thomas (alias Sanghyuk), Gwen (mention spéciale olympiade des doctorants), Guillaume, Rafaël et Chloé ( mention spéciale PPT/orthographe !).

Un immense merci aussi à tous mes collègues du LCI pour tous les bons moments passés aux laboratoires (autour d'un repas de Noël, d'un barbecue, de manip, d'un cleaning day ou écriture d'article) et ailleurs. . . Merci aux permanents, je citerais plus particulièrement Talal, Vincent, Katell, Yu, Gulia, Anne, Amélie, Ally et Fred ;). Un merci un peu spécial à Zak (pour son « bonjour » chuchoté dans le couloir), Sandra et surtout Laure et Jean-No pour les bons moments passés entre bières, concerts ou dîners. Merci aussi à tous les non-permanents du LCI et plus particulièrement merci à Feng, Fatima, Arnaud, et Guillaume. Merci aussi à Benjamin (alias JIM Henry Cabane) pour

nos discussions philosophiques, photo-montages et écriture de livres. Clémence, qui me suit depuis la prépa et veille sur moi les grands soirs, Antoine pour ton sens de l'humour hors du commun et ta langue natale, un français pas comme les autres, Irene pour les incessantes et toujours joyeuses propositions pour aller au mexicain, Khaled pour tes conseils et toutes ces bières (allez on en prend une dernière), à Mauri pour son initiation aux ABPs et les innombrables BBQ, à Linh pour ses blagues en anglais (did you get it ?) et sa cuisine, à Marie pour son fromage sur toast au RU. Merci aussi à Virgile, pour tous ces bons moments jusqu'en haute-Savoie, merci d'avoir toujours pris mes appels de PANIQUE quand j'étais en T.P. . Merci à Christian (même si ton changement de statut au cours de ma thèse te classe désormais hors des non permanents), merci pour tes blagues (surtout celle du KIWI), merci aussi de m'avoir beaucoup soutenu, d'avoir relu une bonne partie de ma thèse et d'accepter de relire (et souvent de réécrire, après m'avoir dit « écoute c'est super, mais ») tous les mails importants que j'ai à envoyer en anglais.

Merci aussi à tous mes collègues du Lem et plus particulièrement Amandine (doriiii), Frederic (et aussi pour ton talent sur photoshop et les mails détentes), Léonard ( flagship is . . . ), Étienne, Hakim, Annick, François, Jean-seb, Juan, Armelle, Cora, Henri, Gader, Hocine, Juba, Yann, Mathieu et Benoît.

Pour finir, je voudrais surtout remercier ma famille qui m'a toujours encouragée et qui s'est déplacée en nombre pour ma soutenance. Tout d'abord merci à Nadine et Bruno, mes supers parents pour leurs soutiens inconditionnels durant toutes ces années, merci aussi à mon frère adoré Ulysse, à mes chers grands-parents (Monique, Marie-France, Édouard et Roger qui malheureusement n'aura pas pu voir la fin de ce travail de thèse), mon oncle, Jean-Yves, ma tante Pascale, Jeannot et mes cousines préférées Marie, Cloé et Lou. Merci aussi aux amis proches de ma famille, Philippe et Catherine, Sophie et Christophe, Jean-Marc, et Stephan et Patricia, mes parents d'adoption lors de ma prépa à Lyon.

Un très grand merci aussi à tous mes amis hors du labo, pour leurs soutiens durant ces trois ans, et qui ont engendré beaucoup des bons moments qui ont ponctués cette thèse. Je commencerais par Ambroise pour son amour et son soutien absolus pendant cette thèse. Merci aussi à Thibault, sans qui ces années à l'ENS n'auraient pas été les mêmes. Merci aussi à mes amies d'enfance, Nini (qui m'a même fait l'honneur de venir) Mathilde, Hugo, Eudox et Martin (+ ferdi) et ma joyeuse bande de copains du collège Justin, Cyrille (qui devient mon préféré puisqu'il est venu à ma thèse), Simon et Valérian. Merci aussi à mes amis rencontrés à l'ENS, Mathilde, Benjamin, Clémence, Loulou, FX pour nos soirées, surtout au pantalon. Un grand merci aussi à Jérémie (meilleur binôme de TP au monde et pas que. . . ) et à Claire (+Guillaume) (pour ces nombreux moments ensemble à rédiger nos thèses respectives, c'était top) et pour nos nombreuses sorties. Enfin merci à Pégase qui a mis quelques paillettes dans ces trois ans de thèse.

# Contents

# Introduction

The constant effort of the scientific community to explore the infinitely small, has lead during the last decades of the twentieth century, to the observation and design of materials at a nanometric scale. Two complementary new fields of research flourished : nanoscience and nanotechnology. The first one concerns the understanding of the new properties appearing at this small size. The second one refers to the study of the fabrication process and the characterization of such nano-structures. These two domains are rapidly expanding and many applications are imagined, tested and used in more and more domains from medicine to electronics.

It's in this context that carbon nanotubes have been brought to the forefront by Iijima while observing the synthesis of fullerenes. Since this observation, carbon nanotubes have been studied from every angle, highlighting their exceptional mechanical, electronic, optical and thermal properties. Their small size combined with their unique properties, makes them excellent candidates in a wide spectrum of applications in the nanotechnology. A carbon nanotube is an hexagonal pattern of carbon atoms rolled-up into the form of a tube. But there are many different ways to arrange the hexagonal carbon lattice into a cylinder, these different arrangements defines the chirality of the tube. Therefore many possibles structures of nanotubes exist. The scenery becomes much more complicated because opposite physical properties can be found from one structure to another. For instance, as a function of its chirality, a carbon nanotube can be metallic or semiconducting with a large range of gaps depending on its diameter. For the majority of the imagined applications, homogenous and specific properties are required, especially in electronics where the use of both semiconducting and metallic materials at the same time, drastically degrades the performance of the devices.

Today, one of the major obstacle for further integration of carbon nanotubes relies on the difficulty to obtain high quantity of an unique structure of carbon nanotubes possessing thus similar properties. Two complementary research directions have been developed to reach this aim : sorting tubes after their synthesis and respectively, realizing selective synthesis. Up to now, despite the great efforts made in both sides, none of them provide solutions attractive enough to enable widespread of nanotube in the microelectronic industry. Recent sorting techniques succeed in isolating single chirality tubes, however the scalability and the cost of this techniques is still a strong barrier for industrial applications. Moreover, in many cases, this post-synthesis treatment induces structural defects in the SWCNT (Single Wall Carbon Nanotube), limiting their performances.

Few quite chiral selective synthesis of SWCNTs through chemical vapor deposition (CVD) has been up to now reported. CVD method is well adapted to industrial applications due to its low cost and ease of use. Up to now only 6 different chiralities have been obtained ((6,5), (9,8), (6,6), (12,6), (16,0), (14,4) ) and only the (6,6) synthesis has been reported to be 100% selective but with a very poor yield. Then the use of post-synthesis sorting is still needed. Unfortunately, the mechanism leading to selectivity is still a totally open question preventing great progress in the domain.

In this context, the first aim of this thesis was to contribute to the understanding of the observed selectivity in synthesis.

The first chapter of this thesis will briefly describe the main structural, physical, and optical properties of the SWCNT. Then the experimental strategy employed in the literature for obtaining structurally controlled nanotubes during the synthesis will be detailed. Finally few applications of carbon nanotubes will be presented.

Recent progresses in the structural control during the synthesis of SWCNTs have in common the use of bimetallic catalysts. Although the exact role played by the bimetallicity is not fully understood, it seems to be a key point for selective synthesis. One of the main difficulties to understand the impact of the metal catalyst on the SWCNT growth is the lack of characterizations of the catalysts, and the drastically different CVD processes and set-ups used in various reported studies, thus preventing easy comparison.

We are then proposing to develop a new generic method, based on coordination chemistry, for designing small bimetallic nanoparticle catalyst of various compositions, in the same range of sizes and under the same conditions for their preparation and use. The description of this new method of catalyst synthesis will constitute the third chapter of this thesis.

SWCNTs growth from this new catalysts will be performed. From a synthesis run to another, all CVD parameters are fixed except the temperature. Then the impact of both metal catalyst nature and of the growth temperature upon the final characteristics of the as-grown SWCNTs can be analyzed. We used mainly Raman spectroscopy for the characterizations. This parametric study will be the center of the fourth chapter. According to the various tested parameters, we have observed modifications of the yield, the diameters distribution and metal/semiconducting type ratio. Possible mechanism leading to these variations will be proposed in connection with the theoretical calculations and the experimental results available in the literature.

In a fifth chapter, we will describe the integration of the SWCNTs synthesized from various growth conditions in a basic bottom-gate SWCNT-FET (Field Effect Transistor) device. The performance of the transistors will be analyzed but the main objective of this integration was to confirm that different populations of SWCNTs' characteristics have been obtained. In a last short section, preliminary results for the use of as-fabricated SWNT-FETs, for the detection of $NO_2$ will be presented.

Finally, we have also modified the SWCNT properties by functionalizing them. New hybrid-SWCNT systems with a pyrene-ruthenium photo-active complex were obtained. This is the focus of the last chapter. When this chromophore is used into functionalized SWCNT-FET devices, a modulation up to three orders of magnitude in the device's conduction is observed under specific light illumination. In a first section, the ability of the chromophore to stack on the SWCNT sidewall will be discussed. Then a characterization of the response of the hybrid system in FET devices will be presented. Finally, based on theoretical calculation and the experimental observations, a mechanism of the interaction between SWCNT and the chromophore will be proposed.

# Chapter 1

# State of art

Carbon is well-known for having many allotropic forms such as graphite, diamond, graphene, fullerenes or nanotubes, each of them being used for their specific properties in a large field of applications. The accidental discovery of fullerenes in 1985 [1] marks the start of a new range of applications for carbon : nanotechnology. Moreover, the observation of multi-walls carbon nanotubes (MWCNT) during fullerene synthesis by Iijima in 1991 [2] efficiently promoted the research on this new form of carbon : nanotubes. We have to note that nano-sized carbon tubular structures had been observed as early as 1952 by Radushkevich et al. [3] and in 1976 by Oberlin et al. [4], without creating a significant breakthrough.

In 1993, the formation of single-wall carbon nanotubes (SWCNTs) has been reported by two independent teams [5] [6]. SWCNTs are the central focus of this work. Very fine and various physical effects are nowadays under study, here, we only briefly describe the background knowledge necessary for the understanding of the following chapter. First of all, we will describe the single wall carbon nanotubes structure in order to understand how it is closely linked to their unique properties. Then the different ways to control the SWCNT structure will be discussed. Finally, a last part will be devoted to the various applications of SWCNTs and their functionalization with organic molecules.

## 1.1 Physical properties of carbon nanotubes

### 1.1.1 Structural properties

Graphene (a monolayer of graphite) is commonly used as a starting point to describe the structure and properties of carbon nanotubes. Structurally, carbon nanotubes can be seen as one (SWCNT) or several (MWCNT) concentric sheets of graphene rolled into a cylinder as shown in Figure 1.1.

Graphene has a two-dimensional lattice of $sp^2$ hybridized carbon, leading to a honeycomb structure of carbon atoms. Two non-equivalent sites (named A and B on Figure 1.2) are necessary to define the unit cell of graphene. The honeycomb structure can be seen as a hexagonal Bravais lattice with a two

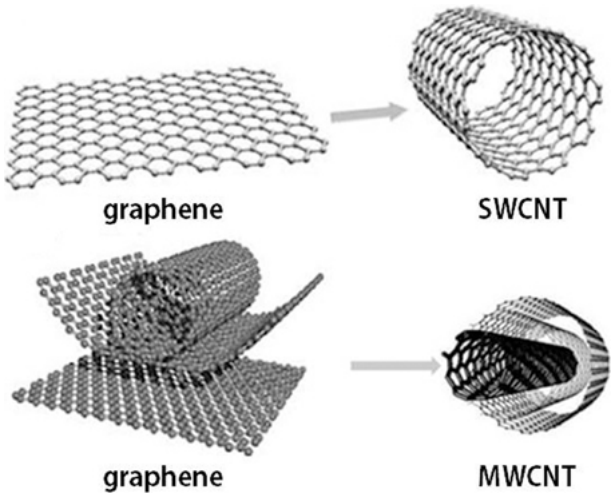


FIGURE 1.1: Single-wall carbon nanotube and multi-wall carbon nanotube from [7].

atoms basis, where $\vec{a_1}$ and $\vec{a_2}$ are the basis vector of the Bravais lattice (see Figure 1.2). In an orthogonal base ( $\vec{ex}$, $\vec{ey}$)

$$\vec{a_1} = \frac{\sqrt{3}}{2b}\vec{ex} - \frac{1}{2b}\vec{ey}; \qquad \vec{a_2} = \frac{\sqrt{3}}{2b}\vec{ex} + \frac{1}{2b}\vec{ey} \tag{1.1}$$

$b = \sqrt{3}a$ ; a is the carbon-carbon atom distance.

Obtaining carbon nanotubes from graphene consists in rolling the sheet in order to merge two crystallographically equivalent sites (A or B). Thus the $sp^2$ carbon hybridization is preserved. Hence, a SWCNT can be entirely defined with a unique vector named the chirality vector $\vec{C_h}$, which only depends on a set of two integers (n,m), the chiral indices.

$$\vec{C_h} = n\vec{a_1} + m\vec{a_2} \tag{1.2}$$

As shown in Figure 1.2 three different structural types of SWCNT can be generated

- Armchair tube where n=m;
- Zigzag tube where m=0 ;
- Chiral tube for all the other possibilities;

Chiral indices also allow the definition of the translation vectors $\vec{T}$, parallel to the tube axis and perpendicular to $\vec{C_h}$

$$\vec{T} = t_1\vec{a_1} + t_2\vec{a_2} \tag{1.3}$$

As

$$\vec{T}.\vec{C_h} = 0 \tag{1.4}$$

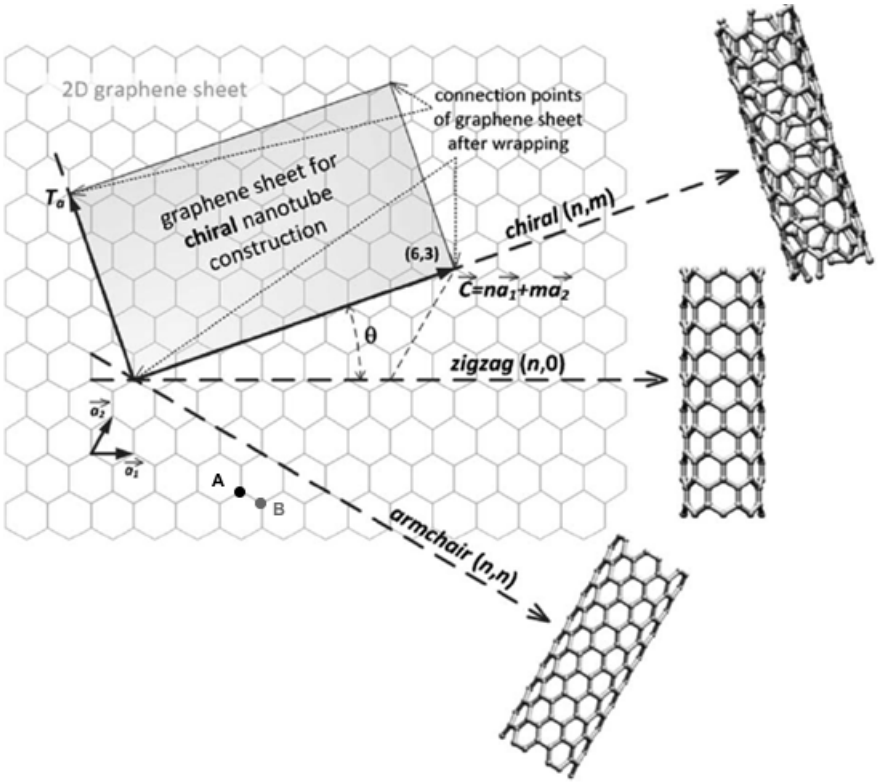


FIGURE 1.2: Geometrical construction of a (6,3) SWCNT; from [8]

We find

$$t_1 = \frac{2m+n}{d_r}; \qquad t_2 = -\frac{2n+m}{d_r} \tag{1.5}$$

Where $d_r$ is the least common denominator of 2m+n and n+2m. $\overrightarrow{C_h}$ and $\overrightarrow{T}$ define the unit cell of a carbon nanotube.

The angle between $\overrightarrow{a_1}$ and $\overrightarrow{C_h}$ named chiral angle $\theta$ (comprised between 0° and 30°) is also used to describe a nanotube :

$$cos(\theta) = \frac{2n+m}{2\sqrt{n^2+m^2+nm}} \tag{1.6}$$

The perimeter of a nanotube corresponds to the norm of the chiral vector. Then the diameter ($d_t$) of the nanotube can be expressed as :

$$d_t = \frac{||\overrightarrow{C_h}||}{\Pi} = \frac{b}{\pi}\sqrt{n^2+m^2+nm} \tag{1.7}$$

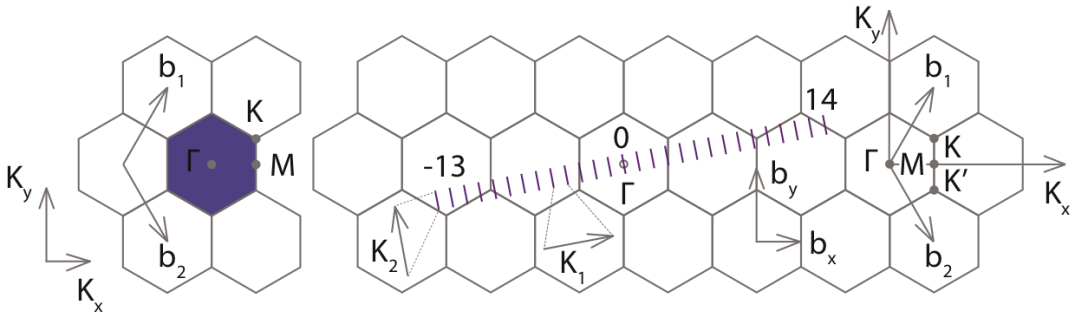


FIGURE 1.3: Representation of the hexagonal reciprocal lattice of Graphene. **Left** : The Brillouin zone (shaded hexagon) **Right** : The parallel equidistant lines represent the cutting lines for the (4, 2) nanotube adapted from [9].

### Description in the reciprocal space

In the reciprocal space of graphene (unrolled nanotube), the unit cells of SWCNT can be described with $\vec{K_1}$ and $\vec{K_2}$ related to $\vec{C_h}$ and $\vec{T}$ by the following equations

$$\vec{C_h}.\vec{K_1} = 2\pi; \qquad \vec{C_h}.\vec{K_2} = 0; \qquad \vec{T}.\vec{K_1} = 0; \qquad \vec{T}.\vec{K_2} = 2\pi; \tag{1.8}$$

Leading to

$$\vec{K_1} = \frac{1}{N}(-t_2\vec{b_1} + t_1\vec{b_2}); \qquad \vec{K_2} = \frac{1}{N}(-m\vec{b_1} + n\vec{b_2}) \tag{1.9}$$

Where $\vec{b_1}$ and $\vec{b_2}$ are the primitive vector of the reciprocal space of graphene and N is the number of hexagons contained in the SWCNT unit cell

$$N = \frac{|\vec{C_h} \wedge \vec{T}|}{|\vec{a_1} \wedge \vec{a_2}|} = \frac{2(n^2 + nm + m2)}{d_r} \tag{1.10}$$

The first Brillouin Zone (BZ) of graphene is defined as shown in Figure 1.3, the BZ center is named $\Gamma$ when the two apex of the hexagon are named K and K'.

Since a carbon nanotube can be described as a quasi-1D system, a quantification of the wave vector $\vec{k_t}$ will occur in the circumference direction in order to preserve the continuity of the wave function. The authorized value for $\vec{k_t}$ must respect the following condition

$$\vec{k_t}.\vec{C_h} = 2\pi p \tag{1.11}$$

Where p is an integer and varies from 0 to N-1 to respect the periodic condition of the SWCNT construction. Conversely, no periodic condition is necessary along the tube axis, and as a consequence :

$$\vec{k_t}.\vec{K_2} = \frac{k}{|\vec{k_2}|}; \qquad -\pi/T < k < \pi/T \tag{1.12}$$

Finally, we obtain N allowed $\vec{k_t}$ vector for a carbon nanotube, in the form of the following equation

$$\vec{k_t} = \mu\vec{k_1} + k\frac{\vec{k_2}}{|\vec{k_2}|}; \qquad \mu = 0, 1...N-1; \qquad -\pi/T < k < \pi/T \tag{1.13}$$

### 1.1.2 Electronic properties

#### Graphene band diagram

The electronic structure of SWCNTs can be modeled from the graphene band structure. Commonly, the band structure of graphene is obtained by using the electron tight binding (TB) approach to the carbon $\pi$ electrons [10]. The sigma level is far away from the Fermi level, and therefore these electrons don't affect the properties that will be considered in this work. Thus they can be neglected in further calculations [11]. By limiting the interaction to the first nearest neighbors and neglecting the overlap matrix elements (s) between neighboring $p_z$ orbitals, the dispersion relation is [11] :

$$E(K) = \pm\gamma_0\sqrt{1 + 4cos(\frac{\sqrt{3}ak_x}{2})cos(\frac{k_ya}{2}) + 4cos^2(\frac{k_ya}{2})} \tag{1.14}$$

Where $\gamma_0$ is the transfer integral, which corresponds to the energy of the interaction between the $p_z$ orbitals of the first nearest neighbor carbon atoms.

Figure 1.4 shows the band structure obtained from equation 1.14. The valence band and the conduction band are tangential at each K and K' points of the BZ. These particular positions are located at the Fermi level ($E_f$), which is the zero-energy reference. Thus graphene is a semiconductor with a zero gap, also called "semi-metal".

Close to the Fermi level, the energy dispersion relationship can be considered as linear [11] :

$$E^{\pm}(\delta k) \simeq \pm(\frac{\sqrt{3}a}{2}\gamma 0||\delta k||) \tag{1.15}$$

In this approximation, the $\pi$ and $\pi^*$ bands (conduction band and valence band respectively) were symmetric around the Fermi level. Nevertheless, DFT calculations forecast that the antibonding band should be located at higher energy. Other formalisms, but more complicated, and outside the scope of this introduction, can be used to take account for this asymmetry [13].

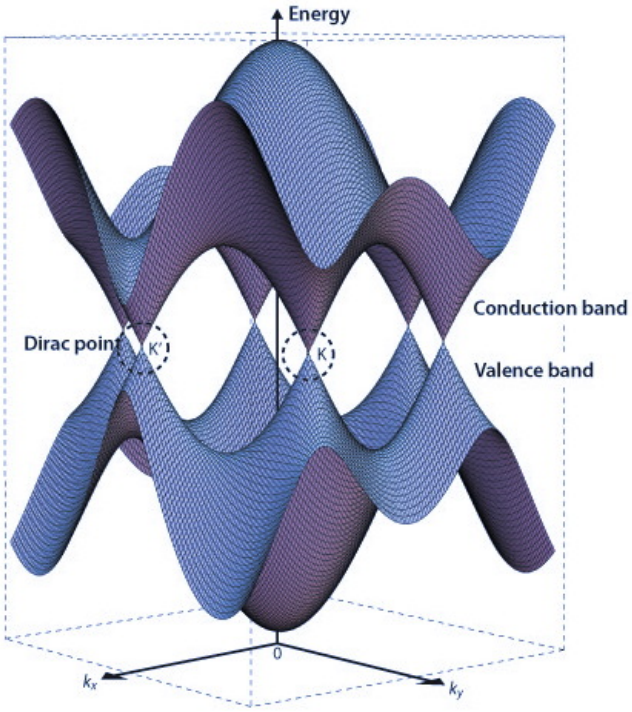


FIGURE 1.4: Graphene band diagram from [12].

### Carbon nanotubes' band diagram

The carbon nanotube band diagram can be obtained from that of graphene by using the zone folding approximation. The idea is to impose the periodic boundary conditions of the carbon nanotube to the dispersion curve of graphene. As shown before, allowed wave vectors of a carbon nanotube are quantized perpendicularly to the tube axis. Limiting the graphene band diagram only to these particular allowed values of wavevectors leads to the nanotube band diagram. Thus, under this approximation the dispersion relation of carbon nanotubes can be found by injecting the nanotube's wavevectors (see equation 1.13) into the graphene dispersion.

$$E_{Nt} = E_{graphene}(\mu\vec{k_1} + k\frac{\vec{k_2}}{|\vec{k_2}|}) \tag{1.16}$$

with

$$\mu = 0, 1...N-1; \qquad -\pi/T < k < \pi/T$$

Examples of wavevector of two zig-zag nanotubes ((10,0) and (9,0)) are given in Figure 1.5. In the case of the (9,0) SWCNT (Figure 1.5a), we observe that the $\vec{k}$ vector intersects the K point of the BZ, where the graphene dispersion is zero, rendering the nanotube metallic. On the other hand, no $\vec{k}$ vector of the (10,0) nanotube intersect the K point (Figure 1.5b). Consequently, a gap opening occurs leading to a semiconducting nanotube.

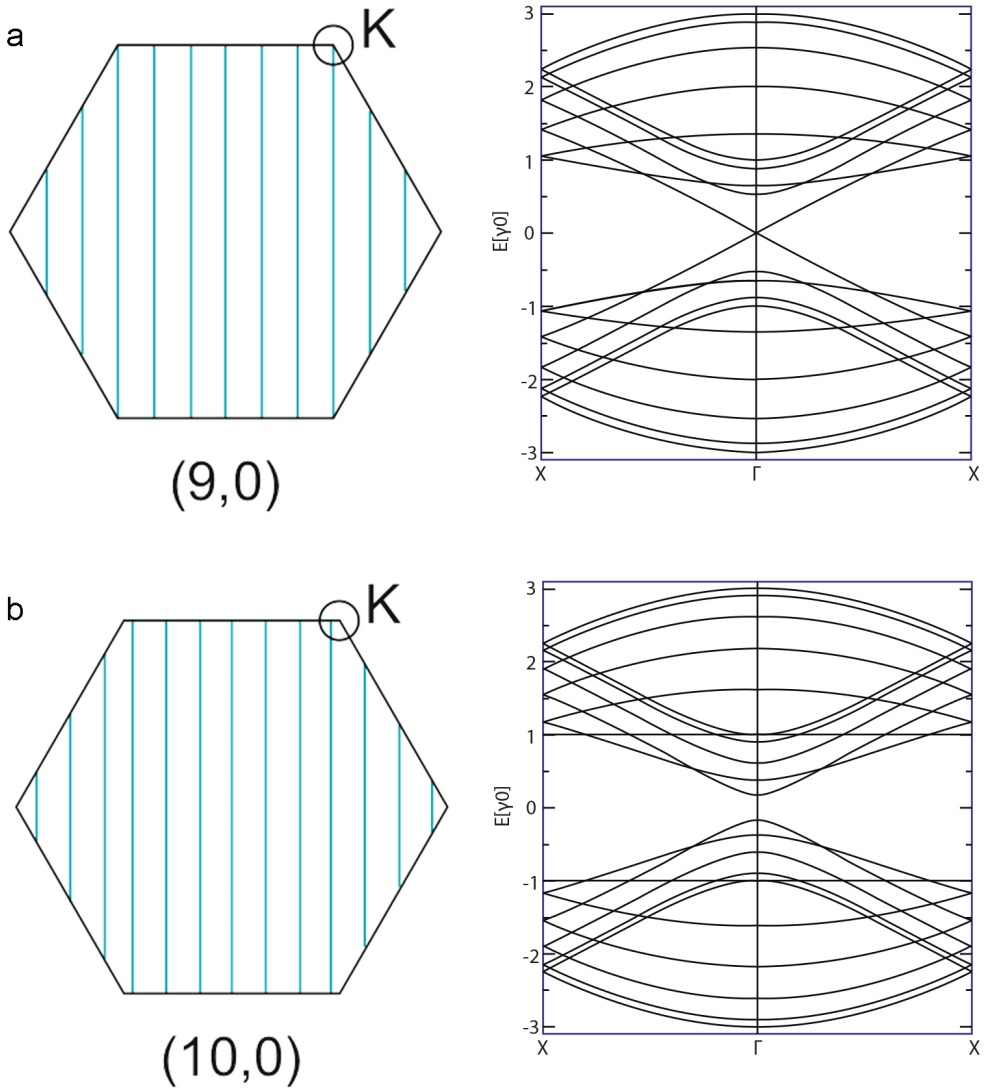


FIGURE 1.5: **a Left** First Brillouin zone of a graphene sheet together with allowed states for a (9,0) tube. **Right** : band structure for a (9,0) zigzag nanotube within the zone-folding model. The Fermi level is located at zero energy. **b Left**: First Brillouin zone of a graphene sheet together with allowed states for a (10,0) tube. **Right**: band structure a for a (10,0) zigzag nanotube within the zone-folding model. Adapted from [11].

Finally, when $\vec{k_t}$ (allowed $\vec{k}$ vectors for a nanotube) intersects a K point, the nanotube will be metallic otherwise the nanotube will be semiconducting. In order to obtain a more convenient law, we will search a condition on n and m, to obtain a metallic tube, i.e. , when $\vec{k_t}$ intersects a K point.

Coordinate of K point can be defined by $\overrightarrow{K\Gamma} = \dfrac{\vec{b_1} - \vec{b_2}}{3}$

The intersection between $\vec{k_t}$ with K leads to the following relation :

$$\begin{aligned} \overrightarrow{KT}.\overrightarrow{C_h} &= 2\pi p \\ \frac{\vec{b_1}-\vec{b_2}}{3}.(n\vec{a_1}+m\vec{a_2}) &= 2\pi p \\ 2\pi\frac{n-m}{3} &= 2\pi p \\ \frac{n-m}{3} &= p \\ p \in \mathbb{N} \Rightarrow mod(n-m,3) &= 0 \end{aligned} \tag{1.17}$$

Thus, the electronic behavior of a SWCNT can be determined by analyzing its n and m indices :

- If mod(n-m,3) = 0 the nanotube is metallic
- If mod(n-m,3) $\neq$ 0 the nanotube is semi-conductor.

Figure 1.6 presents a summary of the metallic and semiconducting families of carbon nanotubes according to their chiral numbers.

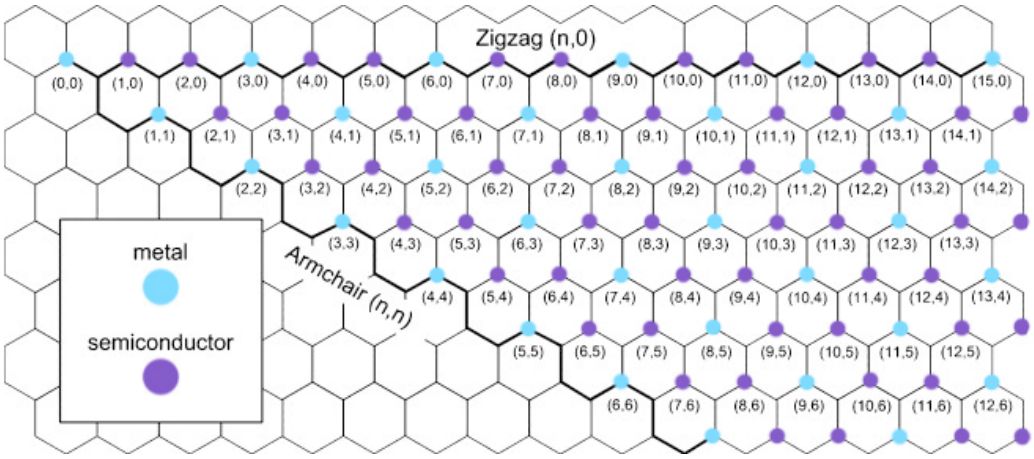


FIGURE 1.6: Periodic table of carbon nanotube.

### Density of states

The density of state (DOS) represents the number of states available to be occupied for a given energy interval. Figure 1.7 presents the DOS of metallic (9,0) and semiconducting (10,0) nanotubes. These DOS show singularities in $1/\sqrt{(E)}$ named Van Hove singularities (VHS), characteristic of a 1D system. An expression for the DOS, in the tight-binding approximation can be found in [11].

As shown in Figure 1.7a in the example of a (9,0) SWCNT, for metallic nanotubes, the density of states is non-zero at the Fermi level. In contrast, the DOS at fermi level is zero for semiconducting nanotubes (see Figure 1.7b). For

a semiconducting nanotube, close to a K point by using equation 1.16 and 1.15 one can find :

$$E_{gap} = \frac{2a\gamma 0}{d_t} \tag{1.18}$$

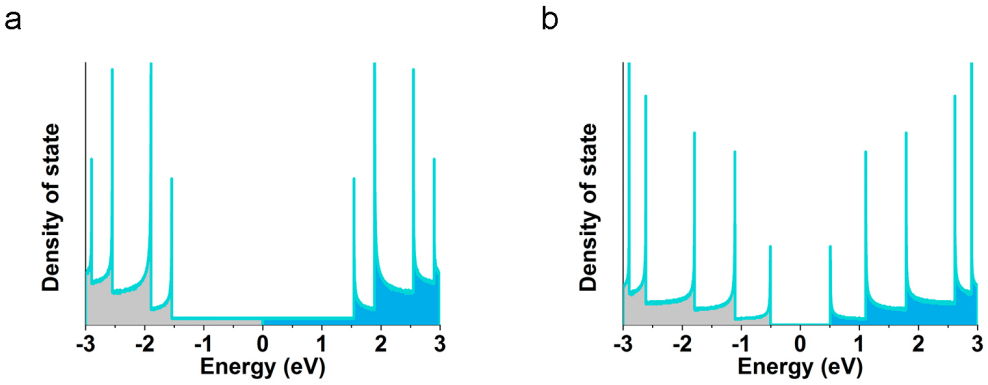


FIGURE 1.7: Calculated DOS of **a** (9,0) metallic nanotube **b** (10,0) semiconducting nanotube ; from [14].

### 1.1.3 Optical properties

In a first approximation, optical transitions of a nanotube can be observed between Van Hove singularities. Transitions for semiconducting and metallic tubes are named $S_{ij}$ and $M_{ij}$ respectively, where i and i' refer to the $i^{th}$ Van Hove singularity in the valence band and $j^{th}$ in the conduction band (see Figure 1.8a).

#### Absorption and photoluminescence spectroscopy

Several experiments such as photoluminescence (PL) and absorption give access to these optoelectronic transitions. Figure 1.8 presents an example of absorption and photoluminescence spectra of a sample of CoMoCat® (95% (6,5)) single wall carbon nanotubes. On the absorption spectra (see Figure 1.8b), the energy range of transitions of metallic and semiconducting SWCNTs are indicated by the shaded areas. The different peaks arise from the different chiralities present in the sample. In this CoMoCat sample, the $S_{11}$ (982 nm) and $S_{22}$ (571 nm) transitions of (6,5) nanotubes are easily identifiable. In case of semiconducting nanotubes, optical transitions are also accessible through photoluminescence (PL) experiments. Figure 1.8d shows a typical photoluminescence excitation (PLE) map corresponding to the sample of Figure 1.8b. The sample was excited between 350 and 650 nm. For each excitation step, the corresponding PL spectrum between (900 and 1500 nm) were recorded. The result is plot in the form of a map where the x axis represents the emission wavelength, the y axis

represents the excitation wavelength and the color represents the normalized number of photons. We can see here that an excitation at 571 nm leads to an emission at 982 nm. The scheme in Figure 1.8c explains the PLE map : the nanotube absorbs on the $S_{22}$ state, then a non-radiative relaxation to the $S_{11}$ occurs which finally relaxes by emitting a photon. One can note that in the presented experiment only transitions between symmetrical singularities are observed. Other experiments, resolved in polarization can give access to other transitions [15, 16].

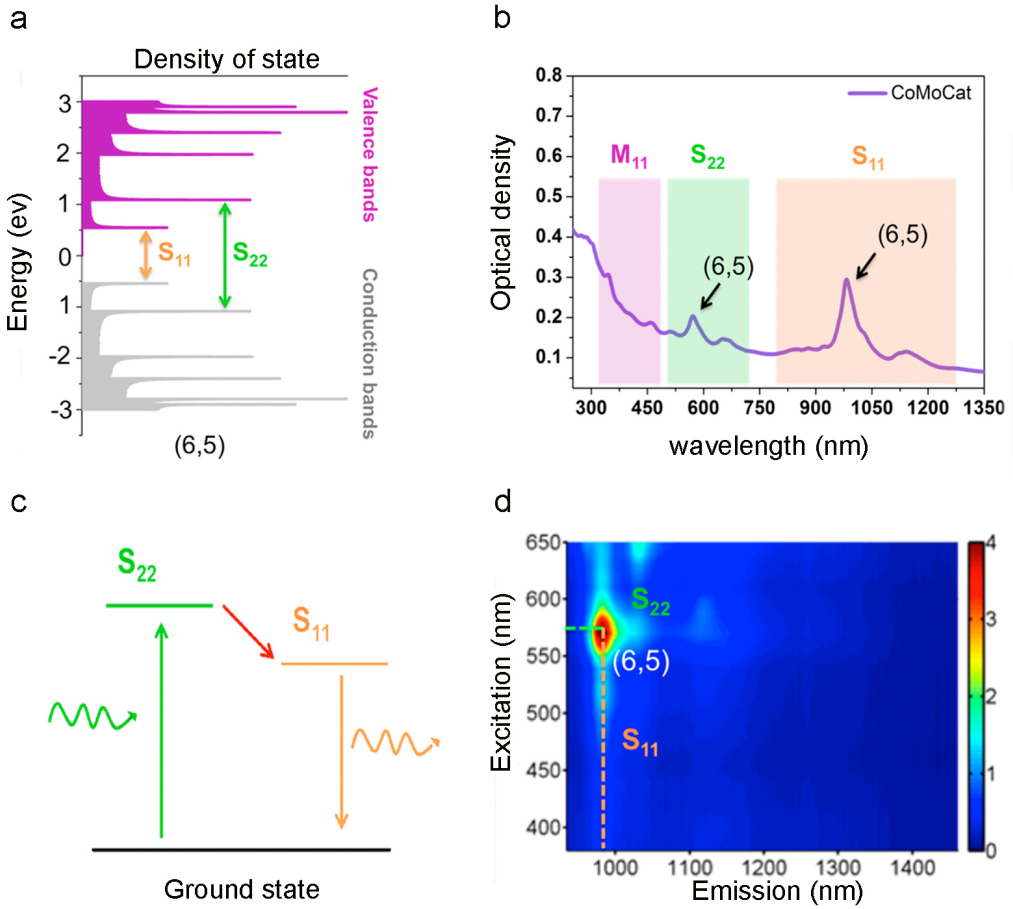


FIGURE 1.8: **a** Calculated DOS of (6,5) SWCNT from [14] **b** Optical absorption of a CoMoCat sample dispersed in sodium cholate micelle **c** Scheme of excitonic state of SWCNTs **d** PLE map of CoMoCat sample dispersed in sodium cholate micelle.

### Link with the electronic structure

Using the approximations presented before, when close to the fermi level, the linearity of the electronic dispersion of graphene shows that the energy of VHS can be expressed by the following expression :

$$E_i = q\frac{a\gamma 0}{\sqrt{3}d_t} \tag{1.19}$$

Where

- q = i for a semiconducting nanotube
- q = 3i for a metallic nanotube

Energy between two symmetrical Van Hove singularities can be expressed as :

$$S_{ii} = 2i\frac{a\gamma 0}{\sqrt{3}d_t} \tag{1.20}$$

$$M_{ii} = 6i\frac{a\gamma 0}{\sqrt{3}d_t} \tag{1.21}$$

Using this approximation, the energy of transitions only depends on the diameter of the tube (see equation 1.20 and 1.21). But, experimentally, the measurement of these optical transitions ($S_{ii}$ and $M_{ii}$) highlights a deviation from the simple $1/d_t$ law. We will try to briefly explain three major causes responsible for the mismatch between calculated and measured optical transition.

First, away from the K point, the linear approximation is no longer valid. A deviation from linearity is observed, and the iso-energy lines that contour around K or K' point present a trigonally distorted shape called “trigonal wrapping” (TW) [17, 18]. This TW effect, is among others, responsible for the "family behavior", which describes a systematic chirality dependence of the transition of semiconducting SWCNTs according to the values 1 (type I on Figure 1.9) or 2 (type II on Figure 1.9) of their mod(n-m, 3) [19].

Upon, the tight-binding approximation, Schrödinger equation was solved for a one-particle Hamiltonian. Thus electron-electron interaction and hole/electron interaction are not considered, but in carbon nanotubes, electrons or holes are highly confined because of their quasi-1D structure. These interactions become no longer negligible [20] and must be taken into account for the calculation of optical transition energies. In order to improve the calculation of transition energy and obtain a better fit with the experimental result, this effect has been highly studied in the literature under the name “many body effect” [21].

Finally, in the folding zone approximation, only interactions between $\pi$ orbitals are considered. The curvature of the graphene sheet for obtaining carbon nanotubes leads in fact to hybridization between $\sigma$ and $\pi$ orbitals. This hybridization can be taken on board by extending the basis set to the atomic s, $p_x$, $p_y$, and $p_z$ orbitals [22] leading to Extended Tight Binding model (ETB). In this model, a DFT framework is used to calculate the transfer and overlap integrals [23].

Various plots of optical transitions energies (calculated or measured) versus the diameter of the nanotube are presented in the literature. These plots are named Kataura plot, in reference to the first scientist who established it [24].

In this thesis, we used Kataura's plot provided by Saito's group [14]. The $E_{ii}$ are calculated from ETB model combined with many body correction [25, 26].

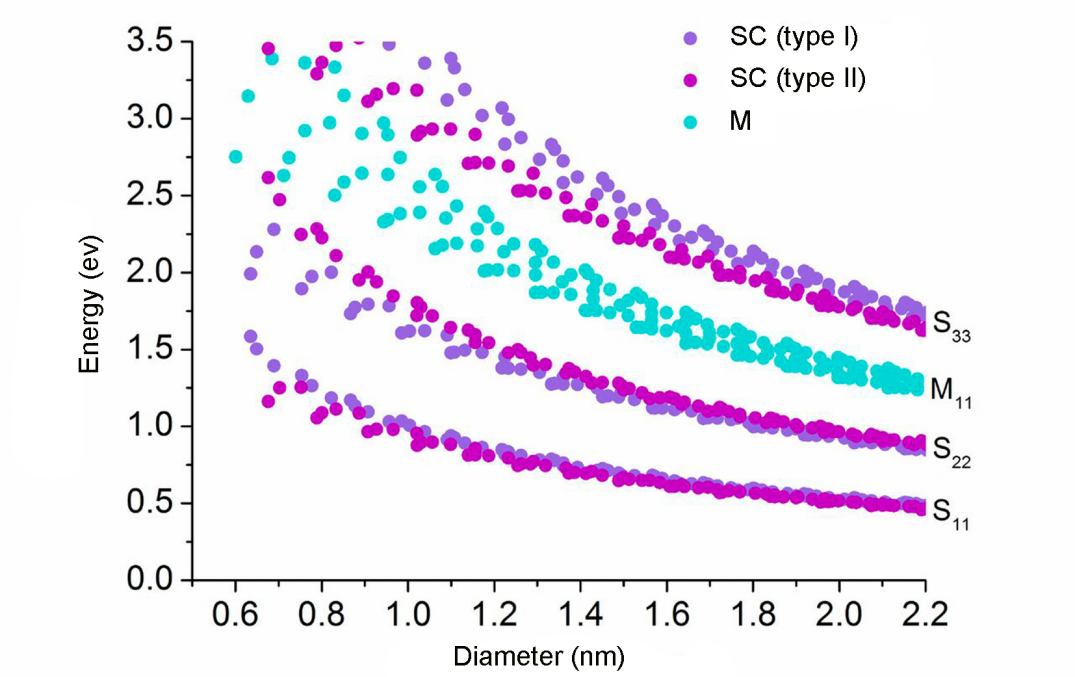


FIGURE 1.9: Energy transition of SWCNTs versus diameter established by Saito group [25, 26].

## 1.2 Carbon nanotube synthesis methods

### 1.2.1 High temperature synthesis methods

The first methods to produce carbon nanotubes were the so-called high temperature synthesis methods. These methods rely on the sublimation of graphite under a controlled atmosphere followed by a rapid condensation of carbon atoms leading among other to carbon nanotube structure formation. Temperatures involved in this synthesis techniques are between 3000°C and 4000°C in order to sublimate the graphite target. Two approaches are currently used: electric arc discharge and laser ablation.

#### Arc electric discharge

Electric Arc discharge was the method originally used by Iijima when he observed carbon nanotubes [2]. In this technique, a difference of potential is applied between two graphite electrodes. The electrodes are brought closer together until the formation of an electric arc discharge. In the plasma region generated between the two electrodes, the temperatures can reach 6000°C, allowing the sublimation of graphite. When the anode is composed of pure

graphite, fullerenes, amorphous carbon, graphitic sheets and multi-wall carbon nanotubes are formed [27]. The anode electrode can also be filled with a mixture of graphite and metals powder. Under these conditions, SWCNT can be obtained. First experiments used iron [5] and cobalt [6] as metal catalysts. Various gaseous atmospheres during the synthesis [28] and various catalysts (metals or mixtures of metals) have also been tested [29]. Electric arc discharge is an inexpensive technique and allows the formation of SWCNT with few structural defects.

### Laser ablation

Laser ablation was first developed by Smalley's group to synthesize fullerenes [1], and carbon nanotubes [30]. A pulsed or continuous laser beam is used to sublimate a graphite target placed in a hot furnace under an inert atmosphere. The buffer gas carries the produced species to a water-cooled trap, which is used as a collector [31]. As in the arc discharge synthesis, addition of metal catalyst (usually cobalt, nickel, platinum and bimetallic catalyst [32]) is an absolute prerequisite to obtain SWCNTs. Many efforts have been done to improve yields, chirality or diameter dispersion [33] by playing with different parameters such as catalysts [34], laser power and furnace temperature [33, 35–37]...

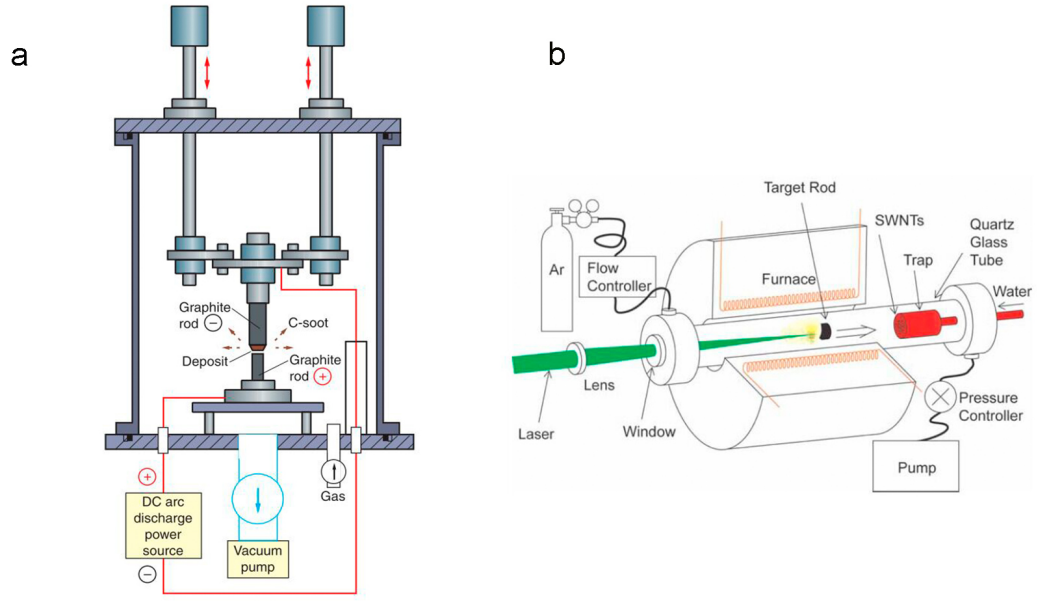


FIGURE 1.10: Schematic view of **a** arc electric discharge set up **b** laser ablation set up from [38].

### Conclusion

High temperature methods enable the formation of good quality carbon nanotubes with high yield. The main advantage of the high temperature methods is

the highly crystalline quality of the carbon nanotubes obtained. However, many other allotropic forms of carbon are co-produced (soot, fullerenes, amorphous carbon...). As a result many purifications steps are necessary for obtaining pure CNTs. Moreover, control of CNTs' structure, that is particularly desired for application remains difficult [39]. Especially, because of the difficulties to control the growth conditions in such processes that are highly outside thermodynamic equilibrium. Consequently, high temperature synthesis is less and less employed in favor of chemical vapor deposition (CVD) processes, that will be described in the following section.

### 1.2.2 Chemical Vapor Deposition synthesis

#### Principles

CVD rests on the transformation of a gaseous precursor into a solid material over the surface of a catalyst, which can be in the form of nanoparticles or films. In fact, syntheses of "carbon filaments" (now called multi-walls carbon nanotubes) have been already achieved using this technique, for instance by Oberlin and co-workers [4] well before Iijima's report in 1991. The catalyst-assisted CVD (CCVD) allows the formation of carbon nanotubes with good yield at lower temperatures with an improved control of growth conditions.

The most simple implementation of a CCVD technique consists of passing a flow of a carbonaceous gas precursor through a tube furnace (600-1200°C) where metal catalyst nanoparticles are present.

Many variations of the classical CVD exist such as PECVD (plasma enhanced chemical vapor deposition) or HFCVD (hot filament chemical vapor deposition). In PECVD, plasma is used to increase the dissociation rate of hydrocarbons molecules over the catalyst surface, allowing lower growth temperature [40].

In HFCVD, a hot tungsten filament is used to pre-decompose the gas precursor into more active gaseous molecules/radicals [41] in order to lower the synthesis temperature without loss in crystalline quality. This is also the technique that we chose for the synthesis of SWCNTs in this thesis.

In the frame of the CCVD, the metal catalyst can be formed in situ in the gas phase (floating catalyst synthesis) or deposited on a support material (supported catalyst synthesis).

In a floating catalyst synthesis, a gaseous metal catalyst precursor is used. Usually the precursor is an organometallic compound (ferrocene [42], iron pentacarbonyl [43], $Ni(acac)_2$ [44]...). The process can take place in the gas phase entirely or partially. For instance, the HiPco (for High Pressure catalytic decomposition of Carbon monoxide catalyst) process, developed by Nikkolaev and co-workers [45] is exploited for mass production of SWCNTs with diameters between 0.7 to 1.1 nm.

In case of supported catalyst, the catalyst material is previously deposited on a support material such as silicon oxide, alumina, quartz or sapphire. Catalyst material is usually under the form of either :

- a thin film of metal deposited by sputtering or vacuum evaporation;
- a layer of metallic complex deposited by coating;
- a layer of nanoparticles deposited by coating from a suspension or through a sputtering method.

**Metal catalyst** Iron, nickel and cobalt nanoparticles, which present finite carbon solubility, are the most common catalyst used for SWCNT synthesis although other transition metal such as Pd, Pt, Cu [46], Ru [47], Mn [48],Cr [49], Mo [49], noble metals (Ag, Au [46]), elements of the carbon family (diamond [46], Ge and Si [50]) or lanthanides (Sm [49] Gd or Eu [51]) have also been successfully used. Mixtures of metals have also been tested and several studies tend to prove that bimetallicity is a key point for structurally control SWCNT synthesis. For instance, The CoMoCat synthesis developed by E. Resasco and co-workers [52] works with an in situ formed cobalt nanoparticles as catalyst on a molybdenum carbide under CO atmosphere. SWCNTs with a very small diameter and a majority of (6,5) nanotubes are obtained.

**Carbon precursor** Numerous carbon-containing gases can be chosen for the synthesis of carbon nanotubes, such as alkanes, alcohols or aromatic hydrocarbons. However, methane, ethylene, acetylene and carbon monoxide remain the most widely used precursors. Jourdain et al. [53] discussed the thermodynamic stability of various precursors by using Gibbs free energy diagrams. These considerations must be taken into account in order to optimize the CVD parameters such as pressure or temperature to ensure efficient gas precursor decomposition.

**Conclusion** CCVD, being closer to a thermodynamic equilibrium, is a very versatile method. Indeed, huge varieties of catalysts, precursors gases, substrates, and growth conditions can be developed. Moreover SWCNTs can be synthesized under many forms, such as powder, films of different thicknesses where SWCNTs can be aligned, dispersed or percolated. Patterned substrates can also be used to selectively induce growth in desired predefined places. Carbon nanotubes production at an industrial scale is nowadays performed using this technique.

### 1.2.3 Growth mechanisms

#### Description of the mechanisms

Growth mechanism of CNTs by CVD processes is not yet fully understood despite the great efforts done in theoretical calculation and the development of in-situ growth observation by TEM. Anyhow, a few general steps based on vapor–liquid–solid model (VLS) [54] re-adapted by Baker [55] for the growth of carbon fibers are commonly accepted. First, the catalytic decomposition of the carbon precursor on the catalyst surface occurs. Then the diffusion of released carbon through a liquid particle takes place until carbon saturation. This carbon saturation leads to solid carbon precipitation, which can give rise to formation of carbon nanotubes. Bulk diffusion or surface diffusion of carbon through the catalyst particle are still poorly understood as well as the physical state of the catalyst particle during this process [56]. Hypothesis of particles in solid form during the growth has been validated in some cases by in-situ HRTEM measurements and lead to formulation of a vapor-solid-solid (VSS) model (see Figure 1.11). In-situ TEM observations demonstrated that carbon nanotube growth starts with the formation of a carbon cap at the surface of the catalyst particle [57], confirming the hypothesis formulated by Dai [58]. Numerical simulations support that the formation of carbon caps in the particle's surface occurs after carbon saturation in the particle [59–61].

In the case of the supporting catalyst approach (see previous paragraph), the catalyst-support interaction plays a determinant role. Two different mechanisms are generally proposed, a root-growth (see Figure 1.12b) in the case of a strong catalyst-support interaction or a tip-growth in the case of a weak catalyst-support interaction (see Figure 1.12a). Cassell and co-workers observed experimental evidences of these two mechanisms [62].

The exact mechanism of the growth is still ambiguous and several routes are considered. Many questions concerning the detailed mechanism of the growth such as carbon/metal interaction, carbon diffusion into the catalyst particle, and the mechanism that drives the addition of carbon atoms during the growth are still open and will not be detailed in this part. However, as the understanding of the mechanism is determinant to achieve selective synthetic procedure, we propose a short discussion of the general state of the catalyst during CNT's growth.

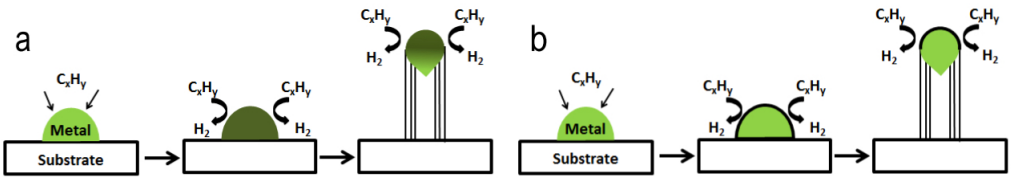


FIGURE 1.11: **a** Vapor-Liquid-Solid mechanism **b** Vapor-Solid-Solid mechanism from [63]

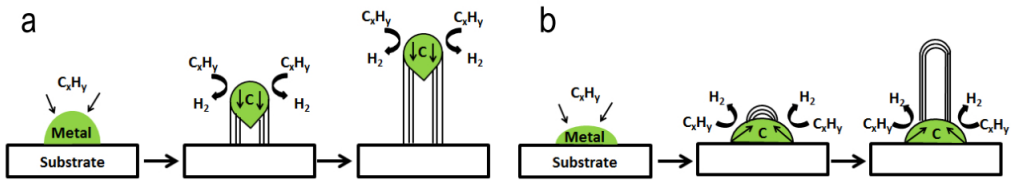


FIGURE 1.12: **a** tip-growth model **b** root-growth from [63]

.

### Metal catalyst and carbon interactions

The interaction between the metal catalyst and the carbon during the growth is also an important issue, and the main questions concern the formation of metal carbide. It is likely that the formation of metal carbide depends on the nature of the metal catalyst which determines for instance its carbon affinity [64]. However, for the same metal [65], some studies highlight the formation of a carbide while others don't [66]. We have to note that each group authors used different growth reactor geometries, different growth conditions (carbon precursor, pressure, temperature, carbon supply, time, flow...) and various shapes for the same metal catalyst. Considering this, it seems possible to attribute the reported differences to the large variations of the experimental conditions used, which could lead to different growth mechanisms. But, in the case of iron, for a same synthesis, Z. He et al. [67] showed by post-growth TEM measurement that the catalyst nanoparticle at the basis of the CNT can be either a carbide or a pure metallic catalyst suggesting that the growth mechanism is even more complex. These results were also confirmed by Wirth et al. [68].

### Physical state

The physical state of the catalyst during the growth is also up to now unclear. In situ TEM measurements on nickel [69], iron [70], cobalt [71] and FeCu [72] showed crystalline nanoparticles even in case of very small nanoparticles [73] [71]. In some cases, although crystallized particles are observed, they are nonetheless highly deformable [70]. Accounting for the large panel of catalysts with various chemical composition, sizes, support type and the diversity of CVD processes used, it seems impossible to actually generalize about the physical state of a given catalyst. Some may be solid, some others may be liquid and some may be partially liquid.

Various catalysts under several forms (size, shape, composition) in conjunction with various carbon sources, have been successfully used in a large range of growth conditions (pressure, temperature, carbon flow, support material, buffer gas). Although the mechanism of CVD CNT growth is still not fully understood, the next section will discuss on the influence of these various parameters upon the structure of the obtained carbon nanotubes.

## 1.3 SWCNT's structure control during CVD synthesis

As shown in the previous section, the SWCNT structure (diameter and chirality) impacts drastically on their properties. In many applications the use of a single chirality may significantly improve the performance of the devices. For example, applications such as transistors need only semiconducting nanotubes. Moreover an adapted band gap can be obtained by controlling the nanotube chirality. Two different ways can be used to achieve this goal, selective growth or post synthesis sorting. Concerning the post synthesis sorting, many techniques were developed and can allow selection of high purity of a specific (n,m) chirality [74]. Among these techniques we should mention chromatography (size exclusion [75], ion-exchange [76], gel-based [77]), density gradient ultracentrifugation of surfactant-wrapped SWCNTs [78] or selective polymer wrapping [79]). Despite the great advances made in this domain, the yield, scalability and the cost of such methods as well as unintended modification of the SWCNT properties induced by the process itself such as length or the additional surface functionalization, are still a barrier for their use in large scale applications. Thus, a direct, chirality selective growth is highly desired. In the following sections, we introduce a brief summary of the strategies proposed in the literature to make synthesis more selective in term of diameter, chirality and conducting properties.

### 1.3.1 Control of diameter

Many studies in the literature have reported various optimizations leading to a better control of the nanotube diameter. Following we introduce the effect of the catalyst size, growth temperature, carbon supply, and precursor gas.

#### Size of the catalyst

It is commonly admitted that in the frame of CCVD, small catalyst nanoparticles preferentially lead to SWCNT growth while larger catalyst nanoparticles induce MWCNT growth. In the following section, we will discuss the influence of the catalyst size for the single wall carbon nanotube synthesis.

In many studies, a tuning of the nanotube diameter distribution has been obtained through a control of the catalyst nanoparticles size distribution. Nevertheless, a direct correlation between the nanoparticle size and the nanotube diameter is not always straightforward. Fiawoo and co-workers [80] showed through post-growth TEM analyses that two different growth types might occur during a CVD synthesis, a tangential mode and a perpendicular mode. In the case of a tangential growth mode the resulting nanotube has a diameter close to the one of the catalyst nanoparticle that was used as a template. In the case of a perpendicular mode, the nanotube and nanoparticle diameters are no longer related. Then, the physical state of the catalyst nanoparticle during the

synthesis has to be considered. During a synthesis a catalyst nanoparticle can be liquid or partially liquid (see section 1.2.3). In these cases, the nanoparticules catalyst will be highly deformable and can not be used as a template for the SWCNT diameter. Based on this consideration a direct correlation between catalyst size and nanotube diameter is not obvious.

Finally a good control of the catalyst size distribution seems to be a good starting point to control the nanotube diameter distribution, but this condition is not sufficient, and other parameters also may influence the distribution of the diameters.

#### Temperature

The influence of the growth temperature on the nanotube diameters has been also deeply studied. Many groups observed an increase of the nanotube diameter with an increase of the growth temperature [81–88]. This effect is explained most of the time by an increase of the catalyst size due to a coarsening mechanism (such as Oswaltd ripening [89]) which leads to the growth of bigger SWCNTs [81–84, 86, 88]. Coarsening effect is known to be activated and intensified with a temperature increase.

Temperature also impacts other growth parameters such as carbon decomposition rate or carbon solubility. These last two parameters have been also reported to impact the diameter distribution [90, 91]. The effect of carbon supply will be developed in the following section, and the effect of solubility will be described more precisely in chapter 4.

#### The carbon supply

Lu and co-worker [91], showed that for polydisperse catalysts, changing the carbon feed (i.e. modifying the carbon gas pressure) changes the SWCNT diameter distribution. At low carbon rate, small diameters are favored and a smaller standard deviation is obtained. At high carbon rate, bigger carbon nanotubes are synthesized, the standard deviation increases and very small nanotubes disappear. Based on this observation, they proposed that for a given synthetic conditions, nucleation occurs from an optimal diameter of nanoparticles. The larger the deviation from the optimal size, the less carbon nanotube from those nanoparticles is promoted. They reported that at low carbon supply, bigger particles are inactive due to carbon underfeeding. At high carbon supply, overfeeding poisons smaller particles. A graphite sheet is formed at the nanoparticle surface and hinders the nanotube nucleation.

However, some opposite results showed that increasing carbon supply promotes small diameter nucleation [92, 93]. In this case, promotion of small diameter nanotubes is explained by a faster initialization of the growth. They reported that at lower carbon supply, the SWCNT growth starts later. During this time lapse, the small particles (described as catalyst of nanotubes of small diameter)

disappear due to coalescence mechanism. Therefore no small SWCNT can grow due to disappearance of their catalysts. From these results, two mechanisms seem to be in competition during the growth : coalescence mechanism and reaching of the carbon saturation limit. It is therefore difficult to find a general law since influence of the carbon supply is highly dependent on the studied system and the other growth conditions.

#### The precursor gas

Precursor gases have been reported to impact the diameter distribution. For the same growth conditions Lolli et al. [94] found that using $CH_4$ instead of CO increases the nanotube diameter and broadens the distribution. They attributed this diameter increase to the influence of $H_2$ produced during the methane decomposition. They reported a similar effect to that described for the influence of carbon supply [92, 93] : $H_2$ delays the start of the SWCNT growth leading to the formation of larger particles and finally larger SWCNTs. He and al. reported the same trend [95] but attributed this phenomenon to a difference in carbon feed rate. They reported that at given pressure and temperature, the catalytic decomposition of CO is much slower than the decomposition of $CH_4$ leading to a slower carbon feed when CO is used. Then, same arguments as those used by Lu and co-worker [91] in section 1.3.1 are given : under their growth condition only small nanoparticles can be activated for the growth when CO is used as the carbon source because the bigger nanoparticle catalysts are "underfeed".

### 1.3.2 Control of the chirality

Some studies reported also chiral selective growth but, as general rule, many studies reported a preferential growth of near armchair nanotubes [96–99]. Few hypotheses, supported by theoretical studies have been put forth to explain this chiral selectivity (nucleation-cap selectivity, growth rate selectivity...) but none of them have been unanimously accepted [53]. Here, we report a short review of the different experimental strategies found in the literature to obtain selective synthesis.

#### Bi-metallic catalyst

Highly selective syntheses have been reported using bi-metallic catalysts. Various bimetallic catalyst such as CoMo [100], FeRu [101], FeCo [98], FeCu [102], FeMn [103] have been shown to induce an enrichment of the (6,5) chirality or (9,8) chirality in case of $CoSO_4/SiO_2$ catalyst [104]. In line with these observations, Chiang and Sankaran showed that the chirality distribution of a synthesis can be tuned by adjusting only the Ni/Fe ratio of a $Ni_xFe_{1-x}$ catalyst [105]. More recently, Yan Li's group reported syntheses with a single chirality exceeding 80% selectivity for (12,6) [106], (16,0) [107] and (14,4) [108]

by using a $W_6CO_7$ catalyst. In view of these results, bimetallicity seems to be a key point for controlling chirality during synthesis, but the nature of this effect is still misunderstood. In most of the cases, the exact composition of the catalyst, its structure and the nanotube/catalyst interaction are not fully characterized, preventing any general understanding.

### Growth conditions

All the syntheses cited above require a delicate and fine setting of the growth conditions. Selective growth occurs only in a narrow window of parameters. Lolli and al. [94] and He and al. [95] showed that under their growth conditions, replacing CO by $CH_4$ results also in an enlargement of the chirality distribution. For CoMocat synthetic processes, replacing the MgO catalyst support by $SiO_2$ catalyst support does not change drastically the diameter distribution but rather the obtained chirality, indicating that catalyst support also plays a determinant role in this synthesis method [94]. Some studies reported also, for a same nanotube a modification of the chirality due to a modification of the growth conditions during the synthesis. For instance, for the same nanotube, Yao and co-workers reported that change in temperature during the synthesis leads to a change in the nanotube chirality [109]. In the case of $W_6CO_7$ catalyst, it was reported that the temperature of the synthesis is used to favor the formation of a specific crystallographic plane of $W_6CO_7$ in order to promote an epitaxial growth. Out of this specific temperature and optimized growth conditions, the synthesis is either non-selective or selective for another chirality. The idea of epitaxial growth is very popular in the literature in order to reach a chirality control [110]. To the best of our knowledge, no clear evidence of any epitaxial growth on metal catalyst has been provided up to now.

### Carbon seed

Finally, along the line of a possible epitaxial growth, other groups proposed the use of designed organic carbon nanorings, nanobelts or caps with the desired structure as a seed for CVD growth. Smalley's group was among the first to develop this idea [111] [112]. They used short opened carbon nanotubes decorated with iron catalyst for CVD growth. They reported that the obtained carbon nanotubes have the same diameter and orientation, suggesting a possible duplication of the original nanotube seed. Based on the same idea, Zhang et al. [113] used small, aligned, and sorted tubes with a defined chirality as a seed but without introducing a metal catalyst. They reported an increase of the length of the carbon nanotube without modification of the chirality of the seed. With the same principle, other groups developed new molecular carbon nanotube precursors using organic chemistry methods, for instance Omachi and co-workers and Liu and co-workers [114,115]. In the two last cases, the synthesis is quite selective in terms of the diameter but chirality mismatch is observed between the seed and the resulting SWCNT. These results suggest that the

growth mechanism is not obvious and the use of carbon seeds is not a sufficient condition for a selective growth. Sanchez-Valencia [116] and co-workers reported a 100% (6,6) chirality selective synthesis of carbon nanotubes by using a planar molecular precursor. First the planar precursor is transformed to its corresponding nanotube's cap by using surface-catalyzed cyclodehydrogenation, and then a carbon source is introduced to carry on the carbon nanotube growth. Even if the synthesis is reported as 100% selective, up to now, the poor growth yield is still an obstacle to the generalization of this method for applications.

Finally, mention should be made that the full characterization of growth sample is not trivial leading to possible biased chiral distribution. For example, Raman spectroscopy allows the observation of SWCNT RBM only when their $E_{ii}$ are in resonance, in photoluminescence spectroscopy, only semiconducting nanotubes are observed... Then, full characterization of a sample cannot be done using only one method which might lead to biased results.

### 1.3.3 Control of the metallic/ semi-conducting type ratio

In absence of methods to obtain a uniquely defined chirality, various ways to control the electronic properties of the carbon nanotubes have been investigated. Two main routes are used, the design of new catalysts or selective etching in-situ.

#### Catalyst design

Concerning the design of the catalyst composition, Chiang et al. [117] used controlled size and composition of the nickel-iron catalyst and reported that 90% of semiconducting nanotubes can be obtained by using $Ni_{0.27}Fe_{0.73}$ nanoparticles with an average diameter of 2.0 nm. Harutyunyan and co-workers [118] reported the possibility of obtaining up to 91% of m-SWCNT with an iron nanocatalyst by changing the vector gas and by adding a combination of $H_2$ and $H_2O$ during the annealing process. The change of the growth atmosphere leads to drastic change in the catalyst particles shape and ripening behavior. They attributed the variation of M/SC ratio to the variation of catalyst shape and faceting.

#### Etching in situ

Based on the fact that metallic nanotubes are chemically more active than semiconducting ones, several gases have also been investigated and added during the synthesis to selectively etch growing metallic carbon nanotubes. Yu and co-workers [119] reported that the use of oxygen in the synthesis increased the semiconducting tube ratio up to 90% by etching m-SWCNT. Similarly, Li group [120] grew s-SWCNT (90%) with iron and cobalt catalysts supported by $CeO_2$, designed to release oxygen during the growth for the etching. Ding and co-workers [121] showed that increasing the methanol ratio in a mixture

of ethanol/methanol as carbon feed, results in an increase of the s-SWCNT proportion. This increase is explained by the formation of hydroxyl radicals from methanol, which etched m-SWCNT. Wang and co-workers [122] confirmed this trend by using various alcohol precursors. They found that the proportion of metallic nanotubes increased when alcohol precursor presents a higher ratio of carbon atoms with respect to oxygen atoms. This effect is explained by a higher amorphous carbon deposition on the SWCNT when long carbon chain alcohol are used as precursors. This amorphous carbon protects the m-SWCNT from the etching effect of hydroxyl radicals. Cheng and co-workers [123] showed that introducing hydrogen during the growth process also leads to a selective etching of m-SWCNT. More recently they have also reported the possibility of obtaining (90%) of s-SWCNT with a small band gap by coupling the use of designed solid catalysts with the addition of hydrogen as etching gas [87]. Zhou et al. detailed the conditions for etching m-SWCNT by the controlled addition of water vapors [124]. Finally, Hong and co-workers found a ratio of 95% of semiconducting tubes (determined by electrical measurement) by applying UV irradiation during the growth. Raman measurements have been performed with a green laser on both the irradiated and the non-irradiated part of a unique as-synthesized sample. While metallic nanotubes are present in the non irradiated-part no metallic signal is observed on the irradiated part [125].

### 1.3.4 Conclusion

In summary, the structural control of the SWCNTs is highly dependent on the growth conditions and the precursors used. This structural control is also system dependent, many studies report opposite trends preventing any conclusion to be reached. Moreover, the decorrelation of the influence of the various CVD parameters is not obvious, complicating the analysis. Up to now, most of the chiral selective syntheses lead to (6,5) SWCNTs although (9,8), (6,6), (16,0), (14,4) and (12,6) syntheses have been reported. For practically all of these reported selective syntheses, the use of bimetallic catalyst is a key point. Unfortunately, the reason of this effect is still unknow, mainly because a decorrelation of the effect of the catalyst chemical composition and the other growth parameters which change drastically from one synthesis to the other, is difficult. Indeed, all the syntheses described in the literature are performed in very different conditions (such as shape of the catalyst, CVD set-up, gaz precursors, physical parameter et cetera) which all can influence on the growth mechanism.

With this mind, the first objective of this thesis was to develop a general and somehow "generic" synthesis method which would allow the formation of small nanoparticles of different mono or bi-metallic catalysts using exactly the same procedure. This would make it easier to compare the influence of the chemical composition of the catalyst on the nanotube growth. The first experimental chapter is devoted to the description of this new method and its application for three bimetallic catalysts based on ruthenium and either iron, cobalt or nickel as co-metal. Iron, cobalt and nickel have been chosen for their ability to grow easily SWCNTs. Alloying them with ruthenium serves several purposes.

First, we want to promote, as much as possible, a solid state of the nanoparticle during the growth. Bulk ruthenium alloys present higher melting temperature than pure iron, cobalt or nickel. Second, ruthenium allows to limit the carbon solubility. Recent theoretical studies show that limiting the carbon solubility favors a tangential growth [126], then a direct control of SWCNT diameter can be considered by controlling the catalyst size. After the synthesis and characterization of this three new catalysts, SWCNT synthesis have been performed in various growth conditions. Here, we will focus on the influence of the growth temperature and the metal catalyst composition on the SWCNT structure.

## 1.4 Application: FET device

Single wall carbon nanotubes are seen as excellent candidates for applications in nanoelectronic devices because of their remarkable electronic and mechanical properties combined with their small size [127]. After synthesis, the SWCNTs obtained during this thesis have been integrated into SWCNT-FET devices. Here we briefly present the FET device and the new possibilities opened when SWCNT are used as a semiconducting channel.

### 1.4.1 Principles

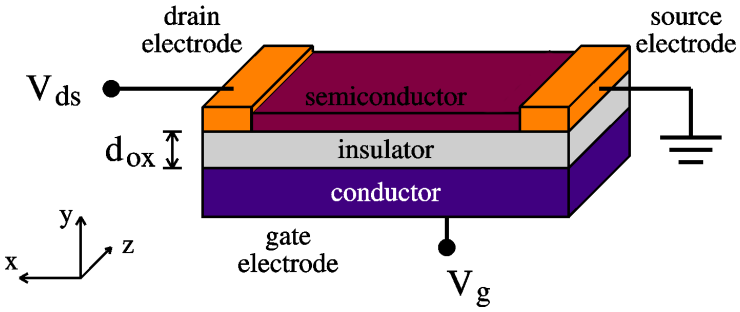


FIGURE 1.13: Schematic view of FET device adapted [128]

.

The basic structure of a FET device includes a channel made of a semiconductor material, typically silicon, connected to two electrodes (a source and a drain), and third electrode called the gate, separated from the channel, drain and source by an insulating layer (see Figure 1.13). To flow a current in the semiconducting channel an external activation is necessary to get the charge carriers (electrons or holes) over the gap. In a FET device, the activation occurs by applying a voltage at the gate electrode. The electric field, generated by the biased gate, changes the conductivity in the channel by lowering or raising the energy barrier. The minimum applied gate voltage, which leads to conducting FET path, between source and drain is named Vth. Two types of FET device exist as a function of the excess charge carriers circulating in the channel. For positive charge carriers (holes), we talk about p-type while for negative charge

carriers (electrons) we talk about n-type. Thus for a p-type FET applying a positive gate potential will reduce the number of carriers (holes) and decrease the conductance (Off state) while applying a negative potential will lead to accumulation of carriers and increase in conductance (On state), and vice versa for a n-type.

Two types of FET devices are commonly used :

- The JFET (junction field-effect transistor) where the gate is separated from the channel by a reverse p–n junction .
- The MOSFET (metal–oxide–semiconductor field-effect transistor) where an insulator separate the gate and the channel.

### 1.4.2 SWCNT-FET

A SWCNT-FET device is a FET-device where single carbon nanotube or nanotube array are used as a channel. The first reports of CNT-FETs were done in 1998 by Tans and co-worker who placed a SWCNT on the top of two metal electrodes supported by a $SiO_2$/Si wafer [129]. The performance of this device was not optimal due to the poor contact between the SWCNT and the electrodes. Since this first report, many efforts have been made in order to improve the device's performance. Better metal contact was achieved by depositing the metal electrodes on the SWCNT followed by annealing of the contact. Concerning the gate, top gated devices have been designed in order to decrease the thickness of the gate oxide. This leads to a larger electric field at a lower gate voltage (see Figure 1.14b). Wrap-around gate geometry has also been developed. In this case, all the circumference of the tube is gated, reducing leakage current (see Figure 1.14c). Finally, the nanotubes can also be suspended to reduce carrier scattering effects at the SWCNT-substrate interface (see Figure 1.14d).

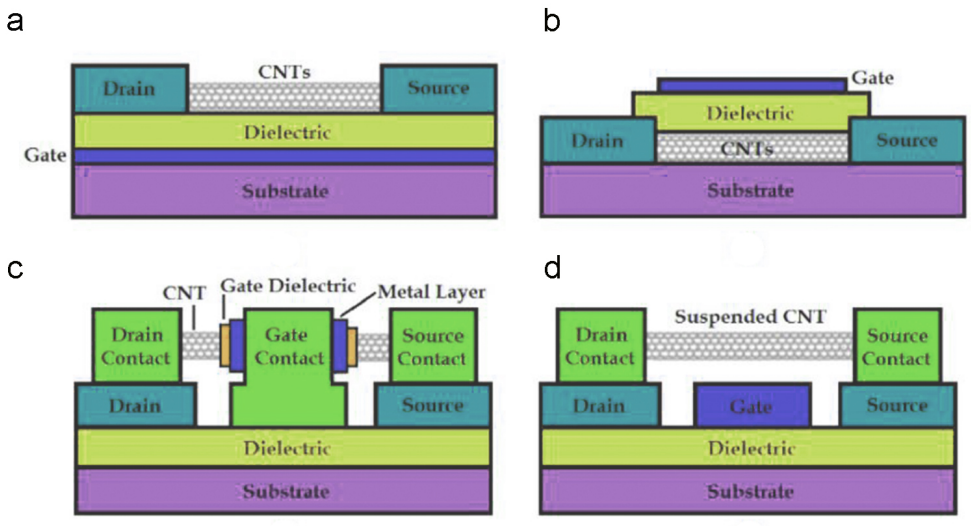


FIGURE 1.14: Schematic view of **a** Bottom gate SWCNT-FET **b** Top gate SWCNT-FET **c** Wrap-around SWCNT-FET **d** Suspended SWCNT-FET from [130].

The 1D nature of the carbon nanotube gives rise to a quantized resistance when put in contact with a 3D material such as the metal electrodes. Discrete energy states of the nanotube overlap the continuous states of the metal electrodes. This mismatch between the number of states that can transport the current in the SWCNT and the electrodes lead to a quantized contact resistance $R_Q$. Other resistances due to Schottky barrier when the nanotube is semiconducting or undesirable resistances due to poor contact can also exist. A ballistic transport regime can be reached when the resistance of the tube is only defined by $R_Q$. No carrier's energy dissipation or scattering occurs in the nanotube. But defects, temperature or "the size of the driving electric field" affect the ballistic transport. Consequently such transport has been in general achieved only for small channel lengths (inferior to 100 nm) or at low temperature.

In a classic MOFSET with heavily doped semiconductors, metal-semiconductor contact is ohmic. For a SWCNT-FET device, charge transfer at the metal-nanotube interface gives rise to Schottky barrier (SB) at each electrode. If one barrier is more important than the other, the transistor is unipolar (p-type or n-type), which means that only one type of carrier (hole or electron respectively) is transported (see Figure 1.15a-b). The magnitude of the SB depends on the CNT band gap and the contacting metal work function. For hole transport, a high metal workfunction leads to a smaller SB [131]. Thus high workfunction metals lead to a p-type transistor. For example, palladium can produce nearly ohmic contacts in p-type transistors [132]. Lower workfunction metals such as aluminum leads to large SBs for p-type transport. In some case, the SB barrier can be thin enough to inject both electrons and holes through the two opposite contacts of the transistor, which then become ambipolar as shown in Figure 1.15c.

The one dimension characteristic of the nanotube gives rise to much thinner Schottky barrier than in 3D systems. Consequently carrier tunneling through the metal-CNT interface becomes dominant rather than the thermally activated emission [133]. The efficiency with which the gate controls the conduction through the channel is also an important parameter of the transistor. It is defined by the inverse sub-threshold slope named S.

$$S = \frac{dV_g}{d\log I_d} \tag{1.22}$$

In a transistor with ohmic contacts, S is limited by the thermionic emission over the channel, typically 60 meV per decade at 300 K. If SB is dominating the transport, S is generally higher (100–150 mV per decade for oxide thickness $t(SiO_2) \sim 10$ nm). In this case, S depends on the electrostatics of the device (thickness and dielectric constant of the gate, electrode geometry...) [134].

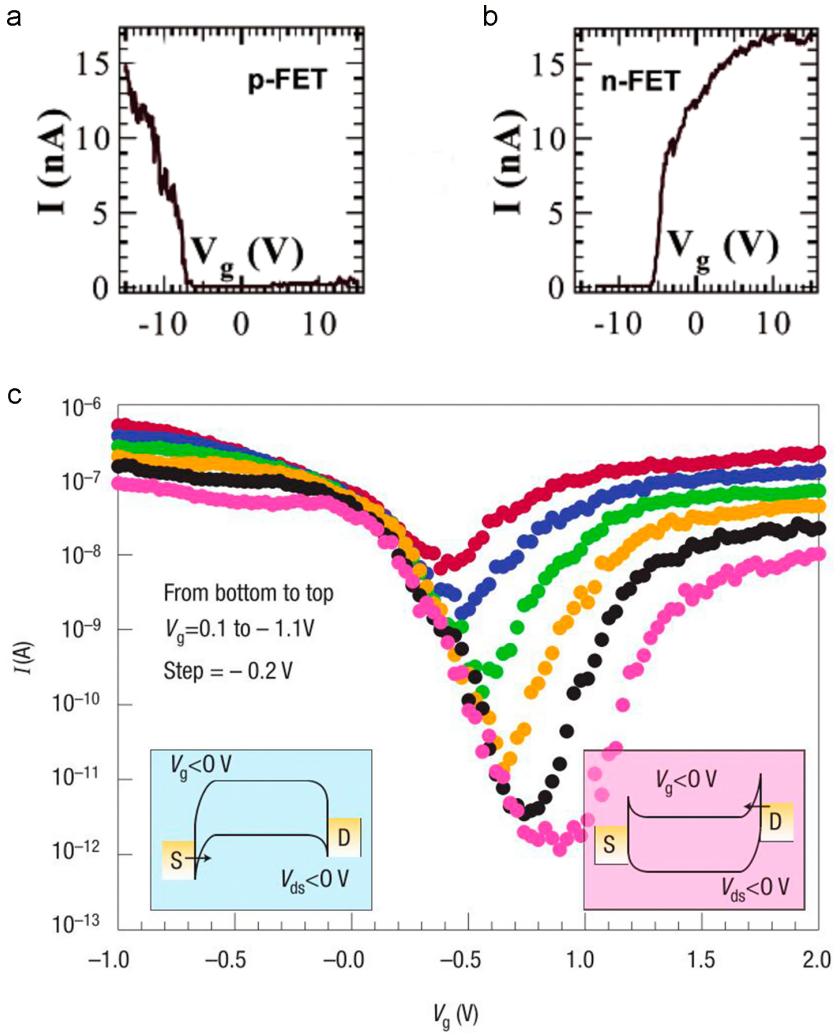


FIGURE 1.15: **a** Current (I) vs gate voltage (V) of a semiconducting SWCNT showing p-type FET behavior **b** Current (I) vs gate characteristics of a semiconducting SWNT after adsorption of PEI showing n-type FET behavior from [135] **c** Ambipolar transfer characteristics (current versus gate voltage). Drain bias increases from –0.1 V to –1.1 V in –0.2 V steps. **inset**: schematic of the band structure of a Schottky barrier semiconducting SWCNT under negative and positive gate bias [127].

### 1.4.3 Sensitivity to the environment

#### Effect of ambient air

Carbon nanotube FET devices present almost exclusive p-type character in air. N-type devices have been obtained only by annealing the device in vacuum or by n-doping the nanotubes [136]. This exclusive p-type character has been explained by an increase of the SB at the metal-nanotube interface thus preventing injection of electrons [133] due to oxygen absorption at the interface. More recent studies suggest that SB is not always the major factor impeding the transport of electrons. Aguirre and co-workers showed that in back-gated

field effect transistors, an $O_2/H_2O$ layer must be adsorbed on the hydrophilic $SiO_2$ insulator thin film leading to an electrochemical charge transfer process that suppresses the electron conduction [137]. They reported that an annealed $SiO_2$ device exposed to $O_2$, $H_2O$ or both, led to a reduction of ON-state n-branch current. No significant effect is observed when an hydrophilic layer of parylene-C isolated the SWCNT from $SiO_2$. Moreover, when both $O_2$ and $H_2O$ are used together, the reduction is 100 times greater than the sum of the effects of the exposure to one of these atmospheres taken alone.

Typical SWCNT-FET devices present a hysteresis curve attributed to various charges trapping. Kim and co-workers [138] were the first to report that the most significant charge traps are water molecules for $Si/SiO_2$ back gate SWCNT-FET device. They suggested that two types of water charge traps exist. The first one involves water molecules adsorbed on the nanotubes' surfaces, while the second one involves $SiO_2$ surface-bound water. While the former type can be easily removed in vacuum, heating in dry environments is necessary to remove the latter type.

### Sensitivity to gas

Many studies have explored the sensitivity of the FET-device to gas exposure [139]. A first example was reported by the Dai group in 2000 [140]. They chose two gases ($NO_2$ and $NH_3$) which exhibit two opposite electronic behaviors. $NO_2$ is an "electron-acceptor" gas, inducing p-type doping of the SWCNT while $NH_3$ is an "electron-donor" gas, inducing n-type doping. The experimental results pointed out an increase of the p-type SWCNT-FET conductance upon exposure to $NO_2$ and a reduction of the p-type SWCNT-FET conductance with $NH_3$. They attributed this effect to a doping of the CNT. The exact mechanism leading to the change of the conductance is still under discussion. As explained above for the oxygen, some groups attribute this change in conduction to a modification of the metal/SWCNT junctions via a modification of the Schottky barrier. Following the same idea, Zhang and al. [141] used palladium (Pd) contacts in a bottom gate configuration with three different configurations:

- a bare device (1)
- A device where the Pd contacts are covered with a thick layer of $SU_8$/PMMA (2)
- A device fully covered with the same polymer (3)

While the bare device (1) shows an immediate strong response to the gas exposure, up to 30 minutes are necessary to see a slow increase of the conductance for (2). They concluded that this slow increase is due to the diffusion of the gas molecules through the polymer layers, up to the contact regions. As no clear difference is obtained with the partially (2) and fully (3) covered devices, they also reported that no doping effect on the channel of the CNT occurs. The sensing of $NO_2$ is caused by chemical modifications at the metal/SWCNT junctions.

Finally, in the case of doping effect, a lateral shift of the V(on) and no change of the sub-threshold slope must be observed. In the case of the Schottky barrier height modulation, a modification of the sub-threshold slope with no shift of the OFF bias interval, should be obtained [142]. By using TFA molecule, S. Auvray and co-workers [142] showed that nanotube's doping and molecule absorption at the metal interface can also take place simultaneously.

## 1.5 Carbon nanotube functionalization with an optically active molecule

Functionalization of SWCNTs is highly desired to provide new functionalities to SWCNT based devices. The basic idea is to merge the properties of SWCNTs with those of the active molecule for tuning the nanotube's properties. For instance, functionalization of SWCNTs has allowed to increase their solubility, to isolate [143] them and to sort them [76]. The new hybrid material can be therefore integrated in devices and drastically improve their potentiality. For example, enzyme-coated SWCNTs integrated in a SWCNT-FET device act as a real-time sensor for enzymatic activities [144]. Chapter 6 of this thesis focuses on the functionalization of SWCNT in FET device with a chromophore. After a brief summary on the different ways to functionalize the SWCNTs, we will focus on the literature reporting interaction of SWCNT with optically active molecules.

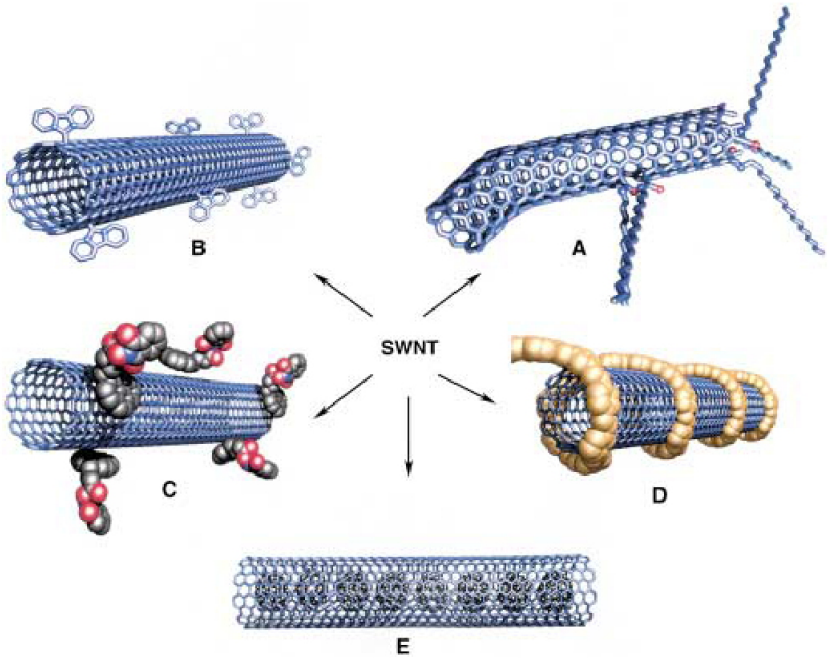


FIGURE 1.16: Schematic view of the SWCNT fuctionnalization process **A** defect-group functionalization, **B** covalent sidewall functionalization, **C** noncovalent exohedral functionalization with surfactant **D** noncovalent exohedral functionalization with polymers, **E** endohedral functionalization with fullerene from [145].

### 1.5.1 Functionalization method

For a SWCNT's sidewall functionalization two general ways exists : the covalent and the non-covalent functionalization. Covalent functionalization consists in creating a covalent bond between the nanotube and a molecule. Non-covalent functionalization leads to van der Waals interaction between the nanotube and the compound of interest. Either method can be used as a function of the targeted application.

#### Covalent functionalization

Covalent functionalization takes advantage of all the classic organic reactions possible on $sp^2$ carbon or on defect sites. Many reactions are possible and used, such as halogenation, cycloaddition, alkylation, radical addition. Figure 1.16A-B presents schematic view of covalent functionalization. Carbon atoms located on defect sites are also more reactive to oxidation reactions, leading to $sp^3$ carbon with carboxylic acid function as terminal group. Surface carboxylic acids can be deprotonated to increase carbon nanotube solubility in organic solvents, and reactivity of carboxylic function can be used to create new functions.

Covalent functionalization induces the transformation of $sp^2$ hybridized carbons into $sp^3$ hybridized carbons, destroying the $\pi$ conjugation and the electronic and optoelectronic properties deriving from it. In order to combine functionalization with the preservation of the CNT's intrinsic electronic properties, most used techniques try to limit the number of $sp^3$ defects. For example, click chemistry allows to design large macro-molecules containing several molecules of interest with only one anchoring point on the nanotube [146] (see Figure 1.17a). Hybrid/supramolecular technique consists in grafting few polymer chain on nanotube and then decorating the polymer with active complexes [147] (see Figure 1.17b). In some cases, a fine-tuning of defect quantity can modify the carbon nanotube's electronic [148] and excitonic properties like brightening carbon nanotube photoluminescence [149]. Recently, Reich's group presented a new covalent functionalization that preserves the $\pi$-conjugation by using new [2+1] cycloaddition [150].

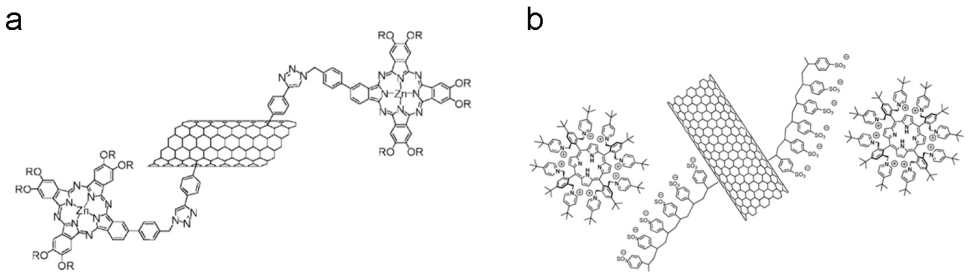


FIGURE 1.17: Example of SWCNT covalent functionalization with **a** molecule design via clik-chemistry adapted from [146] **b** active polymer [151].

### Non covalent functionalization

Non-covalent functionalization relies on the van der Walls interaction, between nanotubes and molecules or polymers. In general, this interaction is $\pi - \pi$ or hydrophobic interaction. Surfactant, aromatic molecules or polymers, constitute the major non covalent functionalizations described in the literature. As for covalent functionalization, non-covalent functionalization was first used to solubilize and isolate carbon nanotubes [143]. The hydrophobic part of an amphiphilic molecule wraps around the nanotube's sidewall and prevents nanotube/nanotube interactions. The hydrophilic part allows the solubilization in water.

Aromatic molecules such as pyrene or porphyrins [152] interact easily with the nanotube via $\pi - \pi$ staking interactions. Then, many examples of SWCNT non covalent functionalization concern molecules or supra-molecules containing a pyrene unit designed to stack on the nanotube sidewall [153, 154] (see for instance Figure 1.18a).

Polymers are also well-known to be able to wrap around carbon nanotubes. For instance, Figure 1.18b shows the wrapping of a DNA molecule around a SWCNT. Because of their chiral properties, DNA molecules can specifically interact with a defined nanotube chirality and then chiral sorting can be performed [76].

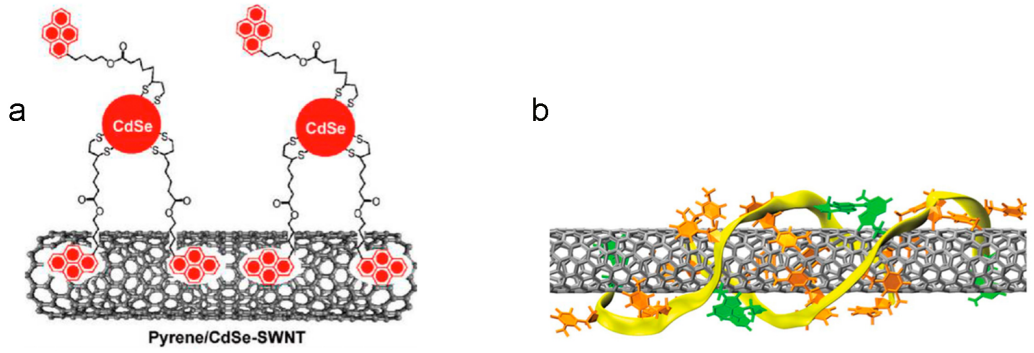


FIGURE 1.18: schematic view of **a** SWCNT functionalized with pyrene CdSe/nanoparticle [154] **b** SWCNT wrapped by DNA molecule [76].

The main disadvantages of non-covalent interactions concern the strength of created bonds, leading to a loss of stability. In contrast to the covalent functionalization, non-covalent functionalization preserves intrinsic properties of the nanotubes such as transport [155] or luminescence [143, 156] which are their main advantages. The non-covalent functionalization is easier to set up and guarantees the preservation of the properties of the nanotube in comparison to covalent functionalization. For these reasons, it will be used to functionalize FET device (see chapter 6).

### 1.5.2 Optoelectronic devices based on hybrid material

Their unique electrical properties make carbon nanotubes excellent candidates to be integrated in multifunctional optoelectronic devices. Many examples in the literature present photo-driven applications involving SWCNT/optically active molecule hybrid for photocatalysis, photovoltaics or photoswitching applications. For instance, Hu and co-workers [154] presented a light induced charge transfer between a pyrene/CdSe nanoparticles and nanotubes, for applications in photovoltaics (see Figure 1.19a). Borghetti and co-workers [157] reported a change of four orders of magnitude of the conductance upon illumination (see Figure 1.19b). Here, the conductance change is explained by an electrostatic doping of the SWCNT induced by photoexcited electrons trapped at the polymer dielectric/interface. The device can be used as an optical memory or a photo-switch depending on the applied gate-bias.

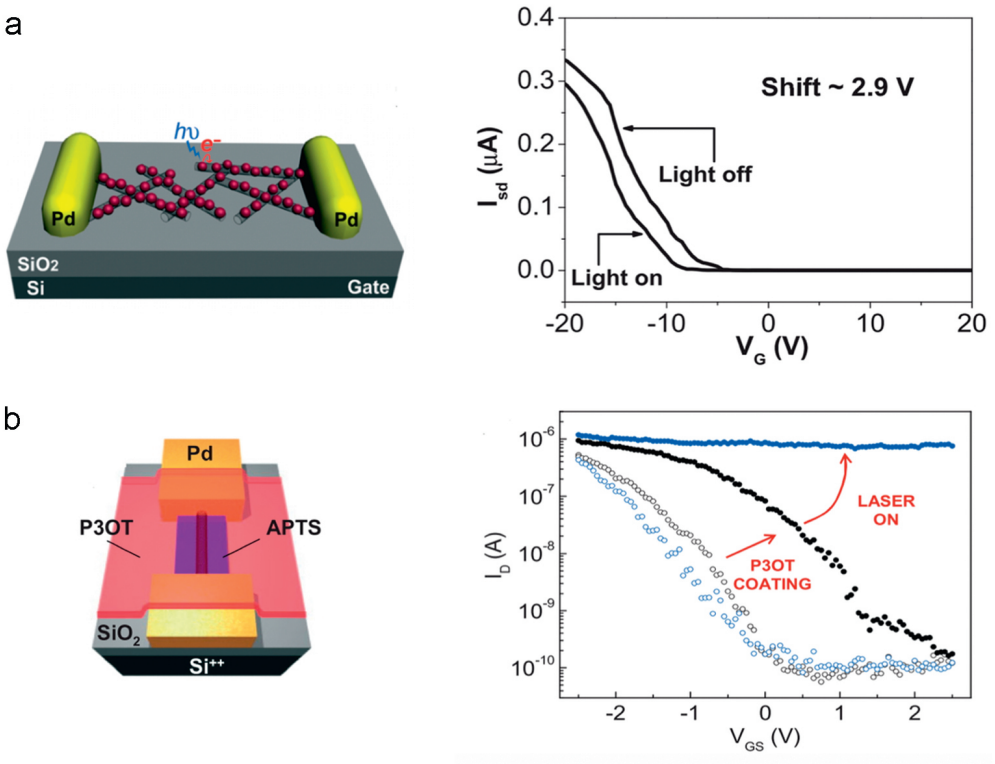


FIGURE 1.19: Photoinducced changes upon irradiation of **a** hybrid system pyrene/CdSe/nanoparticle/nanotube [154] **b** SWCNT coated polymer as a memory device and optical switch adapted from [157].

As presented in part 1.4.3, several mechanisms are responsible for the change in the conduction of the nanotube including electrostatic doping, modification of Schottky barriers and chemical doping (i.e. charge transfer). In order to well understand the light induced charge transfer, the principle of photoexcited electrons generation is necessary (see Figure 1.20). Upon irradiation, an electron from a photo-active molecule reaches an excited state before relaxing via

radiative or non radiative pathways. In case of an acceptor or a donor placed in the surrounding environment of the photo-active molecule, an electron transfer can follow the light excitation (see Figure 1.20). The mechanism is described in the system nanotube/pyrene/CdSe nanotube presented in Figure 1.19a. After light excitation an electron is transferred from the pyrene/CdSe (donor) to the nanotube (acceptor). In most of the studies reporting a charge transfer in a nanotubes/hybrid system, nanotubes play the role of the acceptor, but Elhi and co-workers reported that it may also act as a donor [158]. An energy transfer (radiative or not) can also take place between the photo-excited molecule and the nanotube. Such mechanisms have also been reported in case of nanotube/chomophore hybrid system. For instance Roquelet and al. [152] reported an energy transfer between nanotubes and porphyrin molecules. The energy transfer is evidenced through photoluminescence experiment as upon irradiation within the porphyrin band, the emission from SWCNT is observed.

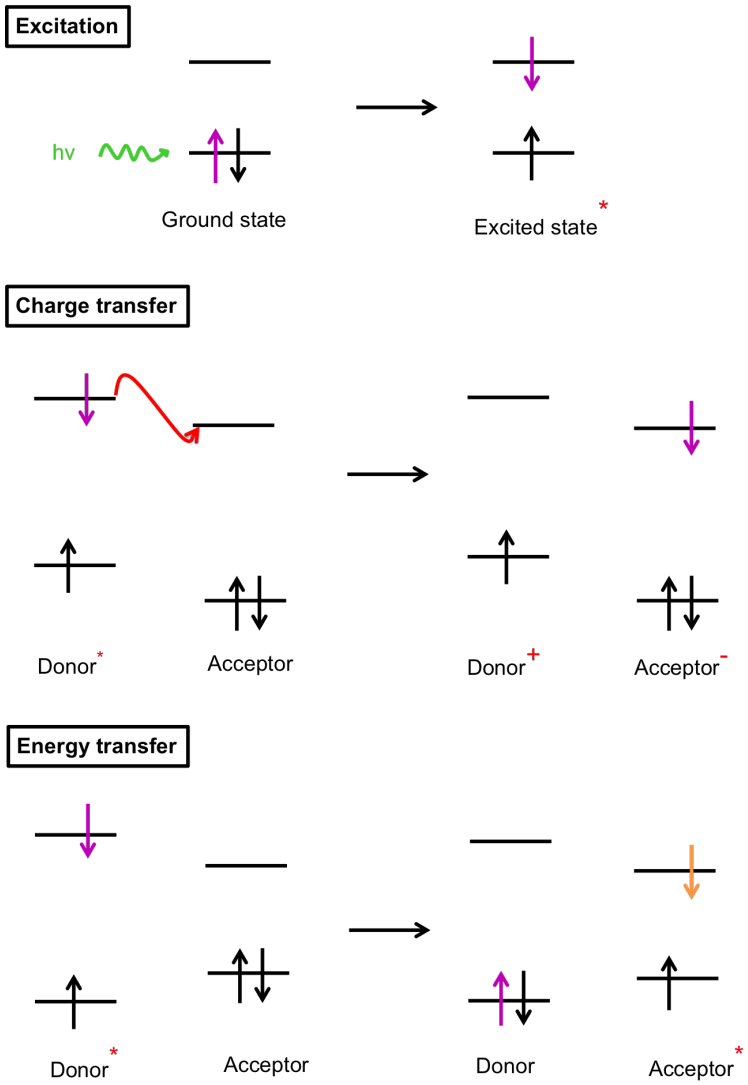


FIGURE 1.20: Schematic view of photoexcitation an electron, electron transfer and energy transfer

To conclude, if a transfer occurs between a SWCNT and an optical active molecule two kinds of mechanism are possible : a charge transfer or an energy transfer. An energy transfer can be evidenced through photoluminescence experiments [152] while charge transfer is usually detected through Raman spectroscopy [159, 160] or transient absorption spectra [158]. A charge transfer also leads to drastic modification of the conduction in FET-device. Nevertheless, a change in conduction can also be induced by electrostatic doping as shown by Borghetti and co-workers [157] or by a modification of the nanotubes/electrodes junction. Then further experiments and characterizations are needed to elucidate the mechanism of the interaction between optical active molecule and a SWCNT and for the mechanism of light induced conduction change in SWCNT-hybrid FET-device.

# Chapter 2

# Experimental techniques

In this thesis, a home-made CVD reactor has been used for the CVD synthesis. In the following chapter, the set-up used for the SWCNT growth and the basic principles of the main employed characterization techniques will be described.

## 2.1 Synthesis

### 2.1.1 CVD set up

The catalyst precursor reductive pretreatment and the SWCNT growth were conducted in a homemade double hot filament chemical vapor deposition (d-HFCVD) reactor, consisting of a cylindrical quartz tube enclosed in an 80 mm wide tubular heater with approximately 250 mm uniform heated length. Before each synthesis run and when the furnace is inactive, the chamber is pumped up to the residual pressure of $10^{-6}$ mbar in order to minimize walls contamination. The reactor is connected to two separate inlets for hydrogen and methane respectively. Each of the two gases has forced to flow over separate tungsten filament (0.38 mm diameter), mounted horizontally near the substrate in the CVD chamber and independently electrically driven at variable power. The temperature and the pressure in the chamber can be controlled and a cool zone is used to stock the sample before the stabilization of all the parameters of the reactor (see Figure 2.1).

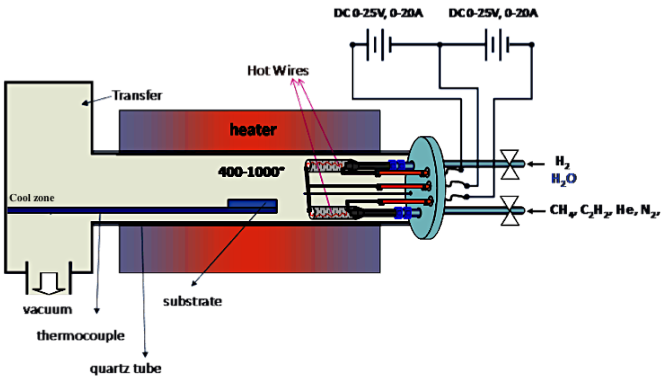


FIGURE 2.1: Schematic view of the CVD reactor.

## 2.2 Characterization

### 2.2.1 Raman spectroscopy

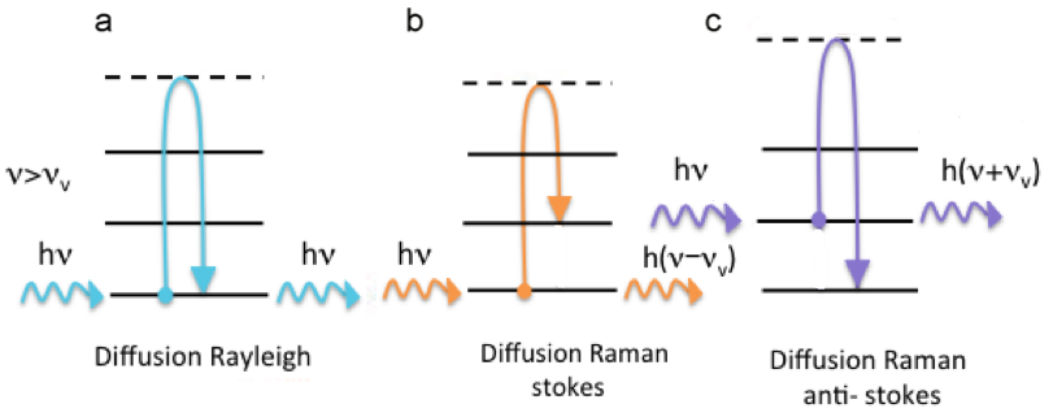


FIGURE 2.2: **a** Rayleigh process **b** Stokes process **c** Anti stokes process.

Raman scattering relates to inelastic scattering of light by a matter. This phenomenon was independently discovered by Râman and Mandelstam in 1928. First, electrons are excited by absorbing a photon, then electrons can be scattered by emitting or absorbing a phonon and finally, relax back to ground state by emitting a photon. Due to electron/phonon interaction, the emitted photon has a different energy from the absorbed one. If the phonon is emitted, the process is called Stokes process (see Figure 2.2b) while anti-stokes process (see Figure 2.2c) result from phonon absorption. If no scattering occurs, we talk about Rayleigh diffusion (see Figure 2.2a).

In the case of anti-stokes process, the absorbed phonon should be already thermally excited and this may not be possible if the phonon energy is large as compared to $k_bT$ ($k_b$ is the Boltzmann constant). Indeed the average number of available phonon m at a temperature T, with energy Eq, is given by the Bose–Einstein distribution [161] :

$$m = \frac{1}{e^{Eq/k_bT} - 1} \tag{2.1}$$

Raman spectra plots the intensity of the photon versus frequency downshifts (or upshift). The wavelength shift depends on the analyzed matter, its chemical composition, crystalline structure and electronic properties. If the energy of either the incident or the scattered light matches an optical transition, the process becomes resonant and a strong enhancement of the Raman intensity occurs (up to 1000 times stronger, see Figure 2.3).

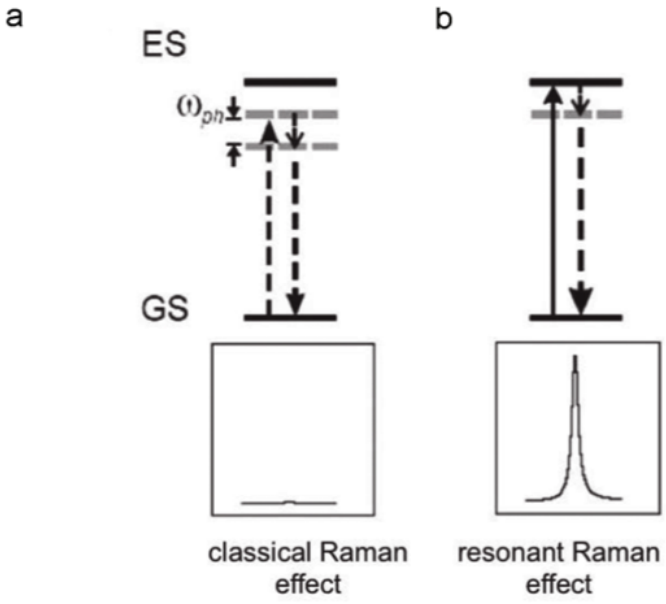


FIGURE 2.3: **a** Non resonant Raman process **b** Resonant Raman process from [162].

For the Raman spectroscopy of SWCNTs, if the laser excitation energy is equal to the energy separation between Van Hove singularities in the valence and conduction bands ($E_{ii}$), the resonant phenomenon occurs leading to an enhancement of the Raman signal. In a given sample, only SWCNTs with $E_{ii}$ in resonance with the laser excitation energy ($E_{laser}$) will contribute strongly to the spectrum. Figure 2.4 shows a typical SWCNT Raman spectrum, where peak corresponding to the radial breathing mode (RBM), the tangential mode (the G band), the D-mode and the G'-mode (or 2D mode) are displayed. We will focus here on the first three mode.

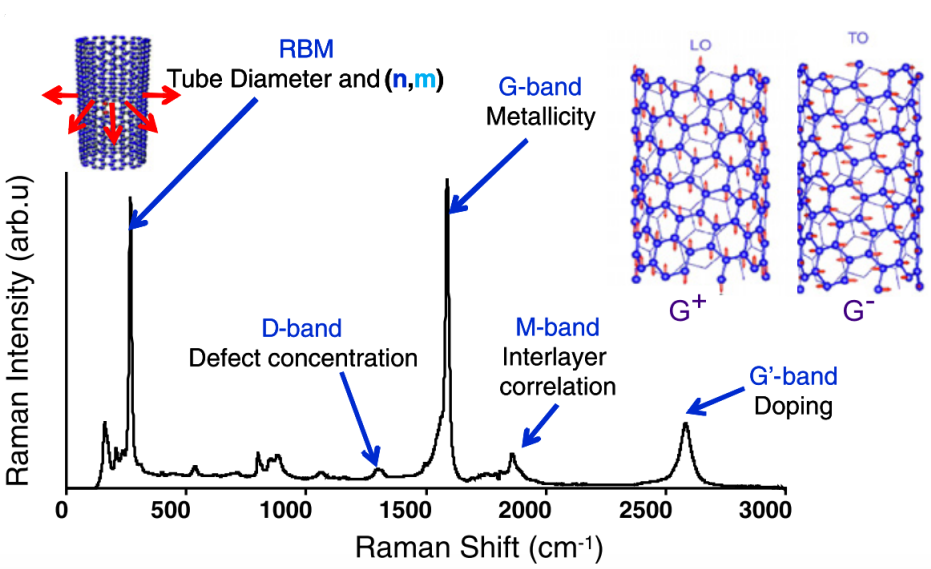


FIGURE 2.4: Raman signal of carbon nanotube [163].

**RBM** The RBM (radial breathing mode) phonon mode corresponds to the coherent vibration of all the carbon atoms in the radial direction. RBM is about 100–500 $cm^{-1}$. The RBM is a characteristic first-order Raman scattering of single wall carbon nanotubes only. RBM frequency is inversely proportional to nanotube diameter. Indeed the larger diameter, the bigger carbon atoms number on the circumference and the bigger mass. An increase of the mass, such as in the case of a classical oscillator, leads to a decrease in the frequency. The relation between the RBM frequency and the nanotube diameter is defined by

$$\mu_{RBM} = \frac{A}{d_t} + B \tag{2.2}$$

Where the A and B parameters are determined experimentally. Various propositions for A and B are given in the literature and depend highly on the carbon nanotube environment. Jorio and al. reported A=248 B=0 for individual SWCNT on $SiO_2$ [164]; A=217 and B=15 for alcohol-assisted SWCNT growth and A=227 and B=0 for water assisted growth has been reported by Araujo and al. in Jorio group [165] . Finally they proposed a more general law [166] :

$$\mu_{RBM} = \frac{227}{\sqrt{1 + C + {d_t}^2}} \tag{2.3}$$

Where C is the adjustable constant that averages the effect of the surrounding medium.

Kataura plot represents the $E_{ii}$ versus the diameter of a nanotube. Then, as we will see later, based on Kataura's plot, analysis of the RBM peaks allows for the calculation of the diameter distribution resonant with a defined $E_{ii}$. Moreover, semiconducting and metallic tubes, even with similar diameters, present different $E_{ii}$ values. Measurements of RBM frequency using several laser energies can be used to characterize the ratio of metallic to semiconducting SWCNTs in a given sample.

**G mode** In graphite the only first-order Raman peak is called the G-mode which corresponds to a displacement of carbon atoms parallel to the graphite sheet. In SWCNT, the tangential G mode gives rise to a multi-peak feature, containing up to six Raman peaks. The two most intense G peaks are labeled $G^+$ and $G^-$, for atomic displacements along the tube axis or atomic displacement along the circumferential direction respectively. The curvature of the nanotube softens the tangential vibration in the circumferential direction, lowering the frequency of the G-mode. In case of metallic nanotubes a characteristic Breit–Wigner–Fano lineshape is observable for the G-band due to the finite value of the electronic density of states at the Fermi energy.

**D mode** The D-mode results from a Raman double-resonance process which involves the elastic scattering of an electron by surface structural defects. It can also indicate the presence of amorphous carbon and structural defect. The intensity ratio between G-band and D-band $I_G/I_D$ is often used to estimate the amount of defects in a sample of nanotubes. Mention must be made that no systematic study has yet been carried out to correlate the presence of the D band with the nature of the different defects. Moreover, experimental studies show that D-band intensity and frequency also depend on diameter and chirality of the nanotube [167].

In this thesis, the Raman spectroscopy was performed on a HORIBA LabRam ARAMIS spectrometer, using a x100 objective, with four excitation wavelengths (473 nm, 532 nm, 633 nm, and 785 nm). For all samples and at each wavelength, several mappings were carried out, at random locations on the substrate to get the most meaningful statistical analysis. The mappings were done on a 50 $\mu m$ by 50 $\mu m$ surface, with a 10 $\mu m$ step.

### 2.2.2 Transmission electronic microscopy (TEM)

Transmission electronic microscope (TEM) runs on several of the same basic principles as the optical microscope. The main differences are the use of electrons instead of light, electromagnetic lenses instead of optic lenses and a vacuum environment due to gas molecules which can easily deflect electrons. Two sources of electrons are used to obtain a beam: a filament or a field emission gun. As filament, tungsten or $LaB_6$ are usually used. The filament is heated and a high voltage is applied between filament and anode leading to a release of electrons, which are accelerated to the anode. In the case of field emission gun, electrons are expelled by applying a very powerful electric field very close to the filament tip. In this case the beam is more coherent and brighter but a higher vacuum is necessary. Then, electrons are usually accelerated between 80 kV and 300 kV and focused before interacting with the sample. The sample (it can be a thin film of the material or a solid deposit on a TEM grid) must be crossed by the electron beam.

Elastic or inelastic interactions are possible between electrons and the TEM sample. The elastic interaction is divided into two contributions : the transmitted beam and the beams diffracted by the crystalline planes of the material. To form the image, we can use the transmitted beam (see Figure 2.5a), which leads to a “bright field image” where the diffracted zone is extinguished. The diffracted beam of a family of plan can also be used (see Figure 2.5b), then diffracted areas are bright, we obtain a “dark field image”. High-resolution TEM corresponds to the interference of several diffracted beam (see Figure 2.5c) The inelastic interaction leads to an energy transfer between the electron beam and the sample. These inelastic interactions lead to a loss of energy of the incident electron and an X-ray emission due to the deexcitation of core electrons of the sample excited by the electron beam. The energy loss and the energy of the X photons depend on the atom in the sample, analysis of this energy lead

to the electron energy loss spectroscopy (EELS) and energy dispersive X-ray spectroscopy (EDX ) respectively.

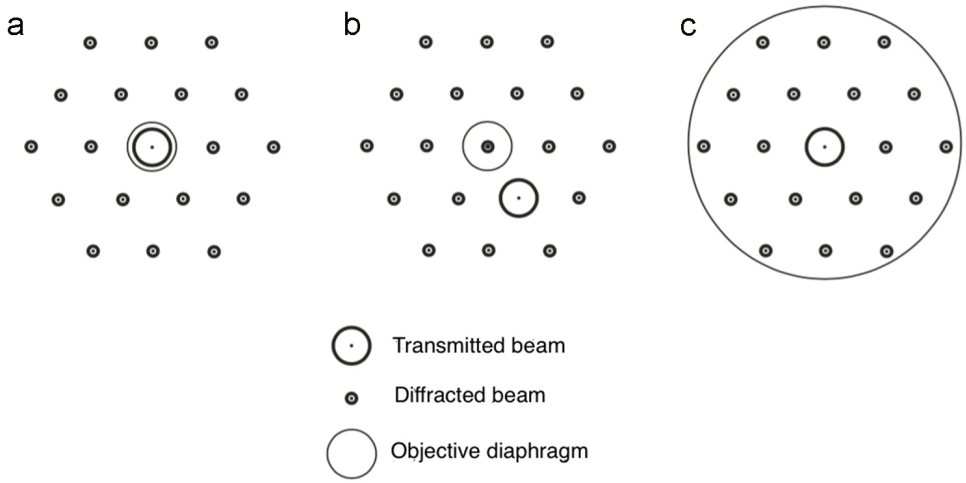


FIGURE 2.5: Schematic representation of a TEM **a** Bright field image will be obtained **b** Dark field image will be obtained **c** HRTEM will be obtained [168].

A scanning mode can also be used (STEM). In this case, the electron beam is focused in a thin spot and the sample is scanned. The principal advantage of this method is to spatially correlate a signal such as characteristic X-rays and the electron energy loss. That is not possible in conventional TEM. In STEM, the most commonly used detector is the High Angle Annular Dark Field (HAADF) detector, which collects only the electrons scattered at high angles (see Figure 2.6). In this case, intensity depends on the atomic number of the analyzed elements: a chemical contrast is obtained.

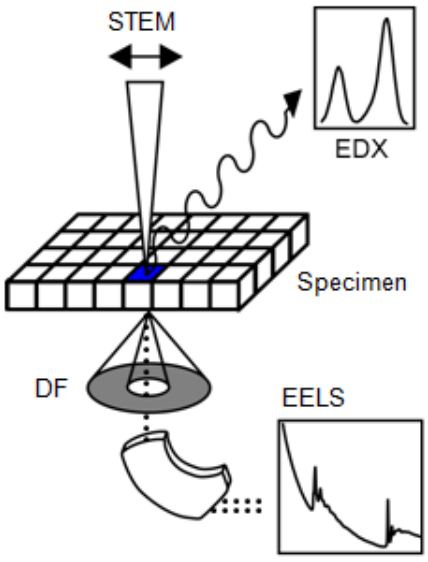


FIGURE 2.6: Schematic representation of a STEM coupled with an EELS and an EDX detector, adapted from [169]

Transmission electron microscopy imaging was performed using an image corrected FEI TITAN TEM as well as on a Libra 200 MC Zeiss microscope equipped with a Gatan Ultrascan camera. For the observation of the catalyst precursor nanoparticles (Prussian Blue analog), the bimetallic catalyst and the SWCNT, the TEM operated at 300, 200 and 80 kV respectively.

### 2.2.3 Scanning electron microscopy (SEM)

Scanning electron microscopy consists in scanning a sample with an electron beam accelerated between 1 and 40 keV.
Interaction of the electron beam with the sample also leads to reemission of particles such as secondary electrons (SE), reflected or back-scattered electrons (BSE), characteristic X-rays and photons (CL) as shown in Figure 2.7.

In conventional SEM, imaging mode corresponds to the collection of the secondary electrons. Secondary electrons arise from ejection of an electron from the conduction band due to inelastic interaction with the electron beam. SE own a weak energy ($\sim$ 50 ev) and consequently detected SE come from the surface, then are very sensitive to any surface variation. The brightness of the signal depends on the number of SE collected. Information about the topography can be obtained.

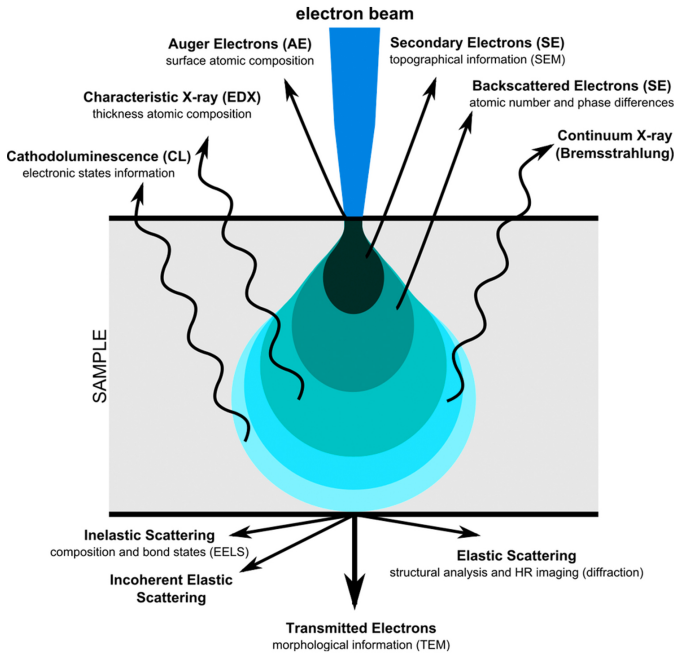


FIGURE 2.7: Schematic view of Electron-matter interaction adapted from [170].

Scanning electron microscopy (SEM) observations were carried out on HITACHI S 4800 microscope at 1 kV (or 0.5 kV) and 10 $\mu A$.

### 2.2.4 Atomic force microscopy (AFM)

AFM relies on the interaction between a tip attached on a flexible cantilever and a surface to analyze. The interaction between tip and surface causes a deflection of the cantilever. The deflection is measured through an optical system composed of a laser and a quad photodiode detector. Two modes are commonly used, the tapping mode and the contact mode. All the AFM measurements performed during this thesis have been done in tapping mode. In tapping mode we impose an oscillation to the cantilever. When a change occurs in the surface (height, material...) frequency, amplitude and phase of the oscillation are modified due to this new interaction. A feed back loop allows to put the amplitude or the frequency of the oscillation constant by moving the probe along z axe. In case of an homogenous sample, variation in the interaction is principally due to a variation of the topography of the sample. Then a topography of the sample can be obtained.

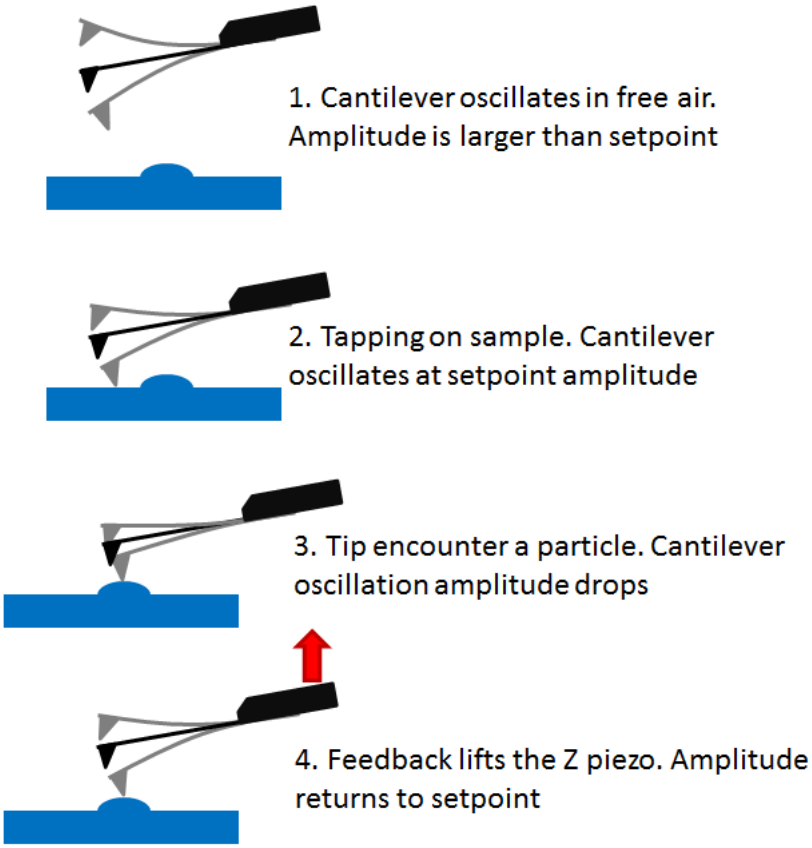


FIGURE 2.8: : Schematic view of AFM measurement in tapping mode [171].

The AFM analysis were performed using di Innova AFM Bruker with NanoDrive v8.02 software. Tapping mode images were acquired using silicon tips from nanosensors (PPP-NCSTR) with a resonance frequency ranging between 76 and 263 kHz. Images were processed using WsXM software.

### 2.2.5 X-Ray Diffraction (XRD)

X-Ray Diffraction (XRD) rests on analyze of constructive interference of monochromatic X-rays and a crystalline sample. When conditions satisfy Bragg's Law (see equation 2.4), the interaction of the incident rays and the sample produces constructive interference leading to a diffracted beam which is detected.

$$2d_{hkl}sin(\theta) = n.\lambda \tag{2.4}$$

with $d_{hkl}$ the d-spacing between layer of atoms, $\lambda$ the incident wavelength and n an integer.

All crystals in the powder material are randomly oriented, then all possible diffraction directions of the lattice can by obtained by scanning the sample through a range of $2\theta$ angles. The plot of the intensity of the diffracted beam as a function of $2\theta$ is called diffractogram. It is unique to every crystalline structure. Lattice parameter can be obtained through the d-spacing ($d_{hkl}$) deducted from Bragg's Law.

X-ray powder diffraction (XRPD) analyses were performed on powder deposited on aluminum plate and recorded on a Phillips Panalytical X'Pert Pro MPD powder diffractor at $CuK\alpha$ (1.5404 Å) radiation equipped with a fast detector.

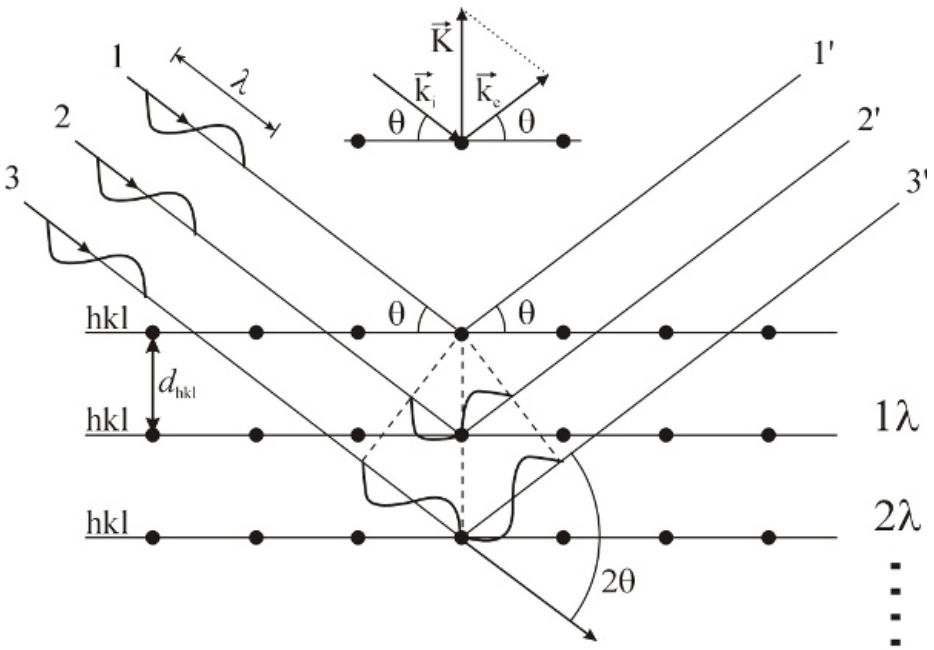


FIGURE 2.9: Schematic view of x-ray diffraction from [172] .

### 2.2.6 X-Ray photoelectron spectroscopy (XPS)

X-Ray photoelectron spectroscopy (XPS) is based on the measurement of the kinetic energy of electrons emitted by a solid under the impact of a beam of X photons with an energy $h\nu$. Any core or valence electrons having a binding energy inferior to $h\nu$ can be ejected. In XPS, the most commonly used X photons is the emission $K\alpha$ of Al ($h\nu = 1486.6$ eV) or of Mg ($h\nu = 1253.6$ eV). The spectrum of the core electrons in number and energy is characteristic of an atom in a given compound. The depth of analysis (from 2 to 10 nm) is limited by the inelastic mean free path of the electrons in the material. It depends on the kinetic energy of the electrons and the matrix in which the element is located. The binding energies of the core levels are sensitive to the chemical environment of the atom leading to chemical shifts range from a few 1/10th eV to a few eV.

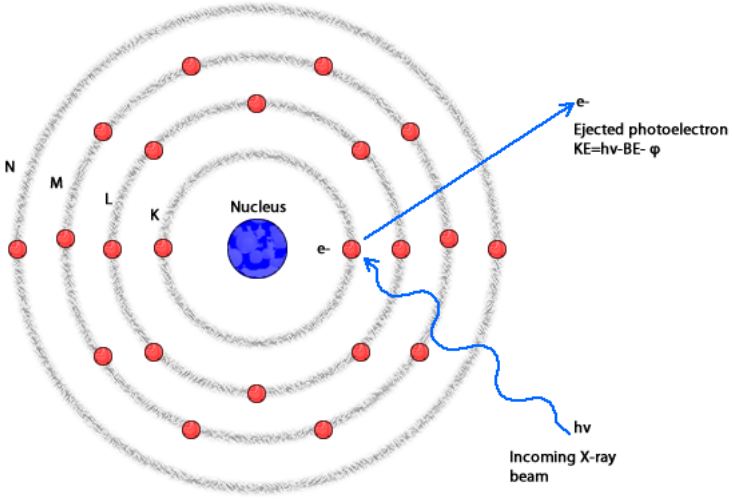


FIGURE 2.10: Schematic view of interaction between photon and electron in XPS measurement from [173].

The XPS studies performed in this thesis were conducted on a homemade synthesis and characterization platform, Facility for Elaboration of Nanomaterials with in-situ and real time characterization @X (FENIX) designed to study in-situ and in real time, by surface analysis techniques (XPS, ultraviolet photoelectron spectroscopy, Auger electron spectroscopy, low energy electron diffraction, cathodoluminescence), the growth of graphitic materials. Large flows of carbon and hydrogen can be locally delivered under the form of confined radicals/molecular beams in ultra-high vacuum to simulate various growth environments (CVD, plasma enhanced CVD, HF-CVD).

### 2.2.7 Absorption spectroscopy

Optical absorption spectroscopy measures the fraction of incident radiation absorbed by a material. According to the energy range we have access to various energy levels of the sample. In this thesis, we performed UV-visible and infrared spectroscopy. In the UV-VIS region, we typically observe transitions between electronic state while vibrational transitions are observed in infrared spectroscopy. The measurement consists in comparing the intensity of a range of monochromatic light before ($I_0$) and after crossing a sample ($I$) (see Figure 2.11). For each incident wavelength, the quantity of transmitted light is defined by T = $I/I_0$ and the absorbance or optical density by

$$OD = -log(T) = log\frac{I_0}{I} \tag{2.5}$$

In case of diluted solution the beer lambert law is valid and the optical density is proportional to the concentration of absorbent molecules.

$$OD = \epsilon.l.c \tag{2.6}$$

Where $\epsilon$ is the molar extinction coefficient ($cm^{-1}.mol.L^{-1}$), l the optical path ($cm$) and c the concentration ($mol.L^{-1}$).

Some shifts can be observed as a function of the environment of the probed object, then information about the surrounding environment can be obtained. An example of UV-Vis measurement of a CoMoCat suspension is shown in Figure1.8b.

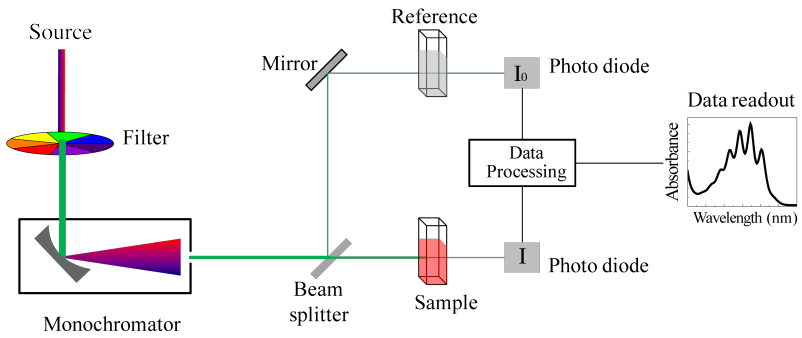


FIGURE 2.11: : Schematic view of UV-VIS spectrometer setup adapted from [174].

The infrared spectroscopy, used for the nanoparticle characterization, has been performed on a Perkin Elmer Spectrum 100 spectrometer. For the UV-VIS absorption, performed on SWCNT we used a Lambda 950 spectrometer from Perkin-Elmer with two lines. In this set-up $I$ and $I_0$ are measured in parallel. Spectrum are recorded between 250 nm and 1350 nm. One-millimeter (i.e. l = 0.1 cm) suprasil quartz cuvettes have been used in all the measurement.

### 2.2.8 Photoluminescence spectroscopy

Photoluminescence corresponds to the emission of light from a material after the absorption of photon. Absorption of a photon can promote an electron in an excited state, in case of photoluminescence compound, the electron relax to the ground state by emitting a photon. In chemistry, according to the relaxation pathway, two different terms (fluorescence and phosphorescence) are used (see Figure 2.12). Fluorescence describes a radiative emission induced by relaxation from a singlet excited state to a singlet ground state while phosphorescence corresponds to radiative relaxation from a triplet excited state to a singlet state. For semiconductors, such as nanotubes, the general term of photoluminescence is commonly used in the literature.

As for absorption, photoluminescence is sensitive to the environment, which can modify the relaxation pathway of the sample. The photoluminescence signal can also be enhanced or quenched through the interaction with other molecules. When emission for a large continuous range of excitation is recorded, the experiment is called photoluminescence excitation (PLE) spectroscopy. An example of PLE map for a CoMoCat sample is shown in figure 1.8d.

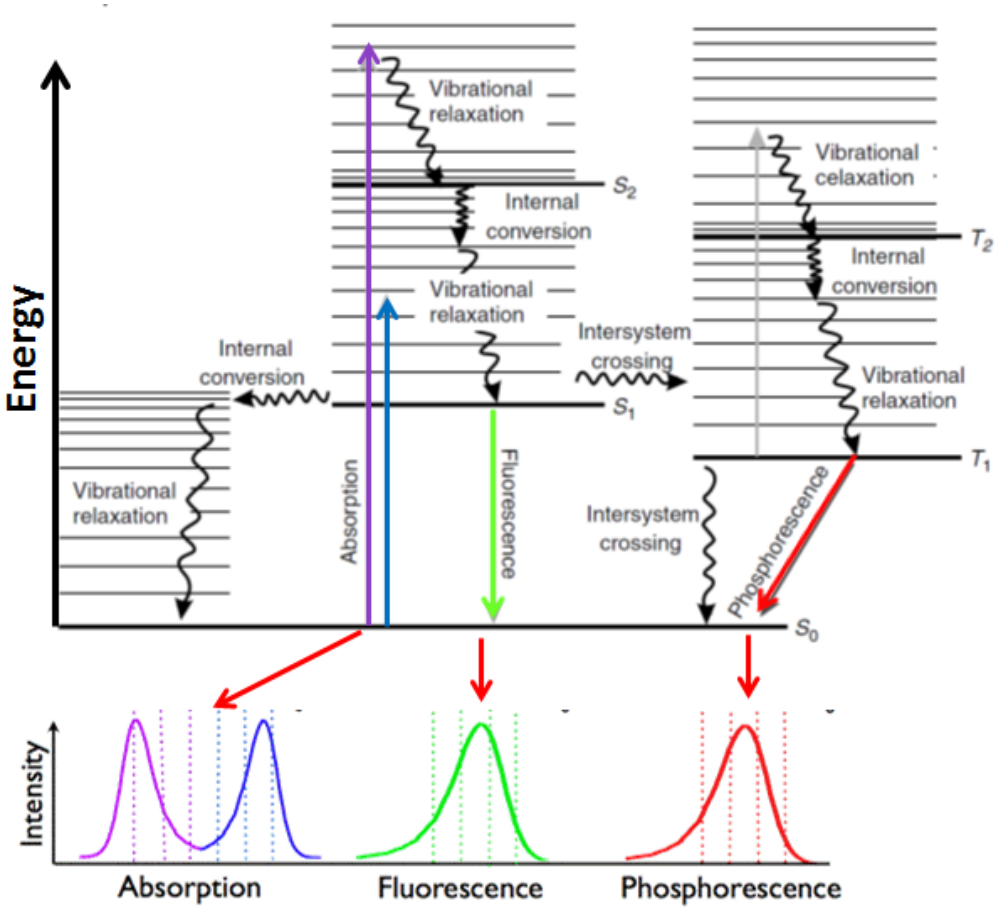


FIGURE 2.12: Perrin Jablonski diagram adapted from [175].

We used the homebuilt system of Pr. J-S. Lauret team for fluorescence and photoluminescence measurement of system in micelle. For SWCNT PLE map, a white xenon source was used (350 and 800 nm, with a resolution of 3-5 nm). The light emission is collected with a monochromator combined with a liquid nitrogen cooled InGasAs photo-detector (Omar V, Toper scientific) or a Peltier cooled CCD camera.

# Chapter 3

# A new SWCNT synthesis approach

In this thesis, we develop a new and versatile approach to grow SWCNTs by means of a variety of bimetallic catalysts that are obtained in-situ from Prussian blue analog (PBA) precursors. Various bi-metallic nanoparticle catalysts were obtained through a standardized method.

## 3.1 Motivation and description of the new synthesis

### 3.1.1 Motivation

Research on single wall carbon nanotubes (SWCNT) is still facing major challenges for the design of efficient devices for many applications as for example nanoelectronics and sensors. This is mainly due to the intricate relation between their physical properties and nanotubes' structure i.e. their chiral angle and diameter. Controlling their structural properties during the growth process is therefore a key point for enabling future progress in this field. As shown in the previous chapter, many past and recent studies focused on the investigation of the role of size, morphology, and composition of catalyst nanoparticles. For the latter, a strategy recently employed by some groups consisted in using bimetallic catalysts for the CVD growth of SWCNTs.

This bimetallic catalyst approach has led to some chiral selectivity, but an overview of these reports points out that both the catalyst nature (size, morphology, structure...) and the growth conditions differ drastically from one study to another, precluding any direct comparison and deep understanding of the effect of the bimetallic catalyst upon the SWCNT growth process. In order to systematically investigate the effect of the chemical nature of the alloys on the structure of SWCNTs, it is crucial to perform the growth process using different alloy catalyst combinations with comparable sizes and morphologies together with fixed and well-known CVD parameters.

In this study, we use three different bimetallic Prussian blue analog precursors for SWCNT synthesis of general formula : $CsNi^{II}Ru^{II}(CN)_6$, $CsCo^{II}Ru^{II}(CN)_6$, and $KFe^{III}Ru^{II}(CN)_6$ as precursors for obtaining NiRu, CoRu and FeRu catalysts. To the best of our knowledge, these bimetallic systems have not all been thoroughly investigated as catalysts for SWCNT growth. FeRu catalyst has been shown to catalyze SWCNT growth with efficiency and a good selectivity (majority of (6,5)) is reported [101] but, the exact nature of the catalyst was not fully investigated. The other systems (CoRu and NiRu) studied here have, to the best of our knowledge, not yet been investigated for the growth of SWCNTs.

### 3.1.2 Description of the synthesis approach

We developed a new synthesis method (see Figure 3.1) based on coordination chemistry and HF-CVD (details on HF-CVD are available in section 1.2.2). Briefly, the oxide surface of a $SiO_2$/Si wafer is covered with a SAM (self assembled monolayer) of a pyridine-functionalized silane (step 1). Then, surface coordination bonds are used to assemble bi-metallic Prussian blue analogs on the preformed organic SAM (step 2). A reductive pretreatment step, performed in the HF-CVD system, allows the reduction of the PBA and lead to the formation of effective catalyst nanoparticles (step 3). The resultant alloy nanoclusters were then used to catalyze SWNTs growth on $SiO_2$/Si substrates via $CH_4$/ $H_2$ double hot-filament chemical vapor deposition (d-HFCVD) (step 4).

One of the main originality of this work rests on the use of PBA as pre-catalyst. Indeed, various compositions of PBA nanoparticles can be synthesized with a narrow size distribution and a well-defined composition [176], thus enabling the control of the catalyst size and its composition. It has also been demonstrated in the literature that it is possible to synthesize PBA nanoparticles with various sizes, by adding shells onto pre-synthesized nanoparticles [177].

The use of a SAM allows one to control the exact quantity of the catalysts over the surface, and this approach is being used here to obtain a monolayer of PBA. Previous work conducted in the inorganic chemistry laboratory (LCI), of Paris Sud University, where we synthesize both the SAM and the PBA, show that density of cyanide-bridged nanoparticles deposited on Si substrates can be controlled. A decreasing of the density of nanoparticles on our substrates could be achieved [178].

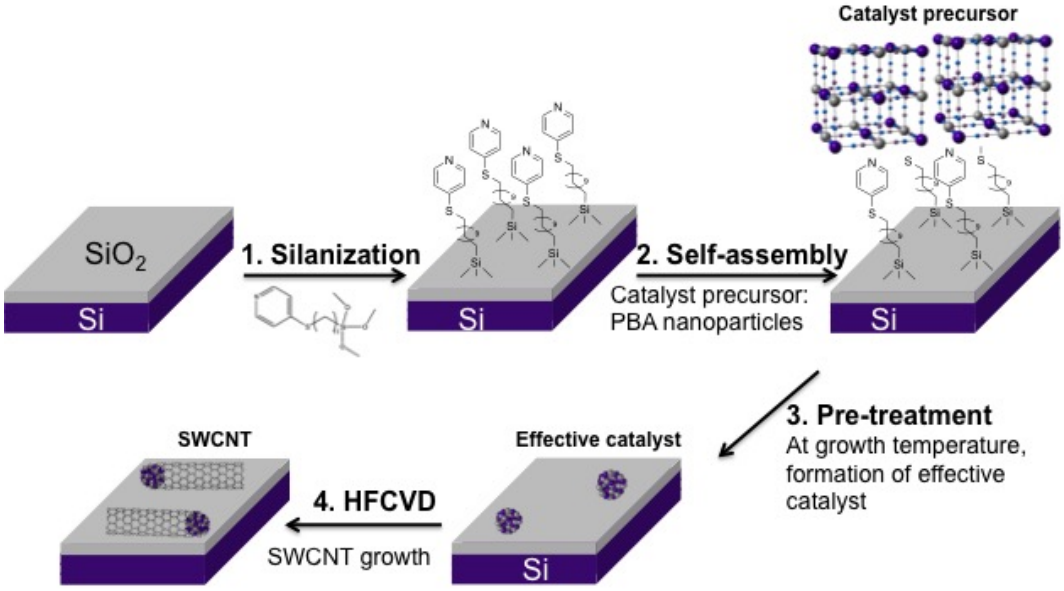


FIGURE 3.1: Schematic view of the SWCNT growth process from PBA precursors.

## 3.2 PBA pre-catalyst : from synthesis to characterization

### 3.2.1 Synthesis of PBA pre-catalyst

PBAs are bimetallic three-dimensional coordination networks with a face-centered cubic (fcc) lattice structure of alternating metal ions linked by cyanide bridges [179] (see Figure 3.2 for schematic structure).

The PBA nanoparticles were synthesized using a co-precipitation method previously described by Catala et al. [176] [180]. Briefly, an aqueous solution containing the potassium hexacyanometallate $[M(CN)_6]^{x+}$ salt and cesium chloride (CsCl) or potassium chloride (KCl), depending on the bimetallic system, was added to an aqueous solution of the hexa-aquo complex $[M'(H_2O)_6]^{2+}$. We synthesized three PBA : $CsNi^{II}Ru^{II}(CN)_6$, $CsCo^{II}Ru^{II}(CN)_6$, and $KFe^{III}Ru^{II}(CN)_6$. Experimental details can be found in section 3.6. For each system, an aqueous dispersion of individualized particles is obtained. The as-obtained PBA nanoparticles are stable in water without any stabilizing agent due to their negative charge, which leaves their surface available to coordinate to an organic ligand. All PBA systems studied here will thereafter be referred to by the two M and M' metals of interest (PBA FeRu for the $KFe^{III}Ru^{II}(CN)_6$ system for instance).

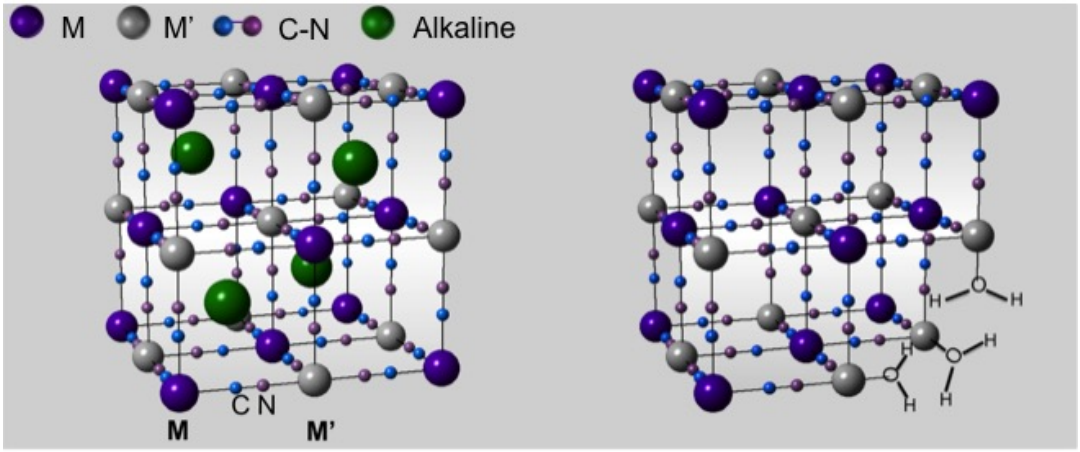


FIGURE 3.2: **Left** PBA schematic structure, the two metal ions M and M' are linked by coordination bonds to cyanide bridges within vacancy free fcc lattice structure with alkali ions present in the interstitial sites. **Right** water molecules replacing $M(CN)_6$ vacancies that may be present in the lattice.

### 3.2.2 Characterization

First of all, the pre-catalyst structure and composition have been thoroughly investigated.

#### Structural characterization

The recorded infrared spectra are displayed in Figure 3.3. For each of the PBA compounds, characteristic bands of the cyanide bridged PBAs (2070-2200 $cm^{-1}$) and solvate water molecule (bending mode of OH bond between 1400 and 1650 $cm^{-1}$) included in the porous networks were observed. As compared to the corresponding hexacyanometallate (Ru-CN) complex, $\nu_{CN}$ are found to be blue-shifted in agreement with the bridging of cyanide ligands (M-CN-M'). The non-bridging (NB) cyanides (M-CN) located at the surface of the nanoparticles can also be observed for CoRu and NiRu catalyst (see Table 3.1).

TABLE 3.1: $\nu_{CN}$ table for all PBA nanoparticle systems (NB: non-bridging)

| Compound | $K_4Ru(CN)_6$ | $KFeRu(CN)_6$ | $CsCoRu(CN)_6$ | $CsNiRu(CN)_6$ |
|---|---|---|---|---|
| $\nu_{CN}(cm^{-1})$ | 2037<br>2056 | 2070 | 2109<br>2067 (NB) | 2170<br>2035 (NB) |

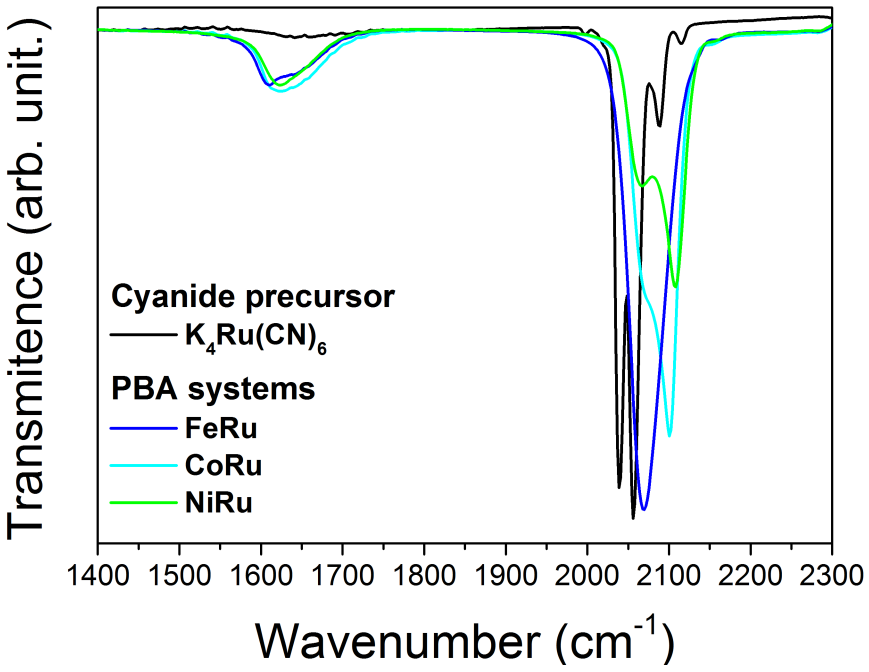


FIGURE 3.3: IR Spectra of all PBA systems in comparison with the corresponding hexacyanometallate complexes used for each synthesis (black line).

Furthermore the fcc crystalline structure of the PBA is confirmed through the XRPD patterns shown below in Figure 3.4. The XRPD patterns are similar for the three compounds, but we observe that in the case of CoRu and NiRu systems the (200) peak is extinct, which can be explained by the presence of cesium in the interstitial sites. The bragg formula was used to extract the lattice parameters from XRPD patterns. The extracted lattice parameters are ranging between 10.44 and 10.56 Å (see Table 3.2) and correspond to expected values for PBA [179]. The Scherrer equation was also used to calculate an approximate crystallite size.

$$T = \frac{k.\lambda}{H\cos(\theta)} \tag{3.1}$$

With k = 0.89, $\lambda$ = 0,1540598 and H the full width at half maximum of the peaks.

The small size of the PBA is confirmed by the calculation of the Scherrer domain size, found to be below 7 nm for each system (see Table 3.2). It should be noted that for crystallites smaller than 10 nm, a significant error on the domain size is expected, then an analyzis of the nanoparticles size have been performed by TEM measurements (see paragraph below).

TABLE 3.2: Table of structural characteristics of PBA nanoparticles (For FeRu system we used the average value calculate on the (200), (220) and (400) peaks and (220) (400) peaks for CoRu and NiRu system).

| Precatalyst | $KFeRu(CN)_6$ | $CsCoRu(CN)_6$ | $CsNiRu(CN)_6$ |
|---|---|---|---|
| Lattice constant | 10.44 Å | 10.56 Å | 10.51 Å |
| Scherrer domain size | 5.6 nm | 6.8 nm | 4.2 nm |

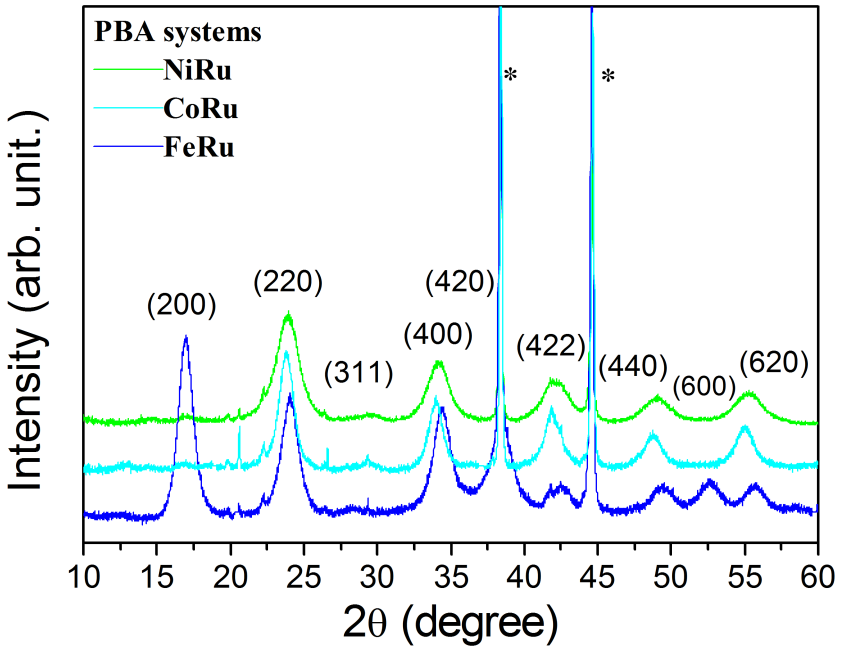


FIGURE 3.4: XRPD patterns of PBA powders deposited on aluminum plate (*) for all studied systems.

### Size determination

TEM statistical studies were carried out over roughly 200 particles for each system and confirm the pre-catalyst (PBA) narrow and small size distribution. For all pre-catalyst PBA nanoparticles, the average size is found to lie between 2.9 and 3.3 nm, that are ideal to generate sub-3 nm bimetallic particles through the reductive pretreatment previously described (see Table 3.3). Typical TEM images of the nanoparticles and their corresponding statistical size distributions are shown in Figure 3.5 and 3.6.

TABLE 3.3: Average size of all the PBA systems.

| Precatalyst | $KFeRu(CN)_6$ | $CsCoRu(CN)_6$ | $CsNiRu(CN)_6$ |
|---|---|---|---|
| size (nm) | $2.9 \pm 1.0$ | $2.5 \pm 1.0$ | $3.3 \pm 0.9$ |

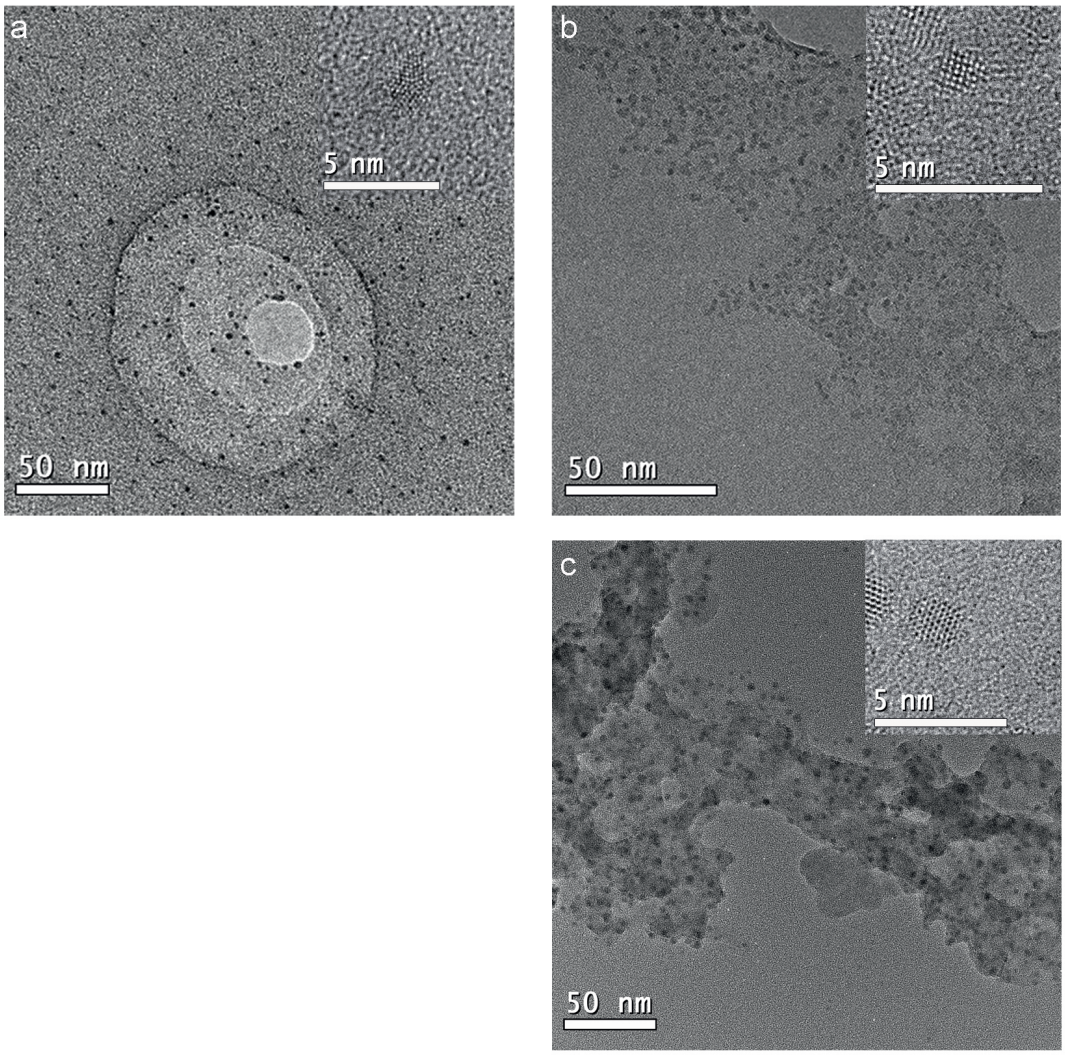


FIGURE 3.5: Example of TEM images of **a** FeRu, **b** CoRu, **c** NiRu

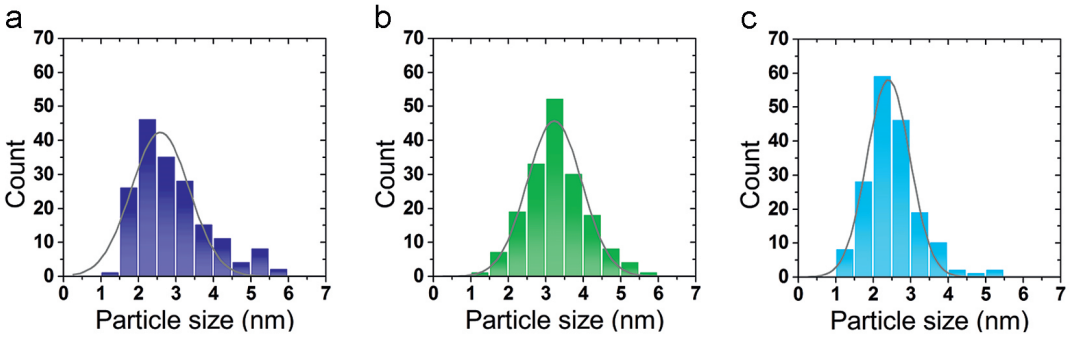


FIGURE 3.6: **Top** Size distribution of **a** FeRu, **b** CoRu, **c** NiRu and an example of TEM images for each system. **Bottom** Average size of all the PBA systems.

### Chemical composition

Finally, chemical composition for the synthesized PBA nanoparticles was derived from SEM-EDX analysis on powder and as expected, metallic ratios of approximately 1:1 ($\pm$ 0.09) were confirmed.

TABLE 3.4: Metallic ratios extracted from the EDX spectra for all PBA systems.

| Precatalyst | $KFeRu(CN)_6$ | $CsCoRu(CN)_6$ | $CsNiRu(CN)_6$ |
|---|---|---|---|
| Metallic ratio | Fe/Ru 0.91 | Co/Ru 0.98 | Ni/Ru 1.04 |

### Morphology of the pre-catalysts

As-synthesized pre-catalysts are subsequently self-assembled on the monolayer of silane molecules having a terminal pyridine group able to form a coordination bond with the PBA nanoparticles. The synthesis of the silane molecule is described in the experimental section 3.6.

The aim of this step is to control the quantity of pre-catalyst in order to obtain *in fine*, well defined and individual catalyst over the surface.

In order to achieve grafting of the PBA nanoparticles, the silanized wafers were immersed in the as-obtained colloidal PBA solution (see section 3.6 for experimental details). In order to ensure that the nanoparticles are effectively grafted on the surface, and to evaluate the quality of the deposition, AFM measurements were conducted for all PBA systems. Typical examples of AFM images of a 2x2 $\mu m^2$ surface are presented in Figure 3.7. AFM study confirms the homogenous assembly of the PBA over the surface and also the small size of the nanoparticles' distribution. Defects on the AFM image of the NiRu PBA systems can be indicative that generally on non-defective surface, a monolayer of pre-catalyst is obtained (Figure 3.7c).

### Conclusion

In conclusion, the synthesis of three stable aqueous solutions of Prussian blue analogs has been performed. XRD and IR measurements confirmed the expected structure. The small size of the nanoparticles has been investigated by statistical TEM measurements and the analyze of the chemical composition shows a metallic ratio of 1:1. Their small size and well-defined composition make them good candidate for design of catalyst for the SWCNT growth.

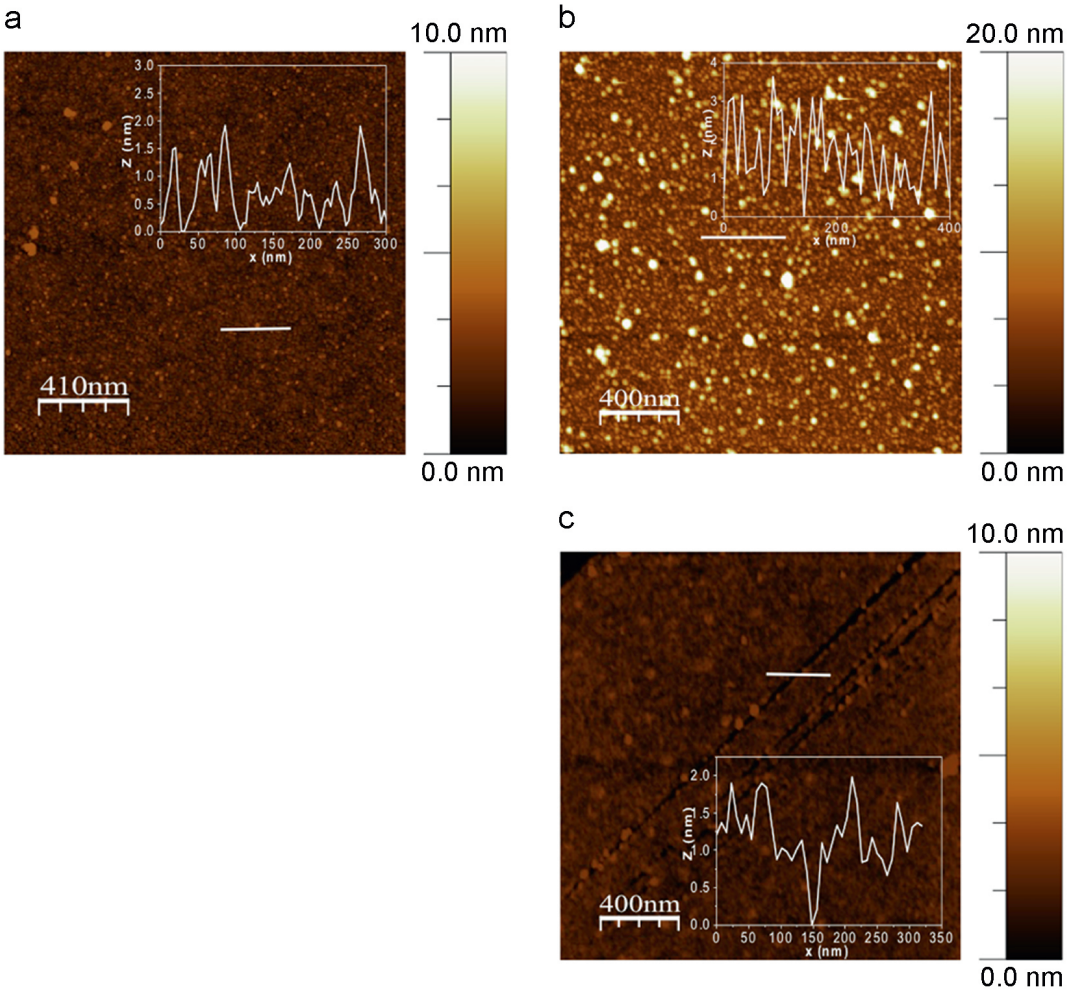


FIGURE 3.7: Characteristic AFM image of PBA system deposited over the wafer **a** FeRu **b** CoRu **c** NiRu

## 3.3 Formation of the effective catalyst

### 3.3.1 Catalyst reductive pretreatment

The reductive pretreatment is conducted in a homemade double hot filament chemical vapor deposition (d-HFCVD) reactor under hydrogen (see section 3.6 for experimental detail). This pretreatment of the catalyst precursor serves two purposes : first for degrading the underlying organic SAM, and second for reducing the PBA precursor nanoparticles into metallic catalyst nanoparticles which are the effective catalyst, for the subsequent SWCNT's growth.

In order to validate the reduction process, an in-situ XPS analysis of the PBA nanoparticles was conducted in the case of the FeRu system using an homemade system : the FENIX facility (see section 2.2.6). XPS analysis was carried out in-situ, before and after reduction of FeRu PBA nanoparticles. Spectra were recorded before the reduction of the PBA nanoparticles grafted on the silanized

wafer (blue curve on Figure 3.8). Then the sample was exposed to activated $H_2$ for 5 min at 800°C, and another XPS spectrum was measured after rapid cooling of the samples (approximately 100 °C per minute, purple curve on Figure 3.8). As shown in the XPS spectra on Figure 3.8, before the reductive pretreatment (blue line), we observe the characteristic edges of :

- $Fe^{III}$ ($Fe^{III}$ $2p_{3/2}$ peak at 710.0 eV, and $2p_{1/2}$ peak at 723.6 eV binding energy)
- $Ru^{II}$ ($Ru^{II}$ $3d_{5/2}$ and $3d_{3/2}$ peaks at 280.9 eV, and 284.9 eV, respectively)
- Nitrogen presents in both the cyanide bridges of PBA nanoparticles ($N_{1s}$ 397.9 eV [181]) and pyridine groups from the underlying organic SAM ($N_{1s}$ 402.1 eV).

Two separate studies of a non-silanized $SiO_2$/Si wafer on which the aqueous solution containing the FeRu PBA nanoparticles was dropped and on a silanized $SiO_2$/Si wafer, confirms that the peak at 397.9 eV at the $N_{1s}$ edge can be attributed to the nitrogen atoms belonging to the cyanide bridges of the PBA structure and the peak at 402.1 eV to the nitrogen of the pyridine group.

After the reductive pretreatment (purple line), we note the disappearance of the characteristic peaks at the $N_{1s}$ edge, indicative of the evolution of the PBA structure to a new one, free of cyanides and of the degradation of the SAM. A significant shift and transformation of the characteristic $Fe_{2p}$ (from 710.0 eV to 707.0 eV for the Fe $2p_{3/2}$, and from 723.6 eV to 719.8 eV for the Fe $2p_{1/2}$ peak) and $Ru_{3d}$ (from 280.9 eV to 279.9 eV for the Ru $3d_{3/2}$ peak, and from 284.9 eV to 284.2 eV for the Ru $3d_{5/2}$ peak) edges, respectively indicate the reduction of $Fe^{III}$ and $Ru^{II}$ to the metallic state. Atomic ratio of carbon, ruthenium and iron have been determined by measuring the intensity of each peak (taken by area), corrected with Scofield factor. As the quantity of ruthenium is stable during the pretreatment, we compare the ratio $I_{carbon}/I_{ruthenium}$ in order to estimate quantity of carbon removed during the pretreatment. We found that around 40% of carbon has been removed during the reductive pretreatment (see table A.2 in appendix A) . The degradation of the PBA was also confirmed by the disappearance of the carbon edge peak (386.4 eV) belonging to cyanide. The pretreatment does not seem to fully remove the carbon originating from the SAM, as a residual peak is still observed after pretreatment.

However, no peaks indicative of the formation of carbides are observable, suggesting that the remaining carbon is not inside the catalyst nanoparticles. Also, no peak indicative of the presence of potassium (that can be present in the FeRu PBA nanoparticles vacancies) around 292.9 eV is detected. This XPS study confirms the reduction of the FeRu PBAs, and the degradation of the SAM at the macroscopic scale.

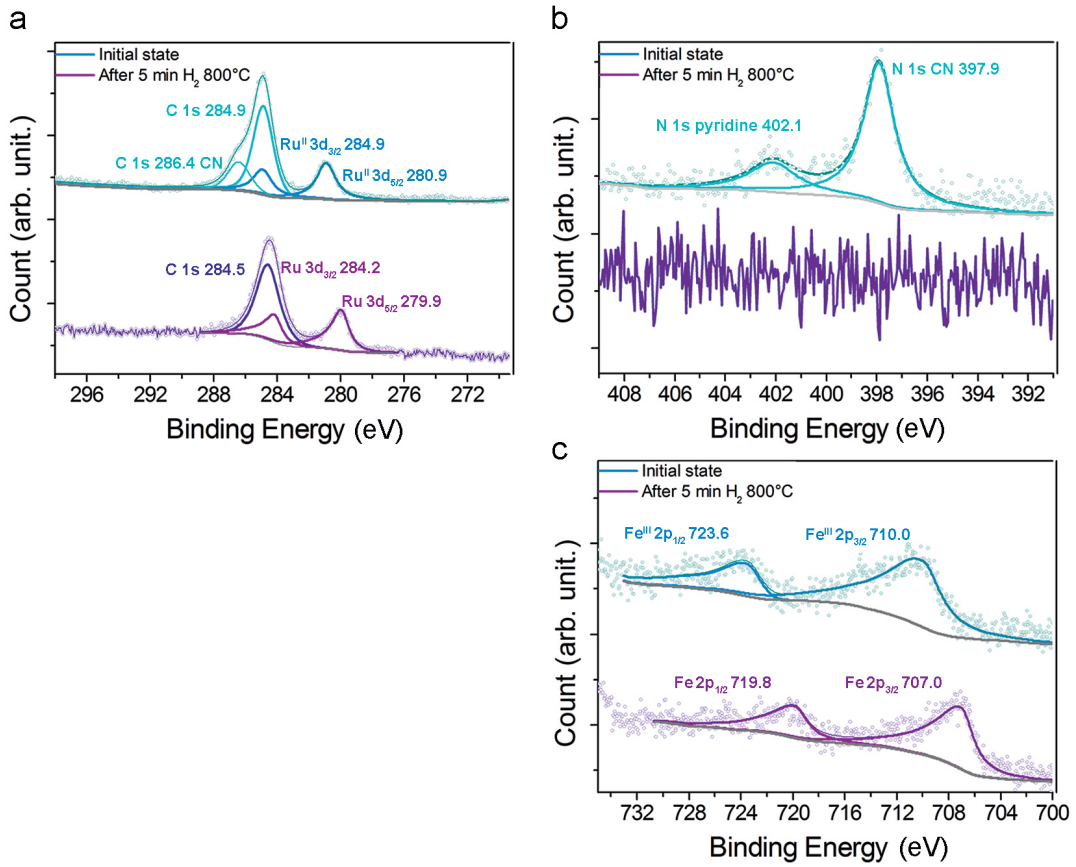


FIGURE 3.8: XPS spectra obtained from in-situ analysis before (blue) and after (purple) reductive pretreatment of FeRu PBA at 800°C under $H_2$ atmosphere: **a** carbon and ruthenium edges **b** nitrogen edge **c** iron edge.

### 3.3.2 Characterization of the catalyst

#### Repartition over the surface

AFM study after the reductive pretreatment shows a clear diminution of the size of the catalyst confirming the effectiveness of the pretreatment. No significant Ostwald ripening is observed after the pretreatment (see Figure 3.9). As expected, an homogenous monolayer of the catalyst is obtained. The size of the reduced catalyst has been analyzed more precisely by TEM measurement in the following paragraph.

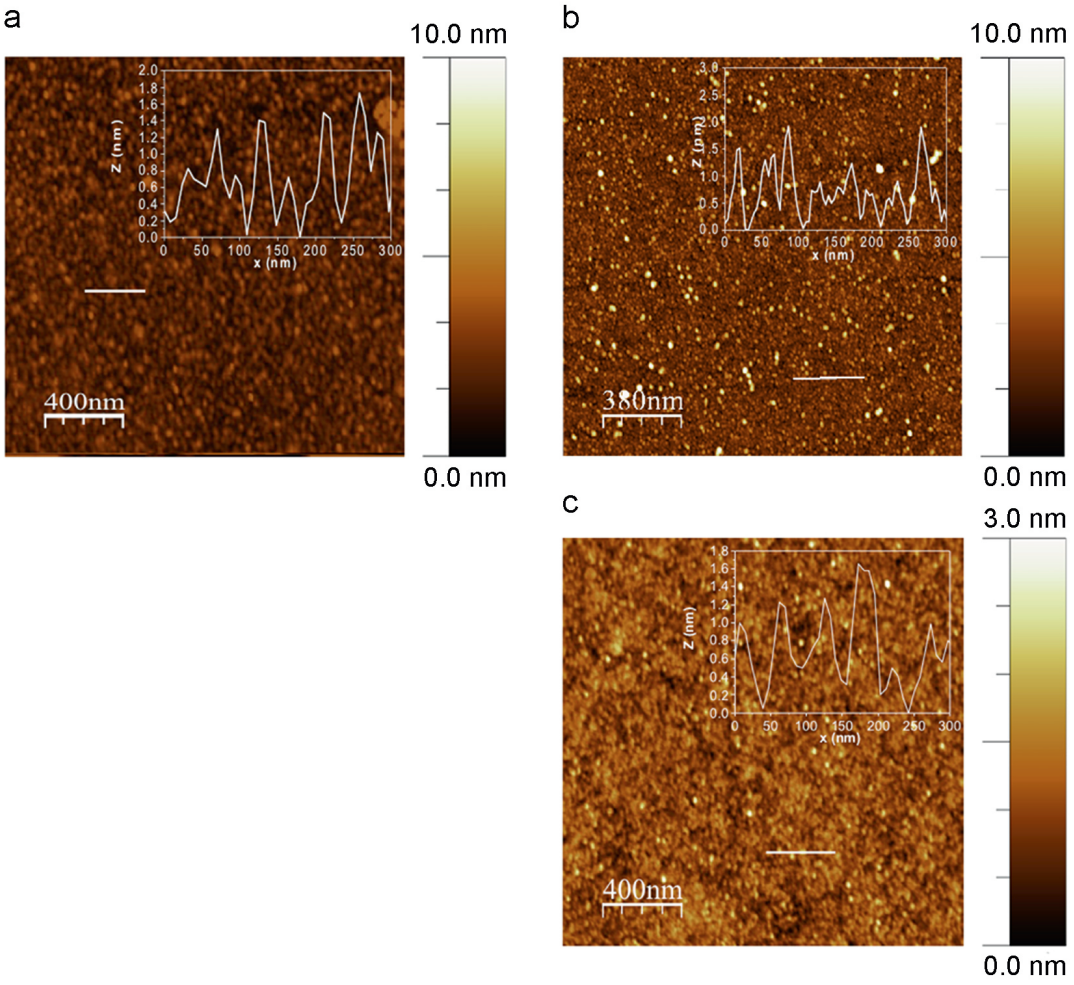


FIGURE 3.9: Characteristic AFM image of PBA system deposited over the wafer **a** FeRu **b** CoRu **c** NiRu.

### Size of the pre-formed catalyst nanoparticles

The size distributions of the catalyst nanoparticles were determined by TEM imaging after their transfer onto carbon membranes (see section 3.6 for details on the transfer method), typical images of each catalyst are available on Figure 3.10. Figure 3.11 shows the size distributions for all the systems in this study. These distributions clearly emphasize that formation of nanoparticles with a controlled size is achieved through our method : for all systems, the diameter distribution is centered between 1.5 and 1.8 nm, with a maximum standard deviation of 0.5 nm as shown in Table 3.5. The observed mean nanocluster sizes for the bimetallic catalysts represents a systematic decrease of about 30% to 50% (depending on the system) of the average size of the initial PBA pre-catalyst nanoparticles ranging from 2.4 to 3.3 nm. This size reduction is directly resulting from the transformation from a PBA structure with a large lattice parameter (approximately 10 Å) to a metallic alloy structure with a smaller lattice parameter. The narrow size distribution found for all

the bimetallic systems demonstrates the fine tuning of the reductive pretreatment we developed, which has the decisive advantage to let well-defined metallic clusters be formed at relatively high temperature whilst the Ostwald ripening is kept within a limited range. A statistical study of the size of the catalyst nanoparticles after SWCNT growth was also carried out by TEM. The mean particle size remains stable even after the growth of the nanotubes (see Figure 3.11c-d-e), with only very small traces of Oswald ripening, showing that the control of the size is maintained throughout the growth process.

TABLE 3.5: Table of the average size of each catalyst after pretreatment and growth step.

| Catalyst size (nm) | FeRu | CoRu | NiRu |
|---|---|---|---|
| Before growth | $1.5 \pm 0.5$ | $1.7 \pm 0.5$ | $1.8 \pm 0.4$ |
| After growth | $1.7 \pm 0.5$ | $1.7 \pm 0.5$ | $1.5 \pm 05$ |

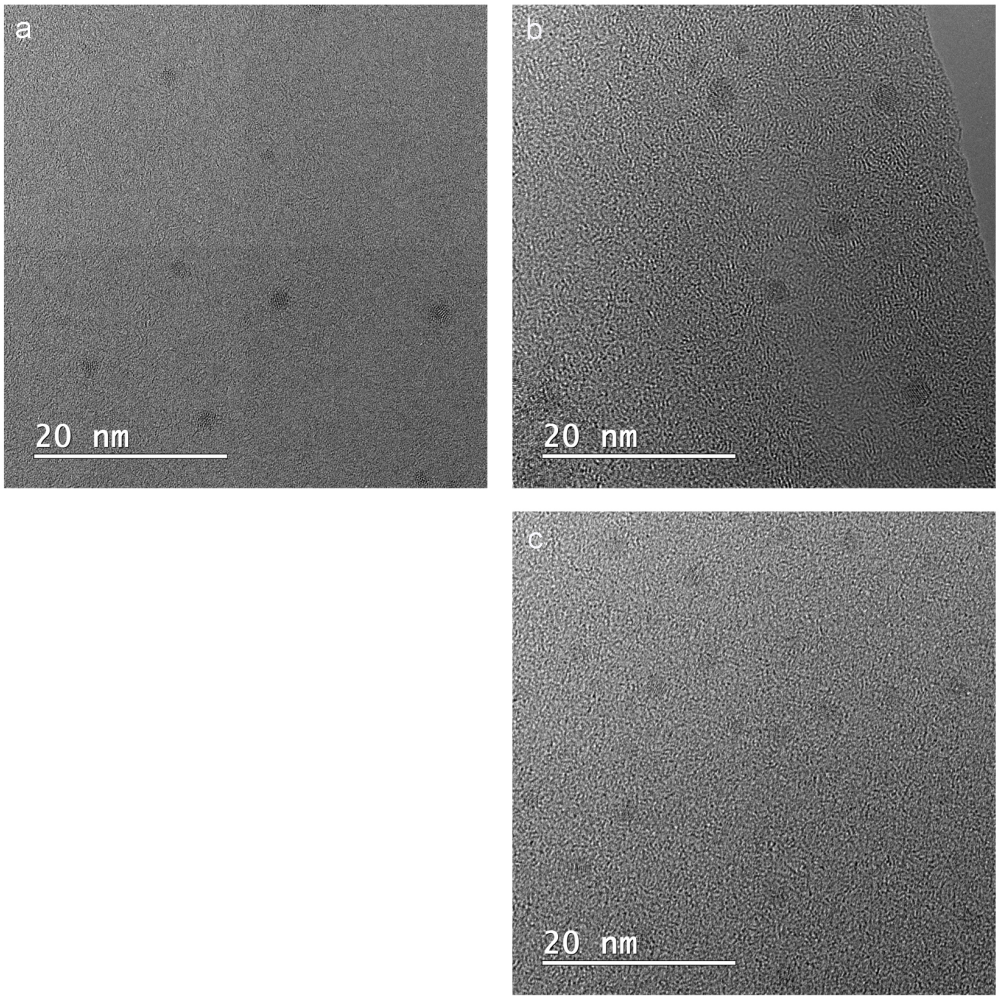


FIGURE 3.10: TEM image exemple of **a** FeRu **b** CoRu **c** NiRu

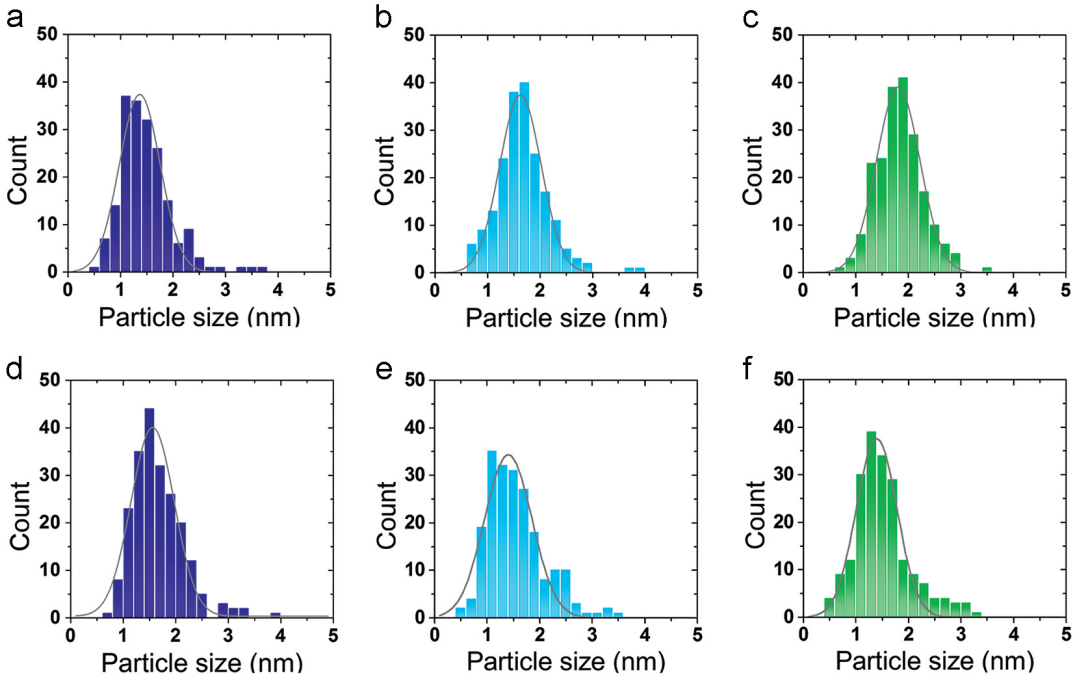


FIGURE 3.11: Size distribution of **a** FeRu **b** CoRu **c** NiRu after pretreatment and Size distribution of **d** FeRu **e** CoRu **f** NiRu after SWCNT growth.

### Catalyst chemical composition

To better understand the composition of the nanoparticles after reduction, a more detailed STEM-EDX study was carried out for all the bimetallic systems. In order to predict more accurately whether the bimetallic nanoparticles can be solid solutions or segregating systems after reduction, we considered the binary phase diagrams for the related bulk systems. The literature is poor on binary phase diagrams at the nanometer scale for the systems studied here. All the bimetallic combinations except for the NiRu systems can form solid solutions in bulk and within the temperature range studied here, for a wide range of compositions including 1:1 stoichiometry [182]. Around 800 °C, the solid solution of the NiRu systems cannot exceed 8% of ruthenium in nickel. We can therefore expect the occurrence of a phase segregation for this system, and the formation of a solid solution for the FeRu, and CoRu systems. Figure 3.12 shows a high angle annular dark field (HAADF) STEM image (see section 2.2.2, for details on these techniques), elemental maps for the two metallic components, and the relative map obtained by superimposing the two elemental maps, for each of the studied systems. Elemental maps were extracted at energies of 6.30-6.50 keV (Fe $K\alpha$), 6.82-7.03 keV (Co $K\alpha$), 7.37-7.58 keV (Ni $K\alpha$), and 2.49-2.63 keV (Ru $L\alpha$). As expected from the corresponding bulk binary phase diagrams, both metals are present, and appear to be intimately mixed in an alloy-like manner for FeRu and CoRu system. In the case of NiRu system, while a phase segregation is expected, an alloy structure seems to be obtained at the nanometric scale. For all systems, the preparation method results in the formation of bimetallic particles that are presumably solid solutions.

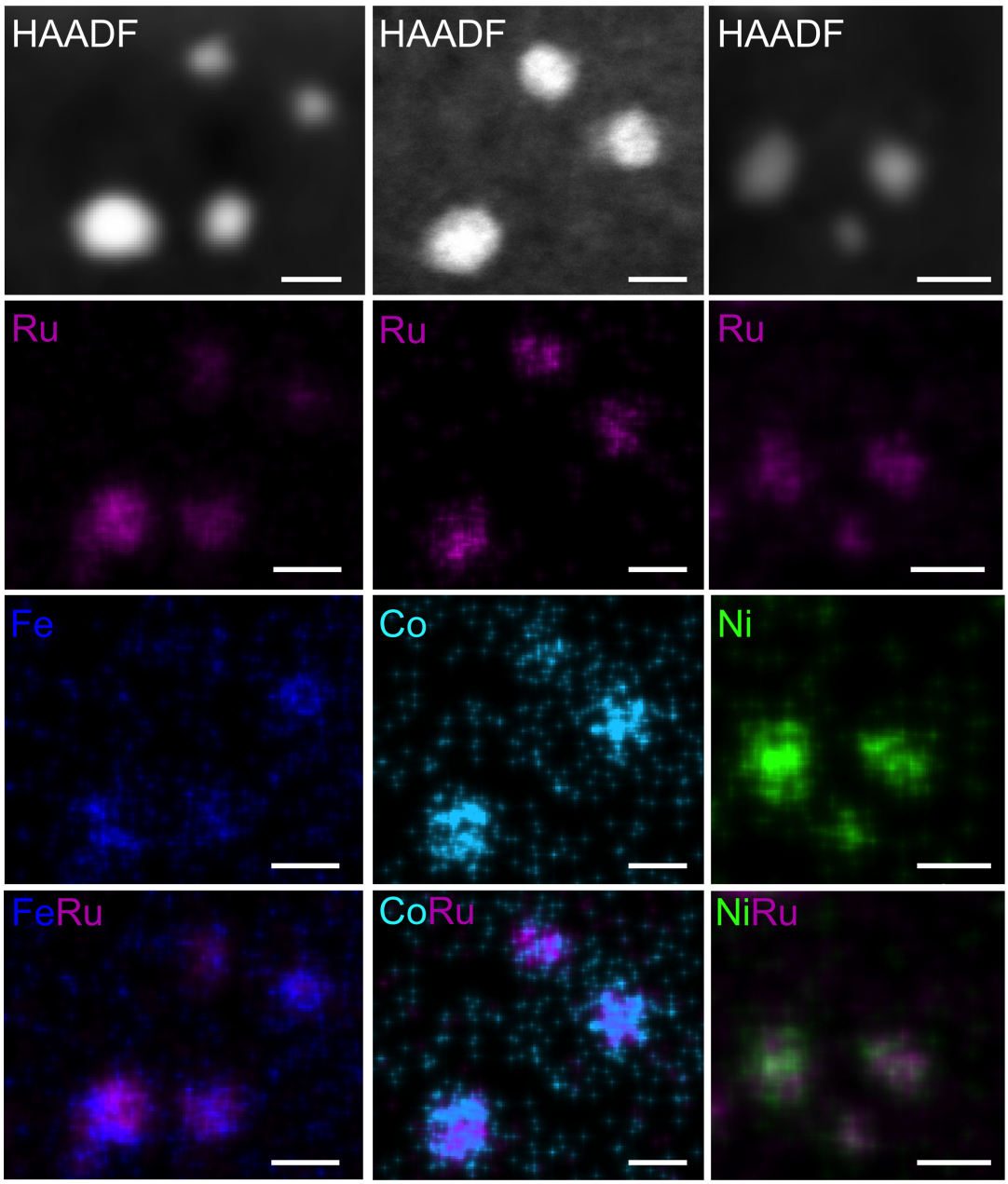


FIGURE 3.12: HAADF-STEM images, and EDX-STEM chemical maps for the three systems (FeRu, CoRu, NiRu). For each image the scale bar is 3nm.

The full EDX spectrum of the nanoparticles of the Figure 3.12 show the absence of potassium (present in the PBA precursor structures for FeRu), Cesium (present in the PBA precursor structures for CoRu and NiRu), chloride and calcium (used during the PBA synthesis process) in the catalyst nanoparticles (see appendix A). We can therefore assume that potassium, cesium, chloride and calcium will do not have any influence on the SWCNT growth process. In the case of the NiRu and FeRu systems for some nanoparticles, a sulfur contamination is observed while for the same synthesis other nanoparticles are sulfur free. The origin of this contamination is up to now, still unclear. The SAM used as an anchoring point for the PBA system contains a sulfur atom which can be

responsible for the contamination. The fact that other systems do not contain sulfur put in doubt that the SAM was at the origin of the contamination.

As proven by the previously discussed SEM-EDX study on the PBA nanoparticles powder, the starting stoichiometry is very close to 1:1 for all the precursors presented in this thesis. Accounting that the PBA structure consists of alternating metal ions of different nature uniformly bridged by the cyanoligands, and that the particles form a single layer grafted on the substrate surface, we could reasonably expect that after the reductive pretreatment, the metallic catalyst nanoparticles will generally be obtained with a 1:1 stoichiometry. Here trustable SEM-EDX quantification can not be performed, indeed, during the TEM experiment, we clearly observed the deterioration of the nanoparticle under the electron beam leading to lose of atoms.

## 3.4 Carbon Nanotube Growth

### 3.4.1 Synthesis

Each of the three bimetallic catalyst systems has been tested for SWCNT growth using the d-HFCVD process previously described (see section 2.1.1). Directly after the pretreatment step and without opening the reactor, methane is introduced as a carbon source for the growth of SWCNT, experimental details of the synthesis are available in section 3.6.

A nanotube growth experiment with identical parameters was also conducted in FeniX facility. As shown in Figure 3.13, no drastic shift is observed for the ruthenium and iron edges between pretreatment and growth indicating that the growth starts from metallic nanoparticles and not from a carbide. Presence of few nanotubes is confirmed by detection of RBM peaks in Raman spectroscopy. To complete this study, a typical as-synthesized HF-CVD sample was also analyzed in FeniX under the same conditions. Similar edges for ruthenium and carbon are observed between the CVD growth samples and the "FeniX" growth. The increase of the carbon peak (relative comparison with the ruthenium peak intensity, stable during the all synthesis process) at 284.4 eV is attributed to the formation of carbon nanotubes. This carbon peak position is also close to the value obtain by Wirth and co-worker for carbon nanotube grown from iron catalyst [66]. We have to note that carbon edge presents a decrease of about 25% of FHWM for the HF-CVD sample, This change is attributed to a much larger amount of nanotubes on the surface for the HF-CVD grown sample which is confirmed also by the Raman spectroscopy measurements. No contribution of carbide peak is observed at the carbon edge. A second small shift and an additional contribution is observed for the iron edge in case of the HF-CVD sample. As no carbide peak is observed for both carbon and ruthenium in the HF-CVD growth, we attributed this peaks to the possible slight oxidation of the iron due to air exposure after growth, which may be divided in a multi-signal.

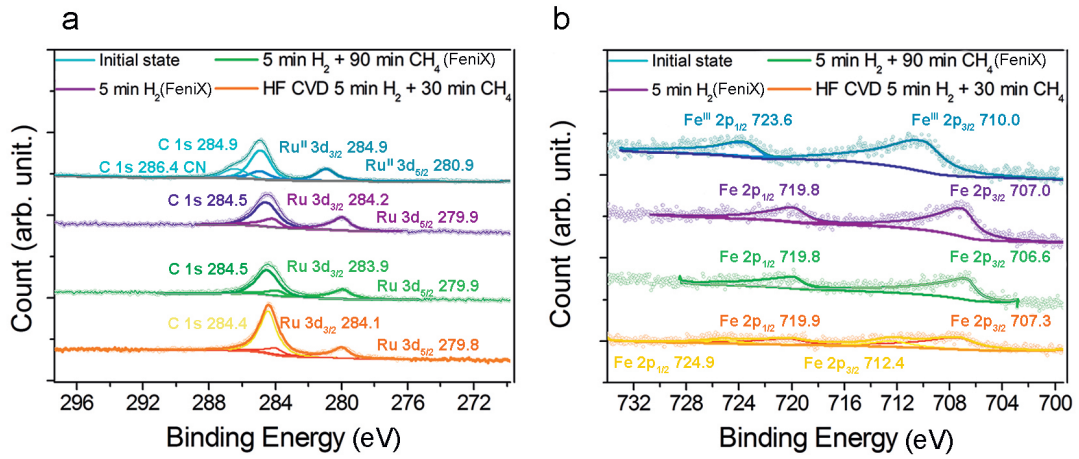


FIGURE 3.13: XPS spectra obtained in FeniX facility: **a** carbon and ruthenium edges **b** iron edge. Purple and green curves show the in-situ XPS spectra obtained after a gas exposure in FeniX facility while orange curve the XPS spectrum after a gas exposure in our HF-CVD reactor.

### 3.4.2 Characterization of as-synthesized SWCNT

### 3.4.3 Electron microscopy

The presence of SWCNT growth on the wafer surfaces in relatively large quantity is sustained through a SEM study and is an indication of the good efficiency of this new catalyst family for the growth of SWCNTs (see Figure 3.14a-c) .

From SEM images, we can observe a difference of the apparent growth efficiency between the different catalysts, for the same growth condition. FeRu and CoRu catalyst give rise to much more SWCNT than NiRu catalyst. TEM observations of the nanotubes after their transfer on carbon membranes (see section 3.6 for details on the transfer method) show the presence of SWCNTs of highly crystalline quality and diameters between 1 and 2 nm as shown in Figure 3.14d-e for SWCNT grown from CoRu catalyst. A substantial amount of poly(methyl methacrylate) (PMMA) residue from the transfer process was observed on the TEM images. As explained in the experimental section 3.6, the rinsing of the PMMA was purposefully only partially done, to ensure that the SWCNTs remain on the TEM grid. We also assume that the organic solvents (mainly acetone) used to rinse off part of the PMMA can contribute to this organic residue.

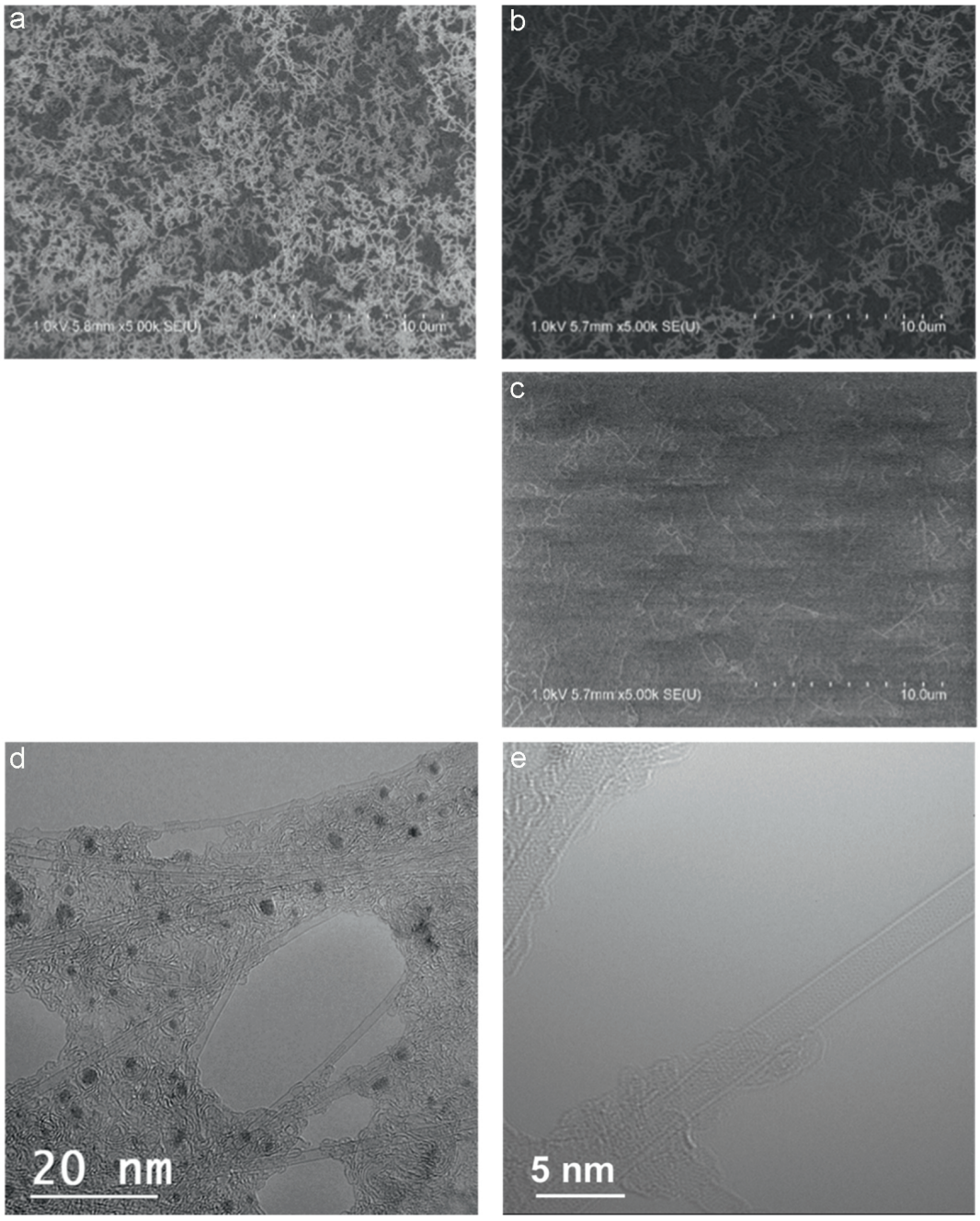


FIGURE 3.14: Typical SEM image for SWCNT growth at 800°C from **a** FeRu **b** CoRu **c** NiRu catalyst **d-e** TEM image of SWCNT growth at 800°C from CoRu catalyst after PMMA transfer.

### 3.4.4 Raman spectroscopy

Raman characterizations were also performed in the two spectral ranges representative for respectively the radial breathing mode (RBM) between 100 and 500 $cm^{-1}$ and between 1200 and 1600 $cm^{-1}$ for the $sp^2$ carbon D and G specific bands [9]. Analysis of the D and G modes indicates the good crystallinity of the carbon nanotubes, with a relatively weak D-band (around 1350 $cm^{-1}$), which

always represents less than 10 percent of the intensity of the G-band (around $1590cm^{-1}$). The presence of strong peaks in the RBM range attests the abundance of SWCNTs as seen in Figure 3.15d, which shows an example of a Raman mapping for growth from CoRu catalyst using a 633 nm laser.

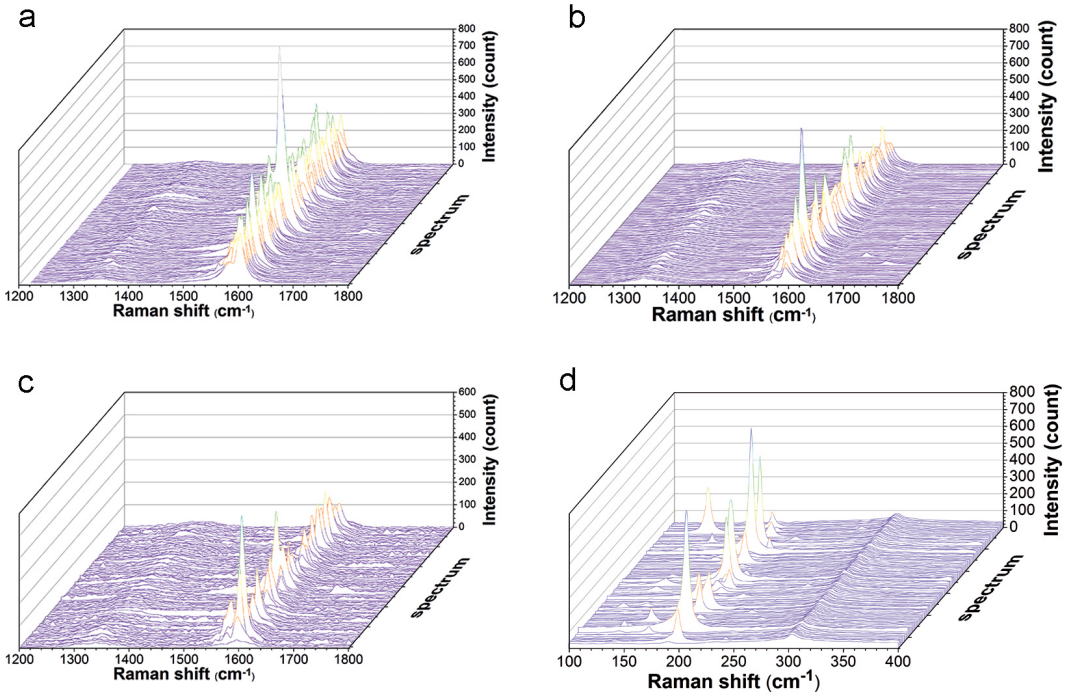


FIGURE 3.15: Raman mapping on a 50 $\mu m$ by 50 $\mu m$ surface (121 spectrum/mapping) in DG mode region at 532 nm for SWCNTs grown from **a** FeRu **b** CoRu **c** NiRu catalyst **d** in RBM mode region excitation at 633 nm for SWCNTs grown from CoRu.

## 3.5 Conclusion

In summary, we have developed a new and original method for designing specific bimetallic catalysts for SWCNT growth from various PBA nanoparticles with narrow size distributions. The structure and the composition of these catalyst precursors have been confirmed by TEM, IR spectroscopy, EDX and XRPD analysis. All data converge to demonstrate that PBAs have been successfully transformed into spherical bimetallic particles. These particles seems to be nanoalloys for all cases inspected by STEM-EDX. The narrow size distribution of the catalyst nanoparticles is thoroughly determined from statistical analyses of TEM images of nanoparticles assemblies. TEM micro-observations were further completed by a macroscopic in-situ XPS monitoring of the reductive pretreatment of the PBA nanoparticles performed for the FeRu system. Finally, we proved that this new family of catalysts allows the growth of SWCNTs with good yield as found from both TEM and Raman analysis.

## 3.6 Experimental details

### 3.6.1 PBA nanoparticles synthesis

30 mL of an aqueous solution containing the hexa-aqua complex $[M'(H_2O)_6^{2+}]$ (5mM) and cesium chloride (5mM) (CsCl) (CoRu and NiRu system) or potassium chloride (KCl) (FeRu system) (5mM), was added to 30 mL of an aqueous solution containing the potassium hexacyanometallate $K_4[Ru(CN)_6]$ salt (5mM). The as obtained PBA nanoparticles are stable in water without any stabilizing agent due to their negative charges, which leave their surface available, to coordinate to an organic ligand.

For their chemical and structural characterization, PBA nanoparticles were recovered as powders by adding an excess of calcium chloride salt ($CaCl_2$) followed by centrifugation, washing with water and drying the powder under vacuum.

| PBA FeRu | $K_4Ru(CN)_6$ | $Fe(NO_3)_3$,$9H_2O$ | KCl |
|---|---|---|---|
| Quantity (mg) | 6.2 | 6.0 | 1.12 |
| PBA CoRu | $K_4Ru(CN)_6$ | $CoCl_2$,$6H_2O$ | CsCl |
| Quantity (mg) | 6.2 | 3.50 | 2.52 |
| PBA NiRu | $K_4Ru(CN)_6$ | $NiCl_2$,$6H_2O$ | CsCl |
| Quantity (mg) | 6.2 | 3.56 | 2.52 |

### 3.6.2 Silane synthesis

The used ligand contains a silane function to allow the self-assembly process on the wafer oxide surface, followed by a long carbon chain in order to obtain a well-organized monolayer and, as a coordinating terminal group, a mercaptopyridine. The mercaptopyridine is able to form a covalent bond with the PBA pre-catalyst and then ensures precatalyst fixation over the surface.

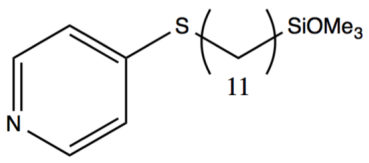


FIGURE 3.16: Schematic view of the synthesized silane.

This ligand is obtained by nucleophile substitution of 4-mercaptopyridine on 11-bromoundecyltrimethoxysilane. In a dry Schlenk, 780 mg of mercaptopyridine (1.1 eq), 2 mL of 11-bromoundecyl trimethoxysilane (1 eq.), 1 mL dry triethylamine ($Et_3N$) were refluxed in 20 mL of distilled dichloromethane ($CH_2Cl_2$) for 24h under an argon atmosphere. After cooling down to ambient temperature, 200 ml of diethyl ether $(C_2H_5)_2O$ were added, a white precipitate appears. After filtration the filtrate was then evaporated under reduced pressure. The product was then triturated with 100 mL of pentane ($C_5H_{12}$) for 2 hours. The pentane supernatant was collected and evaporated under reduced pressure, yielding a yellow oil.

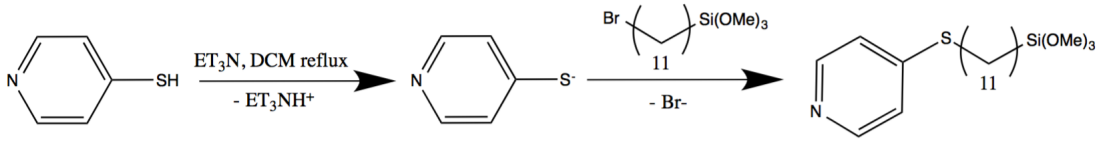


FIGURE 3.17: Schematic view of the synthesis process

### 3.6.3 Substrate preparation and functionalization

All wafers used in this study are 300 nm thermal $SiO_2$ coated silicon wafers purchased from SiMat. Each sample was cleaned by ultrasonication in DCM ($CH_2Cl_2$) for 15 minutes, followed by 10 minutes of Ar-O plasma treatment in order to activate the $SiO_2$ surface. The cleaned $SiO_2$/Si wafers were functionalized with the self-assembled monolayer (SAM) of a silane molecule. The wafers were immersed in a $10^{-3}$ M solution of the silane molecule in distilled toluene ($C_7H_8$) for 12 hours. The samples were subsequently rinsed with toluene and dichloromethane followed by annealing at 100°C for two hours in ambient air. In order to graft the PBA nanoparticles, the silanized wafers were immersed in the as-obtained colloidal PBA solution for one hour. The excess of nanoparticles was rinsed off with deionized water, and the wafers were left to dry under air such as to get coated by a single layer of the PBA nanoparticles.

### 3.6.4 Catalyst preparation and SWCNT growth

The first step of the synthesis process is a hot reductive treatment under hydrogen of the PBA particles into bimetallic particles. For that purpose, the wafers coated by the PBA nanoparticles were placed in the cold zone of the CVD chamber, the chamber was pumped to a $10^{-6}$ mbar pressure, and the temperature was set to 800°C in the hot zone. After stabilization of the temperature, $H_2$ was introduced at 100 sccm (standard cubic centimeters per minute) flow rate, and the corresponding filament power of 160 W turned on. Once the pressure of the chamber was stabilized at 90 mbar, the wafers were moved into the hot zone and maintained in the reductive atmosphere for 5 minutes. This treatment

is immediately followed by the SWCNT synthesis, by directly introducing $CH_4$ (without modifying $H_2$ flow rate) at 20 sccm flow rate and for a corresponding hot filament power of 120 W, while the overall pressure was increased to 100 mbar. These growth conditions are maintained during 30 minutes, after which the chamber was pumped and the samples removed from the hot zone. In order to investigate the step related to the catalyst nanoparticles formation, some samples were removed from the chamber after the reductive pretreatment prior to the SWCNT growth step.

### 3.6.5 Wafer to grid transfer method

TEM and STEM-EDX inspection of the nanoparticles and/or SWCNTs require their transfer from $SiO_2$/Si wafers, used for their formation, onto a TEM grid. For that purpose, we have adapted the conventional poly(methyl-methacrylate) (PMMA) transfer method [183]. First, a thin layer of PMMA (495PMMA A4 purchased from MicroChem) was spin-coated on the wafer at 500 rpm for 90 seconds. This system was dried at ambient temperature for 12 hours. The PMMA film containing the SWCNTs and/or the bimetallic nanoparticles was then lifted off the wafer by etching the $SiO_2$ layer into a sodium hydroxide aqueous solution (NaOH, 1 $mol.L^{-1}$) for a few hours. This film was recovered, transferred and rinsed repeatedly in deionized water. A TEM grid was placed under the film, and a maximum of excess water was removed, until the film stuck onto the grid. The system was then slowly ramped up until 120 °C on a hot plate and left to dry overnight. The dried PMMA was then removed with acetone. In contrast to the requirements for device fabrication [184], characterization of SWCNTs does not require the PMMA to be completely removed as it can serve as a support for the SWCNTs, facilitating their observation. However, the presence of PMMA is a drawback for the characterization of catalyst nanoparticles, being source of contamination, and it is therefore preferable to remove it as much as possible.

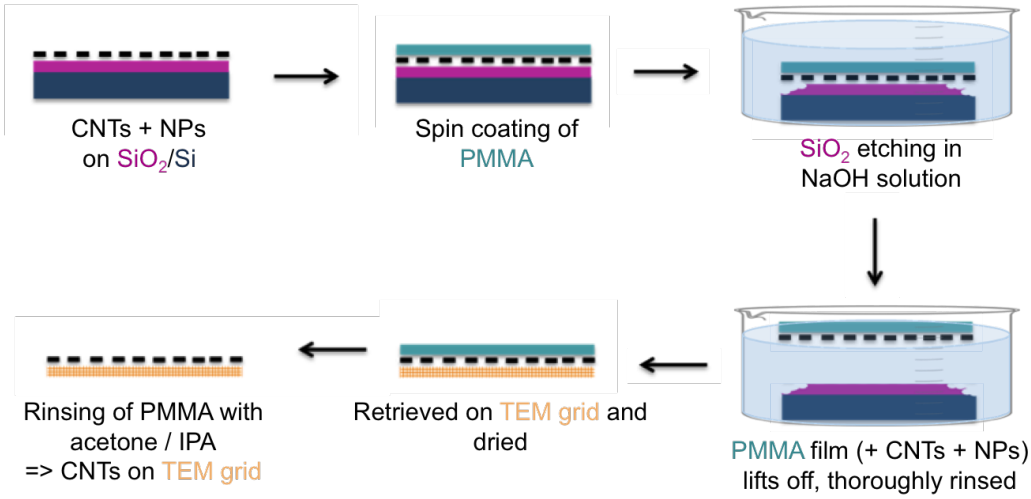


FIGURE 3.18: Schematic view of the transfer process for the deposition of SWCNT and Nanoparticles on TEM grid.

# Chapter 4

# Parametric study of the SWCNT synthesis

Controlling the SWCNT growth for freely tuning their structure is one of the main challenges in SWCNT synthesis. Catalyst assisted CVD growth of SWCNTs is a quite complex process. Various parameters of the CVD growth have been shown to drastically impact the structure of the as-obtained nanotubes (see chapter 1, section 1.3). In this chapter, we propose to focus on the influence of the synthesis temperature and the chemical composition of the catalyst upon the SWCNT synthesis. The bimetallic catalyst nanoparticles described in the previous chapter have been used for growth of SWCNTs at various temperatures. The methodology used and experimental details of this parametric study are described in section 4.5. For this parametric study we mainly characterized the SWCNT by Raman spectroscopy. We are aware of the fact that a full characterization of a sample requires the use of several cross characterization techniques. This is especially true when Raman spectroscopy is used, due to the resonance phenomenon previously described in section 2.2.1 (Chapter 2). Indeed, through this technique only resonant SWCNT with the laser energy could be detected. In order to limit the number of SWCNTs out of resonance, we used four different laser excitation wavelengths (785, 633, 532 and 473 nm). The corresponding available transitions for various nanotube's chiralities can be found using a Kataura plot. In this thesis we used the Kataura plot presented in Figure 4.1 from Saito group's. We will use in this chapter the Raman spectroscopy as a comparative and qualitative tool for several growth conditions and not as a complete tool characterization. For each sample all the statistics have been made on almost 200 peaks and for almost three mapping by laser. Here, we will present the result obtained for a same batch of sample in order to limit variation between the samples (see section 4.5 for experimental details). The reproducibility of the observed trend has been checked by performing the measurement on several batches of samples. A discussion about this reproducibility is proposed on section 4.3.

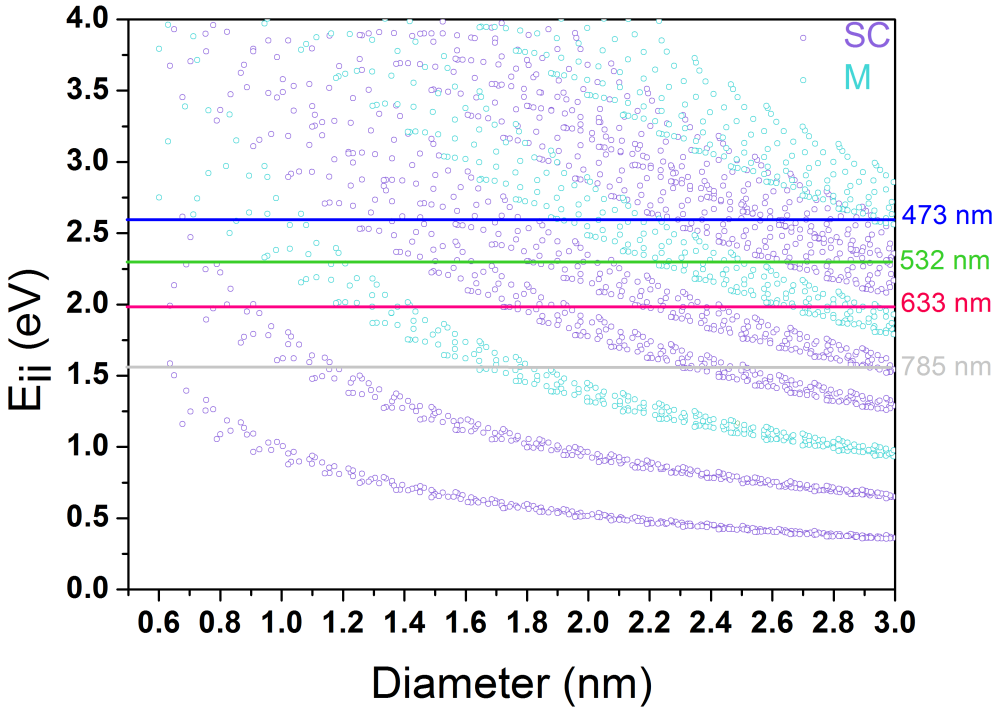


FIGURE 4.1: Kataura plot, energies of the used laser for Raman spectroscopy are represented with a solid line.

## 4.1 Influence of the growth temperature on the SWCNT structure

Temperature is one of the key parameters influencing any chemical reaction and this rest arguably true for any CVD process. In order to evidence the influence of the temperature on the SWCNT synthesis process, we have realized synthesis (including pretreatment and growth, the section 3.6.4 reported the experimental details of the synthesis) at four different temperatures (700°C, 800°C, 900°C and 1000°C) for each catalyst described in the previous chapter (FeRu, CoRu and NiRu catalysts). Through systematic Raman spectroscopy measurements, we have analyzed the diameter range of the as-synthesized nanotubes and the corresponding semiconducting to metallic ratio of the detectable SWCNTs. We also proposed a comparison of the synthesis yield. For each sample in this study we have performed three Raman mapping (50x50, 10 $\mu m$) for each laser wavelength in a random positions over the wafer surface. According to corresponding SEM images, the SWCNT length does not exceed 10 $\mu m$. Concerning the counted number of the carbon nanotubes, as most of the time we obtained well-defined individual RBM peaks (see Figure 3.15d), each identified individual peak in the mapped area is considered as one unique SWCNT whatever its intensity. Indeed, Raman spectroscopy on SWCNT leads to resonant phenomena, the intensity of a peak cannot be directly related to the quantity of SWCNTs present in our case.

### 4.1.1 Evolution of the SWCNT diameter distribution

In order to extract the nanotube's diameter distribution from the RBM peak positions we used the empirical law reported by Jorio and co-workers, for SWCNT grown supported on silicon oxide [164].

$$\mu_{RBM} = \frac{248}{d_t} \tag{4.1}$$

Where $\mu_{RBM}$ is the resonance frequency of the nanotube expressed in $cm^{-1}$ and $d_t$ is the tube diameter expressed in nanometer.

However, one should note that for obtaining an absolute diameter distribution, an adapted law must be found by correlating Raman data with other techniques such as TEM measurements. Indeed, Raman spectroscopy measurements are extremely sensitive to the surrounding environment which can induce important shift of the RBM peak position [185]. Then, great precautions must be taken when attempting to attribute to a RBM peak an exact diameter or chirality, especially in case of supported and/or non-individualized nanotubes. Here, the purpose of this study is to compare the effect of the temperature on the as-obtained carbon nanotubes' diameter distribution and not determining the exact diameter distribution of the SWCNTs in the sample. Under these conditions, the use of Raman spectroscopy and the law detailed in equation 4.1 are justified.

Figure 4.2 presents the average diameter of the SWCNT derived from the Raman measurement analysis for each catalyst and the different growth temperatures. Whatever the type of catalyst used, we observed an increase of the SWCNT average diameter coupled with a broadening of the distribution when the growth temperature is increased. The broadening of the distribution is clearer in the appendix B where the corresponding histogram of the diameters distribution obtained for each growth temperature are presented. One can note that no SWCNT have been obtained at 700°C from the nickel ruthenium catalyst, we will discuss this point in section 4.2.1.

For ease of interpretation and to better evidence the trend, in Figure 4.3 we represented the percentage of SWCNTs counted within given diameter intervals of 0.3 nm. For each of the three catalyst a similar trend is observed. At low temperature (700°C or 800°C for growth from NiRu) a majority of small diameter SWCNTs are obtained and very few larger diameter nanotubes were grown. For instance, for each of the three catalysts, when the growth is performed at the lowest temperature (700°C or 800°C), more than 65% of the counted SWCNT have diameters below 1.3 nm and less than 6% have diameters above 1.6 nm. With the temperature increase, the number of small diameter SWCNTs decreases whilst the number of grown SWCNTs with bigger diameters increases. At 1000°C, less than 23% of the nanotubes are found to have diameters below 1.3 nm and more than 40% above 1.6 nm.

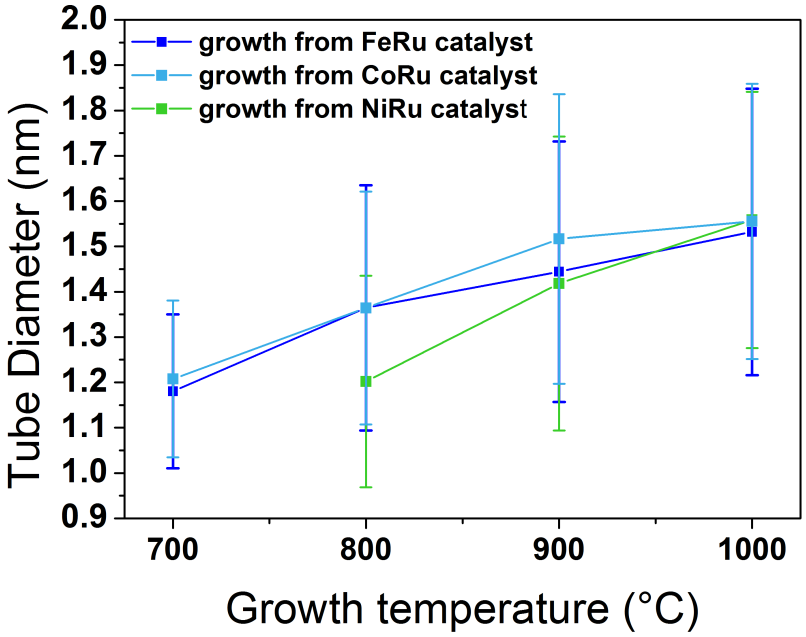


FIGURE 4.2: Average diameter size obtained for the growth at 700, 800, 900 and 1000°C. The error bar correspond to the standard deviation.

Many studies in the literature report also an increase of the grown SWCNT diameter with the temperature (see section 1.3.1 in chapter 1). This general trend is often explained by an increase of the catalyst size due to a coalescence mechanism induced by the increased temperature [81–84, 86, 88, 185, 186].

Few other studies attributed this change to other phenomena induced by temperature change. Lu and co-workers [91], showed for instance that the variation in carbon feed rate leads to a selective activation or poisoning of the catalyst nanoparticles depending on their size. They reported that a change of temperature can lead to variation of the carbon feed rate by modifying the decomposition rate of the carbon precursor at the catalyst surface.

Other key parameters in the SWCNT growth, such as the carbon solubility limit depends both on the catalyst size and the growth temperature [126, 187]. For instance, Picher and co-workers [90, 188] reported that in high temperature and low pressure domain, the small catalyst nanoparticles are not activated due to a higher supersaturation limit compared to that of the larger particles. In the low temperature and high pressure domain, they reported a preferential encapsulation of small nanoparticles which leads to their subsequent poisoning.

All these studies however, underly that the catalyst nanoparticle size is related to the as-grown SWCNT diameter. This hypothesis is valid if a tangential growth is performed. As shown in section 1.3.1 two growth modes are observed during typical CVD synthesis : a tangential mode where the diameter of the catalyst nanoparticle is close to the SWCNT diameter, and a perpendicular mode, where the catalyst nanoparticle diameter and SWCNT nanotube diameter are no longer related.

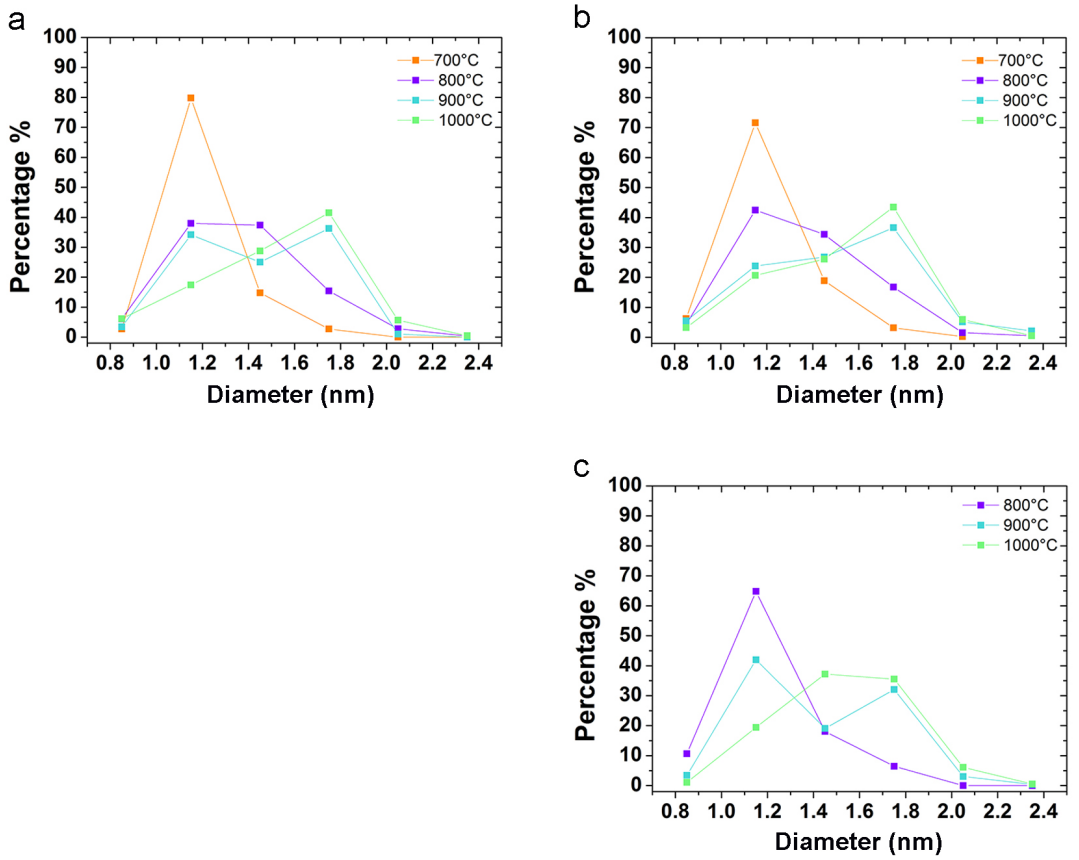


FIGURE 4.3: Diameter distribution for growth from **a** FeRu catalyst **b** CoRu catalyst **c** NiRu catalyst. The point is placed in the middle of the diameter step (0.3 nm).

Here, we assume that under our experimental conditions, mostly a tangential growth is obtained. In this respect, we remind that we have designed our catalyst to privilege a tangential growth. One of the goals was to obtain alloy nanoparticles with a lower carbon solubility which justify the use of ruthenium, in order to favor a tangential mode [126]. Consequently to access potential controlled SWCNT diameter by controlling the catalyst nanoparticles size. TEM observations are indicative of this preferential tangential growth mode. For these observations we used the transfer method described in chapter 3. As shown in Figure 4.4 in the transferred sample, we could clearly observe SWCNTs and their corresponding catalyst nanoparticles but such observations are very rare. Only few "nanotube+nanoparticle" systems have been observed, preventing any true statistical study. This difficult observation could be explained by a detachment of the nanotubes from the catalyst at the end of the growth. Nevertheless, each time that we observe in TEM measurement a nanoparticle with its corresponding nanotube, the growth mode was tangential. The two examples in Figure 4.4 clearly illustrated the tangential growth mode observed.

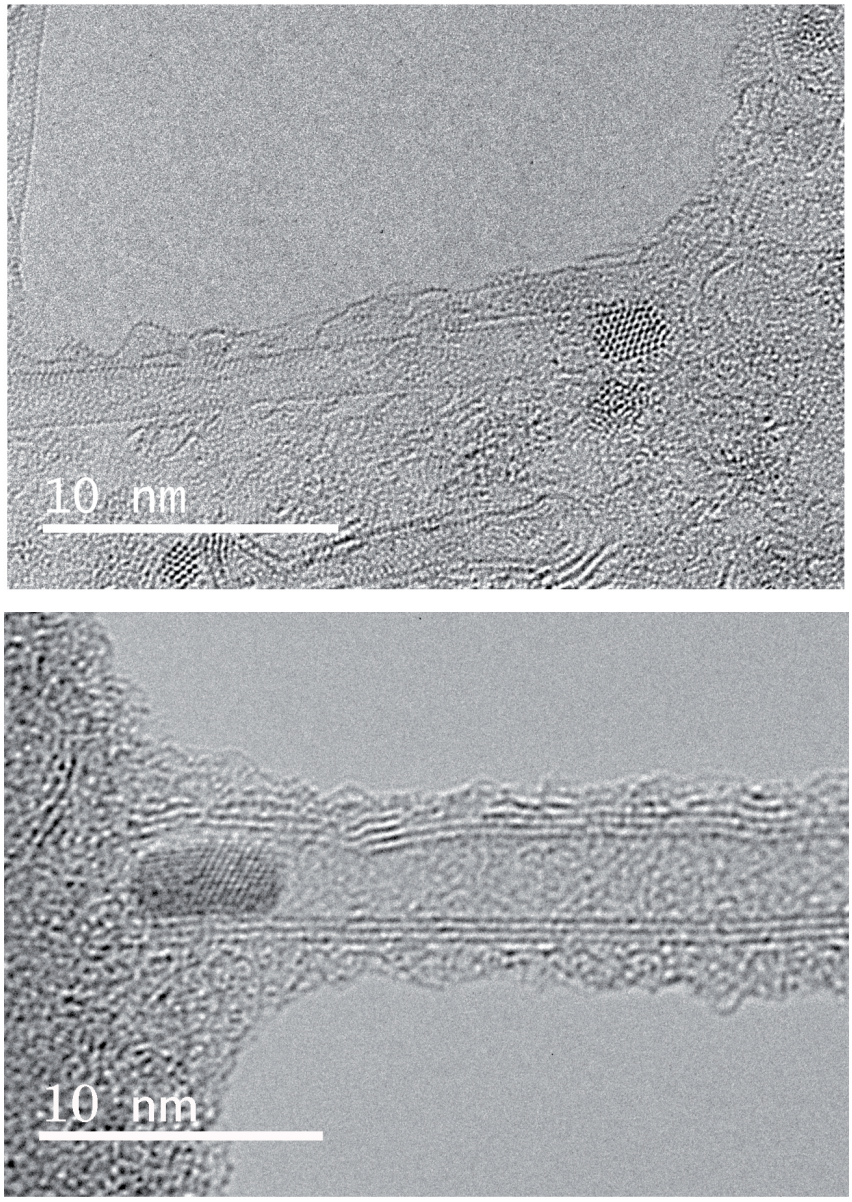


FIGURE 4.4: HRTEM image of the growth mode of **Top** SWCNT from CoRu catalyst at 800°C **Bottom** DWCNT from FeRu catalyst at 900°C

We have previously discussed that the increase of SWCNT diameters with the temperature synthesis is often explained in the literature by an increase of nanoparticle size due to coalescence mechanism. Nonetheless if this mechanism is likely to be activated, it is rarely being demonstrated in the concerning studies. We proposed to performed TEM measurements to compare the catalyst nanoparticles size at two extreme temperatures of our study. Such comparison may confirm or not if a coalescence phenomenon, such as Ostwald ripening [89] is responsible for the disappearance of small nanoparticles at high temperature and thus responsible for the reduced number of small diameter nanotubes that we observed. Figure 4.5a presents the size distribution histogram of FeRu nanoparticles after the five-minute pretreatment (i.e. before introduction of

the carbon gas source) conducted in the HF-CVD reactor at 800°C (purple) and respectively 1000°C (green). The size distribution diagrams obtained are very similar. In both cases, small nanoparticles are mostly present over the surface, 57% of counted nanoparticles are below 1.5 nm at 800°C and 56% at 1000°C (Figure 4.5a). We can reasonably assume that, during our synthesis, after the five-minute pretreatment, when the carbon source is introduced, the same population of nanoparticles are available for the SWCNT growth. At this point, one can assume that the coalescence occurs after introduction of methane during the 30 min of growth, and not during the pretreatment step. In the previous chapter, we demonstrate that a very small coalescence occurs during the half-hour growth at 800°C. We have also checked that at 1000°C the coalescence phenomena also appears very limited. Figure 4.5b presents the catalyst size histogram of the nanoparticle after growth (blue) and after pretreatment (green) steps at 1000°C, only very small traces of coalescence can be supposed.

The unusual limited coalescence observed in our synthesis process is to be attributed to the use of $H_2$ activated (leading to atomic hydrogen $H_{at}$) during all the synthesis process. Previous studies conducted in the laboratory shown that $H_{at}$ induced defects with high trapping energy over the substrate surface [189]. These defects limit the catalyst surface diffusion and increase the pinning effect of the nanoparticles leading to the formation of well-defined and isolated nanoparticles [189–191].

We then compared the SWCNT diameters distribution obtained through Raman spectroscopy with the catalyst size distribution for the two temperatures. We can easily observe that the diameter distribution of SWCNTs and that of of the nanoparticles fit well in the case of growth at 800°C but not in the case of growth at 1000°C (Figure 4.5c and d respectively). If we consider that the diameter of the nanoparticles ($d_{np}$) and the nanotubes ($d_t$) are similar ($d_{np}/d_t \approx 1$) the small nanoparticles appear to be less active for growth at 1000°C. In comparison to the SWCNTs grown at 800°C, the diameter distribution of the SWCNTs grown at 1000°C is shifted towards bigger diameters. This effect is also shown in Figure 4.3a.

Finally, from TEM measurements, we have shown that catalyst nanoparticles available for synthesis are roughly in the same size range whatever the growth temperature, but SWCNT of different diameter ranges are synthesized. From this experiment we can conclude that the hypothesis of coalescence effect leading to an enlargement of the nanoparticle and then of the SWCNT diameter, is definitely not the main mechanism explaining the trends observed in our synthesis experiments.

To confirm that, we have also performed the SWCNT growth step at different temperatures (800 or 1000°C) but from the same starting nanoparticles assembly, obtained by a five-minutes pretreatment at 1000°C. In this experiment, after a five-minute pretreatment at 1000°C we have stored the sample in the cooled zone of the reactor until the furnace reached 800°C. Then, the sample was moved in the hot zone and carbon source was added. If the nanotube diameter increase was triggered by a supposed lack of small nanoparticles after a

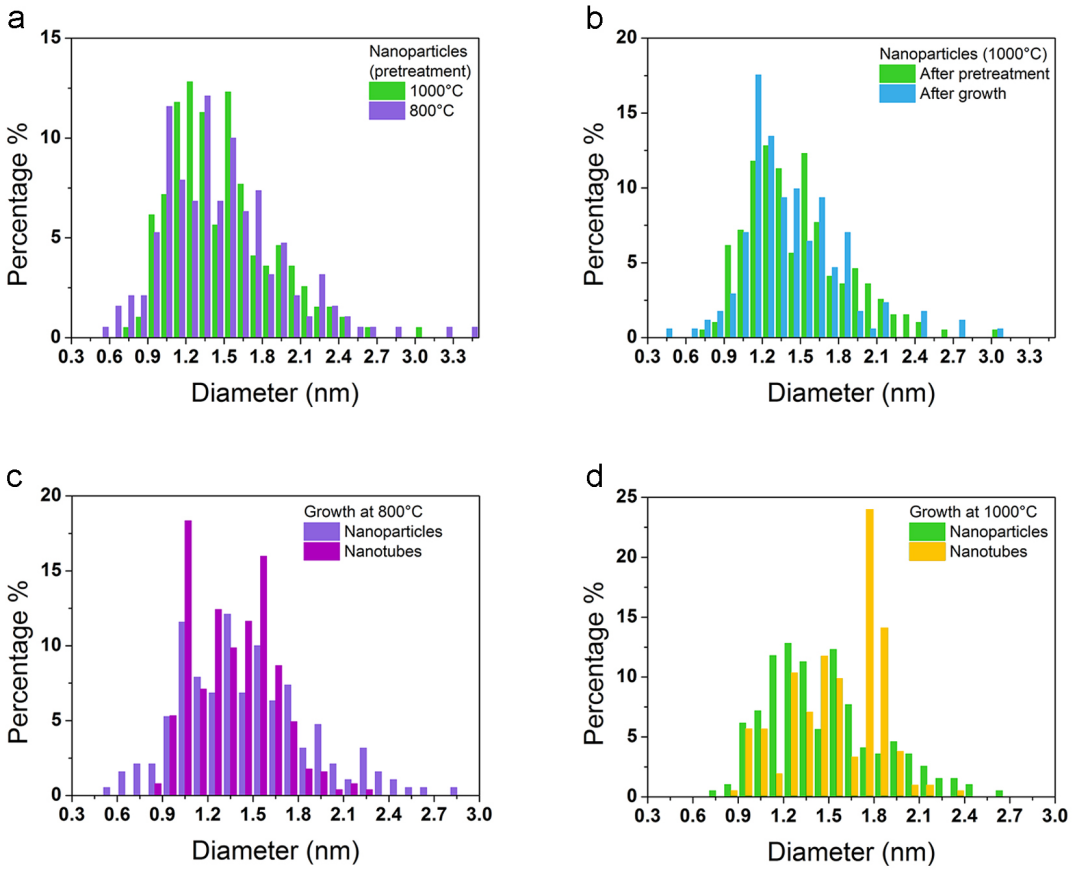


FIGURE 4.5: Size distribution histogram **a** nanoparticles of FeRu after pretreatment at 800°C and 1000°C **b** nanoparticles of FeRu after pretreatment and after growth (1000°C) **c** nanoparticles after pretreatment at 800°C and nanotube for a growth at 800°C **d** nanoparticles after pretreatment at 1000°C and nanotube for a growth at 1000°C. All the statistics have been made on at least 200 nanoparticules or nanotubes.

pretreatment step at a higher temperature, we should then obtain bigger nanotube diameters than in case of a full synthesis at 800°C. The results presented in Figure 4.6 show however that very similar size distribution for the full synthesis at 800°C (purple curve) and the bi-temperature synthesis (gray curve) are obtained. We didn't observe an increase of the biggest nanotube population for the bi-temperature synthesis. For instance, around 35% of nanotubes are found to have diameters between 0.9 and 1.1 nm for the two syntheses, to be compared with the only 15% of SWCNT that are found in this diameter range when the full synthesis is performed at 1000°C.

Nonetheless a difference was observed, not in the nanotubes' diameters distribution but rather in the total yield of the synthesized SWNTs. In comparison to a classical synthesis (pretreatment and growth steps at the same temperature), when the growth step is performed at lower temperature than the pretreatment, very few tubes are obtained. Such result indicates that the cooling of the sample seems to impact the nucleation and/or the nanotube growth. This trend has been observed for all the three catalysts explored in this study. The mechanism of this catalyst poisoning during the cooling has not been deeply

investigated and no evident answer could be found from our limited set of performed experiments. As described in the previous chapter, a carbonaceous SAM is used to control the catalyst density over the substrate surface. One may assume that the carbon contained in this layer, if not effectively removed during the pretreatment step, may interact and could be incorporated within the catalyst nanoparticle. Thus it can lead to the graphitization of the catalyst surface during the cooling. This hypothesis could be valid but disagree with TEM observations performed ex-situ after the pretreatment step. Indeed, we could not evidence any graphite layer over the particle surface (see for example Figure 3.10 in chapter 3). It's also possible that during the cooling, the formed bimetallic catalyst nanoparticle crystallized in a new form, somehow less reactive than the form obtained directly after pretreatment at high temperature. For example, He and co-workers reported that under fixed growth conditions, icosahedral (Ih) gold nanoparticle was inactive to grow SWCNT while the face centered cubic ones allowed the growth. On the basis of a theoretical study, they assigned these differences to the lack of carbon solubility in Ih Au NPs that does not allow the lift-off of the tube nucleus [192].

Looking to our set of experiments, the hypothesis of coalescence can be ruled out. A selective activation or deactivation of the various nanoparticles upon their sizes can be suggested from our experimental observations. Indeed, whatever the pretreatment step temperature, in terms of size distribution, almost the same population of nanoparticles are accessible for the growth but different populations of SWCNT are obtained when growth temperature varies.

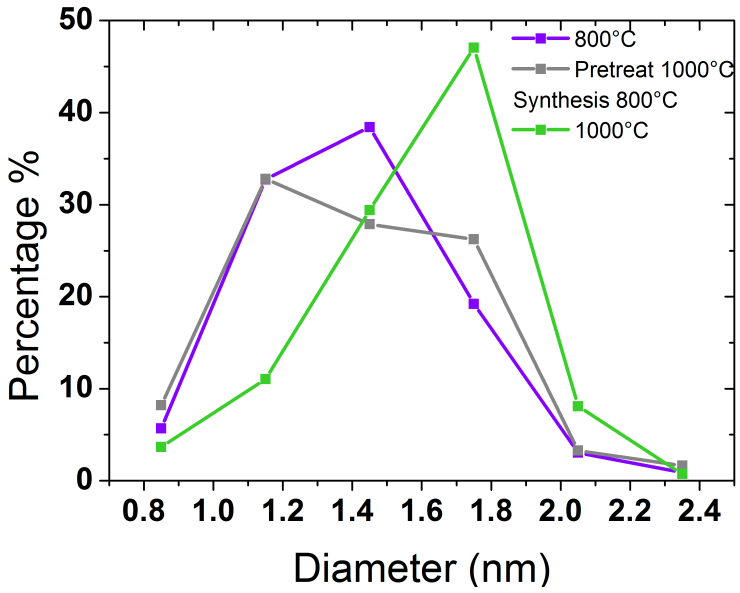


FIGURE 4.6: size distribution histogram of nanotubes from FeRu catalyst for growth, at 800°C (pretreatment+growth) (blue line), pretreatment at 1000°C and growth at 800°C (gray line) and at 1000°C (pretreatment+growth) (green line). We have to mention that samples were characterized here by only three wavelengths only (473 nm, 532 nm and 633nm).

One can note that in our synthesis process, the various parameters are controlled and decoupled to certain extent. A hot filament is used to activate the carbon precursor before its interaction with the catalyst, at a temperature significantly higher (>1700°C) than the actual growth temperature. Then we can reasonably assume that there is no drastic modification of carbon feed rate induced by temperature change in our synthesis. As a consequence, modification of carbon feed rate can not be responsible for the selective activation and deactivation of the nanoparticles, as it was argued by Lu and co-workers in the study previously presented [91].

As discussed in the first chapter, it is commonly admitted that the SWCNT growth can start only after reaching the carbon saturation of the catalyst nanoparticle [59, 61, 193]. This saturation limit is known to depend on both the temperature and the nanoparticle size. In general, for any given liquid and solid compound, the solubility increases when the temperature is increased. The solubility of carbon in metals is no exception to this rule [194]. Then, at high temperature, reaching the carbon saturation is expected to be more difficult. This trend seems also confirmed by a few reported experimental studies which have demonstrated that at high temperature an increase of carbon precursor pressure is necessary to initiate SWCNT synthesis [59, 82, 90, 195]. For the solubility dependence upon the nanoparticle size, as a general trend, many studies, both experimental [196, 197] and theoretical [198, 199] reported a higher impurity solubility with decreasing size of nanoparticles. Concerning carbon, for instance, giant carbon solubility in gold nanoparticles has been reported [200]. Theoretical study forecast also an increase of carbon solubility with the decrease of the nanoparticle size [126, 187, 201].

Based on both size and temperature effects upon solubility, some experimental studies on SWCNT growth report that at high temperature, for given synthesis condition, small nanoparticles are not activated or exhibit a delayed activation due to their higher supersaturation limit [90, 188, 202]. This hypothesis can be used to explain our lack of small diameter SWCNT at high temperature but seems not to be very realistic in respect to our growth conditions. As the partial pressure of methane is relatively high (around 27 mbar), the carbon precursor is activated prior reaching the catalyst and the synthesis time is also relatively long (30 min), it appears difficult to envision as limiting parameter a possible lack of sufficient carbon feed of the catalyst. As a control experiment, an increased of the methane partial pressure for synthesis at high temperature should be performed to verify this point. If more small SWCNTs grow, the hypothesis of carbon feed as a limiting factor can be validated. Along the same line, the lack of bigger nanoparticle activation at low temperature is sometimes attributed to poisoning due to "overloaded carbon" [88, 91], then a decrease of the methane pressure at low temperature should be performed. If the growth of bigger SWCNT diameter occurs, this hypothesis should be considered.

Another interpretation around carbon solubility can also be advanced and seems to better explain our results, in respect to our growth conditions. Aguiar-Hualde and co-workers [203], recently published calculations on SWCNT growth from nanoparticles with various carbon solubility. In case of nanoparticles with low carbon solubility, they observed a strong adhesion and wetting between the initially formed carbon $sp^2$ cap and the nanoparticle causing an encapsulation of the particle. At the opposite, they showed that the high-carbon solubility metal nanoparticles present a too weak adhesion to the $sp^2$ cap/nanotube thus leading to a full detachment of the catalyst from the nanotube. This full detachment actually also induced the SWCNT growth termination. Figure 4.7 presents a scheme of this result.

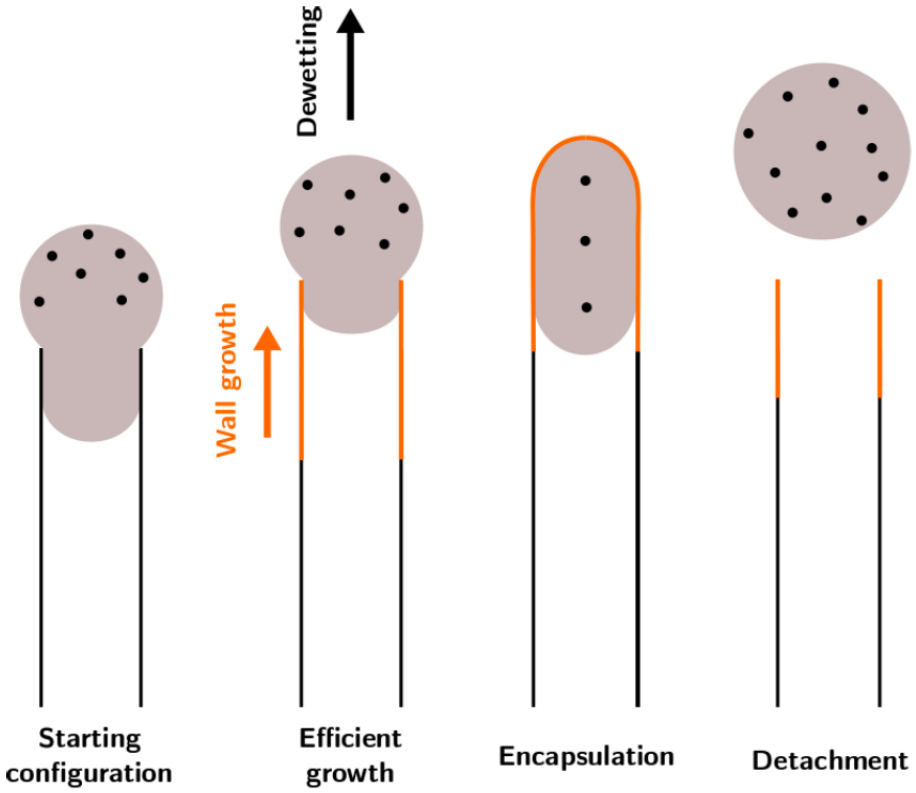


FIGURE 4.7: Sketch of SWNT growth from [203].

Based on this mechanism, the catalyst size selectivity observed in our synthesis may be explained as follows : at low temperature, the carbon solubility of bigger particules is low due to their bigger size and the low temperature in the furnace. This carbon solubility is too weak in regard to the nanoparticle size leading to a lack of subsurface atoms. This lack favors a stronger adhesion of $sp^2$ layer on the catalyst surface leading to a subsequent encapsulation of the nanoparticle instead of carbon cap dewetting and nanotube growth (see Zone 1 on Figure 4.8). As described in the previous section, for the same reason He and co-workers showed by both simulation and experimental study that in given synthesis parameters, icosahedral gold nanoparticles did not catalyze SWCNT while face centered cubic gold nanoparticles can [192]. On the contrary due to

their smaller size and higher carbon solubility, smaller catalyst nanoparticles may allow the dewetting of the $sp^2$ cap and thus the SWCNT growth (see Zone 1 on Figure 4.8). When the temperature increases, carbon solubility in bigger nanoparticles increases allowing the lift-off of the cap (see Zone 3 on Figure 4.8). In turn, as the temperature is increased, the carbon solubility in smaller nanoparticles also increases but time too much, causing a too fast detachment of the carbon cap, thus preventing the nanotube growth (see Zone 3 on Figure 4.8). For the intermediary temperatures, solubility limit of both smaller and bigger nanotube are in the appropriate range to allow both carbon cap dewetting and the nanotubes growth (see Zone 2 on Figure 4.8).

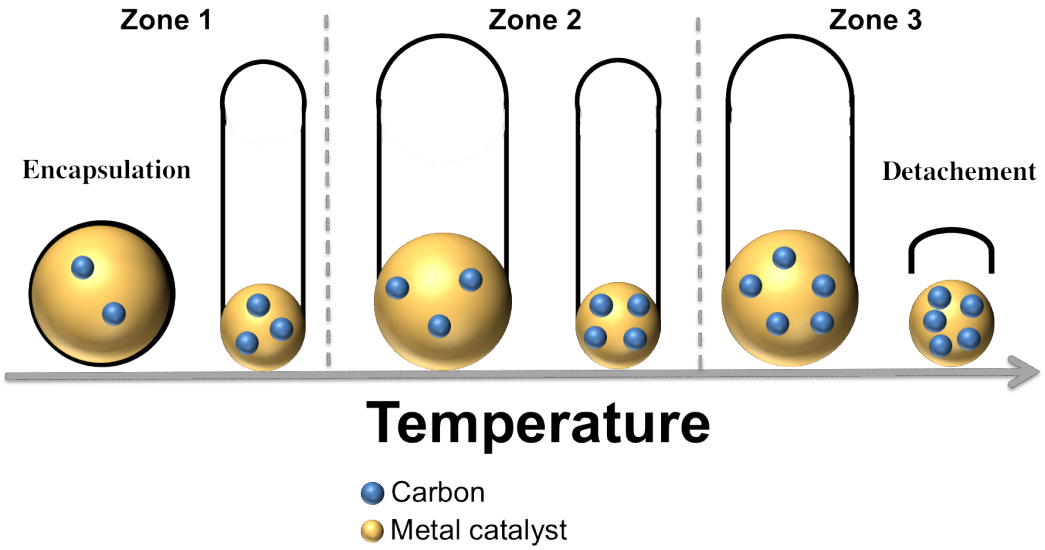


FIGURE 4.8: Schematic view of the proposed mechanism of selective activation of the nanoparticle.

TEM investigations after typical growth show that numerous nanoparticles are encapsulated. Figure 4.9 shows an exemple of nanoparticles after synthesis at 800°C and 1000°C. From this image, we observed that a lot of nanoparticles, especially the biggest one, are encapsulated as expected in our model. It is however difficult to say if this encapsulation occurs during the synthesis or during the cooling of the sample. Indeed, during the cooling, the carbon solubility in nanoparticles decreases inducing a release of excess carbon out of the nanoparticles leading to such structure.

Up to this point we did not perform an analysis of the nanotubes chirality on our samples, their diameters range observed through Raman spectroscopy testify that a large chirality distribution is to be obtained. Nevertheless, to some extent, we were able to show that the synthesis temperature can allow the carbon nanotubes growth from a selected size fraction of the nanoparticles population, for a given catalyst chemical composition. This paves a way for a better control of the SWCNT growth process as one can imagine that, with a more monodisperse catalyst size distribution, we may be reaching a smaller diameter dispersion by adjusting temperature, and then limiting the as-grown nanotubes chiralities.

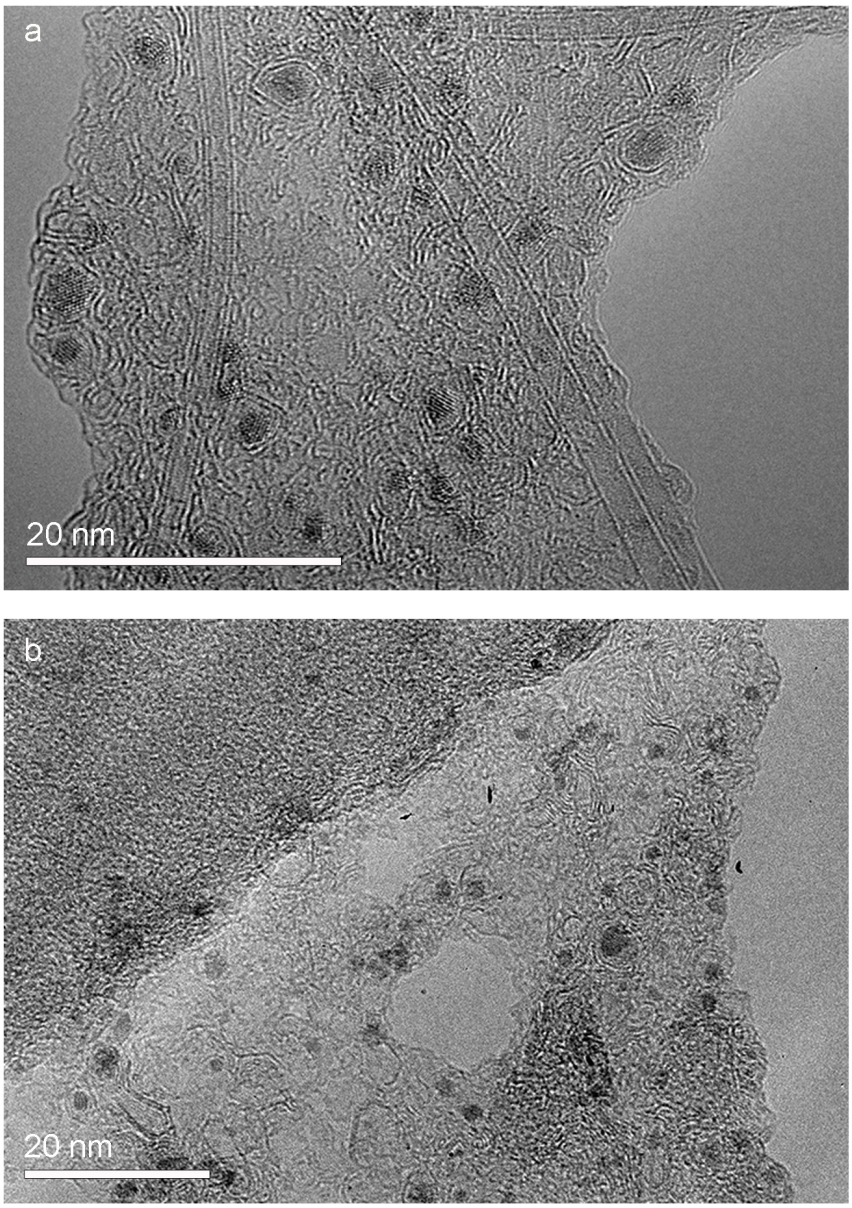


FIGURE 4.9: Typical TEM image of nanoparticle catalyst at **a** 800°C **b** 1000°C after growth experiments.

### 4.1.2 Impact on the SWCNT semi-conducting/metallic ratio

We have also investigated the metallic/semiconducting type nanotubes' ratio obtained from the growth synthesis experiments presented in the previous section. Kataura plot shown in Figure 4.1 was used to assign the semiconducting or metallic character of the nanotubes in each sample.

Figure 4.10 presents the obtained percentage of semiconducting SWCNTs for the different catalysts and for the four different synthesis temperatures. A general trend can also be distinguished for all the catalysts type. According to Raman spectroscopy, we can observe an increase in the semiconducting SWCNTs fraction with the temperature (except for the FeRu catalyst and synthesis at 700°C, that we will discuss in section 4.2.2).

Zhang and co-workers reported that methane plasma can selectively etch carbon nanotubes [204]. They highlighted that in the diameter range of 1.4-2 nm, metallic SWCNTs were selectively etched over semiconducting ones, but in the smaller diameter range (d<1.4 nm) a non-discriminatory etch of the SWCNTs was observed. Li and co-workers reported similar trend with hydrogen as etching gas [123]. These observations may explain that for the synthesis at high temperature, where the majority of the SWCNTs are greater than 1.4 nm, more s-SWCNTs are obtained than at lower temperature due to a selective etching of the m-SWCNT by hydrogen gas used in our process.

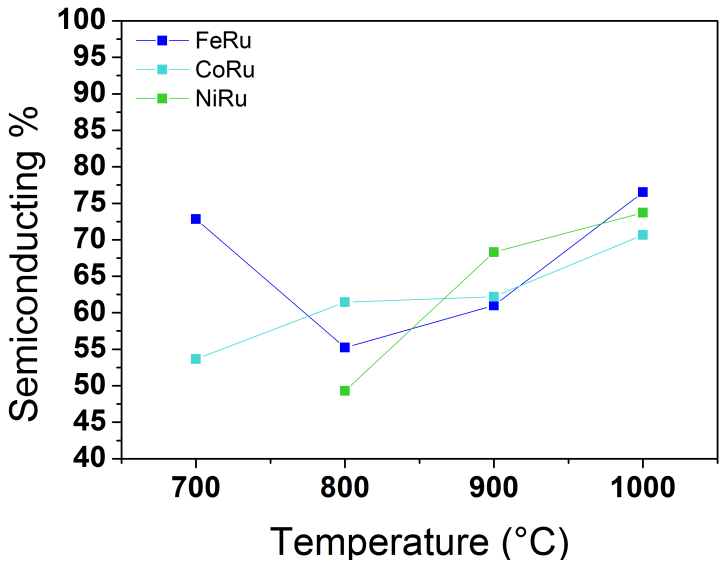


FIGURE 4.10: Percentage of semiconducting SWCNT obtained through Raman spectroscopy analysis for the three catalysts at various temperatures.

In case of non-selective synthesis only one third over all SWCNTs are metallic, then the obtained SC/M ratio should be 2/3 of semiconducting nanotubes and 1/3 of metallic nanotubes. In our syntheses however, at low temperature the metallic percentage reach almost 50% of the counted nanotubes. We don't have

clear answers to explain the increase of m-SWCNT fraction at lower temperature. One may argue that such observed change may be induced only by the use of Raman spectroscopy while a full characterization of the sample with various cross-observation techniques may erase this difference. A preferred experimental technique for nanotubes chirality assignment would be high resolution TEM, but unfortunately have not been performed yet. In order to ensure, to a certain extent, a cross-verification of the Raman spectroscopy measurements, we have used the as-synthesized various SWCNT samples to fabricate field effect transistors and statistically analyze their characteristics. The result of the electrical measurements of the transistors is consistent with an increase of m-SWCNT population at low temperature. This results will be discussed in the following chapter.

### 4.1.3 Different SWCNT "growth yield"

SEM images can be used to give some indication of the cover rate over the sample but a quantitative measurement is difficult, especially in our case where random and sometimes entangled SWCNT are obtained. Examples of SEM image in the case of SWCNTs grown from FeRu are shown in figure 4.11. We observed that a better coverage rate is obtained for growth at 900 and 800°C as compared with sample grown at 1000°C for instance.

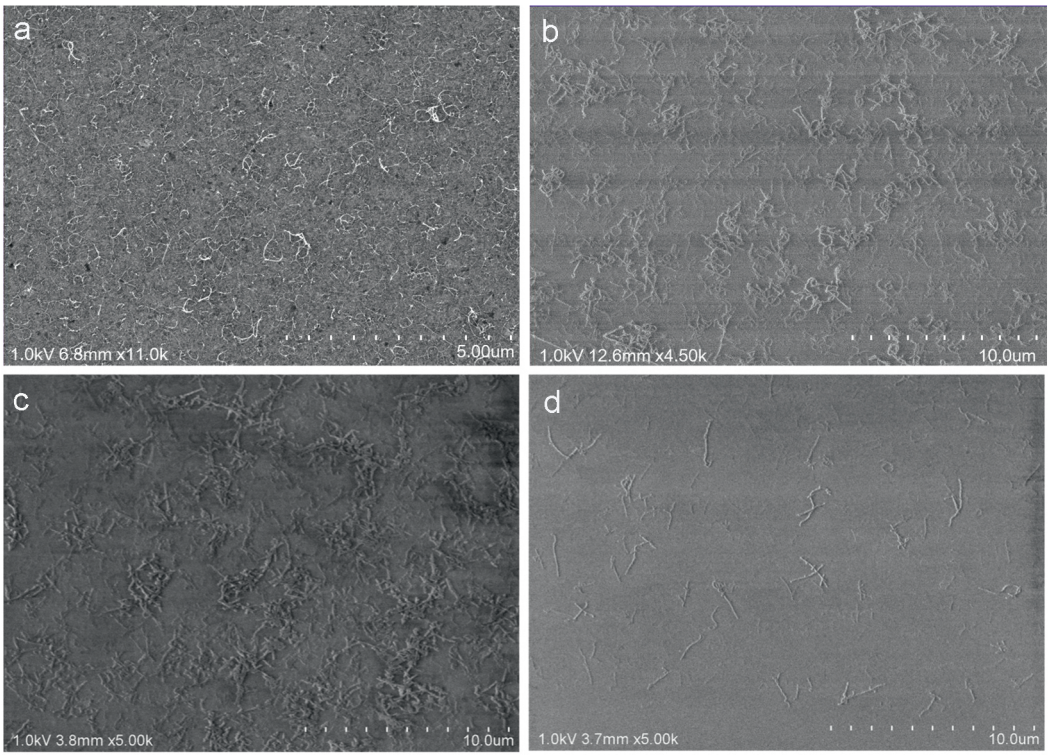


FIGURE 4.11: Typical SEM image of SWCNT grown from FeRu catalyst at **a** 700°C **b** 800°C **c** 900 and **d** 1000°C

In order to retrieve a more quantitative measurement, we calculated the number of SWCNTs detected by Raman spectroscopy in RBMs region, with four lasers (473 nm, 532 nm, 633 nm, 785 nm) under one spot (0.6x0.6 $\mu m^2$ approximately).

$$yield = \frac{Number\ of\ SWCNTs\ detected\ in\ Raman}{Number\ of\ Raman\ spectrum} \tag{4.2}$$

This does not provide an absolute measure of the yield, as the Raman analysis does not detect all present SWCNTs, but it is nonetheless an interesting comparison tool.

Figure 4.12, represents the obtained "Raman yield" for all the three catalysts. For each catalyst, we can already observe an optimal temperature in regards to the synthesis yield. For instance the case of FeRu this optimal temperature is around 900°C. We showed in the previous sections that the nanoparticles populations available for growth at either low and high temperatures are almost the same. We observe now that at the highest growth temperature less SWCNTs seem to be able to grow. If we assume that the temperature increase leads to the deactivation of the smaller nanoparticles which, by number, are the majority population of the sample, we can expect that at a higher temperature less SWCNTs will grow. Following the same idea, at a lower temperature, for a constant growth time, bigger nanoparticles were found to be inactivated. Then, for FeRu and NiRu catalysts, 900°C seems to be the intermediate temperature where bigger nanoparticles starts to be activated whilst the poisoning of small nanoparticles is limited. Thus overall, this temperature leads to a better growth yield. This trend seems to be confirmed by the SWCNT diameters distribution shown in the Figure 4.3a. For the synthesis at 900°C in comparison to 1000°C for FeRu and NiRu catalysts, the number of small diameter SWCNTs (supposed to be grown from the smaller nanoparticles) increases while the number of large diameter SWCNTs is bigger than for synthesis performed at 700°C or 800°C.

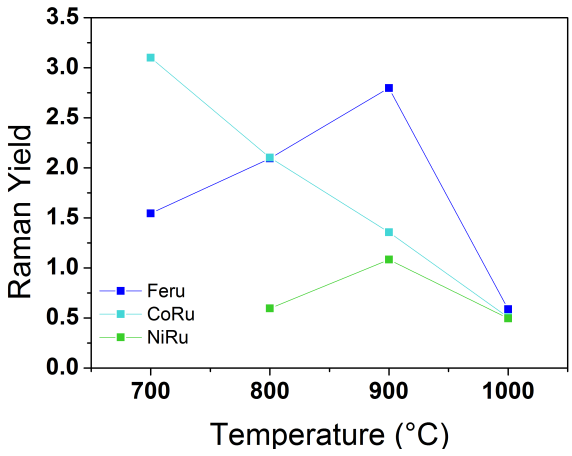


FIGURE 4.12: Estimation of the yield obtained through Raman spectroscopy : number of nanotubes detected under a laser spot for the three catalysts at various temperatures.

## 4.2 Influence of the metal catalyst chemical composition on the SWCNT structure

Bimetallic nanoparticles of FeRu, CoRu and NiRu of equivalent sizes and morphologies have been obtained through a standardized method. Under these conditions, for fixed synthesis parameters we can compare the influence of the chemical composition of the catalyst on the SWCNT growth.

### 4.2.1 Evolution of the SWCNT diameter

We propose now to compare the nanotube diameter distribution obtained at a fixed synthesis temperature for each catalyst type. Figure 4.13a presents the diameter distribution obtained at 800°C for the three catalysts. In terms of diameters distribution, few differences are observed between FeRu and CoRu catalysts, but it appears that the NiRu catalyst leads to the growth of smaller nanotubes. As shown in Figure 4.13a, at 800°C almost 75% of the obtained nanotube from NiRu catalysts are smaller than 1.3 nm in comparison with only 44 and 46% for the nanotubes grown from FeRu and CoRu catalysts respectively. For obtaining similar diameters distribution for SWCNT growth from FeRu and CoRu catalysts, the synthesis temperature must be at 700°C, meaning 100°C lower (see Figure 4.13b). Unfortunately at this temperature, we observed very few SWCNTs grown from the NiRu catalyst preventing any relevant statistic.

The typical diameter distribution of the nanoparticles for the respective three catalysts after pretreatment at 800°C has been presented in chapter 3, in Figure 3.11. As we can note that quite similar size distributions have been obtained for the three catalysts, the observed difference in the SWCNT diameter distribution cannot be correlated with a difference in catalyst size.

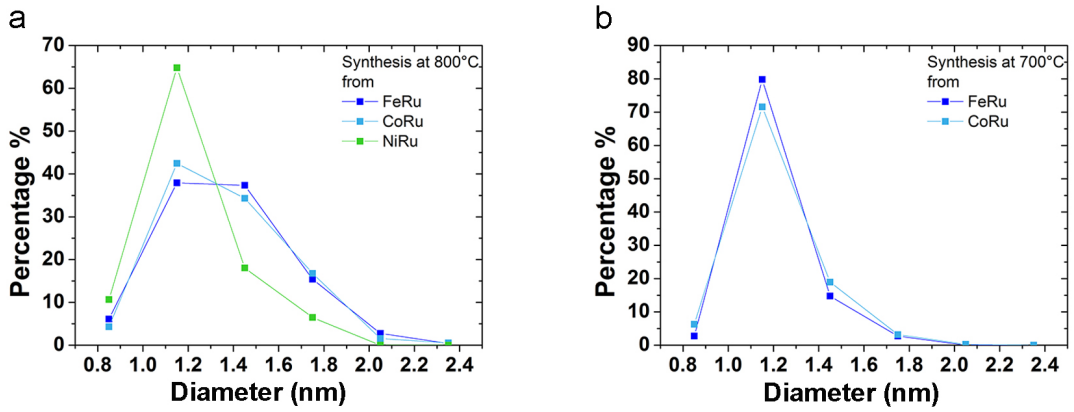


FIGURE 4.13: Repartition of the SWCNT diameter obtained from FeRu catalyst (blue line), CoRu catalyst (light blue line) and NiRu catalyst (green line) for a temperature synthesis of **a** 800°C **b** 700°C.

Based on the previous discussion, a lower carbon solubility in NiRu catalyst type as compared to the two other alloys can explain such result. At the lowest tested temperature (700°C), carbon solubility in the nanoparticles at the available diameter range is too low to induce a growth of SWCNT. With temperature increasing, the carbon solubility increases and we gradually activate the nanoparticles through their size : first the smaller then the bigger ones, until the deactivation of the smaller size ones occurs at high temperature (1000°C).

To verify this, a ternary phase diagram of the three alloys with carbon for nanometric scale would be necessary. To the best of our knowledge this diagram has not been reported in the literature. Nevertheless, one can note first, that pure nickel is known for having a lower carbon solubility than cobalt and especially than iron [53]. Moreover, nickel-ruthenium is expected to lead to a system very different than cobalt ruthenium and iron ruthenium ones. The STEM-EDX analysis, presented in the previous chapter has shown a co-localisation of the iron, cobalt or nickel and the ruthenium tending to prove that alloyed structures have been successfully synthesized. In the case of cobalt/ruthenium and iron/ruthenium the formation of alloy is not surprising. Indeed, the bulk binary diagram of ruthenium with cobalt or iron forecast an alloy structure for any concentration in the case of cobalt and respectively above around 25% of iron in the temperature range 500°C-1000°C [182]. On the contrary the nickel-ruthenium phase diagram shows that alloy structure of nickel/ruthenium in the temperature range (500°C-1000°C) is possible only if the percentage of nickel do not exceed 10% [205]. In our case, a 1:1 stoichiometry is expected due to the used of PBA as a pre-catalyst, then a phase segregation should be observed.

### 4.2.2 Impact on the SWCNT semi-conducting/metallic ratio

The semiconducting/metallic ratio observed for all the three catalyst types is very similar for a given temperature (see Figure 4.10); we do not observe significant differences between the catalysts. For a given temperature, less than 10% of difference is observed between the different catalysts. This difference is not significant insofar as around 10% of difference is observed for two syntheses run performed under in the same conditions (see paragraph 4.3). The only larger difference is evidenced in the case of the growth at 700°C for FeRu catalyst, where 71% of semiconducting nanotubes were obtained. This difference is mainly due to an increase of 30% of the semiconducting SWCNT having a diameter between 1 and 1.1 nm and resonant in the infrared laser excitation (see figure B.2 in appendix B ). The other experiments of synthesis at 700°C done during this thesis have not been characterized with an infrared excitation laser, not available at the beginning of this thesis, then further experiments and characterizations are needed to confirm this observation.

### 4.2.3 Different SWCNT "growth yield"

As described previously, the exact yield of the synthesis is unknown, we can only calculate for each catalyst, the number of SWCNT detected in Raman spectroscopy with four lasers wavelengths under one spot. Figure 4.12 shows the obtained "raman yield" which are consistent with SEM observations (see Figure 3.14 in chapter 3). For each catalyst, we can see that there is an optimal temperature synthesis with respect of the yield. It's at 700°C for the growth from CoRu catalyst and 900°C for the NiRu and FeRu catalyst. We also note that a lower yield is always observed in the case of growth from NiRu catalyst.

## 4.3 Short discussion about the reproducibility of the synthesis

The reproducibility of the synthesis is also a fundamental issue in the SWCNT growth. The final goal is to obtain selective synthesis with a good yield in order to exploit them at an industrial scale. From this point of view, the reproducibility of the proposed synthesis process is a paramount parameter.

The HF-CVD furnace used during this study is an home made system specifically designed to achieve improved control of all the CVD parameters (see section 2.1.1 in chapter 2).

We found that the general trend of our synthesis is reproducible from one run synthesis to another. Similar diameter distributions and metallic/semiconducting ratio (error of about 10%) are obtained for the different synthesis. For instance, Figure 4.14 shows the diameter distribution and the metallic/semiconducting ratio obtained for three different growths on FeRu catalyst for two temperatures where we note that the general shape of the diameter distribution and the semi-conducting ratio are preserved from one synthesis experiment to the other. This reproducibility is an important point in order to validate the previous discussions, indicating that some other parameters, such as metal catalyst and temperature, affects drastically the results of the synthesis.

Nevertheless, looking carefully the figure 4.14 we can note some slight variations from a synthesis experiment to another, despite the great effort conducted to perform all the synthesis under the "same conditions". These variations also indicate that SWCNT synthesis processes are extremely difficult to extensively control and are extremely sensitive to any variation in the processing/synthesis conditions.

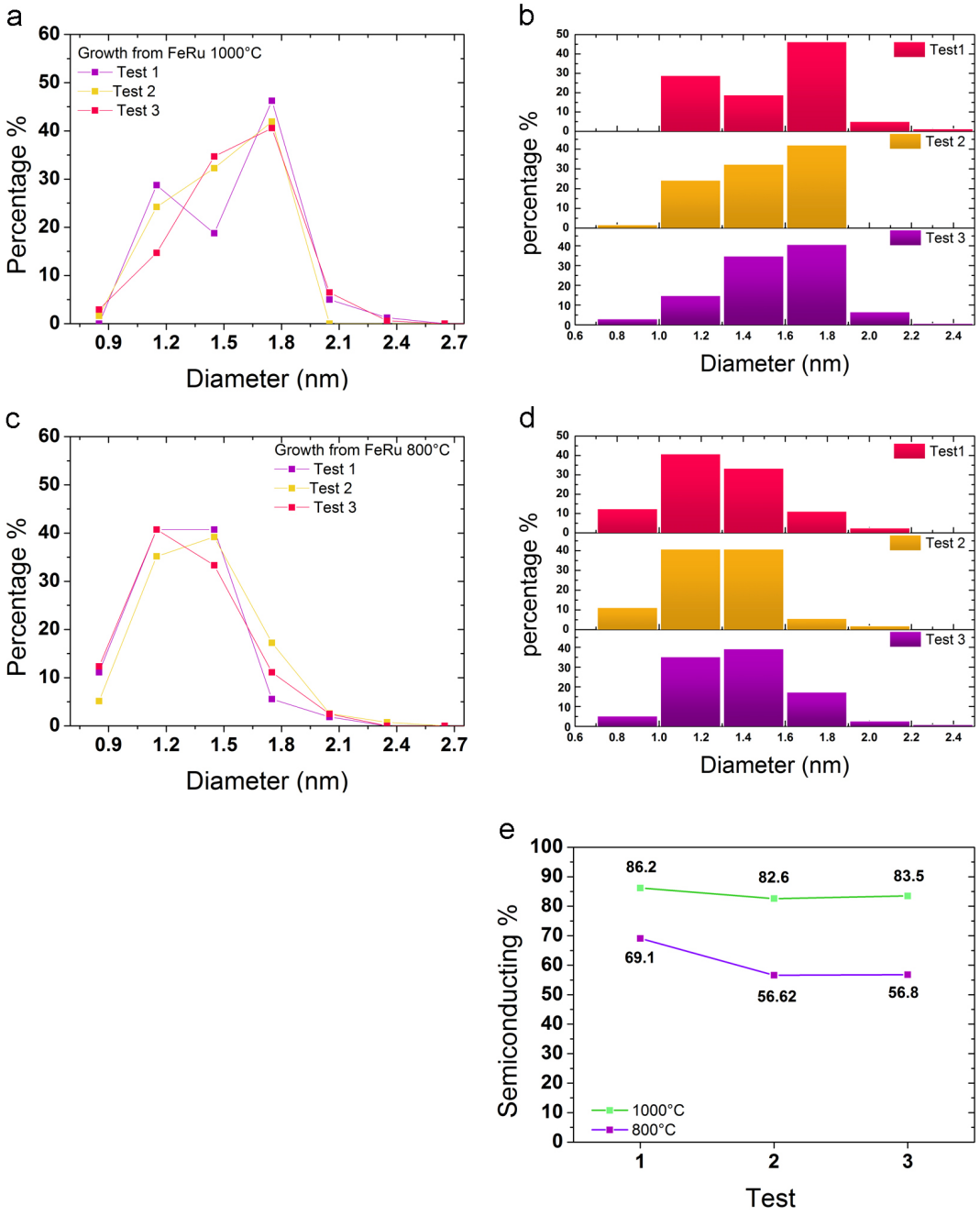


FIGURE 4.14: Repartition of the SWCNT diameter obtained from FeRu catalyst for three different synthesis at **a-b** 1000°C **c-d** 800°C **e** the percentage of semiconducting nanotubes obtained for three different synthesis at 800 and 1000°C The diameter distribution was here obtained through statistical Raman spectroscopy analysis with three wavelengths (532 nm, 633 nm, 473 nm). The fourth wavelength at 783 nm has been used for characterizing the last synthesis only, so its contribution has been removed in order to ensure coherent comparison of the various synthesis.

## 4.4 Conclusion

In this study we first showed that the increase of SWCNT diameter, often reported with the growth temperature increase can be linked to other mechanism than the usually considered coalescence phenomenon. We demonstrated that, under fixed conditions, different diameter populations of SWCNTs are obtained even if the same diameter population of catalyst nanoparticles are available for the synthesis. We also confirmed that for nanoparticles of the same size and morphology, the chemical composition of the catalysts induced differences in the as obtained SWCNT nanotubes. We assume that this difference is triggered by difference of carbon solubility in nanoparticles depending on their size and chemical composition. Indeed, in our case, the use of a bimetallic catalyst seems to allow a drastic modification of the carbon solubility reducing the windows of parameters leading to a SWCNT growth for a given catalyst. Finally, one must also take into account that the SWCNT growth process is extremely sensitive to any variation in the growth conditions increasing the difficulty to have access to relevant observations that help in understanding the underlying growth mechanisms.

## 4.5 Experimental details

### 4.5.1 Methodology

All the experiment have been made on a same batch of sample prepared as follow :

First, a same wafer of $Si/SiO_2$ are splited into several pieces ( $\approx$ 1cm x 1 cm, step 1 on Figure 4.15). Then all the wafers are silanized following the process described in section 3.6.3 (step 2 on Figure 4.15). For each batch, a new solution of PBA of FeRu, CoRu and NiRu is synthesized and the various PBA are grafted on the substrat following the process described in section 3.6.3. Then the SWCNT growth process (including pre-treatment and growth) is performed in the HF-CVD (see section 3.6.4 for experimental details) at 700°C 800°C, 900°C and 1000°C. For each synthesis temperature, the synthesis of SWCNTs are performed on three samples (one of each catalyst) at the same times. Under this condition, we can analyze the effect of the synthesis temperature on the SWCNT structure for a given catalyst (step A on Figure 4.15) or the effect of the catalyst chemical composition for a fixed growth temperature (step B on Figure 4.15)

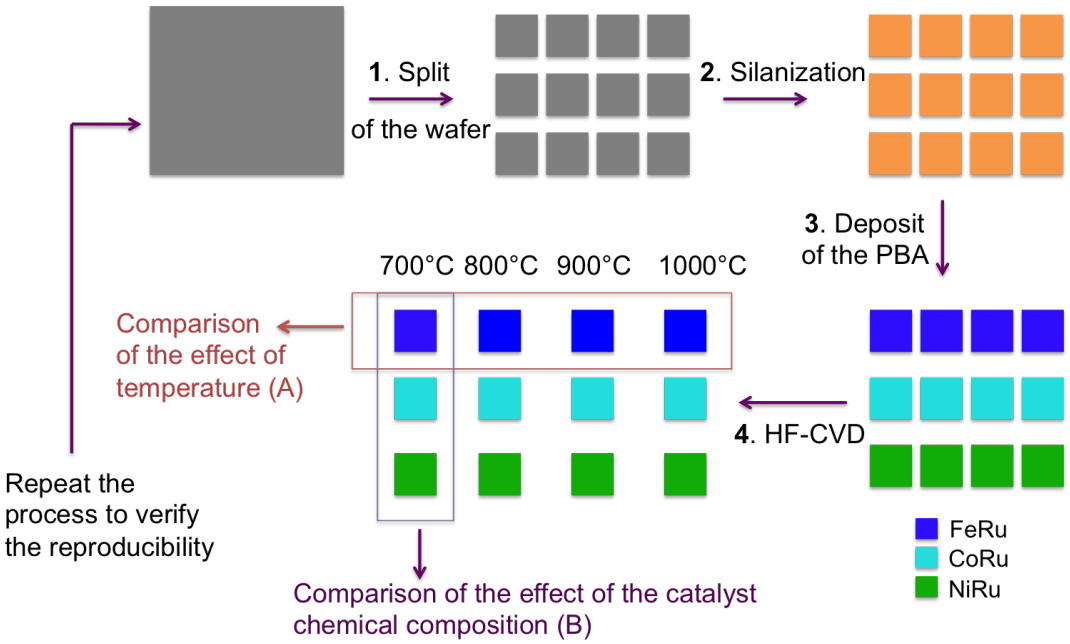


FIGURE 4.15: Schematic view of the synthesis process in order to realized a parametric study.

# Chapter 5

# Application : Integration in FET-device

The previous chapter described a parametric study of the SWCNT growth. Growth of SWCNTs has been performed at different temperatures and from various bi-metallic catalyst. The process is quite reproducible and clear trend is observed concerning the obtained SWCNT population. Between the different grown samples, we observe differences of yield, diameter range and semiconductor/metalic ratio. In this part we will describe the integration of the as-grown SWCNT into FET-device and characterize their electrical properties. The electrical properties of the FET device is highly linked to the electronic properties of nanotubes in its channel. These properties are imposed by the SWCNT respective structure. Then, different populations of SWCNTs are expected to lead to different device performances. We purposed here to compare the characteristics of a set of SWCNT FET devices where SWCNTs are obtained from the various growth conditions described in the previous chapter. This study will clarify to what extent the previous characterizations were relevant and how our SWCNT growth conditions impact the performance of the device. For this purpose, the fabrication and the design of the SWCNT-FET has been chosen for its simplicity and it is far from being well optimized in terms of best achievable FET performance.

## 5.1 Design and performance of the SWCNT-FET devices

### 5.1.1 Design of the SWCNT-FET devices

As the SWCNT growth was performed on a $Si/SiO_2$ wafer, the as-obtained SWCNTs could be directly integrated in bottom gate SWCNT-FET device structure without any transfer step. The doped silicon wafer is isolated from the SWCNTs by a 200 nm thermal silicon oxide layer and is used as a back gate for all the devices. After the growth of SWCNTs, palladium contacts are used for source and drain. The contact are fabricated using standard UV lithography, e-beam evaporation and lift-off processes (see experimental part in section

5.5 for further details). Palladium was chosen for the quality of the contact obtained with SWCNTs and for its high work function. Looking at the SEM image, considering that typically the nanotubes lengths varies from 0.5 to few micrometers, in order to favor direct contact between the source and drain, the channel length of the interdigited electrodes was chosen at 2 $\mu$m. The geometry of the device is shown in the Figure 5.1. SEM images of the channel performed on functional FET devices show that few random isolated nanotubes connect directly the source and drain, as shown on Figure 5.1.

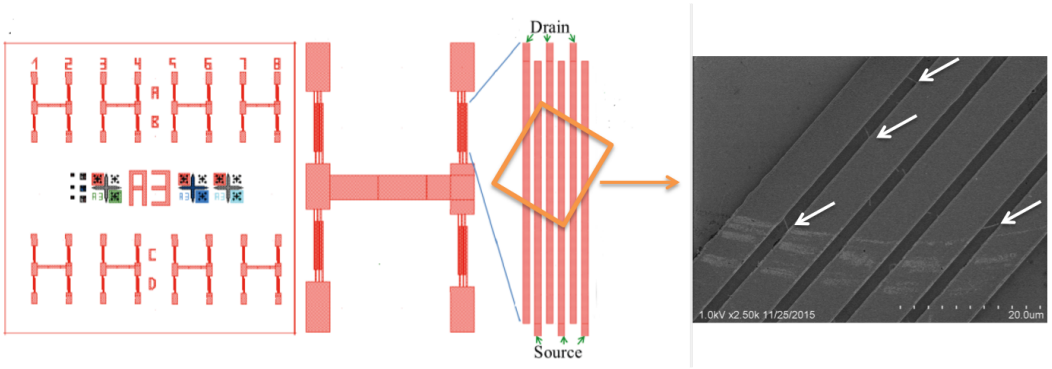


FIGURE 5.1: **Left** Scheme of the geometry of the used transistor **Right** SEM image of a typical SWCNT-FET device

Figure 5.2 presents a typical FET transfer curve for a typical good device. For all the measurements a fixed bias voltage of 1V is applied between source and drain (Vds). A voltage sweep is applied from -40V to +40V to the gate (Vg) electrode and we measure the current flowing between source and drain (Ids). As expected, the device exhibits a p-type characteristic. When Vg is set to a negative value (i.e. -40V) holes flow through the p-doped nanotube (On state), for positive value of Vg up to the threshold voltage where the hole current is blocked (Off state). For all devices a very large hysteresis loop is obtained due to the charge trapping at nanotubes/dielectric interface (see section 1.4.3 chapter 1). The current in the On and Off state will be called $I_{on}$ and $I_{off}$ respectively.

For some devices, a high off current is obtained. This result indicates that a metallic path between the source and drain exists. Such conductive path can be due to lithography defects, presence of metallic SWCNTs or of amorphous carbon. Characterization performed in the previous chapter showed that all our synthesized samples contains some metallic SWCNTs (m-SWCNTs). It is however possible to selectively remove then (or rather say disconnect them from source-drain electrodes) by using the electrical breakdown method developed by IBM [206]. The basic idea of the method is to protect the semiconducting SWCNTs (s-SWCNTs) and then apply a high voltage between source and drain. This high voltage induces formation of defect and overheating of unprotected metallic nanotubes, leading to irreversible damage. During the process the s-SWCNT are protected by depleting them from their carriers, through the application of an adapted gate voltage to set the FET device in its Off state (positive Vg, in case of p-type). The progressive destruction of the m-SWCNTs can be monitored electrically, each removal leads to a significant drop in the

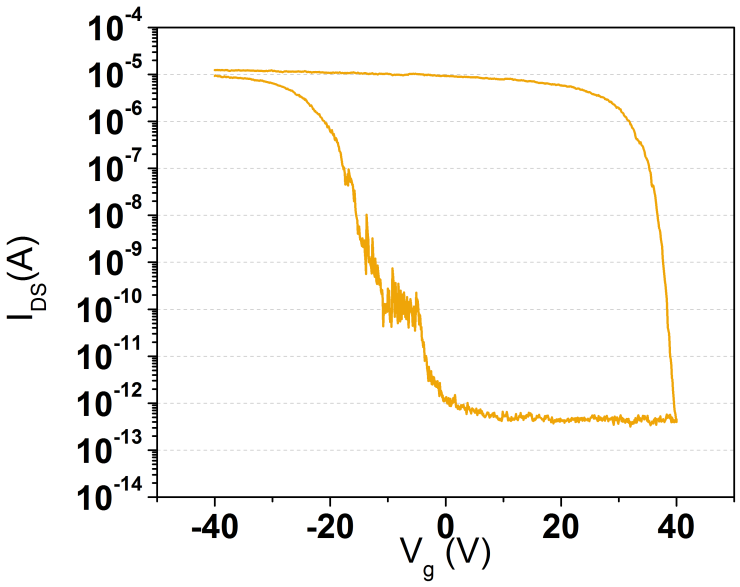


FIGURE 5.2: Intensity flowing between source and drain obtained for a gate voltage from -40V to +40V; Vds = 1V.

current flowing between source and drain. Here, this method will serve two purposes, first to improve the device performance, second some qualitative indication of the quantity of m-SWCNTs is given as a function of the efficiency of the method. Figure 5.3a presents a device initially exhibiting a high Off current (yellow curve) and the resulted characteristic obtained after the electrical breakdown (red curve). The breakdown process has been monitored by measuring the source drain current as shown in Figure 5.3b.

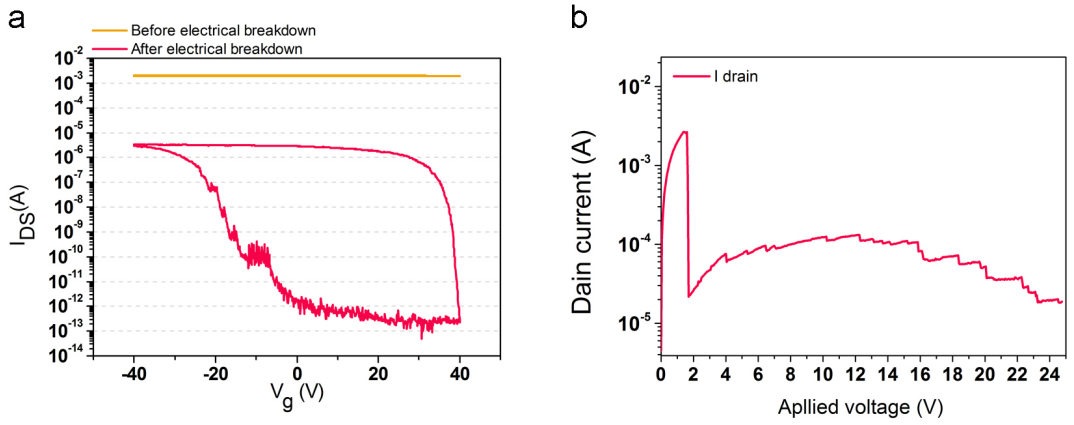


FIGURE 5.3: **a** Typical Id/Vg obtained from -40V to 40V before (yellow curve) after (red curve) electrical breakdown; Vds = 1V **b** Drain current as a function of applied voltage for the electrical breakdown.

### 5.1.2 Performance

Figure 5.4 presents the different Ion/Ioff ratios as a function of the corresponding On current ($I_{on}$) that we obtained for the various transistors realized in this thesis. The yellow circles correspond to the result obtained before any electrical breakdown while the red circles correspond to the result after the electrical breakdown. Black circles indicate the transistors where the electrical breakdown process has been found ineffective. We fabricated transistors with SWCNT synthesized from three different catalyst (FeRu, CoRu and NiRu, as described in the chapter 4) at two different growth synthesis temperatures (1000°C and 800°C). The characterization of the SWCNTs has been presented in the last chapter, justification of the choice of SWCNT will be detailed in the next section.

Table and graphic in Figure 5.5 resume the Ion/Ioff ratios of the various transistor after electrical breakdown. Different average performance are observed, this point will be discussed in the following section. In the best conditions, a majority of transistors present an Ion/Ioff ratio above $10^5$ with few transistors with Ion/Ioff ratio above $10^7$. These performances are on the same order of magnitude of the best devices obtained by use of random percolating networks of SWCNTs as channel reported in the literature [207–209]. For these devices, the On current is in the range $10^{-5} - 10^{-6}$ which is lower than values usually obtained for good transistors based on random percolating network of nanotubes [207]. In our case, as shown on the SEM image on Figure 5.1, transistor's channels are rather made of few nanotubes randomly deposited over the surface with very few percolation. We are in an intermediary configuration between individual carbon nanotube and percolating carbon nanotube arrays. Optimization should be done to improve the performance of the device but that was not the main purpose of this study. The number of connected nanotubes could be further improved by optimizing the devices fabrication process. For instance, as the SWCNT synthesis is not performed in a clean room environment, then few cleaning steps by sonication are needed before the deposition of the Pd-electrode. During these steps, some nanotubes may risk being removed from the substrate. Also, the next step integration approach may be directed towards the use of mono-crystalline specifically oriented and/or patterned substrates that have been reported to lead to synthesis of in-plane aligned SWCNTs. In this case, a better control of the contact electrodes is obtained and parasite percolations are avoided [210].

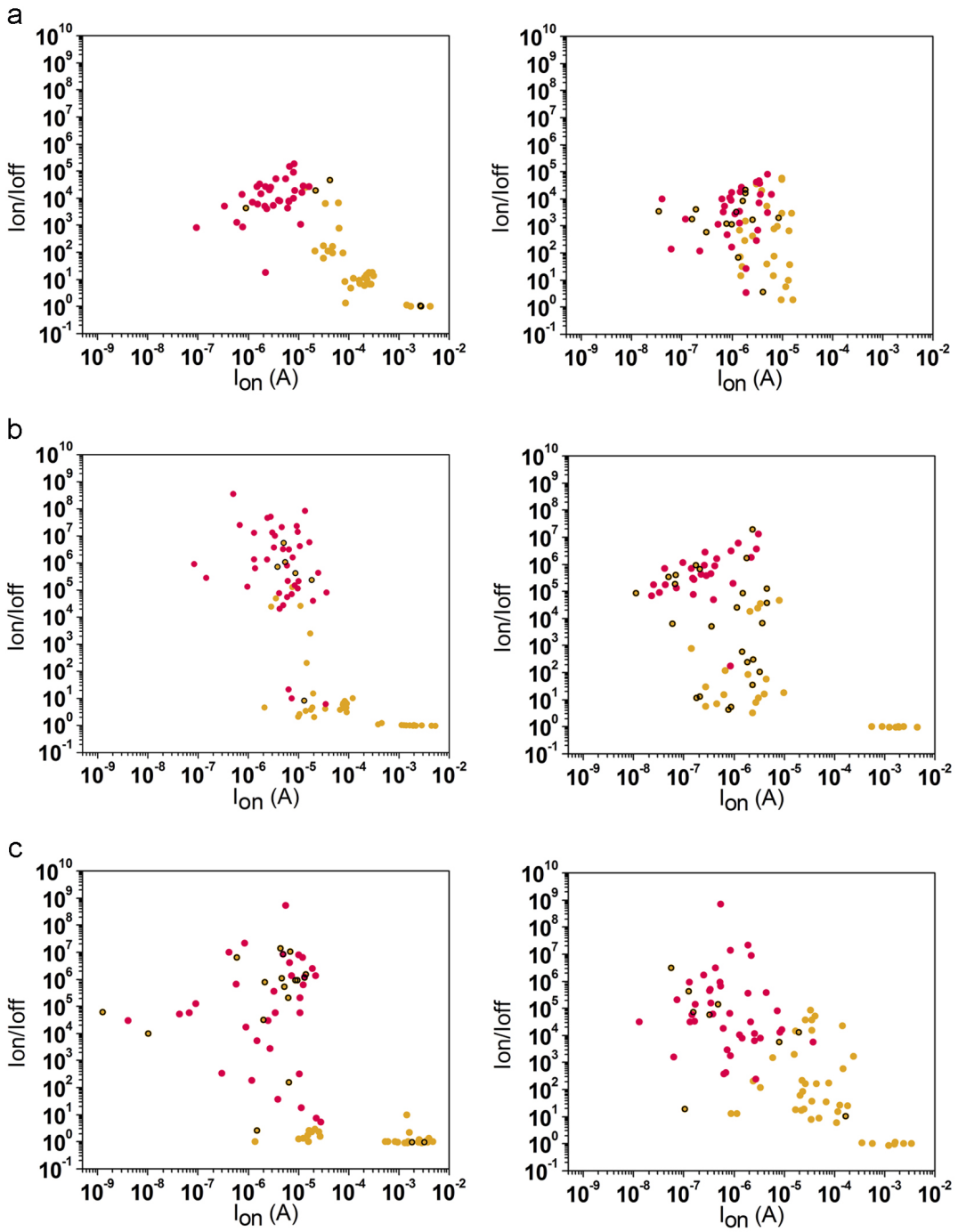


FIGURE 5.4: **a** Ion/Ioff ratio of FET-device fabricated from FeRu catalyst at **left** 800°C **right** 1000°C **b** Ion/Ioff ratio of FET-device fabricated from CoRu catalyst at **left** 800°C **right** 1000°C **c** Ion/Ioff ratio of FET-device fabricated from NiRu catalyst at **left** 800°C **right** 1000°C. The yellow circles correspond to the result obtained before any electrical breakdown while the red circles correspond to the result after the electrical breakdown. Black circles indicate the transistors where the electrical breakdown process has been found ineffective.

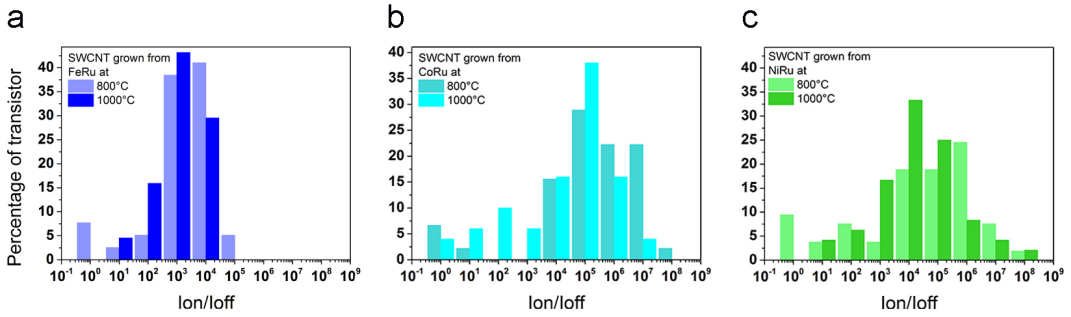


| catalyst | growth temperature | Ion/Ioff $> 10^4$ | Ion/Ioff $> 10^5$ |
|---|---|---|---|
| FeRu | 800°C | 46.15% | 5.12% |
| | 1000°C | 29.54% | 0% |
| CoRu | 800°C | 91.0% | 75.5% |
| | 1000°C | 74% | 58% |
| NiRu | 800°C | 73% | 52.8% |
| | 1000°C | 72.9% | 39.5% |

FIGURE 5.5: **Top** Repartition of the Ion/Ioff ratio of FET-device fabricated from **a** FeRu catalyst **b** CoRu catalyst **c** NiRu catalyst after electrical breakdown (statistics on almost 45 transistors for each catalyst composition and SWCNT growth temperature) **Bottom** Recapitulative table

## 5.2 Influence of the SWCNT growth condition on the FET-devices characteristics

The main aim of this study is directed to highlight the influence of the as-grown SWCNT structural properties on the device performance. Indeed, the metallic/semiconducting ratio, the diameter, the length, the quality or the real density of the SWCNTs integrated in the final devices modify their performances. In the previous chapter, we observed some differences on the properties of the SWCNTs that we synthesized, which motivated the statistical analysis of the transistors realized with SWCNTs obtained through six different growth conditions. We used our three catalysts (FeRu, CoRu and NiRu) at two different growth temperatures to synthesize the SWCNTs. We showed that the greater the difference in the synthesis temperature, the more the properties of the nanotubes obtained are different. We chose then the two extreme temperatures where nanotubes are observed for the three catalysts types. As very few SWCNTs are observed for the growth from NiRu catalyst at 700°C, as a result we chose to use nanotubes grown at 800°C and 1000°C. This study will also be accounted for confirming the previous observations made on our SWCNTs.

### 5.2.1 Effect of the temperature

Figure 5.4 presents the Ion/Ioff ratio versus the On current. Before any breakdown process, for all devices we observe a similar trend as a function of the

SWCNT growth temperature, independent of the SWCNT's catalyst used. First, when SWCNTs grown at the lowest temperature are integrated in a transistor, a majority of the devices are found to be ineffective (i.e. Ion/Ioff ratio lower to 10) as shown on Figure 5.6. For SWCNTs grown at high temperature fewer than 10% of the fabricated transistors are also ineffective. We observed previously that a high Off current, close or identical to the On current can be related to either some lithographic defects, amorphous carbon or m-SWCNT leading to a metallic pathway in the transistor's channel. All transistors were fabricated with an identical process, the only change concerns the starting SWCNTs used. Statistically there is no reason for having an increase of more than 30% of the lithographic defects only in the transistors made with nanotubes grown at 800°C. Hypothesis of more amorphous carbon present over the wafers' surface for synthesis at low temperature can also be ruled out. First, deposition of amorphous carbon in CVD process is usually favored at high temperature by pyrolysis mechanism. In Raman spectroscopy, presence of amorphous carbon can be detected through the so-called D-band around 1350 $cm^{-1}$, also present for other allotropic forms of carbon. Gao and co-worker, showed that for isolated SWCNTs, the full width half maximum (FWHM) is between 20 $cm^{-1}$ up to 40 $cm^{-1}$ for an excitation at 632 nm [211]. Picher and co-worker [90], for an excitation at 532 nm, reported a FWHM D-band between 50-60 $cm^{-1}$ for CVD SWCNTs comparable with the FWHM D-band of HiPco nanotubes in the same condition (FWMH 45 $cm^{-1}$). On the contrary they found a D-band FWHM in the range of 130-190 $cm^{-1}$ for amorphous carbon. In our synthesis, the full-width half-maximum of the D-band is found between 60-80 $cm^{-1}$ and no significative difference in the FWHM is observed for the different synthesis temperature for any of the studied catalysts (see table in Figure 5.6). Moreover, at 800°C, the FWHM of the D-band for a given catalyst is always lower. This result indicates that the deposition of amorphous carbon is probably a little more important at high temperature. Representative spectrum in the Raman D-G band area of the various samples are available in appendix C.

The electrical breakdown of all the measured transistors has been realized. One can observe that the electrical breakdown process has a limited effect on transistors made with nanotubes grown at 1000°C. As shown on Figure 5.4 very weak improvement of the Ion/Ioff ratio is obtained and the ON-current stays relatively constant. Figure 5.6b presents the percentage of transistors presenting an improvement of Ion/Ioff ratio superior to 3 decades after the electrical breakdown. Such improvement concerns between 6 and 38% of transistors made from 1000°C grown nanotubes and between 28 and 78% of transistors with 800°C grown SWCNT. For a given catalyst, a difference exceeding 20% in the number of transistors improving their Ion/Ioff ratio above $10^3$ is found according to the growth temperature. This is confirming the weak impact of the electrical breakdown process on transistors made with nanotubes grown at 1000°C, especially in comparison to ones made with nanotubes grown at 800°C. The electrical breakdown is very efficient to remove m-SWCNT which improves the Ion/Ioff ratio. Since few changes are observed after electrical breakdown, one can conclude that only a weak proportion of m-SWCNT connects source

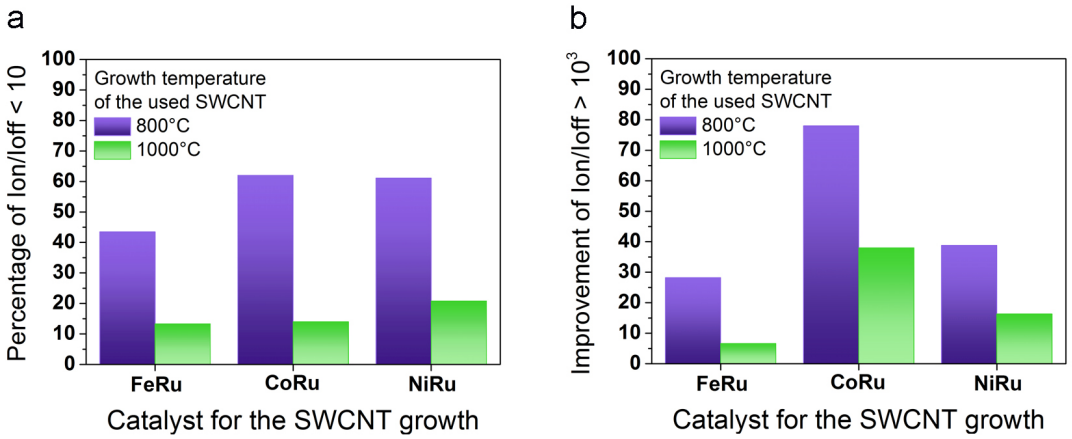


| catalyst | growth temperature | FWMH (excitation at 532nm) |
|---|---|---|
| FeRu | 800°C | 72.6 ± 2.4 |
| | 1000°C | 79.9 ± 2.2 |
| CoRu | 800°C | 59.8 ± 2.5 |
| | 1000°C | 63.9 ± 5.1 |
| NiRu | 800°C | 71.4 ± 0.98 |
| | 1000°C | 72.4 ± 2.66 |

FIGURE 5.6: **a** Percentage of transistors presenting an Ion/Ioff ratio inferior at 10 for integrated SWCNT grown from each catalyst at 800 and 1000°C (before electrical breakdown) **b** Percentage of transistors presenting an improvement of their Ion/Ioff ratio superior at $10^3$ after electrical breakdown for integrated SWCNT grown from each catalyst at 800 and 1000°C **Table** Table of the FWMH of the Raman D-band of samples grown from each catalyst at 800 or 1000°C.

and drain in this case. This hypothesis is also consistent with the Raman spectroscopy measurements where a weaker proportion of m-SWCNTs were being found for the growth at 1000°C (see Figure 4.10 in chapter 4). On the contrary, the electrical breakdown appears to be more effective for transistors made from SWCNT grown at 800°C. After the breakdown, for each of the transistors with 800°C grown-nanotubes, the Ion/Ioff ratio increased and the ON-current decreased (see Figure 5.4 and Figure 5.6b). Such results are expected when the contribution of m-SWCNTs is suppressed. This result highlights a higher contribution of m-SWCNT in this type of transistors. The results are consistent with the Raman characterization performed in the previous chapter, a higher yield and a more important metallic SWCNT ratio have been found for growth at 800°C as compared to that at 1000°C. The probability to connect a metallic nanotube between source and drain is then expected to be much higher.

One can note that after the electrical breakdown, the as obtained transistor made from 800°C grown-nanotubes exhibit on average better performance than those with 1000°C grown nanotubes (see Figure 5.4). This difference lead to a lower off-current obtained in case of 800°C grown-nanotubes transistors (see Figure C.4 in appendix C). We propose to analyze this result, in the light of the previous characterization of SWCNTs. We showed in the previous chapter that

SWCNTs obtained at lower temperature have a smaller diameter, then concerning the semiconducting part of these nanotubes a bigger gap is expected. Figure 5.7 presents the diameter distribution of the semiconducting tube detected through Raman spectroscopy. Whatever the used catalyst we confirm that at 800°C s-SWCNTs tend to have a smaller diameter than at 1000°C. At 800°C the biggest population of nanotubes has diameters between 1.0 and 1.3 so will possess an approximate gap between 1 and 0.77 eV. At 1000°C, the majority population of nanotubes has diameters corresponding to an approximate gap between 0.62 and 0.53 eV. Accounting for the Schottky barrier height, as a same type of contacting electrodes is being used, in case of bigger diameter (low gap) semiconducting nanotubes, the achievable off-current is expected to have higher value than in the case of smaller diameter (larger gap) semiconducting nanotubes. We assume that the difference in on-off ratio after breakdown for the two growth temperatures can be explained by this difference in diameter distribution. After the removal of the m-SWCNT, the transistor made with s-SWCNT grown at lower temperature allows a better commutation of the transistor due to their smaller diameter.

In conclusion, the electrical measurements confirm the result obtained in Raman spectroscopy, the nanotube growth at high temperature synthesis seems to produce more s-SWCNTs. As a result, the majority of the obtained transistor are functional as fabricated without any breakdown. Then, the electrical breakdown process generally leads to very weak improvement of the Ion/Ioff ratio. The Ion/Ioff ratio obtained with transistors based on this high growth temperature nanotubes is not so high and we attribute this characteristic to the global bigger diameter of the nanotubes integrated in the transistors' channel. On the contrary, when nanotubes grown at lower temperature are used, a majority of transistors are initially non-functional but become very efficient after a selective removal of the m-SWCNTs through electrical breakdown. We conclude that the nanotubes used for the transistors' channel in this case contains more metallic nanotubes in agreement with Raman spectroscopy. Nevertheless, after electrical breakdown, very high Ion/Ioff ratios can be obtained due to the relatively small diameter of the s-SWCNT produced under these growth condition.

### 5.2.2 Effect of the metal catalyst

The previous section described a general trend observed in the transistor as a function of the chosen SWCNT growth temperature. We also notice, looking at the different results (Figure 5.5 and 5.6), that the metal catalyst used for the SWCNT growth lead also to some differences in the performances of the transistors.

We can see that for the two analyzed temperatures, the electrical breakdown process tend to be less effective on transistors fabricated from FeRu-catalysed nanotubes and the Ion/Ioff ratios are on average, lower. For synthesis at 1000°C, previous Raman measurement, showed that SWCNTs grown from FeRu catalysts have a higher percentage of semiconducting ratio (around 10% more than

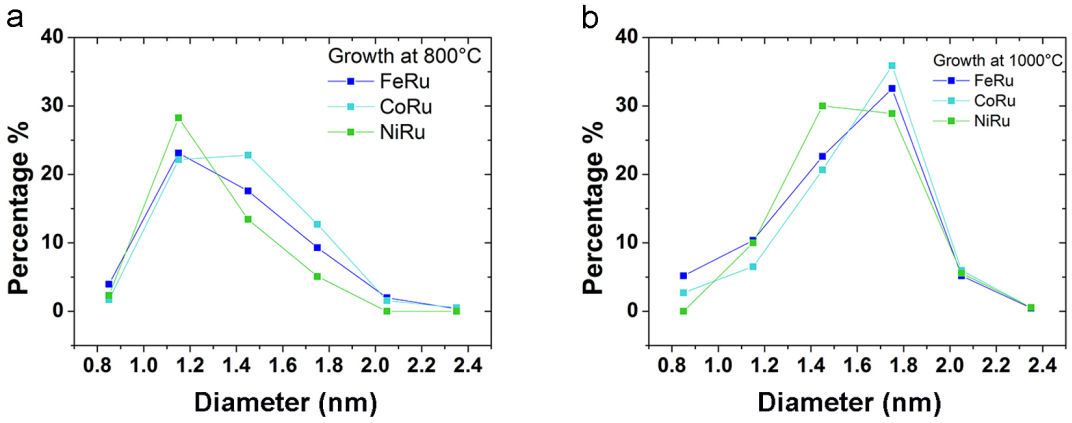


FIGURE 5.7: Diameter distribution obtained through Raman spectroscopy of SWCNT grown at **a** 800°C **b** 1000°C

the other). For this temperature, this higher proportion of s-SWCNT could be a reason for the observed weaker efficiently of the electrical breakdown process. In the case of nanotubes grown at 800°C, Raman spectroscopy analysis showed similar SC percentage concerning CoRu and FeRu catalyst such as a very similar diameter distribution and yield (see Figure 4.10, Figure 4.3 and Figure 4.12). Nevertheless, nanotubes grown from CoRu at 800°C leads on average to better performance of the transistors. These transistors are also on average, the best that we obtained in respect of the Ion/Ioff ratio. They are followed by transistors made from nanotubes grown from NiRu at 800°C where the best Ion/Ioff ratio has also been obtained ($>10^8$). We assume that this difference is probably related to the difference of the characteristics of the SWCNTs used, but our set of characterization tools is too limited to fully explain this result. The use of more wavelengths in Raman spectroscopy coupled with other characterizations such as photo-luminescence/absorption and TEM analysis should be performed, to eventually highlight more differences in the as-synthesized SWCNTs. For the results presented here and for each growth conditions, the SWCNTs used are from the same synthesis run. A statistics on different synthesis experiments under the same growth conditions and for each catalyst has also been planned but not performed yet due to a lack of time. Such statistics will ensure that the differences obtained are effectively induced by a catalyst related change during the SWCNT growth process and not to an artifact due to defects/variations in the transistor fabrication process, for instance.

In conclusion, we designed bottom gate transistors with different nanotubes obtained through different growth conditions. To a certain extent, the measured characteristic of the transistors agree with the observations performed through Raman spectroscopy concerning the SC/M metallic ratio, yield and diameter distribution. Despite the simplicity of the transistor design, good Ion/Ioff ratios have been obtained, up to more than eight decades for the best ones and around $10^5$ on average. We have also observed that the catalyst used for the SWCNT growth, impact the quality of the fabricated transistors. We assume that these observed differences can be related to the variation in the as-obtained SWCNT

properties but more characterizations of the SWCNTs are required to point out the exact nature of the difference and how it's impacting the properties of the transistor (diameter, length, electronic properties and chirality...).

## 5.3 Sensitivity to the gas detection

After the general characterization of the transistors, in the frame of the "André Citroen" industrial Chair at Ecole Polytechnique and in close collaboration with the Dr. Leandro Sacco, we decided to test SWCNT-FETs' ability for the gas detection applications. As presented in the first chapter, due to the high sensitivity of SWCNTs to their surrounding environment, SWCNT-FET devices have been exposed to various gases to analyze their sensing properties. Many exemples in the literature report modification of the conductance in SWCNT-FET devices induced by a modification of the surrounding gaseous atmosphere. Two general mechanisms have been reported to explain the variation on conductance in SWCNT-FET device, a doping of the SWCNT or a Schottky barrier modulation [139]. In the first case, the modification of the charge carrier concentration (increase or decrease) should lead to a lateral shift of the transfer curve at constant sub-threshold slope S. When a Shottky barrier modulation occurs, the sub-threshold slope S should change but no shift of the OFF bias interval should be observed. Schottky barrier modulation and SWCNT doping can also take place simultaneously [142]. In the following section we propose to present the response of our transistors during an exposition of various concentrations of $NO_2$. The $NO_2$ is known for being an electron acceptor gas and has been reported to induce a p-doping of the SWCNT [140, 212–215] and chemical modifications at the interface metal/SWCNTs [141].

For this study, we used transistors made with SWCNTs grown from CoRu catalyst at 800°C which present in average the best transfer characteristics. A home made enclosure was used for the measurement. First, the device was exposed to a constant flow of $N_2$, then an additional constant flow of $NO_2$ mixed and diluted to the initial $N_2$ flow is introduced in the enclosure. The pressure is kept constant to avoid accumulation of $NO_2$ in the enclosure. The electrical response of the device has been monitored as a function of time.

### 5.3.1 Characterization of the device response : a doping effect ?

Figure 5.8 presents the response of the device during exposition to various concentrations of gas. For all the concentrations tested an increase of the current between source and drain is observed. As a function of the time, we observed progressive increase of the current consistent with a progressive adsorption of the $NO_2$ molecules. For the lower concentration, this increase of the current seems to occur with a constant sub-threshold slope. Then, the change of the conductance seems consistent with a change of the SWCNT doping, in agreement

with theoretical calculation [213]. When the concentration of $NO_2$ increases, we observe almost instantly a huge increase of the current, whatever the applied gate voltage value and the device cannot be turned off correctly.

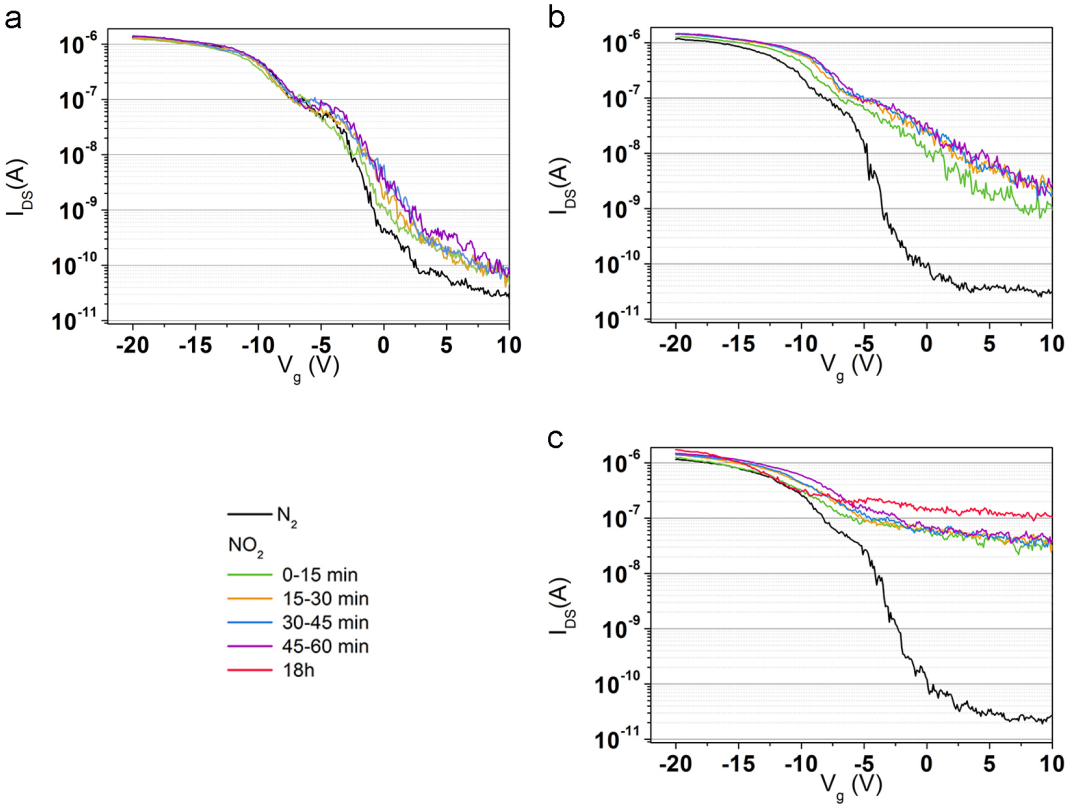


FIGURE 5.8: Id(Vg) characteristic of a same transistor from -20V to 10V after flowing $NO_2$ at **a** 0.8 ppm **b** 2.8 ppm **c** 9.5 ppm; Vds = 1V.

These results are consistent with a heavy p-doping of the SWCNT [142]. This effect, due to its large intensity predominates and prevents the observation of a possible modification of the Shotcky barrier. The effect is also reversible, in few hours under pure $N_2$ atmosphere the initial characteristic of the device is recovered (see Figure 5.9).

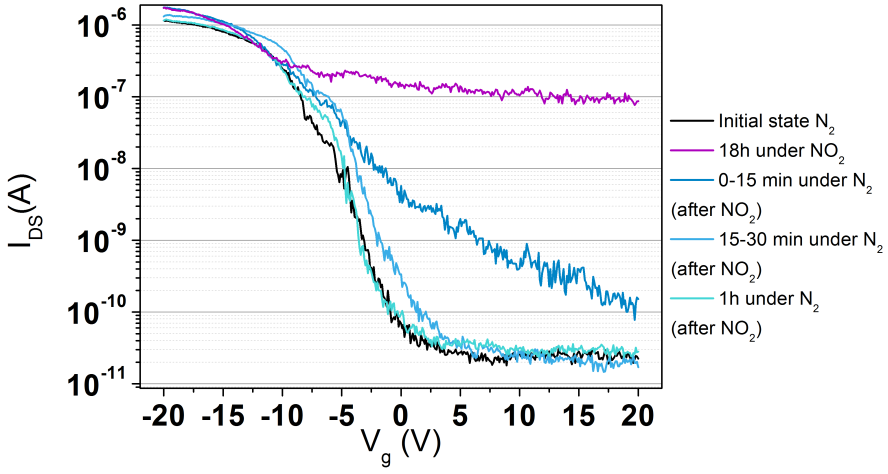


FIGURE 5.9: Id(Vg) characteristic after $NO_2$ flow was stopped and replace by $N_2$ flow; Vds = 1V.

### 5.3.2 Sensitivity

For a same device, the sensitivity (defined by the equation 5.1) as a function of the concentration of the $NO_2$ in the flowing gas has been calculated after 15 min and 60 min of exposure.

$$S = \frac{I_{OFF}(NO_2) - I_{OFF}(N_2)}{I_{OFF}(N_2)} \tag{5.1}$$

As shown on Figure 5.10 concentrations from 0.8 ppm to 14 ppm have been tested. As expected, the sensitivity for a given time exposure increased with the concentration of the $NO_2$. Looking at the shape of the curve it seems that a saturation regime has been reached, but measurements at higher concentration should be done to ensure the validity of this result. In our conditions, small concentrations of $NO_2$ have been detected at room temperature. However measurements at various device's working temperature have to be performed in order to complete the characterization of the device performance for gas sensing.

To conclude, our devices present a strong answer to $NO_2$ gaz exposure due to a doping of the SWCNTs by the adsorbed $NO_2$ molecules. The sensibility of the device should also be tested in ambient air atmosphere in order to check the selectivity of the device. One of the biggest challenge in the use of SWCNT-device as gaz sensor is to obtain a selective response to specific gases. One of the solutions proposed to solve this problem is to functionalized the SWCNT with molecules which exhibit gas-specific responses.

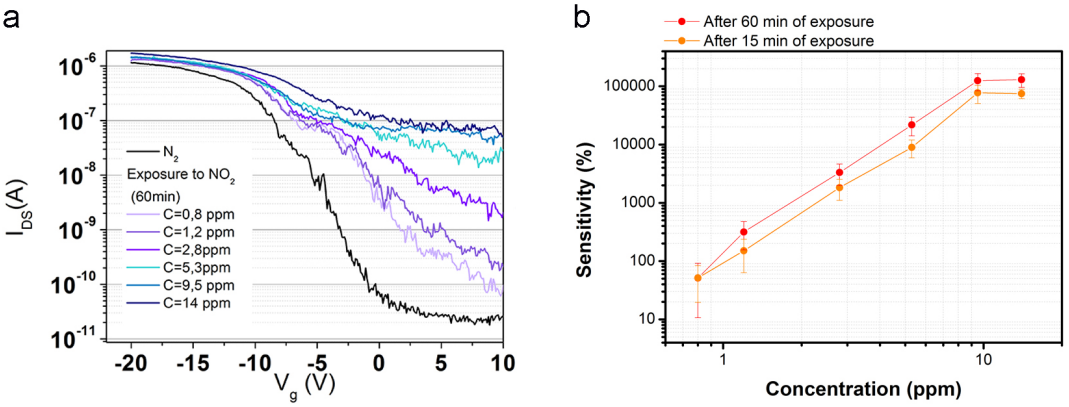


FIGURE 5.10: **a** Id(Vg) characteristic after 60 minutes of $NO_2$ flow at various concentration **b** Sensitivity after $NO_2$ exposure versus the concentratio; Vds= 1V.

## 5.4 Conclusion

We have successfully integrated the SWCNTs obtained from different growth conditions and various catalyst types in FET-devices. We confirmed that the performance of the devices can be easily improved by changing the characteristics of the SWCNTs used in the channel. After electrical breakdown process, in optimized SWCNT growth conditions our devices present a very high Ion/Ioff ratio. The performance of these devices can be further improved by optimizing both the geometry and the transistors' fabrication process. Finally, a very short initial study of the response of such devices to gas exposure has been performed. We observed a clear response for a short exposition (few minutes up to an hour) to $NO_2$ gas, even when very small concentrations (less than 1 ppm) are used. To complete the study, the devices should also be tested in air atmosphere and at various working temperatures.

## 5.5 Experimental detail

### 5.5.1 Deposition of the electrode

UV lithography is used to deposit the palladium electrode. First, the $Si/SiO_2$ substrate with SWCNTs was cleaned by a three minutes sonication process in acetone and respectively isopropanol. Then photosensible resin ($SU_8$) was spin coated (30 seconds at 4000 rpm) and the wafer was annealled for 5 min at 110°C (see step a on Figure 5.11). A patterned quartz mask was used to allow selective UV illumination. After alignement of the mask on the wafer, the sample was illuminated for 7 seconds at 10 mW by the UV-light (see step b-c on Figure 5.11). The sample was then immersed for 25 seconds in a solution of MF 319 (a chemical developer), where the UV-exposed resin was removed (see step d on Figure 5.11). Then the sample is transferred to an evaporator system where

40 nm of palladium is deposited over the sample (see step e on Figure 5.11). Finally, the sample is placed in a boiling acetone solution for few minutes, the remaining photoresin and the metal deposit on it, was removed (see step f on Figure 5.11). Wafer was then rinsed in a boiling isopropanol solution.

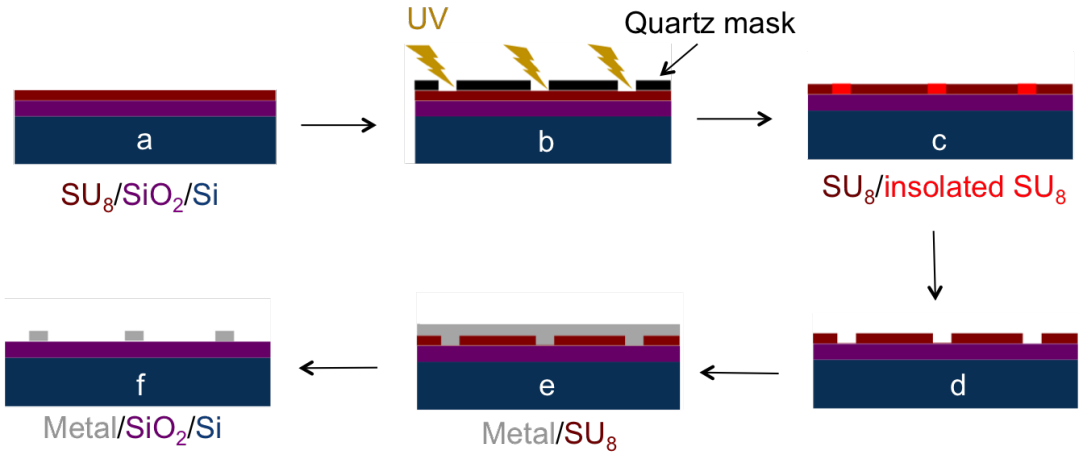


FIGURE 5.11: Schematic view of the lithography process for the deposition of the electrode.

# Chapter 6

# Functionalization of the SWCNT-FET devices

As discussed in chapter 1 (section 1.5), the functionalization of SWCNTs by inorganic complexes or organic molecules is highly desired for applications in nanohybrid electronic devices and sensors. One of the possibilities is to unite the unique transport properties of carbon nanotubes with the optical properties of functionalizing molecules in order to tune the nanotube properties.

The present chapter focuses on the non-covalent functionalization of the nanotubes integrated in the FET devices described previously, by light sensitive molecules. Non-covalent functionalization process has been chosen in order to fully preserve the transport properties of SWCNTs when molecule is inactive. The light-sensitive molecule is a $[Ru^{II} - Pyr]^{2+}$ complex composed of a $[Ru^{II}(bpy)_3]^{2+}$ (bpy = bipyridine) unit connected to a pyrene (Pyr) molecule, and is hereby named 1 (see Figure 6.1). This dyad molecule was designed to take advantage of the photophysical properties of the ruthenium chromophore and the ability of the pyrene motif to form $\pi - \pi$ interactions with the nanotube [154, 216–218].

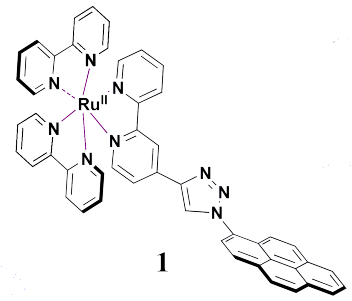


FIGURE 6.1: Schematic view of (Bipyridine)2-(bipyridine-triazol-pyrene) ruthenium hexafluorophosphate named 1

The molecule has been synthesized by Aurelie Baron by using the alkyne-azido click chemistry. The triazole ring does not alter the photophysical and the electrochemical properties of the $[Ru^{II}(bpy)_3]^{2+}$ chromophore and confers a rigid disposition of the two chromophores. These features are essential for the design

of covalent assemblies holding a photoactive unit. The synthetic procedures for the complex 1 $[Ru^{II} - Pyr]^{2+}$ are described in appendix D .

## 6.1 Interaction between SWCNT and the ruthenium complex : Study in liquid phase

### 6.1.1 Process

The first step of this study has been to verify the effective ability of 1 to stack on SWCNT sidewall. UV-visible spectroscopy and fluorescence measurements are the techniques of choice to characterize such interaction. Indeed, modification of the surrounding environment of a species can lead to shift of the peak positions in UV-visible range and to fluctuations of the fluorescence efficiency. Modifications of absorption and/or emission spectra provide clues of the occurring interactions. For the SWCNT's functionalization we followed the method developed by Roquelet et al. [219] based on micelle swelling. This method allows the non-covalent functionalization of an assembly of individualized nanotubes in liquid solutions, then under this condition, optical measurement can be performed.

Briefly, the molecules of interest dissolved in dichloromethane (DCM) are added to a solution of isolated SWCNTs dispersed in sodium cholate micelle. The biphasic system is sonicated with an ultrasound tip enabling the DCM to diffuse into the micelle, bringing molecules in contact with the nanotube. The micelle plays the role of a nano-reactor easing the stack of the molecule on the nanotube. Finally, DCM evaporates and micelles individualize the new hybrid system : molecule/nanotube (see Figure 6.2).

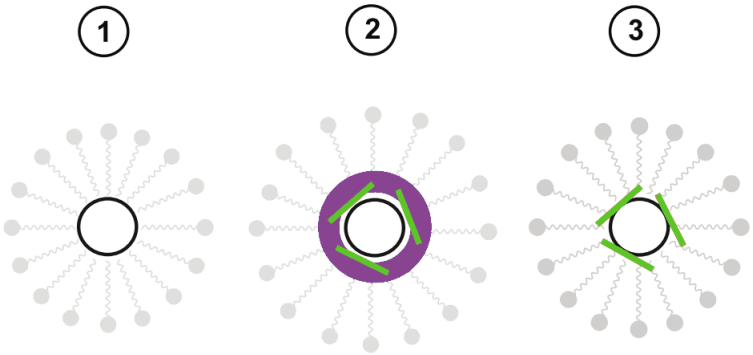


FIGURE 6.2: **1** SWCNT inside the micelle **2** DCM swells the micelle core, bringing molecules **3** DCM evaporates molecules stay inside the micelle adapted from [152].

Experimental details of the dispersion in micelle and micelle swelling performed in this study are described in the experimental part (6.5). Micellar suspension of 1, SWCNT, SWCNT+1, pyrene, SWCNT+pyrene, and SWCNT+$[Ru^{II}(bpy)_3]^{2+}$ have been obtained.

### 6.1.2 UV-visible analysis

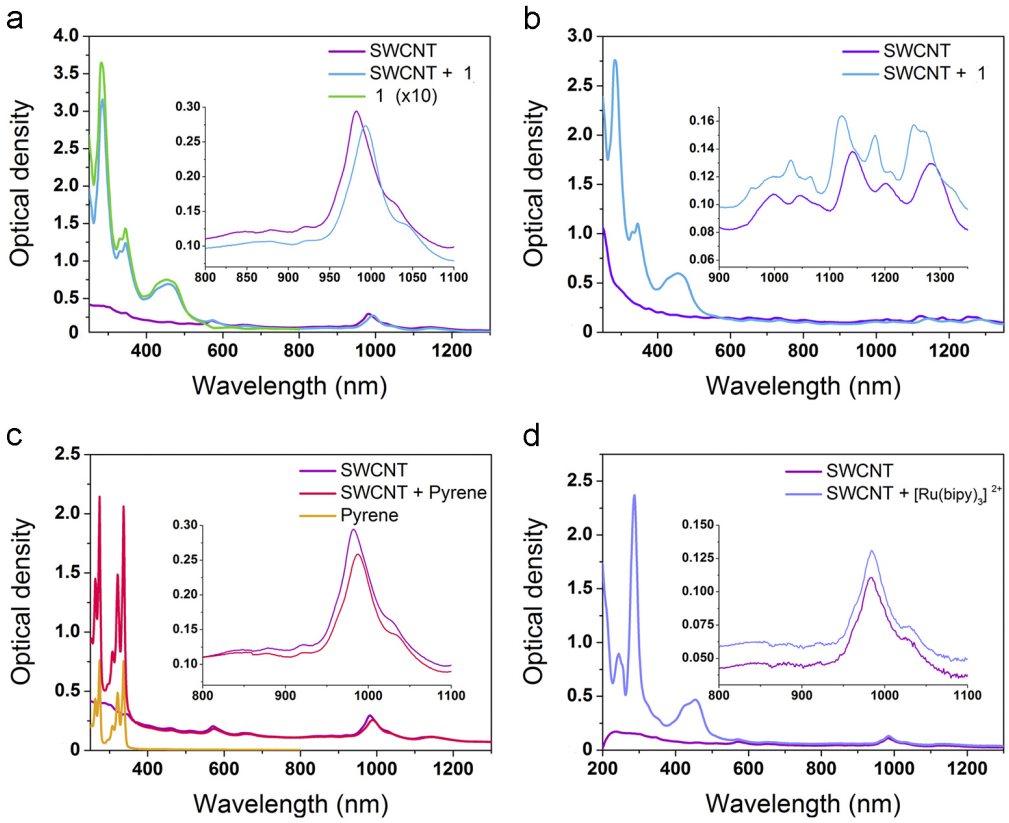


FIGURE 6.3: UV-VIS-NIR absorbance in sodium cholate micelle dispersed in a buffer solution at pH = 8 of : **a** CoMoCat SWCNT (purple), 1 (green) and SWCNT + 1 (blue) **b** HiPco SWCNT (purple), SWCNT + 1 (blue) **c** CoMocat SWCNT (purple), pyrene (yellow) and SWCNT + pyrene (red), **d** CoMocat SWCNT (purple), SWCNT + $[Ru^{II}(bpy)_3]^{2+}$ (no pyrene unit) (mauve).

Figure 6.3a displays the absorption spectra of commercial CoMoCat nanotubes, of complex 1 and of the mixture (1+SWCNT) after micelle swelling process. The spectrum of the bare nanotubes (purple) shows two main absorption bands at 982 nm and 571 nm, attributed to the (6,5) nanotube's $S_{11}$ and $S_{22}$ transitions respectively [219]. In the UV-Vis spectrum of 1 (green) the absorption maximum at 455 nm corresponds to the metal ligand charge transfer (MLCT) band of the $[Ru^{II}(bpy)_3]^{2+}$ chromophore while the absorption at 242, 283 and 345 nm are attributed to intra-ligand transitions. The absorption spectrum of the SWCNTs mixed with 1 contains all the characteristic bands of the two components, but a red shift of 10 nm of the $S_{11}$ nanotube transition band, in comparison with the free SWCNT suspension, is observed. Such a bathochromic shift indicates the modification of the dielectric environment of the SWCNTs [220, 221]. This modification is attributed to the presence of the complex 1 close to the nanotube sidewall and confirmed the interaction between 1 and the SWCNTs. A similar experiment has been performed with commercial HiPco carbon nanotubes (Figure 6.3b). An analogous red shift (between 1 and 20 nm) of $S_{11}$

carbon nanotube absorption bands is obtained, indicating that different chiralities of nanotubes can interact with 1. Moreover, functionalization of the previous suspension of CoMoCat with pyrene molecules, known for easily $\pi$-stacking on SWCNT, presents the same bathochromic shift (Figure 6.3c). On the contrary, no shift is observed when the nanotubes are mixed only with the $[Ru^{II}(bpy)_3]^{2+}$ (no pyrene unit) (Figure 6.3d), suggesting that the interaction can occur via the pyrene unit only.

### 6.1.3 Fluorescence measurement

#### Excitation of the pyrene unit

In the literature, interaction between SWCNT and pyrene is often characterized by a quench of pyrene fluorescence [216, 222, 223]. Fluorescence of pyrene has been investigated by using an excitation wavelength at 325 nm. Fluorescence spectrum of 1 excited at 325 nm presents characteristic peak of the pyrene (350-400 nm) and of the $Ru(bpy)_3$ unit (650 nm) (Figure 6.4a, green curve). After the grafting process (Figure 6.4a, blue curve) for the same concentration of 1, a quench of pyrene fluorescence band at 392 nm of 75% is observed. That constitute a new evidence of the interaction of 1 and the SWCNT. One can note that, an equilibrium between free and grafted molecule always occurs in solution, then, even if the fluorescence quench of grafted molecule is total, fluorescence of free molecule can still be observed.

As a control, similar experiment has been performed with pyrene molecule only. For an equivalent concentration of pyrene, after the micelle swelling process, we also observed a quenching of pyrene fluorescence, see Figure 6.4b. In this case, the quenching is about of 52%. This lower quench can be explain by a less efficient functionnalization process in case of pyrene which can present for instance, a lower kinetics of functionnalisation.

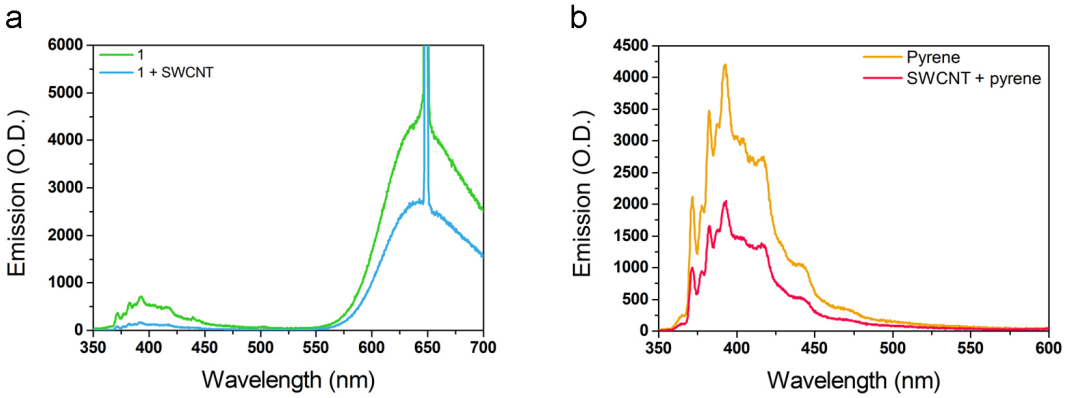


FIGURE 6.4: Emission spectrum for excitation at 325 nm of **a** 1 (green) and SWCNT + 1 dispersion (blue) for a same concentration **b** pyrene (yellow) and SWCNT + pyrene dispersion (red) for a same concentration.

### Excitation of the nanotube

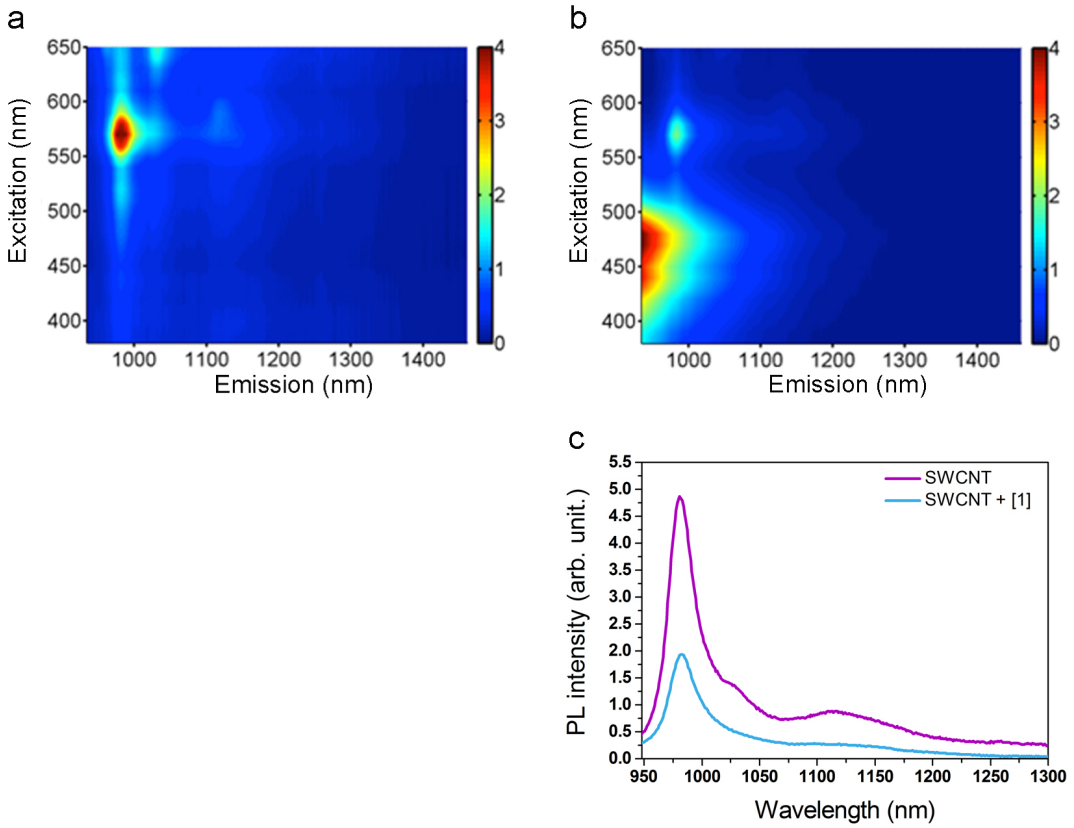


FIGURE 6.5: PLE map in sodium cholate micelle dispersed in a buffer solution at pH = 8 of **a** SWCNT (CoMoCat) (corresponding absorbance spectrum are shown in figure 6.3a-purple line) **b** SWCNT + 1 after micelle swelling process (corresponding absorbance spectrum are shown in Figure 6.3a-blue line) The signal at 900 for an excitation around 450 nm correspond to the band tail of the $[Ru^{II}(bpy)_3]$ fluorescence. **c** PLE cut at 570 nm of the PLE map **a** (purple line) and of the PLE map **b** (blue line).

The PLE spectra of CoMoCat nanotubes were recorded within an excitation domain ranging from 380 to 650 nm. Emission band at 983 nm for an excitation at 570 nm is assigned to the luminescence from the (6,5) $S_{11}$ level resonantly excited on $S_{22}$ level. Unexpectedly, no significant shift of this singlet-singlet transition was detected in presence of 1 that would correspond to the shift of the $S_{11}$ absorption band observed in the UV-Vis measurement. However we observed a significant decrease of PLE intensity. A quench (ca. 60%) of the luminescence of the SWCNT was observed in presence of 1, to respect of an equivalent concentration of SWCNT. We reasoned that this observed luminescence could be attributed to the unfunctionalized SWCNT while the luminescence of the functionalized SWCNT is totally quenched (see Figure 6.5). A luminescence quenching results in a change in the relaxation pathway, induced by charge or energy transfer or static quenching (aggregation...). The mechanism of the quenching has not been fully investigated but is clearly trigger by

the addition of 1 in the SWCNT neighborhood. If SWCNT aggregation can be major reason of photoluminescence quenching, we however assume that it is not the case for our system. Indeed, SWCNT aggregation should also lead to an enlargement of the SWCNT absorption band which has not been observed (Figure 6.3a).

In conclusion, UV-VIS and fluorescence measurements performed tend to prove that 1 is actually able to stack on carbon nanotubes through its pyrene units. For a better understanding of the interaction between 1 and SWCNT, further experiment are needed. For instance, measurements in various concentrations to access the thermodynamic of the reaction. The mechanism responsible of the quench should also be further investigated.

## 6.2 Fonctionalization of SWCNT FET-device

After proving the possible stacking of 1 on the SWCNTs in solution, SWCNT-FET device have been directly functionalized by 1. The design of the SWCNT-FET arrays used in the present study has been reported in the previous chapter. Some of the transport measurement presented here have been first realized by Gurvan Magadur during his thesis [224].

### 6.2.1 Process

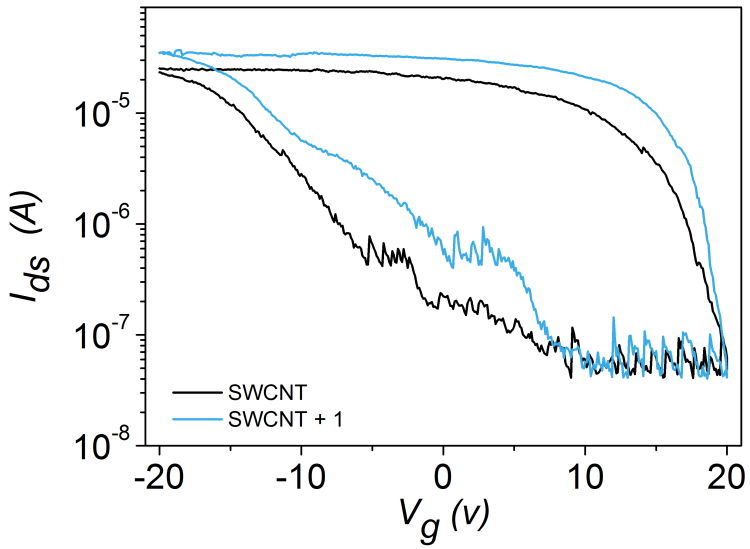


FIGURE 6.6: Ids vs. Vg curves from -20 to 20 V for SWCNT-FET (black) and the same SWCNT-FET modified with 1 (blue); Vds = 2V.

The SWCNT-FETs devices were functionalized by depositing on the transistors a solution droplet of 1 dissolved in dichloroethane (DCE) and leaving it to dry. The device was then thoroughly rinsed with an excess of DCE in order

to eliminate non-grafted complexes. The grafting/washing cycle was repeated three times to maximize the number of molecules grafted on the SWCNTs' sidewalls and minimize the number of residual molecules on the substrate.

The device characteristics do not change drastically upon its modification by molecules of 1 as seen in Figure 6.6. A small increase of the drain current is observed, leading to right hand shift of the Id/Vg plot. This shift is characteristic of a p-doping which can be chemical or electrostatic [157, 225]. A p-doping of the SWCNT by 1 is also consistent with the quenching of SWCNT photoluminescence observed in liquid phase. No modification of the Schottky barrier is evidenced since no change of the slope of the Ids = f(Vg) plot could be observed [142, 226].

### 6.2.2 Raman spectroscopy

In order to directly prove the presence of 1 on SWCNT, we carried out specific Raman spectroscopy experiments. A Raman mapping has been performed in a chosen and marked area between the two SWCNT-FET electrodes before and after functionalization see Figure 6.7. We identified, through their positions, three noticeable SWCNTs by their Radial Breathing Mode (RBM) peaks. The band at 300 $cm^{-1}$ corresponds to the silicon oxide substrate and is present on all spectra. After modifying the device with 1, a blue shift of the RBM modes is observed (see Table in Figure 6.7), characteristic when molecule is in contact with SWCNT [160, 185, 227, 228].

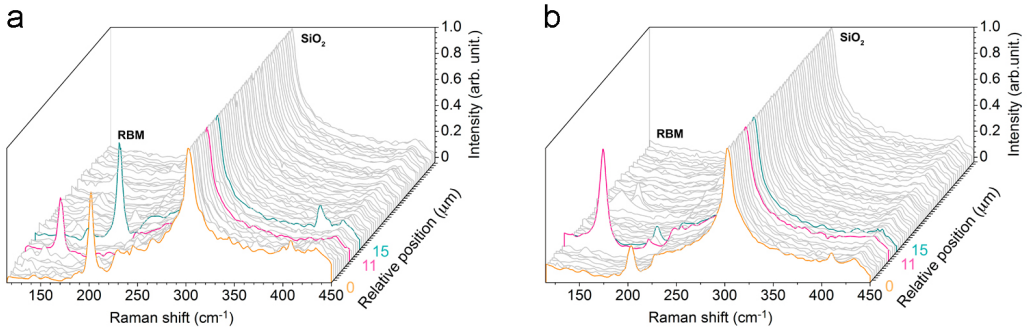


| Nanotube | RBM before grafting | RBM after grafting | Shift |
|---|---|---|---|
| Nanotube 1 | 202.5 $cm^{-1}$ | 203.5 $cm^{-1}$ | +1 $cm^{-1}$ |
| Nanotube 2 | 151.9 $cm^{-1}$ | 155.2 $cm^{-1}$ | +3.3 $cm^{-1}$ |
| Nanotube 3 | 201.9 $cm^{-1}$ | 203.9 $cm^{-1}$ | +1.3 $cm^{-1}$ |

FIGURE 6.7: **Top a** Raman shift (632nm) before grafting, **b** Raman shift (632nm) between the same two electrodes after grafting. Intensity and shift of all the spectra have been calibrated on the silicon substrate peaks at 521 $cm^{-1}$. **Bottom** Table Raman shift in $cm^{-1}$ on selected nanotubes of the FET device before and after grafting.

It's worth noting that the most pronounced shift i.e. 3.3 $cm^{-1}$ is observed for the larger SWCNT (RBM at 151.9 $cm^{-1}$) in good agreement with literature values on the influence of functionalization on the RBM frequencies [229]. Moreover, we note that the intensity of the RBM peaks is also modified, indicating a change in the resonance conditions of the SWCNT, expected after a functionalization process [227].

In summary, we conclude from the shifts of the spectroscopic studies that complexes 1 stack on the sidewall of the nanotubes both in solution and when integrated into the devices. Importantly, the pristine transport properties of the FET devices does not seem significantly altered upon the stacking the molecules. We can then investigate the effect of the light on the devices modified by 1.

## 6.3 Application : Photo-switching

### 6.3.1 Photo-switching characterization

When the SWCNT-FET devices, modified by 1, were irradiated in resonance with the $[Ru^{II}(bpy)_3]^{2+}$ MLCT band (455 nm), their transport characteristics dramatically changed (Figure 6.8a). For positive gate values, $I_{off}$ current increases by several orders of magnitude and the process is perfectly reversible after several irradiation cycles (Figure 6.8a).

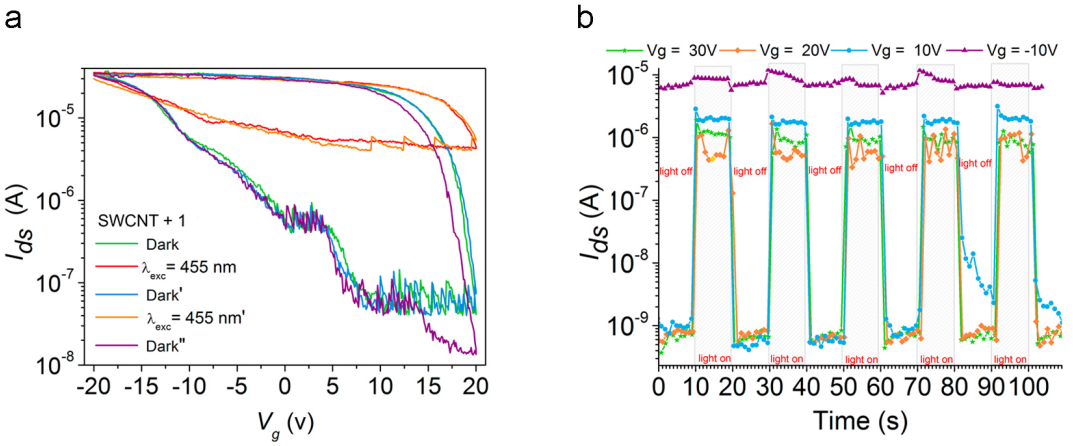


FIGURE 6.8: **a** Ids vs. Vg characteristics SCWNT-FET modified with 1 with (red first excitation; orange second excitation) and without (green initially scan; blue after the first excitation; purple after the second excitation) excitation at 455 nm; Vds = 2 V and **b** variation of Ids for a fixed Vg at ( -10V, 10V, 20V and 30V) of a SWCNT-FET modified with 1 when the 455 nm excitation light is alternatively turned on and off, laser power 30 $mW/cm^2$.

The $I_{ds}$ curves as a function of time curves for different Vg values are depicted in Figure 6.8b for the functionalized device. When the transistor is illuminated in the On state (Vg = -10 V, Figure 6.8b purple line), almost no change is observed

but, a strong amplification factor up to $10^3$ of the $I_{off}$ current occurs when the gate voltage was fixed at + 10V + 20 V and + 30 V (Figure 6.8b, blue, orange and green curves). The light-triggered enhancement of the conductivity of the device is reversible and time persistent only under light excitation; indeed the initial Off current is recovered within much less than 1 second (time resolution of the set up was 1s) after the light is switched off. This fast recovery indicates that no phenomenon of charge trapping at $SiO_2$ interface occurs. These results lead to the conclusion that, upon continuous illumination in the MLCT band of the $Ru^{II}$ chromophore, the conduction becomes almost independent from the gate voltage.

Control experiments under illumination have also been performed and the photoswitch effect of devices modified by 1 is only observed when the wavelength is tuned with the MLCT band of 1 (i.e. at 455 nm). When the light is tuned out of resonance (590 nm) no photomodulation occurs (see Figure 6.9a). FET devices have been also functionalized with 2 (molecule 1 without the photoactive $[Ru^{II}(bpy)_3]^{2+}$ unit see Figure 6.9b). As shown in Figure 6.9b here again no photomodulation is observed at 455 nm.

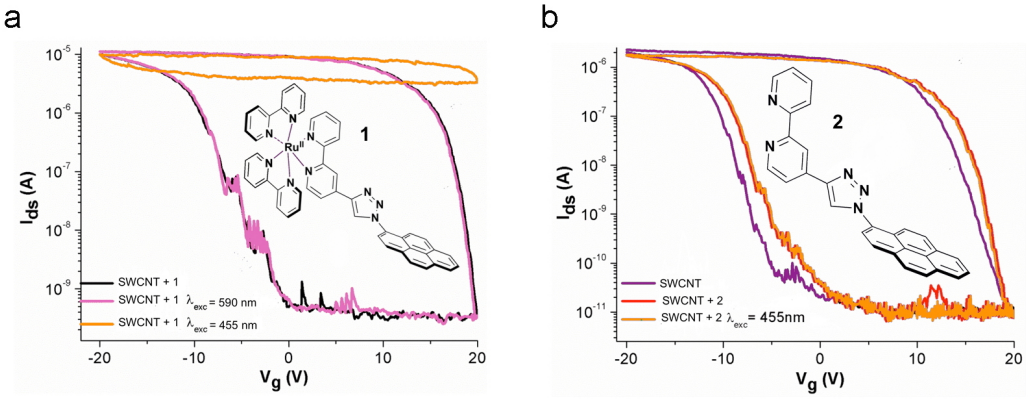


FIGURE 6.9: **a** Ids vs. Vg characteristics SCWNT-FET modified with 1 with (black in dark; pink : under laser excitation at 590 nm and orange under laser excitation at 455 nm **b** Ids vs. Vg characteristics SCWNT-FET modified with 2; Vds = 2V.

## 6.3.2 Photo-switching Mechanism

### Experimental insight

Since the $[Ru^{II} - Pyr]^{2+}$ complexes 1 stack onto the nanotubes through the pyrene group and the light effect is due to irradiation in the MLCT band of the $Ru(bpy)_3$ unit, we suggest that the mechanism responsible for the modulation of the transport behavior involves both the excited state of the $Ru^{(II)}$ moiety and that of the pyrene unit that is in direct contact with the nanotube. We, therefore, propose that the first event of the mechanism involves a triplet-triplet energy transfer process from $^3[Ru^{II}(bipy)_3]^{2+*}$ to the $^3Pyr^*$ present at the

surface of the SWCNT. In order to probe the existence of such triplet-triplet energy transfer the photophysical properties of 1 were investigated by laser flash photolysis in acetonitrile solutions. Excitation of 1 in acetonitrile at 455 nm with a nanosecond laser flash leads to the formation of an excited state, which is detected by emission with a maximum at 618 nm (Figure 6.10a), typical for $Ru^{II}$-polypyridine complexes [230]. However, the emission lifetime (1.0 $\mu s$/ 20% and 4.7 $\mu s$/ 80%) is significantly longer than the one observed for the parent $[Ru^{II}(bipy)_3]^{2+}$ complex (0.8 $\mu s$) (see Figure 6.10b). This is attributed to the fast establishment of the equilibrium between $^3[Ru^{II}(bipy)_3]^{2+*}$ and $^3Pyr^*$ triplet excited states [231]. Figure 6.10c displays the transient absorption spectrum of 1 in acetonitrile. It shows a bleaching at 350 nm and a maximum at 417 nm attributed to the formation of $^3Pyr^*$. The dip in the differential absorption spectrum at about 455 nm is as expected due to the bleaching of the $[Ru^{II}(bipy)_3]^{2+}$ MLCT state due to the formation of some $^3[Ru^{II}(bipy)_3]^{2+*}$ triplet excited state. The triplet-triplet energy transfer in 1 is consequently demonstrated in acetonitrile solution.

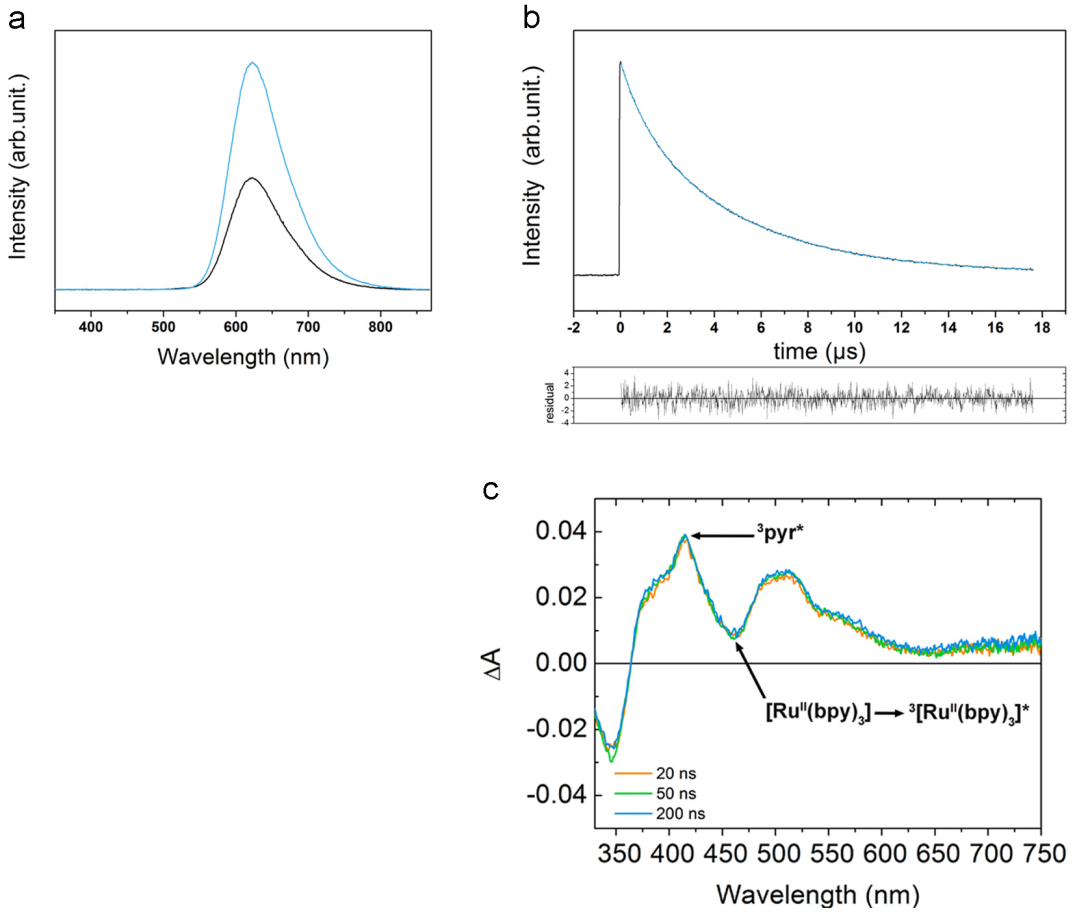


FIGURE 6.10: **a** emission spectra at 20 ns (blue line) and 1$\mu s$ (black line) after laser flash **b** Kinetics of emission of Ar purged sample in MeCN, excitation 455 nm. Biexponential fit: 1.0$\mu s$/20%; 4.7$\mu s$ / 80%. **c** Transient absorption spectra of complex 1 in acetonitrile excited on the $[Ru^{II}(bipy)_3]^{2+}$ MLCT band, delays from laser pulse as indicated in the legend.

Another way to probe the role of the triplet-triplet energy transfer process is to design a derivative of complex 1 where the bipyridine groups are modified with ester groups (1-ester). Indeed, these modifications are known to lower the $^3[Ru^{II}(bipy)_3]^{2+*}$ energy of the dyad [232]. The photophysical properties of 1-ester do not show the presence of the triplet-triplet transfer process between the ruthenium chromophore and the pyrene unit (see Figure 6.11b-c). As shown in Figure 6.11d when 1-ester is stacked on the SWCNT-FET, no photomodulation is observed. Therefore, these results strongly emphasize the requirement to reach the triplet state of the pyrene unit at the surface of the SWNTs in order to observe the change in conductivity (Figure 6.10b) and that the mere presence of the $Ru(bpy)_3$ moiety in the proximity of the nanotube cannot be at the origin of the observed effect.

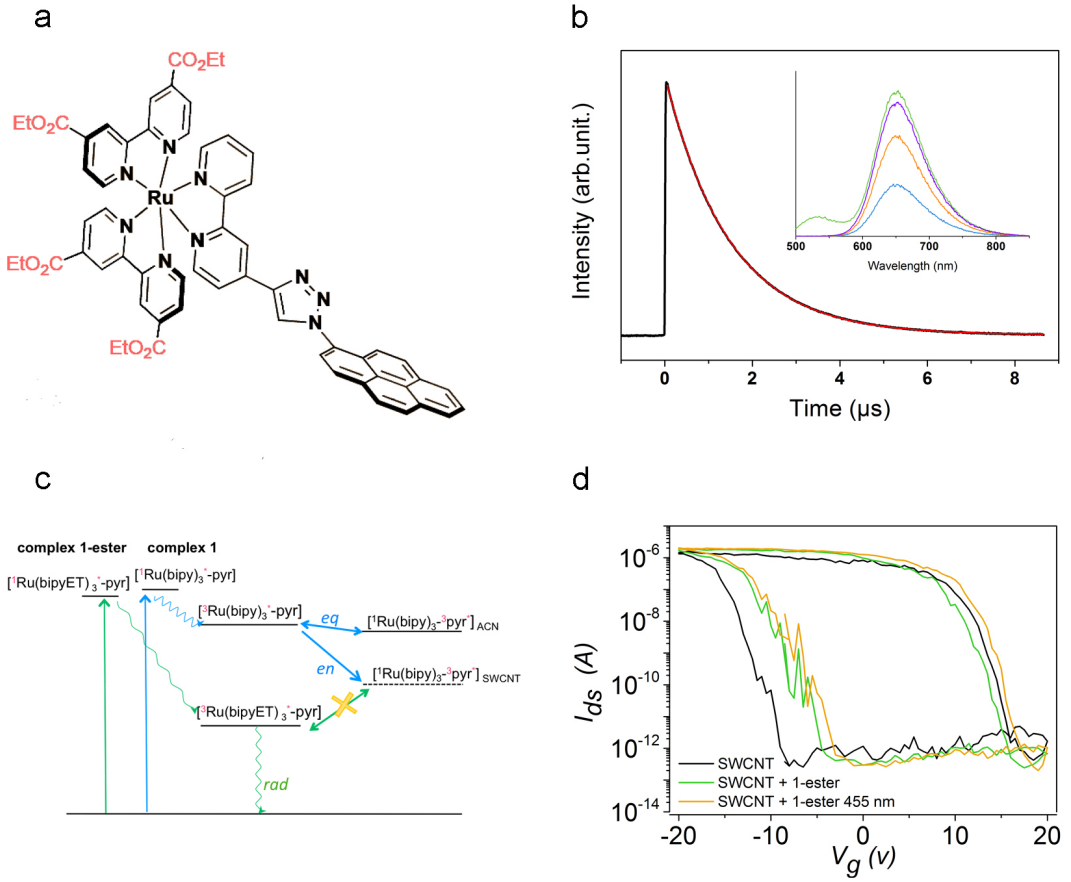


FIGURE 6.11: **a** schematic view of 1-ester **b** Kinetics of emission of 3 in Ar purged MeCN, excitation 455 nm. Red: exponential fit, $\tau = 1.46\ \mu s$. Inset: emission spectra at 10 ns, 100 ns, 500 ns, and 1.5 $\mu s$ after laser flash **c** Energy Scheme for the excited states in$[Ru^{II}(bipy)_3]^{2+}$. The energy are suggested according to the experiments and theoretical calculation **d** Ids Vs. Vg characteristics for a CNFET, the same CNFET modified with 3

### Theoretical insight

Then, the nature of the interaction between SWCNT and pyrene triplet staked on its wall still has to be sorted out. Theoretical experiment have been performed by Nathalie Guihéry team in Toulouse to analyze such interaction.

Broken Symmetry DFT calculations using the range-separated CAM-B3LYP functional [233] were performed. The starting system is a pyrene-triazol deposited on a nanotube. In a first place, nanotubes (10,8) having close diameter (1.204 nm) as those used in the experiments but with various lengths have been computed. The energy of the Highest Occupied Molecular Orbital (HOMO) and the Lowest Unoccupied Molecular Orbtals (LUMO) reported in appendice D, shows that the gap of the nanotube closes upon increasing the nanotube length (L) as expected. The gap as function of 1/L (see Table D.1 in appendix D) shows that it would remain finite at infinite size, hence that the studied nanotube would have the same semi-conductor behavior as those used in the experiments at the thermodynamic limit. The geometry optimization of the pyrene-triazol moiety deposited on the nanotube converges to the structure depicted in Figure 6.12 demonstrating that the pyrene-triazol stacks on the surface with a minimum distance between the carbons of the two subsystems of 3.8 Å. Looking at the orbitals energy of the staked pyrene-triazol unit in its singlet ground state (table 6.1), one may note that its HOMO and LUMO are respectively lower and higher than those of the nanotube. Consequently, the mere stacking of the pyrene-triazol on the nanotube cannot affect the transport properties of the device thought a chemical doping. Then, one can assume that the p-doping observed in section 6.2.1 is due to an electrostatic doping induced by the negative charge of the molecule.

In order to investigate the effect of irradiation, Nathalie Guihéry team computed the energy of the first excited triplet state of both the isolated pyrene-triazol and the whole system (pyrene stacked on the nanotube). The energies of the HOMO and LUMO spin-orbitals located on the pyrene-triazol and the singly occupied molecular orbitals (SOMOs) located on the nanotube in the triplet state of the whole system are reported in table 6.1. They show that the first excited triplet state of the pyrene/nanotube system is not located on the pyrene-triazol unit but on the nanotube. Indeed, the singlet-triplet gap of the isolated pyrene-triazol unit is found to be 2.36 eV while that of the whole system is only 0.73 eV. One could question the reliability of these results because of the finite size of the nanotube used for the calculations. Nevertheless, increasing the length of the nanotube would of course lead to a decrease of the HOMO/LUMO gap while the energy of the HOMO and LUMO of the pyrene-triazol unit will not significantly change, the observed effect would thus be more favorable energetically. One can also see that these last energies are very similar in the singlet and triplet states of the whole system and also similar to those of the isolated unit (-5.52eV, -1.82eV for the HOMO and LUMO respectively), which is in line with the weak nature of the $\pi-\pi$ interactions. Finally, since the excitation on the pyrene-triazol is much higher than that of the nanotube, the most probable mechanism is an excitation transfer from the pyrene-triazol unit to the nanotube. As in its triplet excited

state the conduction band is populated, a conduction of electrons is observed when applying a positive voltage. It is worth noting that this mechanism is also compatible with the reversible character of the observations as it does not chemically change the deposited compound : when the irradiation stops the nanotube relaxes to its ground state and the process can be reproduced.

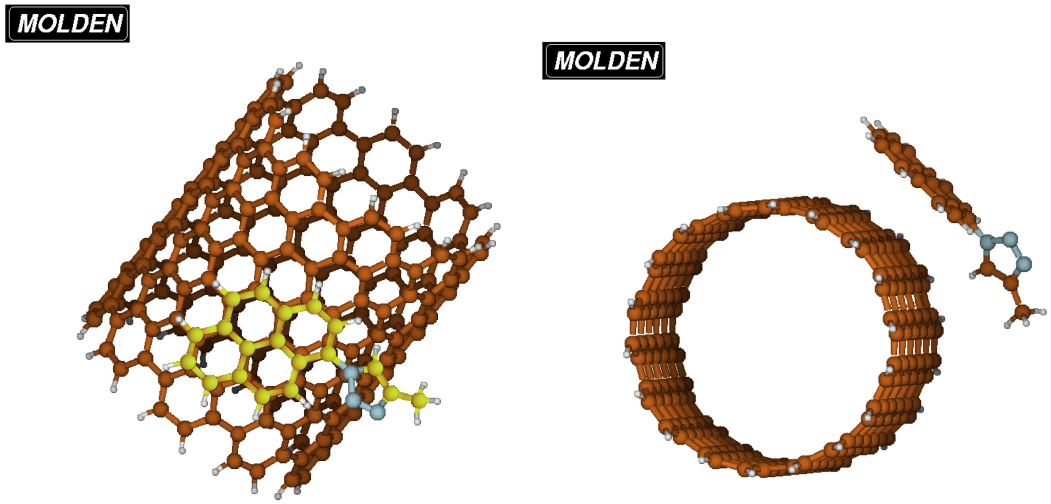


FIGURE 6.12: Two views of the calculated optimized structure of the pyrene-triazol staked on a nanotube of length 1.356nm

TABLE 6.1: Energy of the HOMO and LUMO spin-orbitals located on the pyrene-triazol and of the two SOMOs located on the nanotube in the whole system calculation.

| State | sub system | Orbital | energies(eV) | |
|---|---|---|---|---|
| Singlet ground state | Pyrene-triazol | HOMO | -6.587 | |
| | | LUMO | -0.575 | |
| | | Gap | 6.01 | |
| | nanotube | HOMO | -4.78 | |
| | | LUMO | -2.72 | |
| | | Gap | 2.06 | |
| Excited triplet state | Pyrene-triazol | | $\alpha spin$ | $\beta spin$ |
| | | HOMO | -6.590 | -6.587 |
| | | LUMO | -0.614 | -0.571 |
| | | Gap | 5,976 | 6.016 |
| | nanotube | SOMO1 | -4.76 | |
| | | SOMO2 | -4.05 | |
| | | Gap | 0.70 | |

### Proposed Mechanism

Based on the experimental measurement and the results of the theoretical calculation we proposed the following mechanism :

$$[Ru^{II}\text{-}Pyr]^{2+}\text{–}CNT + h\nu \rightarrow \{[^{3*}Ru^{II}\text{-}Pyr]^{2+}\text{–}CNT \leftrightarrow [Ru^{II}\text{-}^{3*}Pyr]^{2+}\text{–}CNT\} \rightarrow [Ru^{II}\text{-}Pyr]^{2+}\text{–}^{3*}CNT$$

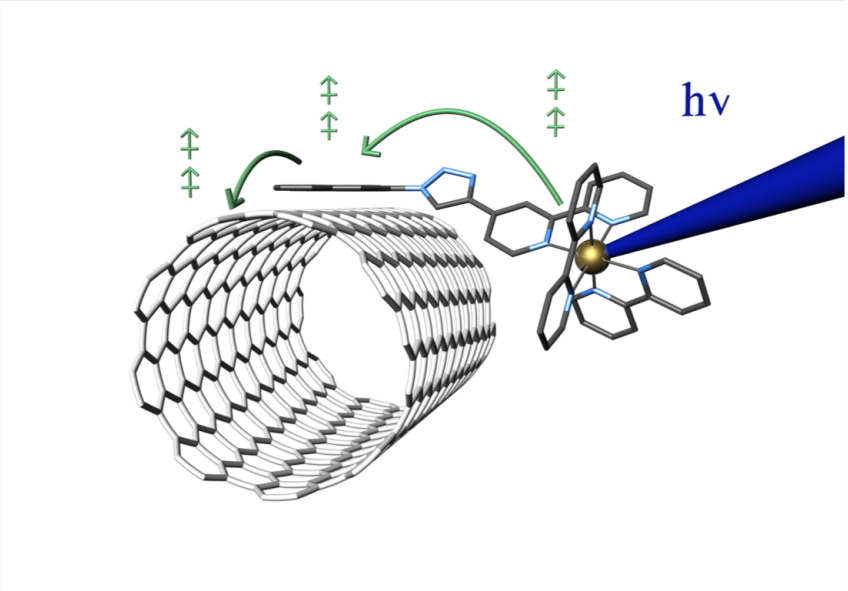


FIGURE 6.13: Schematic mechanism of the formation of the triplet exciton on the nanotube via cascade triplet-triplet energy transfer after illumination of the Ru chromophore. Legend Blue : Nitrogen atom ; Grey : Carbon atom ; Gold : Ruthenium atom.

To confirm this mechanism, experimental observation of the triplet exciton on a nanotube is desirable but, it is a challenge, as shown by the few studies that report such observation [234, 235]. No evidence concerning their effect on the transport behavior of SWCNT-FET devices was evidenced to date. However, to indirectly probe a possible energy transfer which starts from the ruthenium towards the carbon nanotube, we analyze in liquid phase, the emission of the $^3Ru(bpy)_3$ in the molecule 1 in absence and in presence of nanotube. We used for that the micelle swelling method presented in part 6.1.1. Figure 6.14a shows the emission of 1 after excitation at 480 nm (almost same excitation used for illuminating the SWCNT-FET device), the peak at 650 nm correspond to the emission of $^3Ru(bpy)_3$. In presence of the nanotube, for a same concentration of 1, a quench of 47.4% of the $^3Ru(bpy)_3$ peak is observed. This quench is consistent with the energy transfer mechanism. The fact that the quenching of the fluorescence emission is not 100% was expected, due to the presence of some free molecules of 1 in solution. The normalized emission spectra (Figure 6.14b) match perfectly before and after functionalization, pertaining the fact that the residual luminescence in the case of SWCNT + 1 originates from free 1 molecules.

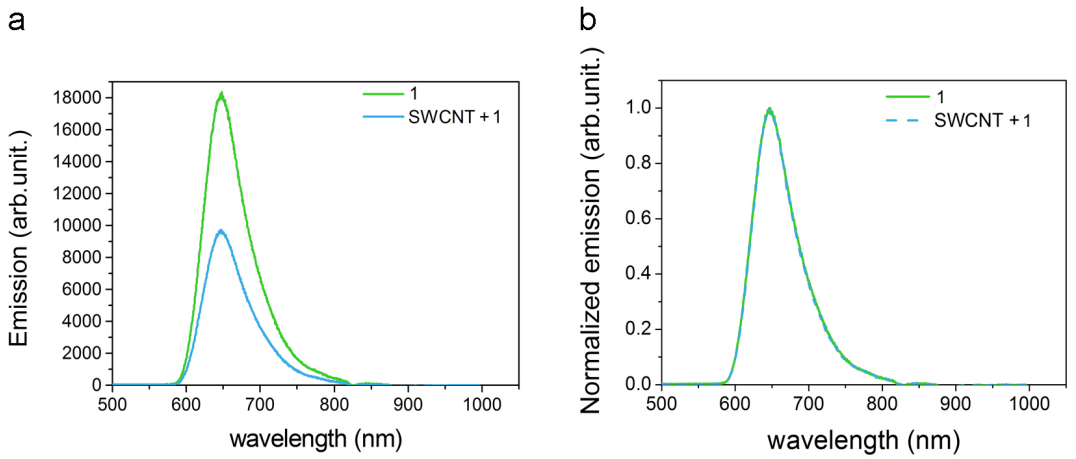


FIGURE 6.14: : **a** Emission spectrum for excitation at 480 nm SWCNT + 1 dispersion (blue line) and 1 (green line) **b** Normalized emission spectra for excitation at 480 nm SWCNT + 1 dispertion (blue line) and 1 (green line).

## 6.4 Conclusion and prospective

We have reported here a very large visible-light photomodulation of the conductivity of a SWCNT-FET devices decorated with molecular sensitizers. This molecular system behaves as a bichromophoric assembly where the role of the $[Ru^{II}(bpy)_3]^{2+}$ unit is two-fold. Firstly, it acts as an antenna to capture visible light and activate the pyrene triplet excited state usually reachable via UV light and only by inter system crossing from the excited singlet state. The excitation of the pyrene ($^3Pyr^*$) being much higher in energy than the first excitation (and probably many excitations) of the nanotube, it is then transferred creating a triplet exciton on the nanotube, thus populating its conduction band by electrons and creating a hole in its valence band leading to drastic change in the conductivity. Thus, the cornerstone of the large change in the conductivity of the FET device is the formation of the triplet state on the pyrene unit, and this state is efficiently accessible through the triplet state of the $Ru(bpy)_3$ chromophore and not by direct excitation of the pyrene.
For a full understanding of the interaction between SWCNT and the $[Ru^{II} - Pyr]^{2+}$ few complementary experiments are required. First, the investigation of the exact nature of the interaction of the SWCNT and the chromophore without light have not been deeply investigated. The SWCNT photoluminescence quench shown during the study in liquid phase such as the current increased when FET-device are coated with the chromophore are consistent with a p-doping but do not constitue an absolute proof. Analysis of the G-band of the SWCNT in Raman spectroscopy and photoluminescence measurement at various concentration can provide relevant information concerning this eventual SWCNT doping. Secondly, pump-probe measurement of the system under light illumination should be performed in order to definitely prove the formation of the triplet exciton on the nanotube induced by the photo-excitation.

## 6.5 Experimental details

### 6.5.1 Micelle swelling method

#### Suspending nanotube in micelle

First, small amont SWCNT powder (CoMoCat or HipCo) was added to a 2 $wt\%$ suspension of sodium cholate micelle into a pH=8 borate buffer ($10^{-2}$ $mol.l^{-1}$). A tip sonication of the micelles/SWCNTs was applied for 1h30 in a thermostatic bath at 2°C. Then, 1h of ultraultracenfugation at 120 000 g was performed to remove bundles nanotubes and amorphous carbon and select isolated nanotube only.

#### Suspending molecule in micelle

400 $\mu L$ of a solution ($S_1$) of the molecule of interested in DCM was added to 4mL of a 2 $wt\%$ sodium cholate micelle suspension into a pH=8 borate buffer. A smooth tip sonication (20%) is then applied to the biphasic system in a thermostat bath at 12°C for one hour.

| System | $S_1$ concentration ($mol.L^{-1}$) |
|---|---|
| molecule 1 | $7.92.10^{-4}$ |
| pyrene molecule | $5.22.10^{-4}$ |

#### Molecule-SWCNT hybrid system fabrication by micelle swelling

400 $\mu L$ of a solution ($S_1$) at of the molecule of interested in DCM was added to 2 mL of the isolated SWCNT solution and 2 mL of a 2 $wt\%$ the sodium cholate micelle suspension into a pH=8 borate buffer. A smooth tip sonication (20%) is then applied to the biphasic system in a thermostat bath at 12°C for one hour.

| System | $S_1$ concentration ($mol.L^{-1}$) |
|---|---|
| 1-SWCNT (CoMoCat) | $7.92.10^{-4}$ |
| 1-SWCNT (HiPco) | $2.61.10^{-4}$ |
| pyrene-SWCNT (CoMoCat) | $5.22.10^{-4}$ |
| $[Ru^{II}(bpy)_3]^{2+}$ -SWCNT (CoMoCat) | $5.22\ .10^{-4}$ |

# Conclusion

This thesis has been dedicated to the SWCNT synthesis in the view of analyzing the growth parameters which can influence the final structure of the grown SWCNTs.

We have focused on the carbon nanotube synthetic process and we developed a new, original, and versatile approach for designing specific homogenous bimetallic catalyst for the CVD SWCNT growth. This approach is based on preformed Prussian Blue Analog nanoparticles which are used to obtain in situ individual and small bimetallic catalyst nanoparticles with a narrow size distribution. The diversity of the Prussian Blue Analog family gives rise to a new and versatile way of easily adjusting the catalyst properties by changing the PBA's metal composition. Under these conditions, it becomes possible to study the effect of changing one or both of the metal components in the bimetallic alloy catalyst upon the selectivity of the SWCNT growth because the growth process can be kept close to identical, except for the nature of the metal in the catalyst. This capability offered by the method presented in this thesis paves a large avenue for investigating SWCNT growth selectivity by tuning properties of the metal catalyst.

We applied this new synthetic method to grow SWCNTs from three different bimetallic catalyst of FeRu, CoRu and NiRu at various temperatures. We observed significant difference between the as-grown SWCNTs as a function of both temperature and metal catalyst composition, especially in terms of diameter distribution. We proved that this effect cannot be attributed to variation of the catalyst nanoparticle size distribution which has been shown to be very similar whatever the growth temperature or the catalyst chemical composition. Indeed, it appears that under fixed growth conditions we could activate selectively different nanoparticle catalyst size population. The exact mechanism of this selective activation is not yet fully understood, but we assume that it relates to the difference in carbon solubility into the nanoparticles depending on their size and their chemical composition. A statistical analysis of both the diameter of the SWCNTs and their own catalyst nanoparticles through HRTEM measurements should be done in the future to consolidate an absolute verification of these selective activation. The observation of such system was difficult in this present study, the samples observed in TEM after a transfer process did not enabled any statistical study. The recent start of the collaborative project Nanomax, for the development of the SWCNT growth in an environmental HRTEM should provide new key for better understanding the growth of SWCNTs and provide nowadays missing statistical measurements. Concerning the

influence of the carbon solubility upon the SWCNT growth activation, theoretical calculations could also be envisioned in order to derive the carbon solubility limit of our nano-alloys as a function of the nanoparticle size and temperature and thus to sustain the proposed mechanism.

We also evidenced, as a function of the temperature, an increase of the s-SWCNT proportion, probably due to a selective etching of the bigger diameter m-SWCNT at high temperature. In order to validate this observations, we fabricated field effect transistors from the SWCNTs obtained at various growth temperatures. A statistical analysis of their characteristics, has confirmed the presence of more metallic SWCNTs when the growth is performed at low temperature. After an electrical breakdown process, these transistors exhibited a very high on-off ratio despite the lack of optimization of our transistor's design and fabrication process. We also noted that after these electrical breakdowns, transistors made with SWCNT grown at lower temperature exhibited on average better on/off ratios. We attribute this effect to the smaller diameter of the SWCNTs and/or a better crystallinity of the nanotubes grown at lower temperature.

Strong modifications of the current flowing in our transistors when they are exposed to weak concentrations of $NO_2$ gas have also been evidenced. Such strong response is related a priori to a doping of the SWCNTs forming the transistor channel. Further experimentations are, however, needed in order to understand the strong response of the device, through a better characterization of the nanotubes effectively connected between source and drain electrodes.

Finally, in the last part of this work we looked into the non-covalent interaction of SWCNTs and a photo active complex of ruthenium-tris-bipyridine covalently linked through a pyrene unit. After proving a possible interaction between the complex and the nanotube via a $\Pi$-stacking of the pyrene unit, we characterized the transport properties of functionalized SWCNT-FET devices. We observed a photo-induced modification of the characteristic of the device, leading to an increase up to three orders of magnitude of the off current. This drastic change is both fast, reversible and wavelength dependent. Through photophysical studies and theoretical calculation, we assumed that the mechanism leading to this photoinduced current rest on a triplet-triplet energy transfer between the photo-active complex and the SWCNT. To confirm this mechanism, the observation of the expected induced triplet state of the SWCNT would be highly desired. Transient absorption measurement after the photo-excitation of the SWCNT/photo active-complex hybrid system could be a possible experiment to reach this aim.

The work of this thesis contributed to proposing a new synthetic process to allow a better understanding of the SWCNT growth mechanism by decoupling as much as possible the various parameters of the CVD synthesis, and potentially lead to more chiral selective synthesis of SWCNTs. The last chapter also showed the great potentiality of the new carbon nanotube/hybrid systems to merge properties of SWCNTs with those of molecules of interest, opening the door to new applications for SWCNTs.

# Appendix A

# Appendix chapter 3

## A.1 XPS quantification

Table A.1: Area of Carbon, Ruthenium and Iron XPS peak uncorrected

| Peak | C 1S | Ru $3d_{3/2}$ | Ru $3d_{5/2}$ | Fe $2p_{1/2}$ | Ru $2p_{1/2}$ |
|---|---|---|---|---|---|
| Intensity before pretreatment (eV) | 2010.04 | 481.19 | 701.12 | 378.72 | 909.29 |
| Intensity after pretreatment (eV) | 677.80 | 256.77 | 372.07 | 307 | 586.63 |
| Scofield factor | 1 | 5.17 | 7.51 | 5.43 | 10.54 |

Table A.2: Total Area of Carbon, Ruthenium and Iron XPS peak corrected with Scofield factor after and before a pretreatement

| Element | Carbon | Ruthenium | C/Ru | Iron | Ru/Fe |
|---|---|---|---|---|---|
| Before pretreatment | 2010 | 187.9 | 10.69 | 156 | 1.22 |
| After pretreatment | 677.8 | 99.2 | 6.83 | 112.2 | 0.88 |

## A.2 STEM-EDX sepctrum

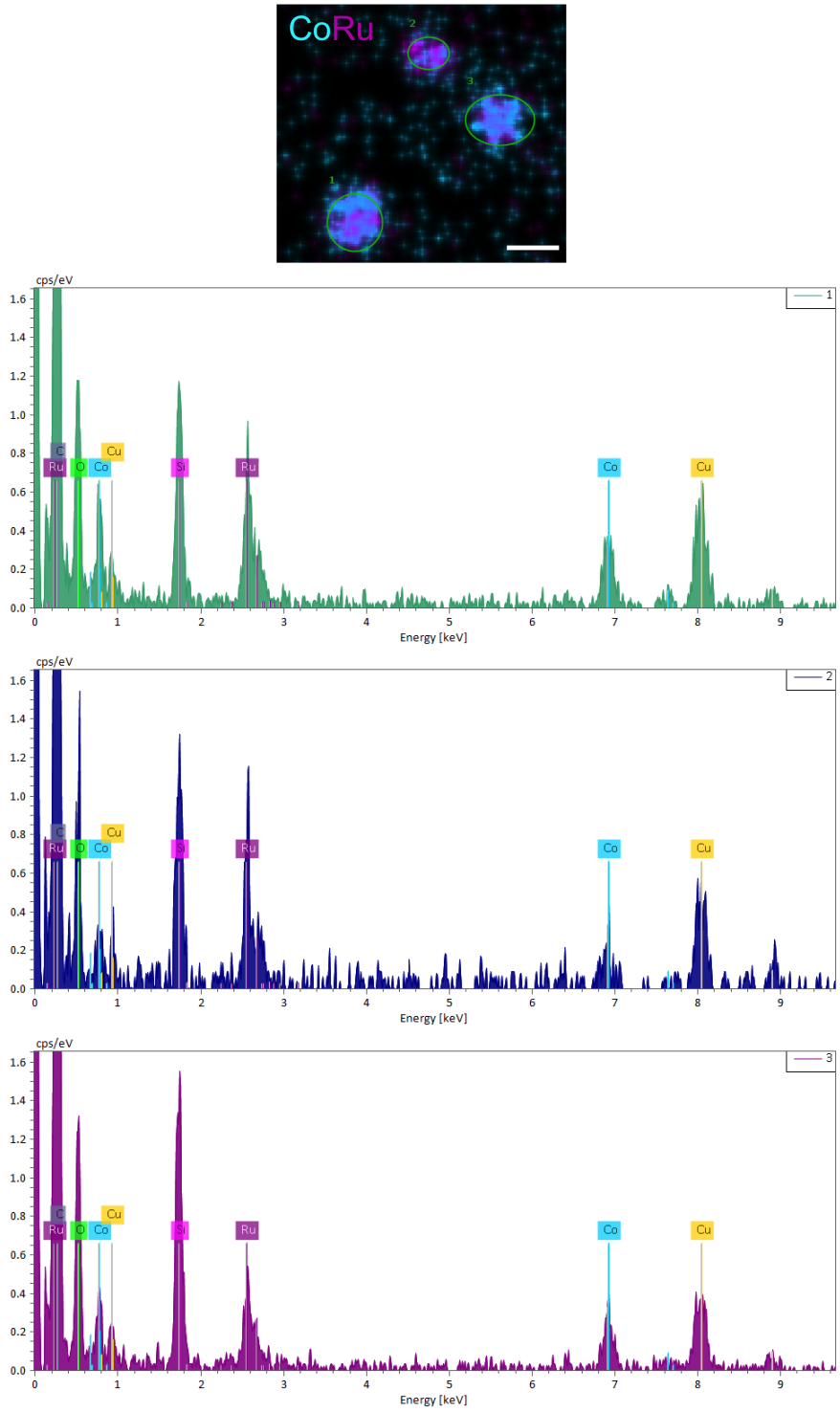


FIGURE A.1: EDX spectrum of the numbered nanoparticle

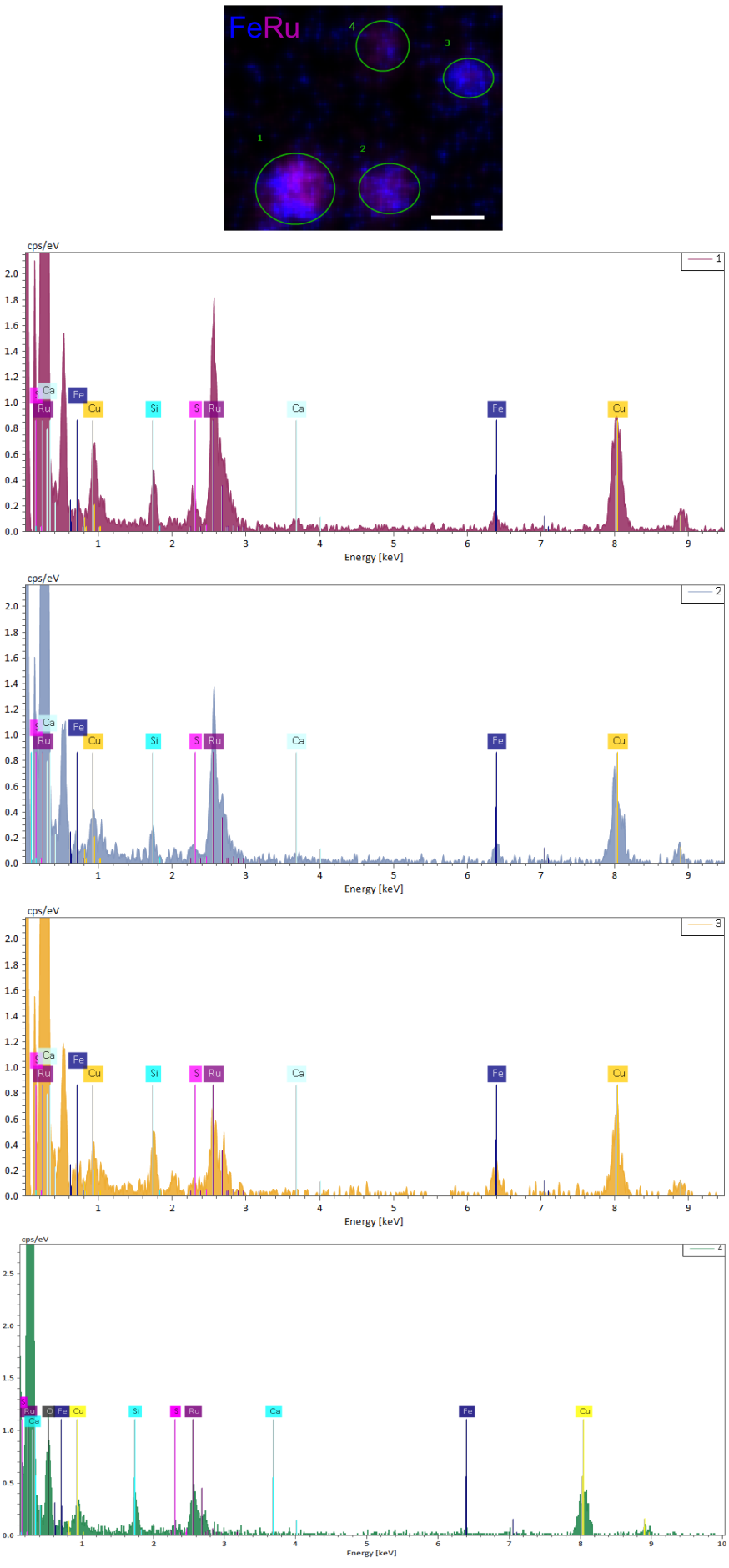


FIGURE A.2: EDX spectrum of the numbered nanoparticle

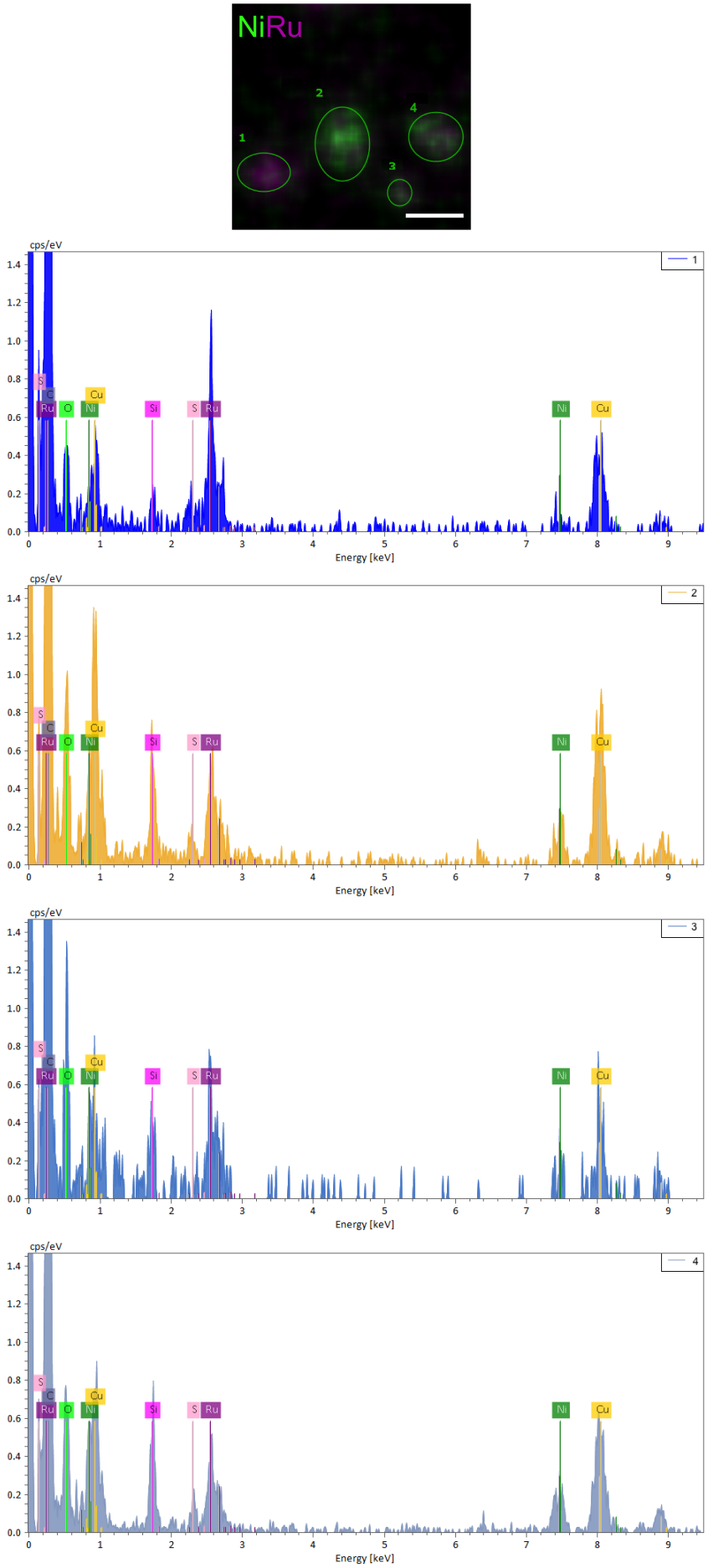


FIGURE A.3: EDX spectrum of the numbered nanoparticle

# Appendix B

# Appendix chapter 4

## B.1 Diameter distribution

### B.1.1 SWCNT grown from FeRu catalyst

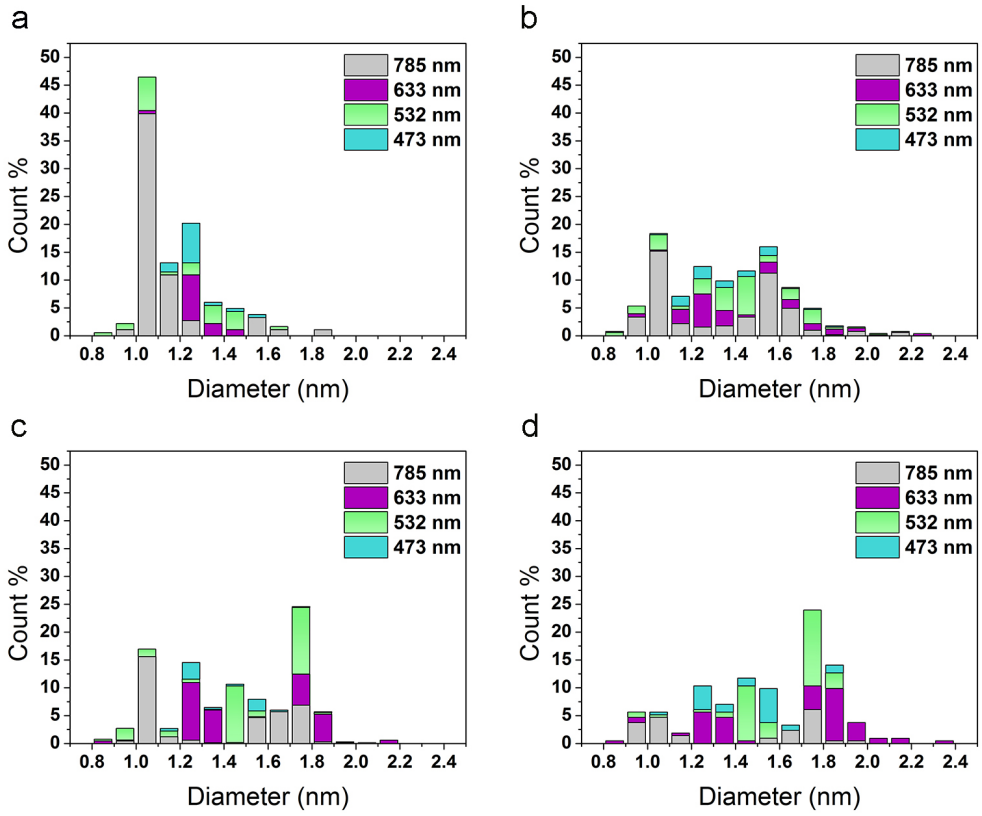


FIGURE B.1: Diameter distribution of SWCNT grown from FeRu catalyst at **a** 700°C **b** 800°C **c** 900°C **d** 1000°C

### B.1.2 SWCNT grown from CoRu catalyst

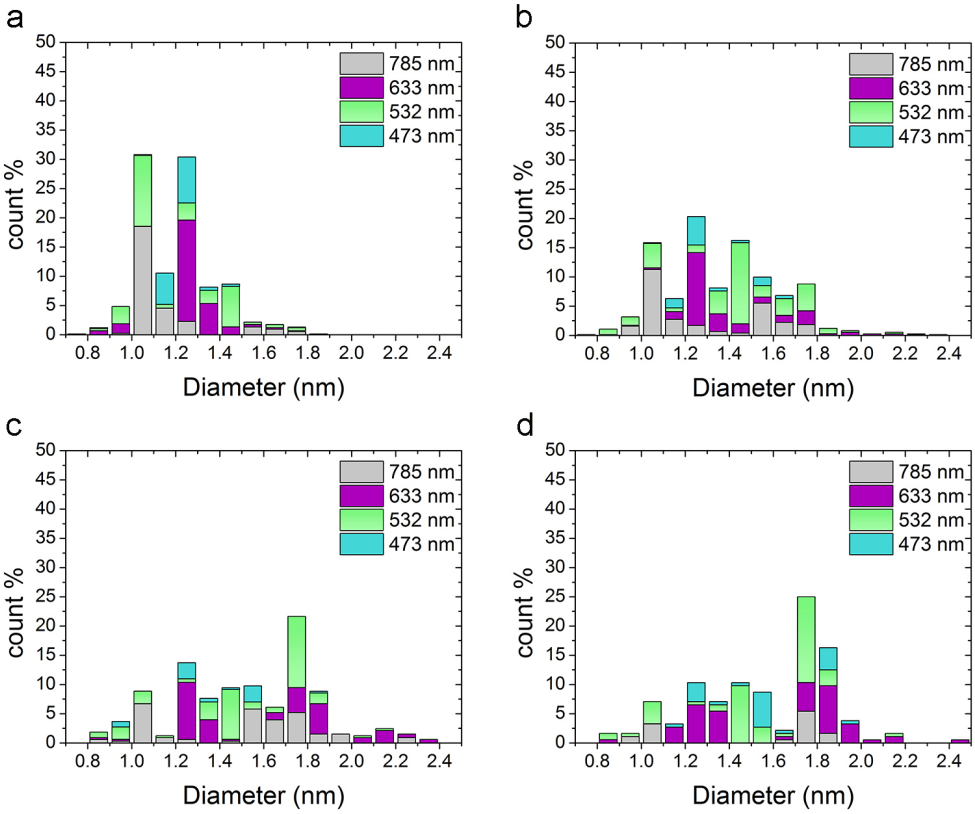


FIGURE B.2: Diameter distribution of SWCNT grown from CoRu catalyst at **a** 700°C **b** 800°C **c** 900°C **d** 1000°C

### B.1.3 SWCNT grown from NiRu catalyst

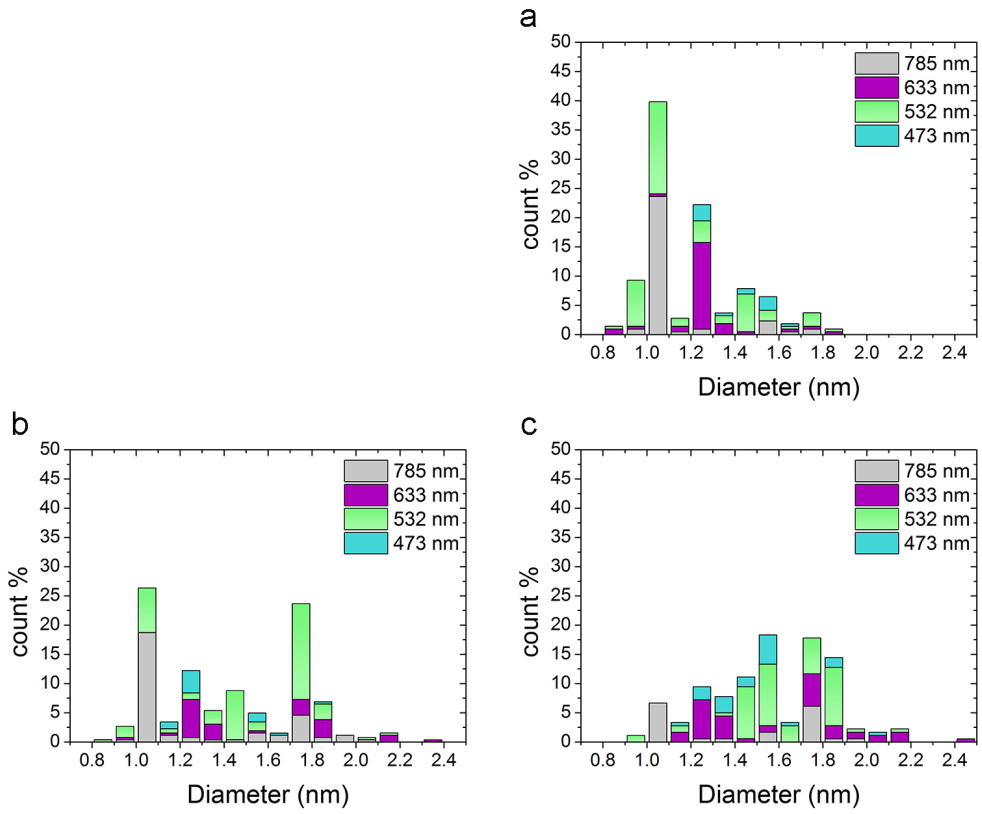


FIGURE B.3: Diameter distribution of SWCNT grown from NiRu catalyst at **a** 800°C **b** 900°C **c** 1000°C

## B.2 Semi-conducting/metallic ratio

### B.2.1 SWCNT grown from FeRu catalyst

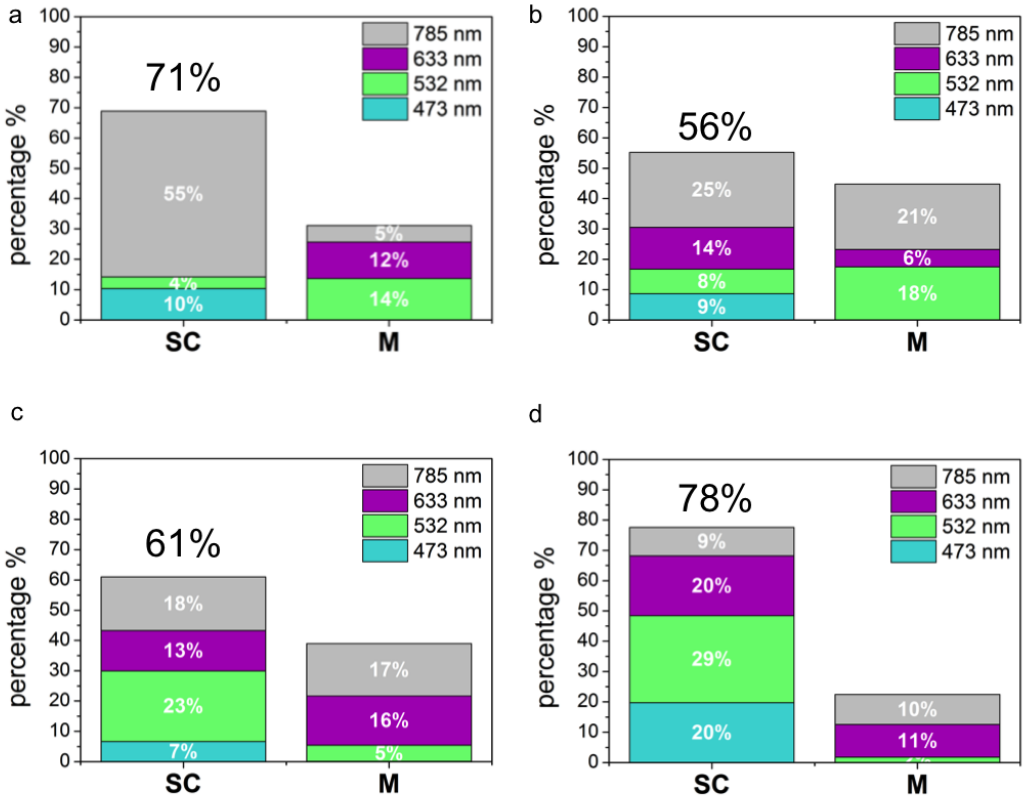


FIGURE B.4: Semi-conducting/metallic ratio of SWCNT grown from FeRu catalyst at **a** 700°C **b** 800°C **c** 900°C **d** 1000°C

### B.2.2 SWCNT grown from CoRu catalyst

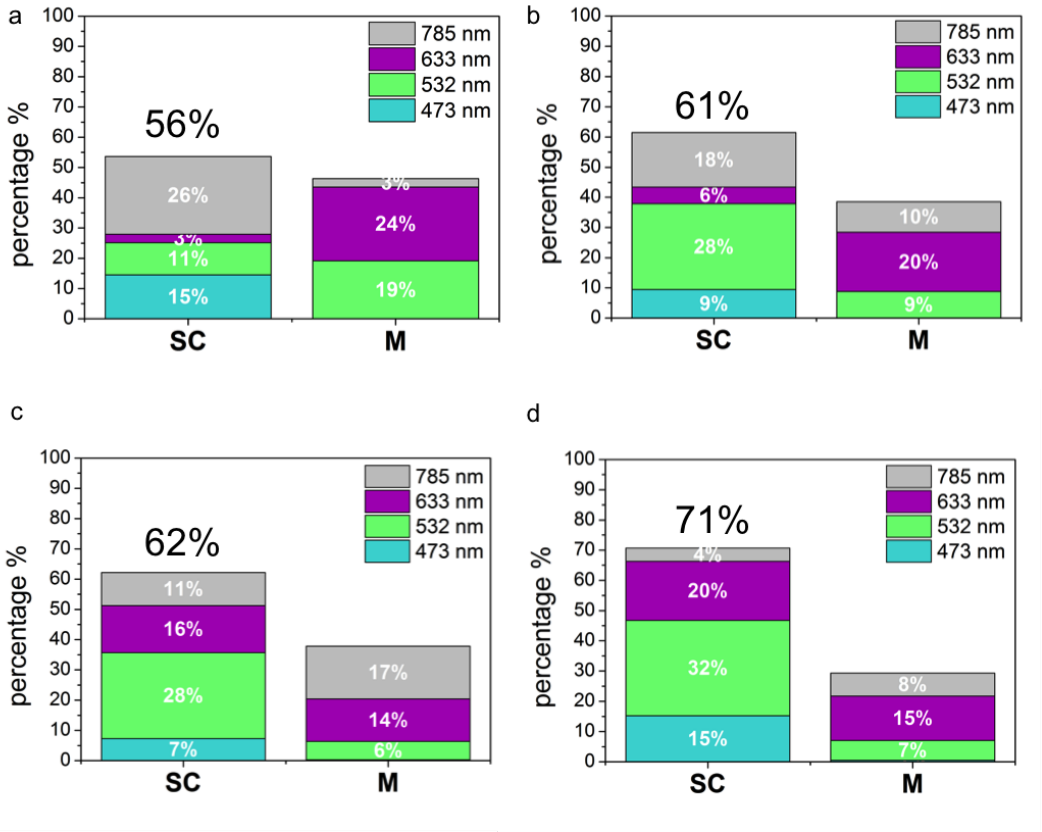


FIGURE B.5: Semi-conducting/metallic ratio of SWCNT grown from CoRu catalyst at **a** 700°C **b** 800°C **c** 900°C **d** 1000°C

### B.2.3 SWCNT grown from NiRu catalyst

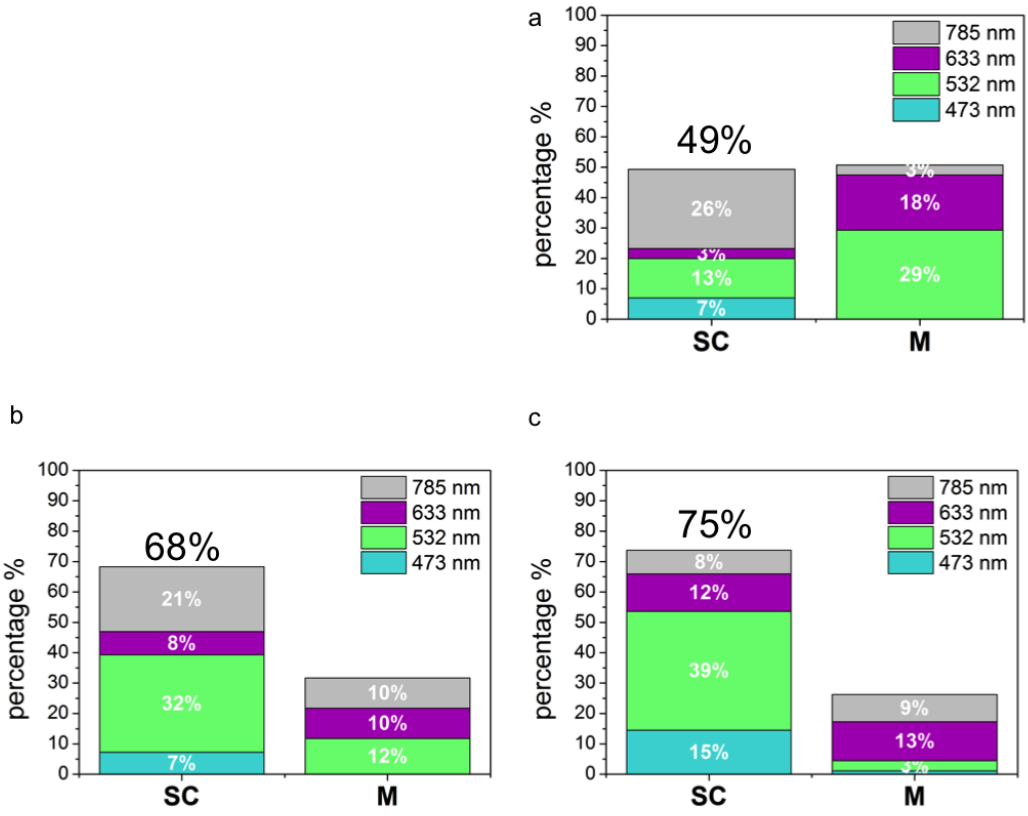


FIGURE B.6: Semi-conducting/metallic ratio of SWCNT grown from NiRu catalyst at **a** 800°C **b** 900°C **d** 1000°C

# Appendix C

# Appendix chapter 5

## C.1 Raman spectroscopy D and G modes

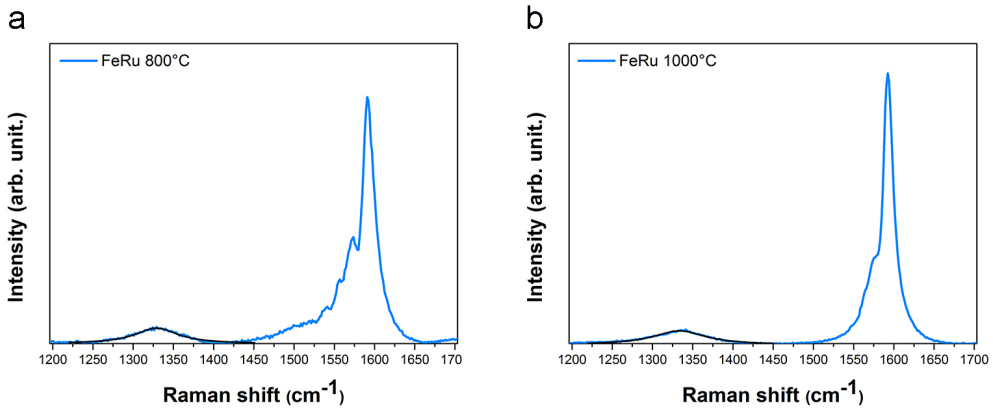


FIGURE C.1: Typical raman spectra of D and G mode of SWCNT grown from FeRu catalyst at **a** 800°C **b** 1000°C

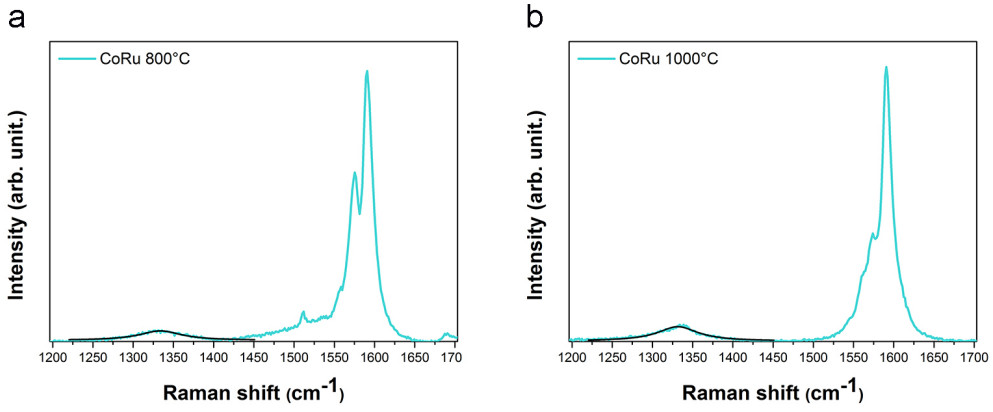


FIGURE C.2: Typical raman spectra of D and G mode of SWCNT grown from CoRu catalyst at **a** 800°C **b** 1000°C

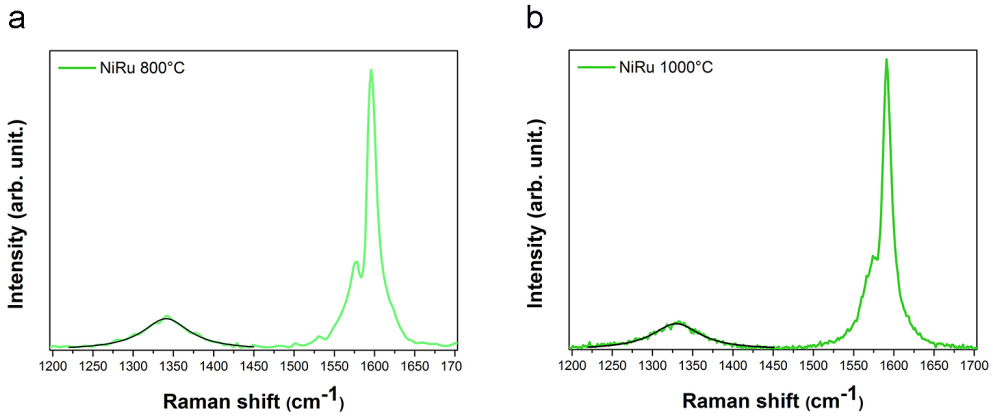


FIGURE C.3: Typical raman spectra of D and G mode of SWCNT grown from NiRu catalyst at **a** 800°C **b** 1000°C

## C.2 Ion/Ioff versus Ioff

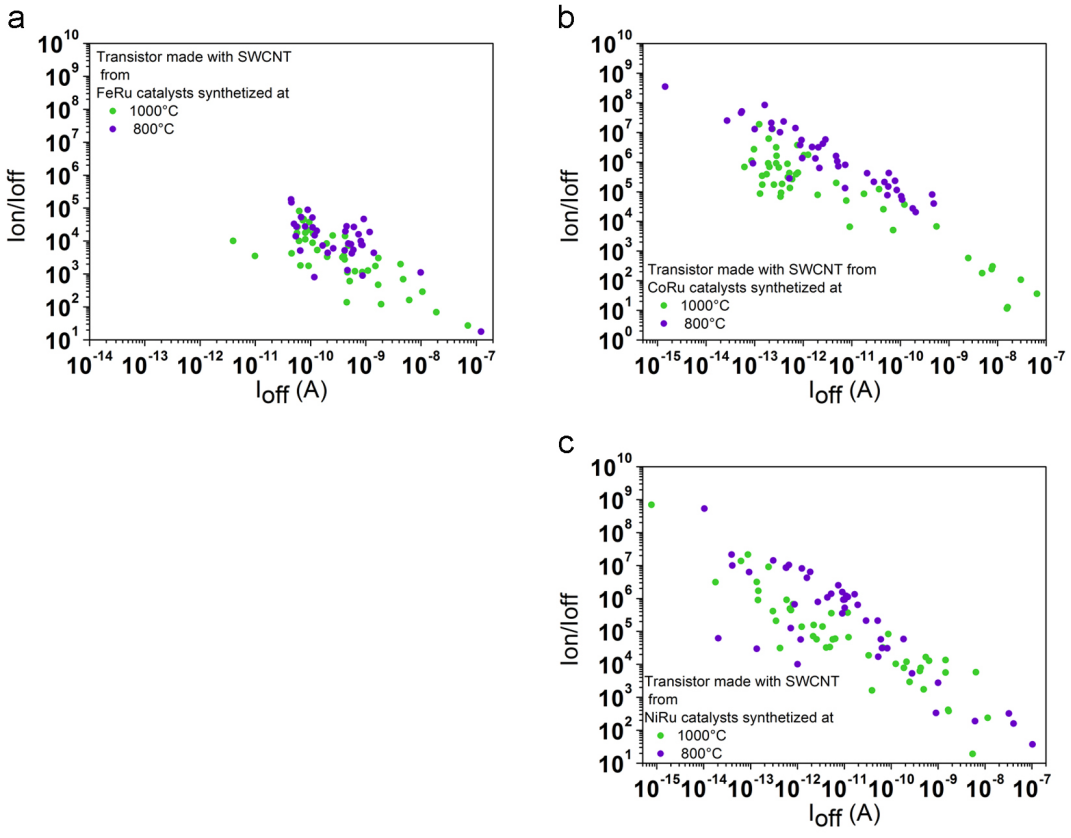


FIGURE C.4: Ion/Ioff ratio versus Ioff of FET-device after electrical breakdown fabricated from textbfa FeRu catalyst textbfb CoRu catalyst textbfc NiRu catalyst

# Appendix D

# Appendix chapter 6

## D.1 Synthesis

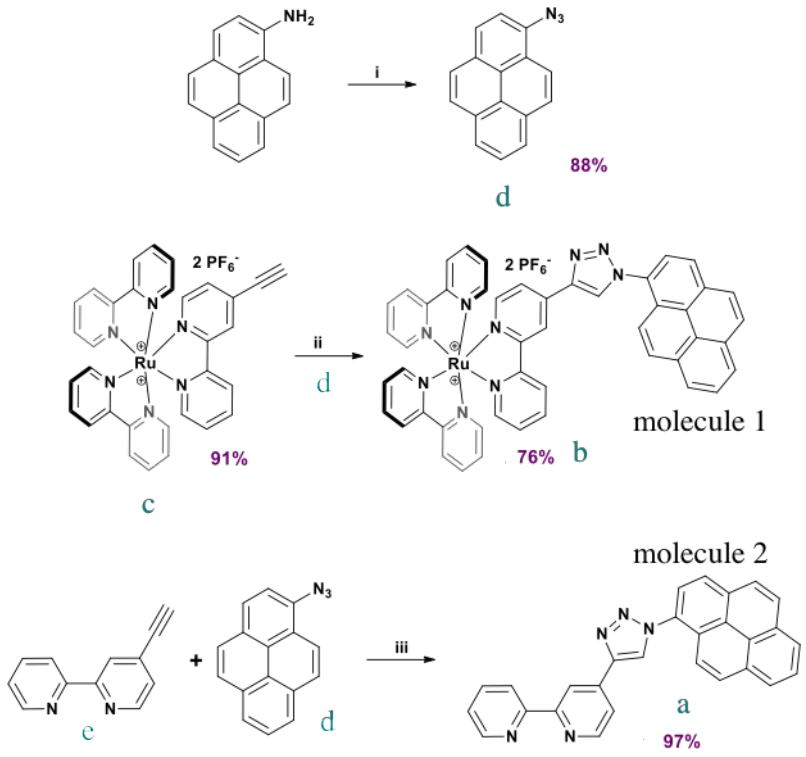


(i) $NaNO_2$, $NaN_3$, $HCl/H_2O$ (88%);d (ii) d, $CuSO4.5H_2O$, sodium ascorbate, $CH_2Cl_2/H_2O$ (1:1) (76%); (iii) CuI, $CH_2Cl_2/C2H5OH/H_2O$ (4:8:3) (97%). Ru-CCH (c) was synthesized according to the literature.

### 1-Azidopyrene (d)

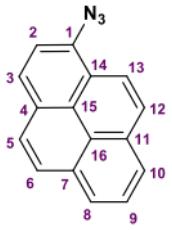


FIGURE D.1: $C_{16}H_9N_3$

To a mixture of 1-aminopyrene (0.44 g, 2.0 mmol, 1.0 eq.) in conc. hydrochloric acid (6.0 mL) and water (48.0 mL) was added sodium nitrite (0.41 g, 6.0 mmol, 3.0 eq) in $H_2O$ (20.0 mL) dropwise under vigorous stirring at 0°C. After 30 min sodium azide (0.78 g, 12.0 mmol, 6.0 eq.) in $H_2O$ (40 mL) was added dropwise to the reaction mixture at 0°C, then the reaction mixture was stirred for 20 min at 0°C. The grey suspension was extracted with $Et_2O$. The organic layers were washed with brine, dried over MgSO4, filtered and evaporated to yield 0.43 g (1.75 mmol, 88%) of 1-azidopyrene as a brown solid.
1H NMR (400 MHz, CDCl3) $\delta$: 8.28 (d, 1H, 3J 9.2 Hz, H-a); 8.16 (d, 1H, 3J 8.2 Hz, H-b); 8.15 (d, 1H, 3J 8.0 Hz, H-8 or H-10); 8.15 (d, 1H, 3J 7.3 Hz, H-8 or H-10); 8.06 (d, 1H, 3J 9.2 Hz, H-a'); 8.00 (br s, 2H, 2 H-c); 7.99 (dd, 1H, 3J 8.0, 3J 7.3 Hz, H-9); 7.81 (d, 1H, 3J 8.2 Hz, H-b').
13C NMR (100 MHz, CDCl3) $\delta$: 133.4, 131.7, 131.5, 128.6 (4 Cq); 127.8 (C-a'); 127.3, 127.0, 126.7 (C-9, 2 C-c); 125.8 (Cq); 125.7, 125.5, 125.3 (C-b, C-8, C-10); 124.7 (Cq); 122.8 (Cq); 121.7 (C-a); 115.7 (C-b').

### Molecule (b)

:

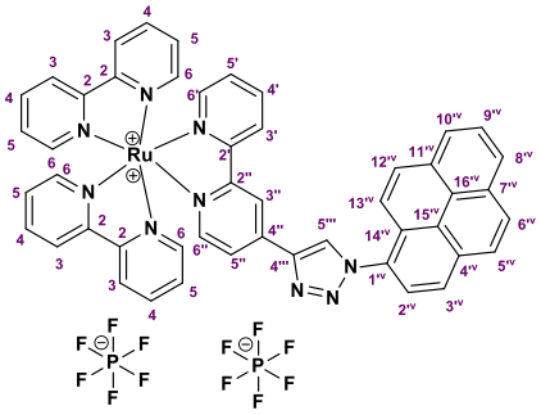


FIGURE D.2: $(C_{48}H_{33}F_{12}N_9P_2Ru)$(Bipyridine)2-(bipyridine-triazol-pyrene) ruthenium hexafluorophosphate (b)

Ru-CCH (3) (132.5 mg, 0.15 mmol, 1.0 eq.) was suspended in $CH_2Cl_2$ (7.5 mL) under an argon atmosphere. 1-Azidopyrene (4) (54.7 mg, 0.23 mmol, 1.5 eq.) was added, followed by the successive addition of water (7.5 mL), sodium ascorbate (13.4 mg, 0.07 mmol, 0.45 eq.) and copper sulfate pentahydrate (5.6 mg, 0.02 mmol, 0.15 eq.). After 20 hours of stirring at room temperature, a saturated aqueous solution of ammonium hexafluorophosphate was added and the reaction mixture was extracted with $CH_2Cl_2$. The organic layers were washed with a saturated aqueous solution of NaCl, and concentrated. The crude solid was dissolved in a minimum amount of $CH_2Cl_2$ and then filtered through an alumina plug. The excess of azido derivative was removed by washing with $CH_2Cl_2$, and the desired ruthenium complex (2) was recovered by washing with CH3CN and a solution of ammonium hexafluorophosphate in $CH_3OH$. The solvents were evaporated and the residue was dissolved in a minimum amount of $CH_2Cl_2$, then added drop wise at a large volume of pentane. The formed precipitate was filtered, washed several times with cold $H_2O$ and $Et_2O$ and dried under vacuum to yield 128.5 mg (0.11 mmol, 76%) of the desired hexafluorophosphate ruthenium complex (2) as an orange/red solid.

1H NMR (400 MHz, CD3CN) $\delta$: 9.08 (dd, 1H, 4J 1.9, 5J 0.4 Hz, H-3"); 9.03 (s, 1H, H-5"'); 8.71 (ddd, 1H, 3J 8.3, 4J 1.2, 5J 1.0 Hz, H-3'); 8.57-8.49 (m, 4H, 4 H-3); 8.46 (d, 1H, 3J 8.3 Hz, Hpyr-A); 8.43 (dd, 1H, 3J 7.7, 4J 0.8 Hz, H-8'v or H-10'v); 8.39 (dd, 1H, 3J 7.8, 4J 0.8 Hz, H-8'v or H-10'v); 8.34 (d, 1H, 3J 9.0 Hz, Hpyr-B); 8.29 (d, 1H, 3J 9.0 Hz, Hpyr-B'); 8.29 (d, 1H, 3J 9.4 Hz, Hpyr-C); 8.22 (d, 1H, 3J 8.3 Hz, Hpyr-A'); 8.19 (dd, 1H, 3J 7.8, 3J 7.7 Hz, H-9'v); 8.10 (ddd, 1H, 3J 8.3, 3J 8.0, 4J 1.4 Hz, H-4'); 8.12-8.05 (m, 4H, 4 H-4); 7.97 (dd, 1H, 3J 6.0, 4J 1.9 Hz, H-5"); 7.92 (d, 1H, 3J 9.4 Hz, Hpyr-C'); 7.90 (ddd, 1H, 3J 5.7, 4J 1.5, 5J 0.7 Hz, H-6); 7.83 (dd, 1H, 3J 6.0, 5J 0.4 Hz,H-6"); 7.82-7.75 (m, 4H, 3 H-6, H-6'); 7.47-7.39 (m, 5H, 4 H-5, H-5').

13C NMR (100 MHz, CD3CN) $\delta$: 159.1 (C-2"); 158.4 (4 C-2, C-2'); 155.5 (C-6"); 153.1 (4 C-6, C-6'); 144.8 (C-4"'); 141.1 (C-4"); 139.2 (4 C-4, C-4'); 134.0-132.6-132.0-131.4 (4 Cq-pyr); 131.3 (Cpyr-C); 130.6 (Cpyr-B); 129.1 (C-5'); 129.0 (4 C-5); 128.6 (C-5"'); 128.5 (C-9'v); 128.5 (Cpyr-B'); 128.2-127.7 (C-8'v, C-10'v); 127.3 (Cq-pyr); 126.5 (Cpyr-A); 126.1 (Cq-pyr); 125.9 (C-3'); 125.7 (4 C-3); 125.1 (Cq-pyr); 125.0 (Cpyr-A'); 124.5 (C-5"); 122.2 (Cpyr-C'); 121.5 (C-3"). MS ($ESI^+$): m/z 982.1 $[M^+PF6]^+$. HRMS ($ESI^+$): calculated for $C_{48}H_{33}F_6N_9PRu$ 982.1551, found 982.1522; calculated for $C_{48}H_{33}F_6N_9Ru$ 418.5952, found 418.5951.

**Molecule (a)**

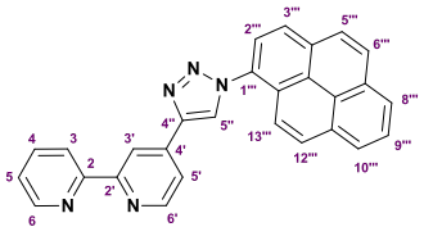

FIGURE D.3: ($C_{28}H_{17}N_5$) 4'-(1"-(pyren-1"'-yl)-1H-1",2",3"-triazol-4"-yl)-2,2'-bipyridine

To a suspension of 4'-ethynyl-2,2'-bipyridine (5) (76.8 mg, 0.43 mmol, 1.0 eq.) and 1-azidopyrene (4) (124.5 mg, 0.51 mmol, 1.2 eq.) in $CH_2Cl_2$/C2H5OH/$H_2O$ (4:7:3, 22.0 mL) was added CuI (113.7 mg, 0.60 mmol, 1.4 eq.). After 20 hours of stirring at room temperature, the reaction mixture was concentrated. The residue was suspended in a solution of aqueous HEDTA (50 mL) and vigorously stirred for 2h. The mixture was extensively extracted with $CH_2Cl_2$. The combined organic phases were washed with $H_2O$ and brine, then dried over MgSO4. The filtrate was concentrated and the crude residue was suspended in a minimum amount of $CH_2Cl_2$, then filtered through a silica plug. The excess of azido derivative was removed by washing with $CH_2Cl_2$, and the desired product (1) was recovered by washing with $CH_2Cl_2$/$CH_3OH$ (95:5). The solvents were evaporated and the residue was dried under vacuum to yield 176.1 mg (0.42 mmol, 97%) of 4'-(1"-(pyren-1"'-yl)-1H-1",2",3"-triazol-4"-yl)-2,2'-bipyridine (1) as a brown solid.

1H NMR (400 MHz, CDCl3) $\delta$: 8.82 (dd, 1H, 4J3',5' 1.8, 5J3',6' 0.6 Hz, H-3'); 8.82 (dd, 1H, 3J6',5' 5.1, 5J6',3' 0.6 Hz,H-6'); 8.68 (ddd, 1H, 3J6,5 4.8, 4J6,4 1.7, 5J6,3 0.9 Hz, H-6); 8.56 (s, 1H, H-5"); 8.47 (ddd, 1H, J3,4 8.1, 4J3,5 1.0, 5J3,6 0.9 Hz, H-3); 8.29 (dd, 1H, 3J 7.7, 4J 0.8 Hz, H-8"' or H-10"'); 8.28 (d, 1H, 3J 8.1 Hz, H-a); 8.25 (dd, 1H, 3J 7.9, 4J 0.8 Hz, H-8"' or H-10"'); 8.20 (d, 1H, 3J 9.0 Hz, H-b); 8.15 (d, 1H, 3J 9.3Hz, H-c); 8.14 (d, 1H, 3J 9.0 Hz, H-b'); 8.12 (dd, 1H, J5',6' 5.1, 4J3',5' 1.8 Hz, H-5'); 8.11 (dd, 1H, 3J 7.9, 3J 7.7 Hz, H-9"'); 8.08 (d, 1H, 3J 8.1 Hz, H-a'); 7.90 (d, 1H, 3J 9.3 Hz, H-c'); 7.84 (ddd, 1H, J3,4 8.1, J4,5 7.4, 4J4,6 1.7 Hz, H-4); 7.32 (ddd, 1H, J4,5 7.4, J5,6 4.8, 4J3,5 1.0 Hz, H-5).

13C NMR (100 MHz, CDCl3) $\delta$: 157.0 (C-2'); 156.0 (C-2); 150.4 (C-6'), 149.4 (C-6); 146.0 (C-4"); 139.1 (C-4'); 137.3 (C-4); 132.7, 131.3, 130.8 (3 Cq); 130.2 (C-b'); 130.2 (Cq); 129.4 (C-b); 127.2 (C-9"'); 127.1 (C-c); 126.8, 126.5 (C-8, C-10); 126.3, 125.3 (2 Cq); 125.0 (C-a); 124.8 (C-5"); 124.3 (Cq); 124.2 (C-5); 123.5 (C-a'); 121.5 (C-3); 121.1 (C-c'); 120.4 (C-5'); 117.7 (C-3'). MS ($ESI^+$): m/z 424.2 $[M+H]^+$. HRMS ($ESI^+$): calculated for C28H18N5 424.1557, found 424.1546.

**Molecule 1-ester) (g)**

:

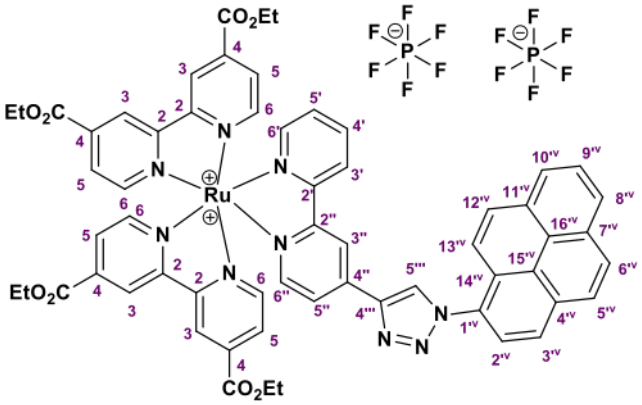

FIGURE D.4: ($C_{60}H_{49}F_{12}N_9O_8P_2Ru$) Diethyl [2,2'-bipyridine]-4,4'-dicarboxylate)2-(bipyridine-triazol-pyrene) ruthenium hexafluorophosphate

$Ru(CO2Et)_4$ − CCH (f) was synthesized by the same method as Ru-CCH (c). $Ru(CO2Et)_4$−CCH (f) (117.2 mg, 0.10 mmol, 1.0 eq.) was suspended in $CH_2Cl_2$ (5.0 mL) under an argon atmosphere. 1-Azidopyrene (d) (36.5 mg, 0.15 mmol, 1.5 eq.) were added, followed by successive addition of water (5.0 mL), sodium ascorbate (8.9 mg, 0.045 mmol, 0.45 eq.) and copper sulfate pentahydrate (3.7 mg, 0.015 mmol, 0.15 eq.). After 20 hours of stirring at room temperature, a saturated aqueous solution of ammonium hexafluorophosphate was added and the reaction mixture was extracted with $CH_2Cl_2$. The organic layers were washed with a saturated aqueous solution of NaCl, then concentrated. The crude solid was dissolved in a minimum amount of $CH_2Cl_2$ then filtered through an alumina plug. The excess of azido derivative was removed by washing with $CH_2Cl_2$, then the desired ruthenium complex (2-ester) was recovered by washing with CH3CN and a solution of ammonium hexafluorophosphate in $CH_3OH$. The solvents were evaporated. The residue was dissolved in a minimum amount of $CH_2Cl_2$, then added dropwise to a large volume of pentane. The formed precipitate was filtered, washed several times with cold $H_2O$ and $Et_2O$ and dried under vacuum to yield 71.5 mg (0.05 mmol, 51%) of the desired hexafluorophosphate ruthenium complex (g) as a brown solid.

1H NMR (400 MHz, CD3CN) $\delta$: 9.14-9.04 (m, 5H, 4 H-3, H-3"); 9.05 (s, 1H, H-5"'); 8.74 (ddd, 1H, 3J 8.1, 4J 1.1, 5J 0.7 Hz, H-3'); 8.46 (d, 1H, 3J 8.2 Hz, Hpyr-A); 8.44 (dd, 1H, 3J 7.6, 4J 0.8 Hz, H-8'v or H-10'v); 8.44 (dd, 1H, 3J 7.7, 4J 0.8 Hz, H-8'v or H-10'v); 8.35 (d, 1H, 3J 9.0 Hz, Hpyr-B); 8.30 (d, 1H, 3J 9.0 Hz, Hpyr-B'); 8.29 (d, 1H, 3J 9.3 Hz, Hpyr-C); 8.22 (d, 1H, 3J 8.2 Hz, Hpyr-A'); 8.19 (dd, 1H, 3J 7.7, 3J 7.6 Hz, H-9'v); 8.16 (ddd, 1H, 3J 8.1, 3J 7.7, 4J 1.4 Hz, H-4'); 8.10 (d, 1H, 3J 5.9 Hz, H-6a); 7.99 (d, 1H, 3J 5.7 Hz, H-6b); 7.98(dd, 1H, 3J 6.0, 4J 1.8 Hz, H-5"); 7.94 (d, 1H, 3J 6.0 Hz, H-6c); 7.93 (d, 1H, 3J 5.8 Hz, H-6d); 7.92 (d, 1H, 3J 9.3 Hz, Hpyr-C'); 7.90 (dd, 1H, 3J 6.0, 4J

1.7 Hz, H-5c); 7.90 (dd, 1H, 3J 5.7, 4J 1.6 Hz, H-5b); 7.84 (dd, 1H, 3J 5.8, 4J 1.8 Hz, H-5d); 7.83 (dd, 1H, 3J 5.9, 4J 1.7 Hz, H-5a); 7.76 (d, 1H, 3J 6.0 Hz, H-6"); 7.71 (ddd, 1H, 3J 5.5, 4J 1.4, 5J 0.7 Hz, H-6'); 7.46 (ddd, 1H, 3J 7.7, 3J 5.5, 4J 1.1 Hz, H-5'); 4.48-4.47 (2q, 8H, 3J 7.1 Hz, 4 OCH2); 1.42 (2t, 12H, 3J 7.1 Hz, 4 CH3).

13C NMR (100 MHz, CD3CN) $\delta$: 164.8 (4 C=O); 159.0-158.6 (4 C-2, C-2"); 157.9 (C-2'); 154.5-154.3 (4 C-6); 153.7 (C-6"); 153.3 (C-6'); 144.7 (C-4"'); 142.0 (C-4"); 140.8 (4 C-4); 140.2 (C-4'); 134.1, 132.6 (2 Cq-pyr); 131.3 (Cpyr-C); 131.3, 131.1 (2 Cq-pyr); 130.7 (Cpyr-B); 129.5 (C-5'); 128.8 (C-5"'); 128.6 (C-9'v); 128.5 (Cpyr-B'); 128.2 (Cq-pyr); 128.1-128.0 (4 C-5); 127.8, 127.3 (C-8'v, C-10'v); 126.5 (Cpyr-A); 126.2 (C-3'); 126.1 (Cq-pyr); 125.3 (4 C-3); 125.2 (Cq-pyr); 125.0 (Cpyr-A'); 124.7 (C-5"); 122.2 (Cpyr-C'); 121.8 (C-3"); 64.2 (4 CH2); 14.8 (4 CH3). MS ($ESI^+$): m/z 1270.2 $[M + PF6]^+$. HRMS ($ESI^+$): calculated for $C_{60}H_{49}F_6N_9O_8PRu$ 1270.2400, found 1270.2413.

## D.2 theoretical calculation

Restricted (for singlet states) and Unrestricted (for triplet states) DFT calculations were performed using CAM-B3LYP functional and double-zeta SDDALL basis set for all atoms. Geometry optimization have been performed for both the singlet and triplet states of both the isolated pyrene-triazol unit and pyrene-triazol unit deposited on the nanotube. The reported energies are given for the singlet geometry as the system would not have time to relax. However, calculations using the triplet geometry of the pyrene-triazol unit have also been performed in order to check that the proposed interpretation would not be affected by the geometrical changes.

| | | | | | | |
|---|---|---|---|---|---|---|
| Length | 33.24 | 28.32 | 25.86 | 23.39 | 18.47 | 13.56 |
| HOMO | -4.37 | -4.31 | -4.59 | -4.58 | -4.79 | -4.78 |
| LUMO | -3.47 | -3.48 | -3.21 | -2.40 | -2.89 | -2.72 |
| Gap | 0.90 | 0.83 | 1.37 | 2.18 | 1.90 | 2.06 |

TABLE D.1: Energy (in eV) of the HOMO and LUMO orbitals of nanotubes of various lengths.

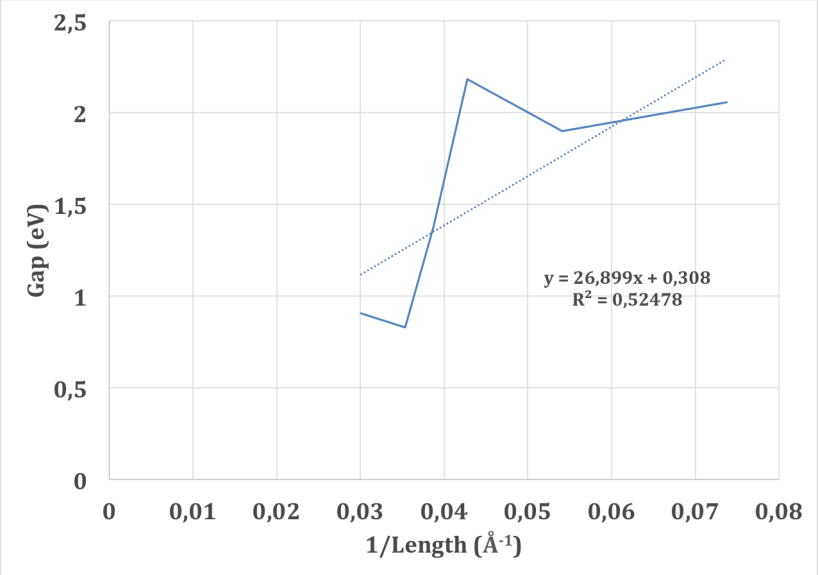


FIGURE D.5: Energy gap between the HOMO and LUMO orbitals in nanotubes of various lengths (L) as function of 1/L and linear regression of the calculated points. The extrapolation to 0, i.e. to an infinite length gives a roughly evaluated gap of 0.308 eV.

# Résumé de la thèse

En raison de leurs propriétés optiques et électroniques exceptionnelles, les nanotubes de carbone ont été à l'avant garde dans le domaine de l'électronique moléculaire au cours des deux dernières décennies. Cependant leurs intégrations dans des dispositifs efficaces pour des applications en nanoélectronique ou en capteurs représentent encore aujourd'hui un défi pour la communauté scientifique. Ceci est principalement dû à la relation complexe entre les propriétés physiques des nanotubes et leurs structures, à savoir leurs angles chiraux et leurs diamètres. Le contrôle des propriétés structurelles des nanotubes de carbone pendant le processus de croissance fait donc partie des éléments clés de la progression dans ce domaine. D'après les différentes recherches publiées dans la littérature, nous pouvons voir que le contrôle de la morphologie du catalyseur, de sa composition chimique ainsi qu'un fin contrôle des paramètres physiques de la croissance (température, pression, précurseur carboné...) représentent les pistes les plus prometteuses pour réaliser des synthèses sélectives.

Nous avons donc dans un premier temps, mis en place et développé une nouvelle méthode de synthèse basée sur la chimie de coordination. Celle-ci permet de jouer sur la composition chimique de catalyseurs bimétalliques sans faire varier leur taille, avec un processus de synthèse de nanotube générique. Le principe général de cette synthèse est basé sur l'utilisation comme précurseur des analogues de bleu de Prusse bimétalliques (ABP) dont la stœchiométrie est parfaitement contrôlée. Ces analogues de bleu de Prusse vont être réduits insitu dans le réacteur de dépôt chimique en phase vapeur (CVD) afin de former le catalyseur actif souhaité. Des analyses de microscopie électronique en transmission couplées à des analyses dispersives en énergie ainsi que de la spectroscopie de photoélectrons X ont été utilisées pour suivre la taille et la composition chimique des catalyseurs au cours des différentes étapes de synthèse. La preuve de concept de cette synthèse de nanotubes est détaillée dans cette thèse pour trois compositions différentes de catalyseurs : Fer-Ruthénium, Cobalt-Ruthénium et Nickel-Ruthénium.

Nous avons ensuite analysé l'influence de la composition chimique des catalyseurs et de la température de synthèse sur la croissance des nanotubes par CVD, afin de mieux comprendre les mécanismes mis en jeu lors de la synthèse. Les nanotubes ont principalement été caractérisés par spectroscopie Raman et microscopies électroniques. En fonction de ces deux paramètres nous avons pu observé des différences significatives en terme de distribution de diamètre, de distribution des propriétés électroniques et en terme de rendement. Un mécanisme basé sur des différences de solubilité est proposé pour expliquer les différents résultats obtenus.

Après caractérisation des nanotubes synthétisés, nous avons réalisé et caractérisé des transistors à partir des nanotubes de carbone obtenus et nous avons comparé leurs performances en fonction des propriétés des nanotubes utilisés. Ces mesures nous ont permis de confirmer les observations faites en spectroscopie Raman, notamment en ce qui concerne les différences de propriétés électroniques. Lorsque les conditions de synthèses des nanotubes sont adéquates, les transistors présentent des ratios Ion/Ioff allant jusqu'à 8 ordres de grandeurs. Une rapide étude sur la détection de vapeur de $NO_2$ à l'aide des meilleurs transistors est aussi présentée.

Enfin dans une dernière partie, nous avons fonctionnalisé des nanotubes de carbone avec un complexe inorganique photo-actif de ruthénium. La fonctionnalisation non covalente des nanotubes intégrés à ces transistors nous a permis de moduler par simple impulsion lumineuse la conductivité circulant dans le nanotube sur plus de trois ordres de grandeur. En croisant les résultats expérimentaux à une étude théorique, nous avons proposé un mécanisme pour l'interaction nanotube/molécule sous lumière, celui-ci est basé sur des transferts d'énergie successifs du ruthénium jusqu'au nanotube.

# Bibliography

[1] H. W. Kroto, J. R. Heath, S. C. O'Brien, R. F. Curl, and R. E. Smalley, "C 60: buckminsterfullerene," *Nature*, vol. 318, p. 162, 1985.

[2] S. Iijima, "Helical microtubules of graphitic carbon," *Nature*, vol. 354, pp. 56–58, nov 1991.

[3] L. V. Radushkevich LV, "O strukture ugleroda, obrazujucegosja pri termiceskom razlozenii okisi ugleroda na zeleznom kontakte," 1952.

[4] A. Oberlin, M. Endo, and T. Koyama, "Filamentous growth of carbon through benzene decomposition," *Journal of Crystal Growth*, vol. 32, no. 3, pp. 335–349, 1976.

[5] S. Iijima and T. Ichihashi, "Single-shell carbon nanotubes of 1-nm diameter.," *Nature*, vol. 363, pp. 603–605, 1993.

[6] D. S. Bethune, C. H. Klang, M. S. de Vries, G. Gorman, R. Savoy, J. Vazquez, and R. Beyers, "Cobalt-catalysed growth of carbon nanotubes with single-atomic-layer walls," *Nature*, vol. 363, pp. 605–607, jun 1993.

[7] R. Vidu, M. Rahman, M. Mahmoudi, M. Enachescu, T. D. Poteca, and I. Opris, "Nanostructures: a platform for brain repair and augmentation," *Frontiers in Systems Neuroscience*, vol. 8, pp. 1–24, jun 2014.

[8] J. Prasek, J. Drbohlavova, J. Chomoucka, J. Hubalek, O. Jasek, V. Adam, and R. Kizek, "Methods for carbon nanotubes synthesis," *Journal of Materials Chemistry*, vol. 21, no. 40, p. 15872, 2011.

[9] M. Dresselhaus, G. Dresselhaus, R. Saito, and A. Jorio, "Raman spectroscopy of carbon nanotubes," *Physics Reports*, vol. 409, pp. 47–99, mar 2005.

[10] P. R. Wallace, "The band theory of graphite," *Physical Review*, vol. 71, no. 9, pp. 622–634, 1947.

[11] J. C. Charlier, X. Blase, and S. Roche, "Electronic and transport properties of nanotubes," *Reviews of Modern Physics*, vol. 79, no. 2, pp. 677–732, 2007.

[12] T. Ando, "The electronic properties of graphene and carbon nanotubes," *NPG Asia Mater.*, vol. 1, pp. 17–21, 2009.

[13] S. Reich, J. Maultzsch, C. Thomsen, and P. Ordejón, "Tight-binding description of graphene," *Physical Review B*, vol. 66, p. 035412, jul 2002.

[14] "http://www.photon.t.u-tokyo.ac.jp/~maruyama/kataura/1D_DOS.html."

[15] Y. Murakami, E. Einarsson, T. Edamura, and S. Maruyama, "Polarization Dependence of the Optical Absorption of Single-Walled Carbon Nanotubes," *Physical Review Letters*, vol. 94, p. 087402, mar 2005.

[16] J. Lefebvre, J. M. Fraser, P. Finnie, and Y. Homma, "Photoluminescence from an individual single-walled carbon nanotube," *Physical Review B*, vol. 69, no. 7, pp. 1–5, 2004.

[17] R. Saito, G. Dresselhaus, and M. Dresselhaus, "Trigonal warping effect of carbon nanotubes," *Physical Review B*, vol. 61, no. 4, pp. 2981–2990, 2000.

[18] A. G. Souza, A. Jorio, G. G. Samsonidze, G. Dresselhaus, M. S. Dresselhaus, A. K. Swan, M. S. Unlu, B. B. Goldberg, R. Saito, J. H. Hafner, C. M. Lieber, and M. A. Pimenta, "Probing the electronic trigonal warping effect in individual single-wall carbon nanotubes using phonon spectra," *Chemical Physics Letters*, vol. 354, no. 1-2, pp. 62–68, 2002.

[19] M. Y. Sfeir, "Optical Spectroscopy of Individual Single-Walled Carbon Nanotubes of Defined Chiral Structure," *Science*, vol. 312, pp. 554–556, apr 2006.

[20] T. Ando, "Excitons in Carbon Nanotubes," *Journal of the Physical Society of Japan*, vol. 66, pp. 1066–1073, apr 1997.

[21] C. L. Kane and E. J. Mele, "Ratio problem in single carbon nanotube fluorescence spectroscopy.," *Physical review letters*, vol. 90, no. 20, p. 207401, 2003.

[22] V. N. Popov, "Curvature effects on the structural, electronic and optical properties of isolated single-walled carbon nanotubes within a symmetry-adapted non-orthogonal tight-binding model," *New Journal of Physics*, vol. 6, no. February 2004, 2004.

[23] D. Porezag, T. Frauenheim, T. Köhler, G. Seifert, and R. Kaschner, "Construction of tight-binding-like potentials on the basis of density-functional theory: Application to carbon," *Physical Review B*, vol. 51, no. 19, pp. 12947–12957, 1995.

[24] H. Kataura, Y. Kumazawa, Y. Maniwa, I. Umezu, S. Suzuki, Y. Ohtsuka, and Y. Achiba, "Optical properties of single-wall carbon nanotubes," *Synthetic Metals*, vol. 103, pp. 2555–2558, jun 1999.

[25] K. Sato, R. Saito, J. Jiang, G. Dresselhaus, and M. S. Dresselhaus, "Discontinuity in the family pattern of single-wall carbon nanotubes," *Physical Review B*, vol. 76, p. 195446, nov 2007.

[26] A. R. T. Nugraha, R. Saito, K. Sato, P. T. Araujo, A. Jorio, and M. S. Dresselhaus, "Dielectric constant model for environmental effects on the exciton energies of single wall carbon nanotubes," *Applied Physics Letters*, vol. 97, no. 9, p. 091905, 2010.

[27] T. W. Ebbesen, "Carbon Nanotubes," *Annual Review of Materials Science*, vol. 24, no. 1, pp. 235–64, 1994.

[28] Y. Ando, "The Preparation of Carbon Nanotubes," *Fullerene Science and Technology*, vol. 2, no. 2, pp. 173–180, 1994.

[29] Y. Saito, K. Nishikubo, K. Kawabata, and T. Matsumoto, "Carbon nanocapsules and single-layered nanotubes produced with platinum-group metals (Ru, Rh, Pd, Os, Ir, Pt) by arc discharge," *Journal of Applied Physics*, vol. 80, no. 5, p. 3062, 1996.

[30] A. Thess, R. Lee, P. Nikolaev, H. Dai, P. Petit, J. Robert, C. Xu, Y. H. Lee, S. G. Kim, A. G. Rinzler, D. T. Colbert, G. E. Scuseria, D. Tomanek, J. E. Fischer, and R. E. Smalley, "Crystalline ropes of metallic carbon nanotubes.," *Science*, vol. 273, pp. 483–487, jul 1996.

[31] T. Guo, P. Nikolaev, A. G. Rinzler, D. Tomanek, D. T. Colbert, and R. E. Smalley, "Self-Assembly of Tubular Fullerenes," *The Journal of Physical Chemistry*, vol. 99, no. 27, pp. 10694–10697, 1995.

[32] T. Guo, P. Nikolaev, A. Thess, D. T. Colbert, and R. E. Smalley, "Catalytic growth of single-walled nanotubes by laser vaporization.," *Chemical Physics Letters*, vol. 243, pp. 49–54, 1995.

[33] R. Sen, Y. Ohtsuka, T. Ishigaki, D. Kasuya, S. Suzuki, H. Kataura, and Y. Achiba, "Time period for the growth of single-wall carbon nanotubes in the laser ablation process: evidence from gas dynamic studies and time resolved imaging," *Chemical Physics Letters*, vol. 332, no. 5-6, pp. 467–473, 2000.

[34] M. Yudasaka, Y. Kasuya, F. Kokai, K. Takahashi, M. Takizawa, S. Bandow, and S. Iijima, "Causes of different catalytic activities of metals in formation of single-wall carbon nanotubes," *Applied Physics A: Materials Science and Processing*, vol. 74, no. 3, pp. 377–385, 2002.

[35] S. Bandow, S. Asaka, Y. Saito, a. Rao, L. Grigorian, E. Richter, and P. Eklund, "Effect of the Growth Temperature on the Diameter Distribution and Chirality of Single-Wall Carbon Nanotubes," *Physical Review Letters*, vol. 80, pp. 3779–3782, 1998.

[36] H. Kataura, Y. Kumazawa, Y. Maniwa, Y. Ohtsuka, R. Sen, S. Suzuki, and Y. Achiba, "Diameter control of single-walled carbon nanotubes," *Carbon*, vol. 38, no. 11, pp. 1691–1697, 2000.

[37] O. Jost, A. A. Gorbunov, W. Pompe, T. Pichler, R. Friedlein, M. Knupfer, M. Reibold, H.-D. Bauer, L. Dunsch, M. S. Golden, and J. Fink, "Diameter grouping in bulk samples of single-walled carbon nanotubes from optical absorption spectroscopy," *Applied Physics Letters*, vol. 75, no. 15, p. 2217, 1999.

[38] Y. Ando, X. Zhao, T. Sugai, and M. Kumar, "Growing carbon nanotubes," *Materials Today*, vol. 7, pp. 22–29, oct 2004.

[39] C. Journet, M. Picher, and V. Jourdain, "Carbon nanotube synthesis: from large-scale production to atom-by-atom growth," *Nanotechnology*, vol. 23, no. 14, p. 142001, 2012.

[40] S. Hofmann, C. Ducati, J. Robertson, and B. Kleinsorge, "Low-temperature growth of carbon nanotubes by plasma-enhanced chemical vapor deposition," *Applied Physics Letters*, vol. 83, no. 1, pp. 135–137, 2003.

[41] D. Varshney, B. R. Weiner, and G. Morell, "Growth and field emission study of a monolithic carbon nanotube/diamond composite," *Carbon*, vol. 48, no. 12, pp. 3353–3358, 2010.

[42] B. C. Satishkumar, A. Govindaraj, R. Sen, and C. N. R. Rao, "Single-walled nanotubes by the pyrolysis of acetylene-organometallic mixtures," *Chemical Physics Letters*, vol. 293, no. 1-2, pp. 47–52, 1998.

[43] K. Bladh, L. Falk, and F. Rohmund, "On the iron-catalysed growth of single-walled carbon nanotubes and encapsulated metal particles in the gas phase," *Applied Physics A: Materials Science & Processing*, vol. 70, no. 3, pp. 317–322, 2000.

[44] A. G. Nasibulin, A. Moisala, D. P. Brown, and E. I. Kauppinen, "Carbon nanotubes and onions from carbon monoxide using Ni(acac)2 and Cu(acac)2 as catalyst precursors," *Carbon*, vol. 41, no. 14, pp. 2711–2724, 2003.

[45] P. Nikolaev, M. J. Bronikowski, R. K. Bradley, F. Rohmund, D. T. Colbert, K. a. Smith, and R. E. Smalley, "Gas-phase catalytic growth of single-walled carbon nanotubes from carbon monoxide," *Chemical Physics Letters*, vol. 313, no. 1-2, pp. 91–97, 1999.

[46] D. Takagi, Y. Homma, H. Hibino, S. Suzuki, and Y. Kobayashi, "Single-walled carbon nanotube growth from highly activated metal nanoparticles," *Nano Letters*, vol. 6, no. 12, pp. 2642–2645, 2006.

[47] Y. Qian, B. Huang, F. Gao, C. Wang, and G. Ren, "Preferential Growth of Semiconducting Single-Walled Carbon Nanotubes on Substrate by Europium Oxide," *Nanoscale Research Letters*, vol. 5, no. 10, pp. 1578–1584, 2010.

[48] B. Liu, W. Ren, L. Gao, S. Li, Q. Liu, C. Jiang, and H.-m. Cheng, "Manganese-Catalyzed Surface Growth of Single-Walled Carbon Nanotubes with High Efficiency," *Journal of Physical Chemistry C*, vol. 112, pp. 19231–19235, 2008.

[49] D. Yuan, L. Ding, H. Chu, Y. Feng, T. P. McNicholas, and J. Liu, "Horizontally aligned single-walled carbon nanotube on quartz from a large variety of metal catalysts," *Nano Letters*, vol. 8, no. 8, pp. 2576–2579, 2008.

[50] D. Takagi, H. Hibino, S. Suzuki, Y. Kobayashi, and Y. Homma, "Carbon Nanotube Growth from Semiconductor Nanoparticles," *Nano Letters*, vol. 7, no. 8, pp. 2272–2275, 2007.

[51] M. Swierczewska, I. Rusakova, and B. Sitharaman, "Gadolinium and europium catalyzed growth of single-walled carbon nanotubes," *Carbon*, vol. 47, no. 13, pp. 3139–3142, 2009.

[52] D. E. Resasco, J. E. Herrera, and L. Balzano, "Decomposition of carbon-containing compounds on solid catalysts for single-walled nanotube production.," *Journal of nanoscience and nanotechnology*, vol. 4, no. 4, pp. 398–407, 2004.

[53] V. Jourdain and C. Bichara, "Current understanding of the growth of carbon nanotubes in catalytic chemical vapour deposition," *Carbon*, vol. 58, pp. 2–39, 2013.

[54] R. S. Wagner and W. C. Ellis, "Vapor-liquid-solid mechanism of single crystal growth," *Applied Physics Letters*, vol. 4, no. 5, pp. 89–90, 1964.

[55] R. T. K. Baker, M. A. Barber, P. S. Harris, F. S. Feates, and R. J. Waite, "Nucleation and growth of carbon deposits from the nickel catalyzed decomposition of acetylene," *Journal of Catalysis*, vol. 26, no. 1, pp. 51–62, 1972.

[56] J.-p. Tessonnier and D. S. Su, "Recent Progress on the Growth Mechanism of Carbon Nanotubes: A Review," *ChemSusChem*, vol. 4, pp. 824–847, jul 2011.

[57] M. Picher, P. A. Lin, J. L. Gomez-Ballesteros, P. B. Balbuena, and R. Sharma, "Nucleation of graphene and its conversion to single-walled carbon nanotubes," *Nano Letters*, vol. 14, no. 11, pp. 6104–6108, 2014.

[58] H. Dai, A. G. Rinzler, P. Nikolaev, A. Thess, D. T. Colbert, and R. E. Smalley, "Single-wall nanotubes produced by metal-catalyzed disproportionation of carbon monoxide," *Chemical Physics Letters*, vol. 260, no. 3-4, pp. 471–475, 1996.

[59] Y. Shibuta and S. Maruyama, "Molecular dynamics simulation of formation process of single-walled carbon nanotubes by CCVD method," *Chemical Physics Letters*, vol. 382, pp. 381–386, dec 2003.

[60] H. Amara, C. Bichara, and F. Ducastelle, "Understanding the nucleation mechanisms of carbon nanotubes in catalytic chemical vapor deposition," *Physical Review Letters*, vol. 100, no. 5, pp. 23–27, 2008.

[61] J. Zhao, a. Martinez-Limia, and P. B. Balbuena, "Understanding catalysed growth of single-wall carbon nanotubes.," *Nanotechnology*, vol. 16, no. 7, pp. S575–81, 2005.

[62] A. M. Cassell, J. A. Raymakers, J. Kong, and H. Dai, "Large scale CVD synthesis of single-walled carbon nanotubes," *The Journal of Physical Chemistry B*, vol. 103, no. 31, pp. 6484–6492, 1999.

[63] L. Ma, X. Dong, M. Chen, L. Zhu, C. Wang, F. Yang, and Y. Dong, "Fabrication and Water Treatment Application of Carbon Nanotubes ( CNTs ) -Based Composite Membranes : A Review," *Membranes*, vol. 7, 2017.

[64] S. Hofmann, R. Blume, C. T. Wirth, M. Cantoro, R. Sharma, C. Ducati, M. Hävecker, S. Zafeiratos, P. Schnoerch, A. Oestereich, D. Teschner, M. Albrecht, A. Knop-Gericke, R. Schlögl, and J. Robertson, "State of transition metal catalysts during carbon nanotube growth," *Journal of Physical Chemistry C*, vol. 113, no. 5, pp. 1648–1656, 2009.

[65] S. Esconjauregui, C. M. Whelan, and K. Maex, "The reasons why metals catalyze the nucleation and growth of carbon nanotubes and other carbon nanomorphologies," *Carbon*, vol. 47, no. 3, pp. 659–669, 2009.

[66] C. Wirth, S. Hofmann, and J. Robertson, "State of the catalyst during carbon nanotube growth," *Diamond and Related Materials*, vol. 18, pp. 940–945, may 2009.

[67] Z. He, J.-l. Maurice, A. Gohier, C. S. Lee, D. Pribat, and C. S. Cojocaru, "Iron Catalysts for the Growth of Carbon Nanofibers: Fe, Fe 3 C or Both?," *Chemistry of Materials*, vol. 23, pp. 5379–5387, dec 2011.

[68] C. T. C. Wirth, B. C. B. Bayer, A. A. D. Gamalski, S. Esconjauregui, R. S. Weatherup, C. Ducati, C. Baehtz, J. Robertson, and S. Hofmann, "The Phase of Iron Catalyst Nanoparticles during Carbon Nanotube Growth," *Chemistry of Materials*, vol. 24, pp. 4633–4640, dec 2012.

[69] S. Hofmann, R. Sharma, C. Ducati, G. Du, C. Mattevi, C. Cepek, M. Cantoro, S. Pisana, A. Parvez, F. Cervantes-Sodi, A. C. Ferrari, R. Dunin-Borkowski, S. Lizzit, L. Petaccia, A. Goldoni, and J. Robertson, "In situ observations of catalyst dynamics during surface-bound carbon nanotube nucleation," *Nano Letters*, vol. 7, no. 3, pp. 602–608, 2007.

[70] H. Yoshida, T. Shimizu, T. Uchiyama, H. Kohno, Y. Homma, and S. Takeda, "Atomic-scale analysis on the role of molybdenum in iron-catalyzed carbon nanotube growth," *Nano Letters*, vol. 9, no. 11, pp. 3810–3815, 2009.

[71] M. He, H. Jiang, B. Liu, P. V. Fedotov, A. I. Chernov, E. D. Obraztsova, F. Cavalca, J. B. Wagner, T. W. Hansen, I. V. Anoshkin, E. A. Obraztsova, A. V. Belkin, E. Sairanen, A. G. Nasibulin, J. Lehtonen, and E. I. Kauppinen, "Chiral-Selective Growth of Single-Walled Carbon Nanotubes on Lattice-Mismatched Epitaxial Cobalt Nanoparticles," *Scientific Reports*, vol. 3, p. 1460, dec 2013.

[72] M. He, B. Liu, A. I. Chernov, E. D. Obraztsova, I. Kauppi, H. Jiang, I. Anoshkin, F. Cavalca, T. W. Hansen, J. B. Wagner, A. G. Nasibulin, E. I. Kauppinen, J. Linnekoski, M. Niemelä, and J. Lehtonen, "Growth mechanism of single-walled carbon nanotubes on iron-copper catalyst and chirality studies by electron diffraction," *Chemistry of Materials*, vol. 24, no. 10, pp. 1796–1801, 2012.

[73] L. Zhang, M. He, T. W. Hansen, J. Kling, H. Jiang, E. I. Kauppinen, A. Loiseau, and J. B. Wagner, "Growth Termination and Multiple Nucleation of Single-Wall Carbon Nanotubes Evidenced by in Situ Transmission Electron Microscopy," *ACS Nano*, p. acsnano.6b05941, 2017.

[74] M. C. Hersam, "Progress towards monodisperse single-walled carbon nanotubes," *Nature Nanotechnology*, vol. 3, pp. 387–394, jul 2008.

[75] B. S. Flavel, M. M. Kappes, R. Krupke, and F. Hennrich, "Separation of Single-Walled Carbon Nanotubes by 1-Dodecanol-Mediated Size-Exclusion Chromatography," *ACS Nano*, vol. 7, pp. 3557–3564, apr 2013.

[76] X. Tu, S. Manohar, A. Jagota, and M. Zheng, "DNA sequence motifs for structure-specific recognition and separation of carbon nanotubes," *Nature*, vol. 460, pp. 250–253, jul 2009.

[77] H. Liu, D. Nishide, T. Tanaka, and H. Kataura, "Large-scale single-chirality separation of single-wall carbon nanotubes by simple gel chromatography," *Nature Communications*, vol. 2, p. 309, may 2011.

[78] M. S. Arnold, A. A. Green, J. F. Hulvat, S. I. Stupp, and M. C. Hersam, "Sorting carbon nanotubes by electronic structure using density differentiation," *Nature Nanotechnology*, vol. 1, p. 60, oct 2006.

[79] F. M. Chen, B. Wang, Y. Chen, and L. J. Li, "Toward the extraction of single species of sinale-walled carbon nanotubes using fluorene-based polymers," *Nano Letters*, vol. 7, no. 10, pp. 3013–3017, 2007.

[80] M.-F. C. Fiawoo, A.-M. Bonnot, H. Amara, C. Bichara, J. Thibault-Pénisson, and A. Loiseau, "Evidence of Correlation between Catalyst Particles and the Single-Wall Carbon Nanotube Diameter: A First Step towards Chirality Control," *Physical Review Letters*, vol. 108, p. 195503, may 2012.

[81] W. L. Wang, X. D. X. Bai, Z. Xu, S. Liu, and E. G. E. Wang, "Low temperature growth of single-walled carbon nanotubes: Small diameters with narrow distribution," *Chemical Physics Letters*, vol. 419, pp. 81–85, feb 2006.

[82] K. Tanioku, T. Maruyama, and S. Naritsuka, "Low temperature growth of carbon nanotubes on Si substrates in high vacuum," *Diamond and Related Materials*, vol. 17, pp. 589–593, apr 2008.

[83] N. Li, X. Wang, F. Ren, G. L. Haller, and L. D. Pfefferle, "Diameter tuning of single-walled carbon nanotubes with reaction temperature using a CO monometallic catalyst," *Journal of Physical Chemistry C*, vol. 113, no. 23, pp. 10070–10078, 2009.

[84] C. Z. Loebick, R. Podila, J. Reppert, J. Chudow, F. Ren, G. L. Haller, A. M. Rao, and L. D. Pfefferle, "Selective Synthesis of Subnanometer Diameter Semiconducting Single-Walled Carbon Nanotubes," *Journal of the American Chemical Society*, vol. 132, no. 14, pp. 11125–11131, 2010.

[85] M. S. A. He, A. I. Chernov, E. D. Obraztsova, J. Sainio, E. Rikkinen, H. Jiang, Z. Zhu, A. Kaskela, A. G. Nasibulin, E. I. Kauppinen, M. Niemela, and O. Krause, "Low temperature growth of SWNTs on a nickel catalyst by thermal chemical vapor deposition," *Nano Research*, vol. 4, no. 4, pp. 334–342, 2011.

[86] K. Cui, A. Kumamoto, R. Xiang, H. An, B. Wang, T. Inoue, S. Chiashi, Y. Ikuhara, and S. Maruyama, "Synthesis of subnanometer-diameter vertically aligned single-walled carbon nanotubes with copper-anchored cobalt catalysts," *Nanoscale*, vol. 8, no. 3, pp. 1608–1617, 2016.

[87] F. Zhang, P.-X. Hou, C. Liu, B.-W. Wang, H. Jiang, M.-L. Chen, D.-M. Sun, J.-C. Li, H.-T. Cong, E. I. Kauppinen, and H.-M. Cheng, "Growth of semiconducting single-wall carbon nanotubes with a narrow band-gap distribution.," *Nature communications*, vol. 7, p. 11160, 2016.

[88] B. Hou, C. Wu, T. Inoue, S. Chiashi, R. Xiang, and S. Maruyama, "Extended alcohol catalytic chemical vapor deposition for efficient growth of single-walled carbon nanotubes thinner than (6,5)," *Carbon*, vol. 119, pp. 502–510, 2017.

[89] P. W. Voorhees, "The theory of Ostwald ripening," *Journal of Statistical Physics*, vol. 38, no. 1-2, pp. 231–252, 1985.

[90] M. Picher, E. Anglaret, R. Arenal, and V. Jourdain, "Self-deactivation of single-walled carbon nanotube growth studied by in situ Raman measurements.," *Nano letters*, vol. 9, no. 2, pp. 542–7, 2009.

[91] C. Lu and J. Liu, "Controlling the Diameter of Carbon Nanotubes in Chemical Vapor Deposition Method by Carbon Feeding," *Journal of Physical Chemistry B*, vol. 110, pp. 20254–20257, oct 2006.

[92] B. Wang, L. Wei, L. Yao, L.-j. Li, Y. Yang, and Y. Chen, "Pressure-Induced Single-Walled Carbon Nanotube ( n,m ) Selectivity on CoMo Catalysts," *The Journal of Physical Chemistry C*, vol. 111, pp. 14612–14616, oct 2007.

[93] T. Saito, S. Ohshima, T. Okazaki, S. Ohmori, M. Yumura, and S. Iijima, "Selective Diameter Control of Single-Walled Carbon Nanotubes in the Gas-Phase Synthesis," *Journal of Nanoscience and Nanotechnology*, vol. 8, pp. 6153–6157, nov 2008.

[94] G. Lolli, L. Zhang, L. Balzano, N. Sakulchaicharoen, Y. Tan, and D. E. Resasco, "Tailoring (n,m) structure of single-walled carbon nanotubes by modifying reaction conditions and the nature of the support of CoMo catalysts," *Journal of Physical Chemistry B*, vol. 110, no. 5, pp. 2108–2115, 2006.

[95] M. He, H. Jiang, E. I. Kauppinen, and J. Lehtonen, "Diameter and chiral angle distribution dependencies on the carbon precursors in surface-grown single-walled carbon nanotubes," *Nanoscale*, vol. 4, no. 7394, pp. 7394–7398, 2012.

[96] D. A. Tsyboulski, J. D. R. Rocha, S. M. Bachilo, L. Cognet, and R. B. Weisman, "Structure-dependent fluorescence efficiencies of individual single-walled carbon nanotubes," *Nano Letters*, vol. 7, no. 10, pp. 3080–3085, 2007.

[97] R. Arenal, P. Löthman, M. Picher, T. Than, M. Paillet, and V. Jourdain, "Direct Evidence of Atomic Structure Conservation Along Ultra-Long Carbon Nanotubes," *The Journal of Physical Chemistry C*, vol. 116, no. 26, pp. 14103–14107, 2012.

[98] Y. Miyauchi, S. Chiashi, Y. Murakami, Y. Hayashida, and S. Maruyama, "Fluorescence spectroscopy of single-walled carbon nanotubes synthesized from alcohol," *Chemical Physics Letters*, vol. 387, no. 1-3, pp. 198–203, 2004.

[99] M. He, L. Zhang, H. Jiang, H. Yang, F. Fossard, H. Cui, Z. Sun, J. B. Wagner, E. I. Kauppinen, and A. Loiseau, "Fe Ti O based catalyst for large-chiral-angle single-walled carbon nanotube growth," *Carbon*, vol. 107, pp. 865–871, oct 2016.

[100] S. M. Bachilo, L. Balzano, J. E. Herrera, F. Pompeo, D. E. Resasco, and R. B. Weisman, "Narrow (n,m)-distribution of single-walled carbon nanotubes grown using a solid supported catalyst," *Journal of the American Chemical Society*, vol. 125, no. 37, pp. 11186–11187, 2003.

[101] X. Li, X. S. C. w. C. S. o. S.-W. C. N. f. C. S. Tu, S. Zaric, K. Welsher, W. S. Seo, W. Zhao, and H. Dai, "Selective Synthesis Combined with Chemical Separation of Single-Walled Carbon Nanotubes for Chirality Selection," *Journal of American Chemical Society*, vol. 129, pp. 15770–15771, dec 2007.

[102] M. He, A. I. Chernov, P. V. Fedotov, E. D. Obraztsova, J. Sainio, E. Rikkinen, H. Jiang, Z. Zhu, Y. Tian, E. I. Kauppinen, M. NiemelaÃà, A. O. I. Krause, and M. Niemela, "Predominant ( 6 , 5 ) Single-Walled Carbon Nanotube Growth on a Copper-Promoted Iron Catalyst," *Journal of the American Chemical Society*, vol. 132, pp. 13994–13996, oct 2010.

[103] M. He, P. V. Fedotov, A. Chernov, E. D. Obraztsova, H. Jiang, N. Wei, H. Cui, J. Sainio, W. Zhang, H. Jin, M. Karppinen, E. I. Kauppinen, and A. Loiseau, "Chiral-selective growth of single-walled carbon nanotubes on Fe-based catalysts using CO as carbon source," *Carbon*, vol. 108, no. July, pp. 521–528, 2016.

[104] H. Wang, L. Wei, F. Ren, Q. Wang, L. D. Pfefferle, G. L. Haller, and Y. Chen, "Chiral-Selective CoSO 4 /SiO 2 Catalyst for (9,8) Single-Walled Carbon Nanotube Growth," *ACS Nano*, vol. 7, pp. 614–626, jan 2013.

[105] W.-H. Chiang and R. Mohan Sankaran, "Linking catalyst composition to chirality distributions of as-grown single-walled carbon nanotubes by tuning NixFe1-x nanoparticles," *Nature Materials*, vol. 8, pp. 882–886, nov 2009.

[106] F. Yang, X. Wang, D. Zhang, J. Yang, D. Luo, Z. Z. Xu, J. Wei, J.-Q. Wang, Z. Z. Xu, F. Peng, X. Li, R. Li, Y. Y. Li, M. Li, X. Bai, F. Ding, and Y. Y. Li, "Chirality-specific growth of single-walled carbon nanotubes on solid alloy catalysts.," *Nature*, vol. 510, no. 7506, pp. 522–4, 2014.

[107] F. Yang, X. Wang, D. Zhang, K. Qi, J. Yang, Z. Xu, M. Li, X. Zhao, X. Bai, and Y. Li, "Growing Zigzag (16,0) Carbon Nanotubes with Structure-Defined Catalysts," *Journal of the American Chemical Society*, vol. 137, no. 27, pp. 8688–8691, 2015.

[108] F. Yang, X. Wang, J. Si, X. Zhao, K. Qi, C. Jin, Z. Zhang, M. Li, D. Zhang, J. Yang, Z. Zhang, Z. Xu, L.-M. Peng, X. Bai, and Y. Li, "Water-Assisted Preparation of High-Purity Semiconducting (14,4) Carbon Nanotubes," *ACS Nano*, p. acsnano.6b06890, 2016.

[109] Y. Yao, Q. Li, J. Zhang, R. Liu, L. Jiao, Y. T. Zhu, and Z. Liu, "Temperature-mediated growth of single-walled carbon-nanotube intramolecular junctions.," *Nature materials*, vol. 6, no. 4, pp. 283–286, 2007.

[110] F. Zhang, P.-X. Hou, C. Liu, and H.-M. Cheng, "Epitaxial growth of single-wall carbon nanotubes," *Carbon*, vol. 102, pp. 181–197, 2016.

[111] R. E. Smalley, Y. Li, V. C. Moore, B. K. Price, R. Colorado, H. K. Schmidt, R. H. Hauge, A. R. Barron, and J. M. Tour, "Single Wall Carbon Nanotube Amplification: En Route to a Type-Specific Growth Mechanism," *Journal of American Chemical Society*, vol. 128, no. 49, pp. 15824–15829, 2006.

[112] Y. Wang, M. J. Kim, H. Shan, C. Kittrell, H. Fan, L. M. Ericson, W. F. Hwang, S. Arepalli, R. H. Hauge, and R. E. Smalley, "Continued growth of single-walled carbon nanotubes," *Nano Letters*, vol. 5, no. 6, pp. 997–1002, 2005.

[113] J. Liu, C. Wang, X. Tu, B. Liu, L. Chen, M. Zheng, and C. Zhou, "Chirality-controlled synthesis of single-wall carbon nanotubes using vapour-phase epitaxy," *Nature Communications*, vol. 3, p. 1199, nov 2012.

[114] H. Omachi, T. Nakayama, E. Takahashi, Y. Segawa, and K. Itami, "Initiation of carbon nanotube growth by well-defined carbon nanorings.," *Nature chemistry*, vol. 5, no. 7, pp. 572–576, 2013.

[115] B. Liu, J. Liu, H. B. Li, R. Bhola, E. A. Jackson, L. T. Scott, A. Page, S. Irle, K. Morokuma, and C. Zhou, "Nearly exclusive growth of small diameter semiconducting single-wall carbon nanotubes from organic chemistry synthetic end-cap molecules," *Nano Letters*, vol. 15, no. 1, pp. 586–595, 2015.

[116] J. R. Sanchez-Valencia, T. Dienel, O. Gröning, I. Shorubalko, A. Mueller, M. Jansen, K. Amsharov, P. Ruffieux, and R. Fasel, "Controlled synthesis of single-chirality carbon nanotubes," *Nature*, vol. 512, pp. 61–64, aug 2014.

[117] W.-H. Chiang, M. Sakr, X. P. A. Gao, and R. M. Sankaran, "Nanoengineering Ni x Fe 1-x Catalysts for Gas-Phase, Selective Synthesis of Semiconducting Single-Walled Carbon Nanotubes," *ACS Nano*, vol. 3, pp. 4023–4032, dec 2009.

[118] A. R. Harutyunyan, G. Chen, T. M. Paronyan, E. M. Pigos, O. A. Kuznetsov, K. Hewaparakrama, S. M. Kim, D. Zakharov, E. A. Stach, and G. U. Sumanasekera, "Preferential growth of single-walled carbon nanotubes with metallic conductivity," *Science*, vol. 326, pp. 116–120, oct 2009.

[119] B. Yu, C. Liu, P. X. Hou, Y. Tian, S. Li, B. Liu, F. Li, E. I. Kauppinen, and H. M. Cheng, "Bulk synthesis of large diameter semiconducting single-walled carbon nanotubes by oxygen-assisted floating catalyst chemical vapor deposition," *Journal of the American Chemical Society*, vol. 133, no. 14, pp. 5232–5235, 2011.

[120] X. Qin, F. Peng, F. Yang, X. He, H. Huang, D. Luo, J. Yang, S. Wang, H. Liu, L. Peng, and Y. Li, "Growth of semiconducting single-walled carbon nanotubes by using ceria as catalyst supports," *Nano Letters*, vol. 14, no. 2, pp. 512–517, 2014.

[121] L. Ding, A. Tselev, J. Wang, D. Yuan, H. Chu, T. P. McNicholas, Y. Li, and J. Liu, "Selective growth of well-aligned semiconducting single-walled carbon nanotubes.," *Nano letters*, vol. 9, no. 2, pp. 800–5, 2009.

[122] Y. Wang, Y. Liu, X. Li, L. Cao, D. Wei, H. Zhang, D. Shi, G. Yu, H. Kajiura, and Y. Li, "Direct enrichment of metallic single-walled carbon nanotubes induced by the different molecular composition of monohydroxy alcohol homologues," *Small*, vol. 3, no. 9, pp. 1486–1490, 2007.

[123] W.-S. Li, P.-X. Hou, C. Liu, D.-M. Sun, J. Yuan, S.-Y. Zhao, L.-C. Yin, H. Cong, and H.-M. Cheng, "High-quality, highly concentrated semiconducting single-wall carbon nanotubes for use in field effect transistors and biosensors.," *ACS nano*, vol. 7, no. 8, pp. 6831–9, 2013.

[124] W. Zhou, S. Zhan, L. Ding, and J. Liu, "General rules for selective growth of enriched semiconducting single walled carbon nanotubes with water vapor as in situ etchant," *Journal of the American Chemical Society*, vol. 134, no. 34, pp. 14019–14026, 2012.

[125] G. Hong, B. Zhang, B. Peng, J. Zhang, W. M. Choi, J.-Y. Choi, J. M. Kim, and Z. Liu, "Direct growth of semiconducting single-walled carbon nanotube array.," *Journal of the American Chemical Society*, vol. 131, no. 41, pp. 14642–14643, 2009.

[126] M. Diarra, A. Zappelli, H. Amara, F. Ducastelle, and C. Bichara, "Importance of carbon solubility and wetting properties of nickel nanoparticles for single wall nanotube growth," *Physical Review Letters*, vol. 109, no. 18, pp. 1–5, 2012.

[127] P. Avouris, Z. Chen, and V. Perebeinos, "Carbon-based electronics.," *Nature nanotechnology*, vol. 2, no. 10, pp. 605–15, 2007.

[128] P. Stallinga and Wiley InterScience (Online service), *Electrical characterization of organic electronic materials and devices*. John Wiley & Sons, 2009.

[129] S. Tans, A. Verschueren, and C. Dekker, "Room-temperature transistor based on a single carbon nanotube," *Nature*, vol. 672, no. 1989, pp. 669–672, 1998.

[130] R. Vargas-Bernal and G. Herrera-Prez, "Carbon Nanotube- and Graphene Based Devices, Circuits and Sensors for VLSI Design," in *VLSI Design*, pp. 41–66, InTech, jan 2012.

[131] Z. Chen, J. Appenzeller, J. Knoch, Y.-m. Lin, and P. Avouris, "The role of metal-nanotube contact in the performance of carbon nanotube field-effect transistors.," *Nano Letters*, vol. 5, no. 7, pp. 1497–502, 2005.

[132] A. Javey, J. Guo, Q. Wang, M. Lundstrom, and H. Dai, "Ballistic carbon nanotube field-effect transistors.," *Nature*, vol. 424, no. 6949, pp. 654–657, 2003.

[133] S. Heinze, J. Tersoff, R. Martel, V. Derycke, J. Appenzeller, and P. Avouris, "Carbon nanotubes as schottky barrier transistors.," *Physical review letters*, vol. 89, no. 10, p. 106801, 2002.

[134] P. Avouris and J. Chen, "Nanotube electronics and optoelectronics," *Materials Today*, vol. 9, pp. 46–54, oct 2006.

[135] H. Dai, "Carbon Nanotubes: Synthesis, Integration, and Properties," *Accounts of Chemical Research*, vol. 35, pp. 1035–1044, dec 2002.

[136] V. Derycke, R. Martel, J. Appenzeller, and P. Avouris, "Carbon Nanotube Inter- and Intramolecular Logic Gates," *Nano Letters*, vol. 1, no. 9, pp. 453–456, 2001.

[137] C. M. Aguirre, P. L. Levesque, M. Paillet, F. Lapointe, B. C. St-Antoine, P. Desjardins, and R. Martel, "The Role of the Oxygen/Water Redox Couple in Suppressing Electron Conduction in Field-Effect Transistors," *Advanced Materials*, vol. 21, pp. 3087–3091, aug 2009.

[138] W. Kim, A. Javey, O. Vermesh, Q. Wang, Y. Li, and H. Dai, "Hysteresis caused by water molecules in carbon nanotube field-effect transistors," *Nano Letters*, vol. 3, no. 2, pp. 193–198, 2003.

[139] P. Bondavalli, P. Legagneux, and D. Pribat, "Carbon nanotubes based transistors as gas sensors: State of the art and critical review," *Sensors and Actuators, B: Chemical*, vol. 140, no. 1, pp. 304–318, 2009.

[140] J. Kong, "Nanotube Molecular Wires as Chemical Sensors," *Science*, vol. 287, pp. 622–625, jan 2000.

[141] J. Zhang, A. Boyd, A. Tselev, M. Paranjape, and P. Barbara, "Mechanism of NO 2 detection in carbon nanotube field effect transistor chemical sensors," *Applied Physics Letters*, vol. 88, no. 12, pp. 10–14, 2006.

[142] S. Auvray, J. Borghetti, M. F. Goffman, A. Filoramo, V. Derycke, J. P. Bourgoin, and O. Jost, "Carbon nanotube transistor optimization by chemical control of the nanotube-metal interface," *Applied Physics Letters*, vol. 84, no. 25, pp. 5106–5108, 2004.

[143] S. M. Bachilo, "Structure-Assigned Optical Spectra of Single-Walled Carbon Nanotubes," *Science*, vol. 298, pp. 2361–2366, dec 2002.

[144] K. Besteman, J. O. Lee, F. G. M. Wiertz, H. A. Heering, and C. Dekker, "Enzyme-coated carbon nanotubes as single-molecule biosensors," *Nano Letters*, vol. 3, no. 6, pp. 727–730, 2003.

[145] A. Hirsch, "Functionalization of single-walled carbon nanotubes," *Angewandte Chemie - International Edition*, vol. 41, no. 11, pp. 1853–1859, 2002.

[146] S. Campidelli, B. Ballesteros, A. Filoramo, D. D. Diaz, G. de la Torre, T. Torres, G. M. A. Rahman, C. Ehli, D. Kiessling, F. Werner, V. Sgobba, D. M. Guldi, C. Cioffi, M. Prato, and J.-P. Bourgoin, "Facile Decoration of Functionalized Single-Wall Carbon Nanotubes with Phthalocyanines via Click Chemistry," *Journal of the American Chemical Society*, vol. 130, pp. 11503–11509, aug 2008.

[147] D. M. Guldi, G. N. a. Rahman, J. Ramey, M. Marcaccio, D. Paolucci, F. Paolucci, S. Qin, W. T. Ford, D. Balbinot, N. Jux, N. Tagmatarchis, and M. Prato, "Donor-acceptor nanoensembles of soluble carbon nanotubes.," *Chemical communications (Cambridge, England)*, vol. 1, no. 18, pp. 2034–2035, 2004.

[148] M. S. Strano, "Electronic Structure Control of Single-Walled Carbon Nanotube Functionalization," *Science*, vol. 301, pp. 1519–1522, sep 2003.

[149] Y. Piao, B. Meany, L. R. Powell, N. Valley, H. Kwon, G. C. Schatz, and Y. Wang, "Brightening of carbon nanotube photoluminescence through the incorporation of sp3 defects.," *Nature chemistry*, vol. 5, no. 10, pp. 840–5, 2013.

[150] A. Setaro, M. Adeli, M. Glaeske, D. Przyrembel, T. Bisswanger, G. Gordeev, F. Maschietto, A. Faghani, B. Paulus, M. Weinelt, R. Arenal, R. Haag, and S. Reich, "Preserving $\pi$-conjugation in covalently functionalized carbon nanotubes for optoelectronic applications," *Nature Communications*, vol. 8, p. 14281, 2017.

[151] D. M. Guldi, G. M. A. Rahman, F. Zerbetto, and M. Prato, "Carbon nanotubes in electron donor - Acceptor nanocomposites," *Accounts of Chemical Research*, vol. 38, no. 11, pp. 871–878, 2005.

[152] C. Roquelet, J.-S. Lauret, V. Alain-rizzo, C. Voisin, R. Fleurier, M. Delarue, D. Garrot, A. Loiseau, P. Roussignol, J. A. Delaire, and E. Deleporte, "Pi-stacking functionalization through micelles swelling: Application to the synthesis of single wall carbon nanotube/porphyrin complexes for energy transfer," *Condensed matter*, pp. 1–6, oct 2009.

[153] P. D. Tran, A. Le Goff, J. Heidkamp, B. Jousselme, N. Guillet, S. Palacin, H. Dau, M. Fontecave, and V. Artero, "Noncovalent modification of carbon nanotubes with pyrene-functionalized nickel complexes: Carbon monoxide tolerant catalysts for hydrogen evolution and uptake," *Angewandte Chemie - International Edition*, vol. 50, no. 6, pp. 1371–1374, 2011.

[154] L. Hu, Y. L. Zhao, K. Ryu, C. Zhou, J. F. Stoddart, and G. Grüner, "Light-induced charge transfer in pyrene/CdSe-SWNT hybrids," *Advanced Materials*, vol. 20, no. 5, pp. 939–946, 2008.

[155] X. Dang, H. Yi, M.-h. Ham, J. Qi, D. S. Yun, R. Ladewski, M. S. Strano, P. T. Hammond, and A. M. Belcher, "Virus-templated self-assembled single-walled carbon nanotubes for highly efficient electron collection in photovoltaic devices," *Nature Nanotechnology*, vol. 6, no. 6, pp. 377–384, 2011.

[156] C. Kittrell, J. Ma, R. H. Hauge, R. B. Weisman, R. E. Smalley, M. J. O'Connell, S. M. Bachilo, C. B. Huffman, V. C. Moore, M. S. Strano, E. H. Haroz, K. L. Rialon, P. J. Boul, and W. H. Noon, "Band Gap Fluorescence from Individual Single-Walled Carbon Nanotubes," *Science*, vol. 297, no. 5581, pp. 593–596, 2002.

[157] J. Borghetti, V. Derycke, S. Lenfant, P. Chenevier, A. Filoramo, M. Goffman, D. Vuillaume, and J. P. Bourgoin, "Optoelectronic switch and memory devices based on polymer-functionalized carbon nanotube transistors," *Advanced Materials*, vol. 18, no. 19, pp. 2535–2540, 2006.

[158] C. Ehli, C. Oelsner, D. M. Guldi, A. Mateo-Alonso, M. Prato, C. Schmidt, C. Backes, F. Hauke, and A. Hirsch, "Manipulating single-wall carbon nanotubes by chemical doping and charge transfer with perylene dyes," *Nature Chemistry*, vol. 1, pp. 243–249, jun 2009.

[159] Y. Chen, G. Royal, E. Flahaut, S. Cobo, V. Bouchiat, L. Marty, and N. Bendiab, "Light Control of Charge Transfer and Excitonic Transitions in a Carbon Nanotube/Porphyrin Hybrid," *Advanced Materials*, vol. 29, p. 1605745, may 2017.

[160] A. M. Rao, P. C. Eklund, S. Bandow, A. Thess, and R. E. Smalley, "Evidence for charge transfer in doped carbon nanotube bundles from Raman scattering," *Nature*, vol. 388, pp. 257–259, jul 1997.

[161] R. Saito, M. Hofmann, G. Dresselhaus, A. Jorio, and M. S. Dresselhaus, "Raman spectroscopy of graphene and carbon nanotubes," *Advances in Physics*, vol. 60, pp. 413–550, jun 2011.

[162] C. Thomsen and S. Reich, "Raman Scattering in Carbon Nanotubes," *Carbon Nanotubes*, vol. 232, pp. 115–234, 2007.

[163] M. S. Dresselhaus, "Fifty years in studying carbon-based materials," *Physica Scripta*, vol. T146, pp. 1–10, 2012.

[164] A. Jorio, R. Saito, J. H. Hafner, C. M. Lieber, M. Hunter, T. McClure, G. Dresselhaus, and M. S. Dresselhaus, "Structural (n,m) Determination of Isolated Single-Wall Carbon Nanotubes by Resonant Raman Scattering," *Physical Review Letters*, vol. 86, pp. 1118–1121, feb 2001.

[165] P. T. Araujo, S. K. Doorn, S. Kilina, S. Tretiak, E. Einarsson, S. Maruyama, H. Chacham, M. A. Pimenta, and A. Jorio, "Third and fourth optical transitions in semiconducting carbon nanotubes.," *Physical review letters*, vol. 98, p. 067401, feb 2007.

[166] P. T. Araujo, I. O. Maciel, P. B. C. Pesce, M. A. Pimenta, S. K. Doorn, H. Qian, A. Hartschuh, M. Steiner, L. Grigorian, K. Hata, and A. Jorio, "Nature of the constant factor in the relation between radial breathing mode frequency and tube diameter for single-wall carbon nanotubes," *Physical Review B*, vol. 77, p. 241403, jun 2008.

[167] M. A. Pimenta, A. Jorio, S. D. M. Brown, A. G. Souza Filho, G. Dresselhaus, J. H. Hafner, C. M. Lieber, R. Saito, and M. S. Dresselhaus, "Diameter dependence of the Raman D-band in isolated single-wall carbon nanotubes," *Physical Review B*, vol. 64, p. 041401, jun 2001.

[168] A. Ghedjatti, *Etude structurale des nanotubes de carbone double parois*. PhD thesis, Pierre et Marie Curie Paris VI, 2016.

[169] "www2.warwick.ac.uk/fac/sci/physics/research/condensedmatt/microscopy/facilities/jeol2100/eels/."

[170] "https://creativecommons.org/licenses/by-sa/4.0."

[171] "http://www.nanophys.kth.se/nanophys/facilities/nfl/afm/fast-scan/bruker-help/Content/TappingMode%20AFM/TappingMode%20AFM.htm."

[172] "Https://fys.kuleuven.be/iks/nvsf/experimental-facilities/x-ray-diffraction-2013-bruker-d8-discover."

[173] Https://wiki.utep.edu/pages/viewpage.action?pageId=51217144, "* X-ray Photoelectron Spectroscopy (XPS)* - Jose Chavez - Confluence."

[174] "https://en.wikipedia.org/wiki/File:Schematic_of_UV-_visible_spectrophotometer.png."

[175] "https://www.lambertinstruments.com/technologies-1/2014/12/4/frequency-domain-flim-basic-equations."

[176] L. Catala, D. Brinzei, Y. Prado, A. Gloter, O. Stéphan, G. Rogez, and T. Mallah, "Core-multishell magnetic coordination nanoparticles: Toward multifunctionality on the nanoscale," *Angewandte Chemie - International Edition*, vol. 48, no. 1, pp. 183–187, 2009.

[177] Y. Prado, L. Lisnard, D. Heurtaux, G. Rogez, A. Gloter, O. Stéphan, N. Dia, E. Rivière, L. Catala, and T. Mallah, "Tailored coordination nanoparticles: assessing the magnetic single-domain critical size," *Chemical Communications*, vol. 47, no. 3, pp. 1051–1053, 2011.

[178] S. Tricard, B. Fleury, F. Volatron, C. Costa-Coquelard, S. Mazerat, V. Huc, C. David, F. Brisset, F. Miserque, P. Jegou, S. Palacin, and T. Mallah, "Growth and density control of nanometric nickel-iron cyanide-bridged objects on functionalized Si(100) surface.," *Chemical communications (Cambridge, England)*, vol. 46, no. 24, pp. 4327–9, 2010.

[179] A. Ludi and H. U. Güdel, "Structural chemistry of polynuclear transition metal cyanides," *Inorganic Chemistry*, pp. 1–21, 1973.

[180] L. Catala, T. Gacoin, J. P. Boilot, É. Rivière, C. Paulsen, E. Lhotel, and T. Mallah, "Cyanide-bridged CrIII-NiII superparamagnetic nanoparticles," *Advanced Materials*, vol. 15, no. 10, pp. 826–829, 2003.

[181] T. Mallah, S. Tricard, and F. Charra, "Sequential growth at the sub 10 nm scale of cyanide bridged coordination networks on inorganic surfaces," *Dalton Transactions*, no. 1990, pp. 15835–15845, 2013.

[182] T. B. Massalski, *Binary Alloy Phase Diagrams, 2nd Edition*. ASM International, 1990.

[183] L. Jiao, B. Fan, X. Xian, Z. Wu, J. Zhang, and Z. Liu, "Creation of Nanostructures with Poly(methyl methacrylate) -Mediated Nanotransfer Printing," *Journal of the American Chemical Society*, vol. 130, no. 38, pp. 12612–12613, 2008.

[184] Y. He, D. Li, T. Li, X. Lin, J. Zhang, Y. Wei, P. Liu, L. Zhang, J. Wang, Q. Li, S. Fan, and K. Jiang, "Metal-film-assisted ultra-clean transfer of single-walled carbon nanotubes," *Nano Research*, vol. 7, pp. 981–989, 2014.

[185] Y. Zhang, J. Zhang, H. Son, J. Kong, and Z. Liu, "Substrate-Induced Raman Frequency Variation for Single-Walled Carbon Nanotubes," *Journal of American Chemical Society*, vol. 127, no. 49, pp. 17156–17157, 2005.

[186] G. Lolli, L. Zhang, L. Balzano, N. Sakulchaicharoen, Y. Tan, and D. E. Resasco, "Tailoring ( n , m ) Structure of Single-Walled Carbon Nanotubes by Modifying Reaction Conditions and the Nature of the Support of CoMo Catalysts," *The Journal of Physical Chemistry B*, vol. 110, pp. 2108–2115, feb 2006.

[187] Y. Magnin, A. Zappelli, H. Amara, F. Ducastelle, and C. Bichara, "Size Dependent Phase Diagrams of Nickel-Carbon Nanoparticles," *Physical Review Letters*, vol. 115, no. 20, 2015.

[188] M. Picher, E. Anglaret, R. Arenal, and V. Jourdain, "Processes Controlling the Diameter Distribution of Single-Walled Carbon Nanotubes during Catalytic Chemical Vapor Deposition," *ACS Nano*, vol. 5, pp. 2118–2125, mar 2011.

[189] H. Jeong, L. Eude, M. Gowtham, B. Marquardt, S. Lim, S. Enouz, C. Cojocaru, K. Park, Y. Lee, and D. Pribat, "Atomic hydrogen-driven size control of catalytic nanoparticles for single-walled carbon nanotube growth," *Nano*, vol. 3, no. 3, pp. 145–153, 2008.

[190] F. Z. Bouanis, C. S. Cojocaru, V. Huc, E. Norman, M. Chaigneau, J.-L. Maurice, T. Mallah, and D. Pribat, "Direct Synthesis and Integration of Individual, Diameter-Controlled Single-Walled Nanotubes (SWNTs)," *Chemistry of Materials*, vol. 26, pp. 5074–5082, sep 2014.

[191] A. Castan, S. Forel, L. Catala, I. Florea, F. Fossard, F. Bouanis, A. Andrieux-Ledier, S. Mazerat, T. Mallah, V. Huc, A. Loiseau, and C. S. Cojocaru, "New method for the growth of single-walled carbon nanotubes from bimetallic nanoalloy catalysts based on Prussian blue analog precursors," *Carbon*, vol. 123, pp. 583–592, 2017.

[192] M. He, H. Amara, H. Jiang, J. Hassinen, C. Bichara, R. H. A. Ras, J. Lehtonen, E. I. Kauppinen, and A. Loiseau, "Key roles of carbon solubility in single-walled carbon nanotube nucleation and growth," *Nanoscale*, vol. 7, no. 47, pp. 20284–20289, 2015.

[193] H. Amara and C. Bichara, "Modeling the Growth of Single-Wall Carbon Nanotubes," *Topics in Current Chemistry*, vol. 375, p. 55, jun 2017.

[194] A. Moisala, A. G. Nasibulin, and E. I. Kauppinen, "The role of metal nanoparticles in the catalytic production of single-walled carbon nanotubes, review," *Journal of Physics: Condensed Matter*, vol. 15, pp. S3011–S3035, oct 2003.

[195] E. Einarsson, Y. Murakami, M. Kadowaki, and S. Maruyama, "Growth dynamics of vertically aligned single-walled carbon nanotubes from in situ measurements," *Carbon*, vol. 46, no. 6, pp. 923–930, 2008.

[196] B. Straumal, B. Baretzky, A. Mazilkin, S. Protasova, A. Myatiev, and P. Straumal, "Increase of Mn solubility with decreasing grain size in ZnO," *Journal of the European Ceramic Society*, vol. 29, no. 10, pp. 1963–1970, 2009.

[197] H. Yasuda and H. Mori, "Phase diagrams in nanometer-sized alloy systems," *Journal of Crystal Growth*, vol. 237-239, no. 1 4I, pp. 234–238, 2002.

[198] G. Ouyang, X. Tan, C. X. Wang, and G. W. Yang, "Solid solubility limit in alloying nanoparticles," *Nanotechnology*, vol. 17, no. 16, pp. 4257–4262, 2006.

[199] J. P. Petropoulos, T. R. Cristiani, P. B. Dongmo, and J. M. O. Zide, "A simple thermodynamic model for the doping and alloying of nanoparticles," *Nanotechnology*, vol. 22, no. 24, p. 245704, 2011.

[200] E. A. Sutter and P. W. Sutter, "Giant carbon solubility in Au nanoparticles," *Journal of Materials Science*, vol. 46, no. 22, pp. 7090–7097, 2011.

[201] F. Ding and K. Bolton, "The importance of supersaturated carbon concentration and its distribution in catalytic particles for single-walled carbon nanotube nucleation," *Nanotechnology*, vol. 17, no. 2, pp. 543–548, 2006.

[202] H. Navas, M. Picher, A. Andrieux-Ledier, F. Fossard, T. Michel, A. Kozawa, T. Maruyama, E. Anglaret, A. Loiseau, and V. Jourdain, "Unveiling the Evolutions of Nanotube Diameter Distribution during the Growth of Single-Walled Carbon Nanotubes," *ACS Nano*, pp. 3081–3088, 2017.

[203] J. M. Aguiar-Hualde, Y. Magnin, H. Amara, and C. Bichara, "Probing the role of carbon solubility in transition metal catalyzing single-walled carbon nanotubes growth," *Carbon*, vol. 120, pp. 226–232, 2017.

[204] G. Zhang, P. Qi, X. Wang, Y. Lu, X. Li, R. Tu, S. Bangsaruntip, D. Mann, L. Zhang, and H. Dai, "Selective Etching of Metallic Carbon Nanotubes by Gas-Phase Reaction," *Science*, vol. 314, pp. 974–977, nov 2006.

[205] H. Okamoto, "Ni-Ru (Nickel-Ruthenium)," *Journal of Phase Equilibria and Diffusion*, vol. 30, no. 4, p. 412, 2009.

[206] P. G. Collins, M. S. Arnold, and P. Avouris, "Engineering Carbon Nanotubes and Nanotube Circuits Using Electrical Breakdown," *Science*, vol. 292, no. 5517, pp. 706–709, 2001.

[207] G. J. Brady, A. J. Way, N. S. Safron, H. T. Evensen, P. Gopalan, and M. S. Arnold, "Quasi-ballistic carbon nanotube array transistors with current density exceeding Si and GaAs," *Science Advances*, vol. 2, pp. e1601240–e1601240, sep 2016.

[208] P. Laiho, K. Mustonen, Y. Ohno, S. Maruyama, and E. I. Kauppinen, "Dry and Direct Deposition of Aerosol-Synthesized Single-Walled Carbon Nanotubes by Thermophoresis," *ACS Applied Materials and Interfaces*, vol. 9, no. 24, pp. 20738–20747, 2017.

[209] D.-m. Sun, M. Y. Timmermans, Y. Tian, A. G. Nasibulin, E. I. Kauppinen, S. Kishimoto, T. Mizutani, and Y. Ohno, "Flexible high-performance carbon nanotube integrated circuits," *Nature Nanotechnology*, vol. 6, no. 3, pp. 156–161, 2011.

[210] K. Otsuka, T. Inoue, Y. Shimomura, S. Chiashi, and S. Maruyama, "Water-assisted self-sustained burning of metallic single-walled carbon nanotubes for scalable transistor fabrication," *Nano Research*, pp. 1–13, 2017.

[211] B. Gao, Y. Zhang, J. Zhang, J. Kong, and Z. Liu, "Systematic comparison of the Raman spectra of metallic and semiconducting SWNTs," *Journal of Physical Chemistry C*, vol. 112, no. 22, pp. 8319–8323, 2008.

[212] J. Li, Y. Lu, Q. Ye, J. Han, and M. Meyyappan, "Carbon Nanotube Based Chemical Sensors for Gas and Vapor Detection," *Chemical Physics Letters*, vol. 313, no. 2, p. 91, 1999.

[213] J. Zhao, A. Buldum, J. Han, and J. P. Lu, "Gas molecule adsorption in carbon nanotubes and nanotube bundles," *Nanotechnology*, vol. 13, pp. 195–200, apr 2002.

[214] X. Liu, Z. Luo, S. Han, T. Tang, D. Zhang, and C. Zhou, "Band engineering of carbon nanotube field-effect transistors via selected area chemical gating," *Applied Physics Letters*, vol. 86, no. 24, pp. 1–3, 2005.

[215] S. Peng and K. Cho, "Chemical control of nanotube electronics," *Nanotechnology*, vol. 11, no. 2, pp. 57–60, 2000.

[216] C. Ehli, G. M. A. Rahman, N. Jux, D. Balbinot, D. M. Guldi, F. Paolucci, M. Marcaccio, D. Paolucci, M. Melle-Franco, F. Zerbetto, S. Campidelli, and M. Prato, "Interactions in Single Wall Carbon Nanotubes/Pyrene/Porphyrin Nanohybrids," *Journal of the American Chemical Society*, vol. 128, pp. 11222–11231, aug 2006.

[217] Y.-L. Zhao, L. Hu, J. F. Stoddart, and G. Grüner, "Pyrenecyclodextrin-Decorated Single-Walled Carbon Nanotube Field-Effect Transistors as Chemical Sensors," *Advanced Materials*, vol. 20, pp. 1910–1915, may 2008.

[218] Y. Choi, I. S. Moody, P. C. Sims, S. R. Hunt, B. L. Corso, I. Perez, G. A. Weiss, and P. G. Collins, "Single-Molecule Lysozyme Dynamics Monitored by an Electronic Circuit," *Science*, vol. 335, pp. 319–324, jan 2012.

[219] C. Roquelet, J.-s. Lauret, V. Alain-rizzo, C. Voisin, R. Fleurier, M. Delarue, D. Garrot, A. Loiseau, P. Roussignol, J. A. Delaire, and E. Deleporte, "$\Pi$-Stacking Functionalization of Carbon Nanotubes through Micelle Swelling," *ChemPhysChem*, vol. 11, pp. 1667–1672, jun 2010.

[220] S. Berger, F. Iglesias, P. Bonnet, C. Voisin, G. Cassabois, J.-S. S. Lauret, C. Delalande, and P. Roussignol, "Optical properties of carbon nanotubes in a composite material: The role of dielectric screening and thermal expansion," *Journal of Applied Physics*, vol. 105, p. 094323, may 2009.

[221] T. Ando, "Environment effects on excitons in semiconducting carbon nanotubes," *Journal of the Physical Society of Japan*, vol. 79, no. 2, 2010.

[222] F. D'Souza, R. Chitta, A. S. D. Sandanayaka, N. K. Subbaiyan, L. D'Souza, Y. Araki, and O. Ito, "Supramolecular carbon nanotube-fullerene donor-acceptor hybrids for photoinduced electron transfer," *Journal of the American Chemical Society*, vol. 129, no. 51, pp. 15865–15871, 2007.

[223] A. Setaro, P. Bluemmel, C. Maity, S. Hecht, and S. Reich, "Non-covalent functionalization of individual nanotubes with spiropyran-based molecular switches," *Advanced Functional Materials*, vol. 22, no. 11, pp. 2425–2431, 2012.

[224] G. Magadur, *Assemblage de complexes inorganiques sur nanotubes de carbone monoparoi : Applications a la spintronique moleculaire et a la photocatalyse*. PhD thesis, Université Paris Sud, 2013.

[225] S. H. Hur, C. Kocabas, A. Gaur, O. O. Park, M. Shim, and J. A. Rogers, "Printed thin-film transistors and complementary logic gates that use polymer-coated single-walled carbon nanotube networks," *Journal of Applied Physics*, vol. 98, no. 11, 2005.

[226] J. Appenzeller, J. Knoch, V. Derycke, R. Martel, S. Wind, and P. Avouris, "Field-modulated carrier transport in carbon nanotube transistors.," *Physical review letters*, vol. 89, no. 12, p. 126801, 2002.

[227] D. A. Britz and A. N. Khlobystov, "Noncovalent interactions of molecules with single walled carbon nanotubes.," *Chemical Society reviews*, vol. 35, no. 7, pp. 637–59, 2006.

[228] L. Alvarez, Y. Almadori, A. Belhboub, R. Le Parc, R. Aznar, P. Dieudonné-George, A. Rahmani, P. Hermet, F. Fossard, A. Loiseau, B. Jousselme, S. Campidelli, T. Saito, G. Wang, and J.-L. Bantignies, "Supramolecular organization of pi-conjugated molecules monitored by single-walled carbon nanotubes," *Journal of Nanophotonics*, vol. 10, no. 1, p. 012514, 2015.

[229] T. Hertel, R. E. Walkup, and P. Avouris, "Deformation of carbon nanotubes by surface van der Waals forces," *Phys. Rev. B*, vol. 58, no. 20, pp. 13870–13873, 1998.

[230] G. J. Wilson, A. Launikonis, W. H. F. Sasse, and A. W.-H. Mau, "Excited-State Processes in Ruthenium(II) Bipyridine Complexes Containing Covalently Bound Arenes," *The Journal of Physical Chemistry A*, vol. 101, no. 27, pp. 4860–4866, 1997.

[231] G. J. Bahun and A. Adronov, "Interactions of carbon nanotubes with pyrene-functionalized linear-dendritic hybrid polymers," *Journal of Polymer Science, Part A: Polymer Chemistry*, vol. 48, no. 5, pp. 1016–1028, 2010.

[232] P. a. Anderson, F. Richard Keene, T. J. Meyer, J. a. Moss, G. F. Strouse, and J. a. Treadway, "Manipulating the properties of MLCT excited states," *Journal of the Chemical Society, Dalton Transactions*, no. 20, p. 3820, 2002.

[233] T. Yanai, D. P. Tew, and N. C. Handy, "A new hybrid exchange-correlation functional using the Coulomb-attenuating method (CAM-B3LYP)," *Chemical Physics Letters*, vol. 393, no. 1-3, pp. 51–57, 2004.

[234] A. D. Mohite, T. S. Santos, J. S. Moodera, and B. W. Alphenaar, "Observation of the triplet exciton in EuS-coated single-walled nanotubes.," *Nature nanotechnology*, vol. 4, no. June 2009, pp. 425–429, 2009.

[235] D. Stich, F. Späth, H. Kraus, A. Sperlich, V. Dyakonov, and T. Hertel, "Triplet-triplet exciton dynamics in single-walled carbon nanotubes," *Nature Photonics*, vol. 8, pp. 139–144, dec 2013.

# List of abreviations

| | |
|---|---|
| **AFM** | Atomic Force Microscopy |
| **BSE** | Back-Scattered Electrons |
| **bpy** | Bipyridine |
| **BZ** | Brillouin Zone |
| **CNT** | Carbon Nanotube |
| **CCVD** | Catalyst assisted Chemical Vapor Deposition |
| **CL** | Cathodoluminescence |
| **CVD** | Chemical Vapor Deposition |
| **CoMoCat** | Cobalt Molybene Catalyst |
| **DFT** | Density Functional Theory |
| **DOS** | Density Of State |
| **DNA** | Deoxyribonucleic Acid |
| **DCE** | Dichloroethane |
| **DCM** | Dichloromethane |
| **d-HFCVD** | double Hot Filament Chemical Vapor Deposition |
| **EELS** | Electron Energy Loss Spectroscopy |
| **EDX/EDS** | Energy-Dispersive X-ray spectroscopy |
| **ETB** | Extended Tight Binding |
| **FCC** | Face Centered Cubic |
| **FENIX** | Facility for Elaboration of Nanomaterials with In-situ at X |
| **Ef** | Fermi level |
| **FET** | Field Effect Transistor |
| **FWHM** | Full Width Half Maximum |
| **HAADF** | High Angle Annular Dark Field |
| **HiPco** | High Pressure catalytic decomposition of Carbon monoxide catalyst |
| **HOMO** | Highest Occupied Molecular Orbital |
| **HRTEM** | High-Resolution Transmission Electronic Microscopy |
| **HFCVD** | Hot Filament Chemical Vapor Deposition |
| **Ih** | Icosahedral |
| **IR** | Infrared |
| **S** | Inverse sub-threshold slope |
| **JFET** | Junction Field-Effect Transistor |
| **LOMO** | Lowest Unoccupied Molecular Orbtals |
| **MeCN** | Acetonitrile |
| **MLCT** | Metal Ligand Charge Transfer |
| **m-SWCNT** | metallic Single Wall Carbon Nanotube |
| **MOSFET** | Metal Oxide semiconductor Field Effect Transistor |
| **MWCNT** | Multi-Walls Carbon Nanotubes |
| **NP** | Nanoparticle |
| **OD** | Optical Density |

| | |
|---|---|
| **PL** | Photoluminescence |
| **PLE** | Photoluminescence Excitation |
| **PECVD** | Plasma Enhanced Chemical Vapor Deposition |
| **PMMA** | Poly(Methyl-Methacrylate) |
| **PBA** | Prussian Blue analog |
| **Pyr** | Pyrene |
| **RBM** | Radial Breathing Mode |
| **SEM** | Scanning Electron Microscopy |
| **STEM** | Scanning Transmission Electronic Microscopy |
| **SB** | Schottky Barrier |
| **SE** | Secondary Electrons |
| **SAM** | Self Assembled Monolayer |
| **s-SWCNT** | semiconducting Single Wall Carbon Nanotube |
| **SWCNT** | Single Wall Carbon Nanotube |
| **SOMO** | Singly Occupied Molecular Orbitals |
| **Vth** | Threshold Voltage |
| **TB** | Tight Binding |
| **TEM** | Transmission Electronic Microscopy |
| **TFA** | Trifluoroacetic Acid |
| **TW** | Trigonal Wrapping |
| **UV-VIS-NIR** | Ultraviolet–Visible-Near infrared |
| **VHS** | Van Hove Singularities |
| **VLS** | Vapor–Liquid–Solid |
| **VSS** | Vapor-Solid-Solid |
| **XPS** | X-Ray Photoelectron Spectroscopy |
| **XRD** | X-Ray Diffraction |
| **XRPD** | X-ray Powder Diffraction |

université PARIS-SACLAY
ÉCOLE DOCTORALE
INTERFACES
Approches Interdisciplinaires : Fondements, Applications et Innovation

**Titre :** Croissance de nanotubes de carbone monoparoi à partir de nanoparticules bimétalliques : une étude paramétrique de la synthèse jusqu'aux potentielles applications en nanoélectroniques.

**Mots clefs :** SWCNT, synthèse, nanoparticules bimetalliques , transistor à effet de champs, fonctionnalisation
**Résumé :** Ce manuscrit présente une étude expérimentale autour de la synthèse des nanotubes de carbone et de leurs possibles intégrations dans des dispositifs. Les remarquables propriétés électroniques et optiques des nanotubes en font un matériau de choix pour entre autres, la nanoélectronique. Néanmoins, l'intégration des nanotubes dans des dispositifs performants est encore aujourd'hui un défi. Cela repose principalement sur la difficulté d'obtenir de grandes quantités de nanotubes mono-paroi avec des propriétés uniformes, propriétés qui sont définies par la structure du nanotube (i.e. leur angle chiral et leur diamètre). Ainsi, réaliser des synthèses de nanotube de carbone avec un contrôle de leur structure représente un point clé pour le progrès dans ce domaine. Nous avons donc mis en place une nouvelle méthode de synthèse de nanotubes de carbone basée sur la chimie de coordination et le dépôt chimique en phase vapeur activé par filament chaud. Cette synthèse permet la conception de nombreux nouveaux catalyseurs bimétalliques pour la croissance des nanotubes de carbone. Comme le procédé mis en place est très générique, des études paramétriques peuvent être réalisées de manière à mieux comprendre l'influence des différents paramètres de la croissance sur la structure des nanotubes obtenue. Nous discuterons ici du rôle de la température et de la composition chimique du catalyseur. Les nanotubes obtenus sont principalement caractérisés par spectroscopie Raman et par microscopies électroniques.
Afin de valider les observations obtenues par spectroscopie Raman, les nanotubes synthétisés ont aussi été intégrés dans des dispositifs de type transistor à effet de champ. Une analyse des performances des transistors en fonction des différents nanotubes utilisés dans le canal est présentée.
Enfin, les nanotubes intégrés dans ces transistors ont été fonctionnalisés avec un chromophore de ruthénium. Nous avons montré que cette fonctionnalisation nous permet de moduler, grâce à une impulsion lumineuse, la conductivité du dispositif sur trois ordres de grandeur.

**Title :** SWCNT growth from bimetallic nanoparticles : a parametric study of the synthesis up to potential applications in nano-electronics.

**Keywords :** SWCNT, synthesis, bimetallic nanoparticle, FET-device, functionalization
**Abstract :** This manuscript presents an experimental study around the single wall carbon nanotube (SWCNT) synthesis and their possible integration in nanodevices. The unique electronic and optical properties of carbon nanotubes make them a choice material for various applications, particularly in nano-electronics. Nevertheless, their integration in effective devices is still a challenge. This is mainly due to the difficulty to obtain large quantity of SWCNT with uniform properties, defined by their structure (i.e. chiral angle and diameter). Therefore, structure controlled growth of SWCNTs is a key point for progress in this field.
Here, we established a new synthesis approach based on coordination chemistry and hot-filament chemical vapor deposition. This approach allows the design of various bimetallic catalyst nanoparticles for the SWCNT growth. As the synthetic process is generic, parametric study can be performed in order to better understand the influence of the various parameters on the structure of the as-grown SWCNTs. In particular, we will discuss the role of the growth temperature and the chemical composition of the catalyst on the final SWCNTs structure. The obtained SWCNTs are mainly characterized by Raman spectroscopy and electronic microscopy.
In order to validate the observations performed by Raman measurement, the synthesized SWCNTs have been also integrated in field effect transistors (FET) devices. An analysis of the performance of the FET-device as a function of the SWCNTs used in its channel will be presented.
Finally, SWCNTs integrated in these transistors have been functionalized with an inorganic chromophore of ruthenium. We demonstrate that the functionalization of the SWCNTs leads to a three order of magnitude reversible switch of the device conductivity triggered by visible light.

**Université Paris-Saclay**
Espace Technologique / Immeuble Discovery
Route de l'Orme aux Merisiers RD 128 / 91190 Saint-Aubin, France